

A Study of Trace Metals in the Surface Microlayer

A thesis submitted to the School of Environmental Sciences of the University of East Anglia in partial fulfilment of the requirements for the degree of Doctor of Philosophy

By

Matthew Ross Jones

September 2011

© This copy of the thesis has been supplied on condition that anyone who consults it is understood to recognise that its copyright rests with the author and that use of any information derived there from must be in accordance with current UK Copyright Law. In addition, any quotation or extract must include full attribution.

Intentionally Blank

Abstract

The processes that dissolved trace metals undergo in the surface microlayer are poorly characterised due to the lack of measurements. However, aquatic processes are extensively characterised and were used to infer processes occurring on trace metals within the microlayer. This work addressed this issue by studying the operationally dissolved fraction (0.2 μm) of iron and other metals: aluminium, manganese, copper, cobalt and arsenic, in the surface microlayer and elucidating their relationships through the progression of a seasonal cycle in a lake. The experimental work provides an insight into the interactions of reduced iron and reactive oxygen species, especially hydrogen peroxide. Their relationship was assessed through three sets of experiments: i) The addition of artificial particulate phases of aluminium, manganese and iron to photochemically active experimental systems; ii) the effect of different irradiating wavelengths on production and loss of hydrogen peroxide and Fe(II) and iii) the affect of atmospheric ozone concentrations on hydrogen peroxide and Fe(II). To undertake these analyses a simple dual analyte, Fe(II) and hydrogen peroxide, configuration was applied to a FIA-Cl system, using luminol, allowing for their quasi-simultaneous measurement. Experimental work considers model marine microlayers over short-term (< 1 hour). Results from the experimental work were used to constrain simple iron and reactive oxygen species models. The model allowed a calculation of kinetic rate constants; amongst these were the rates in relation to the production of superoxide, the ligand to metal charge transfer production of Fe(II) and the rate of superoxide reduction of Fe(III). This work shows that dissolved metals in the surface microlayer are balanced through the interactions of light and particulate material and potentially ozone and particulate material. With respect to irradiating regime there is a distinct measured change in the rates of change of organic constituents as irradiating regime wavelengths increase.

Acknowledgements

To all the folks who helped me thank you indeed. Special thanks goes to my team of supervisors, Prof. Peter Liss, Dr Suzanne Turner, Dr Manuela Martino and Dr Phil Nightingale for all their help, advice and understanding through the course of this project. A thank you to the entire UEA ENV laboratory staff, especially Graham Chilvers for his help and support when using the ICP-MS – I have to say sorry for all that salt that got through. The project would not have been what it is if it were not for Nick Griffin and Simon Cowley for building the FIA-Cl and appropriate software. Thank you also to Dr Peter Croot who set me on the road with the knowledge to use the FIA-Cl system and provide advice on the best way to undertake modelling minimisation. A thank you also to Dr Christop Voelker for his practical tips on iron modelling. To Dr Anthony Kettle, Dr Frankie Hopkins and Godwin Unazi and all those who helped with microlayer sampling, thank you for the patience and fortitude you showed during our exploits removing the microlayer. Jamie, two years in a little rubber boat was a long time. This project and I would not be where we are today if it were not for fellow colleagues and students who have given advice, listened intently and for my friends assisted me away from and helped me back to earth and work. To my family; Nami, who has shown the greatest patience and understanding of all and to Olivia and Winston thank you for the perfect excuse for removing my brain from work. Finally, a note to myself: time to stop.

This work was funded through the NERC Blue Skies Ph.D programme; grant number
NER/S/A/2006/14115.

Table of Contents

Abstract	I
Acknowledgements	II
Contents	III
List of Figures	VIII
List of Tables	XI
List of Abbreviations and Acronyms	XIII
Thesis	XVII

Contents

	page
Chapter One: Introduction	1
1.00 The Surface Microlayer	2
1.01 The Research	5
1.02 The Metals	6
1.03 Organic Material	7
1.04 Photochemistry	9
1.05 Oxidation	10
1.06 Reduction	11
1.07 Hydrogen Peroxide	12
1.08 Ozone	13
1.09 The Research Revisited	15
Chapter Two: General Methods	17
2.00 Introduction	18
2.01 Trace Metal Equipment Cleaning and Sample Handling	18
2.01.01 Equipment Washing	18
2.01.02 Filtration and Storage	19
2.01.03 Dilution and Standard Additions	19
2.02 Broadwater Chlorophyll- α	20

2.03	Metal/Species Specific Analytical Techniques	21
2.04	Inductively Coupled Plasma Mass Spectrometry	21
2.04.01	ICP Multi-Element Techniques	22
2.04.02	ICP-MS	24
2.04.03	Stability	24
2.04.04	Signal Interference Mitigation	26
2.04.05	Analytical Blank	27
2.04.06	Accuracy – CRM Recovery	28
2.04.07	CRM Recoveries as Correction Factors	28
2.04.08	Method for Seawater Experimental Samples	29
2.04.09	ICP-MS Final Configurations	30
Chapter Three: Flow Injection Analysis Method Development		31
3.00	Introduction	32
3.01	Flow Injection Analysis - Chemiluminescence with Luminol	32
3.01.01	Hardware Configuration	34
3.01.02	Valve Configuration	36
3.01.03	Luminol Recipe	37
3.02	Hydrogen Peroxide Analysis	37
3.02.01	H_2O_2 Standards	37
3.02.02	H_2O_2 Development	39
3.02.03	Blank Signal	40
3.03	Iron (II) Analysis	41
3.03.01	Iron (II) Interferences	41
3.03.02	Iron (II) Analysis in Acidified UPW	43
3.03.03	Discrete Iron (II) Measurement	47
3.03.04	Chelex-100 Cleaned Seawater	49
3.03.05	Real Time Iron (II) Calibrations	50
3.03.06	Iron (II) Sensitivity	51
3.04	Quasi-Simultaneous Analysis of Two Analytes	53

Chapter Four: Trace Metals in a Lacustrine Surface Microlayer 55

4.00	Introduction	56
4.01	Sampling Devices	57
4.02	Methods	59
4.02.01	Sample Site	59
4.02.02	Sampling	60
4.03	Ancillary Parameters	62
4.03.01	Meteorological Data	63
4.03.02	Physiochemical Parameters	65
4.03.03	Chlorophyll-a	68
4.03.04	SML Depth	69
4.04	Trace Metals Analysis	71
4.05	Results	72
4.05.01	Temporal Progression of Dissolved Trace Metals	72
4.05.02	Wilcoxon Test	75
4.05.02.01	Wilcoxon Test Results	77
4.05.03	Enrichment Factors	80
4.05.03.01	Annual Average EF	85
4.05.04	Temporal Progression of Enrichment Factors	87
4.06	Discussion	92
4.07	Conclusions	103

Chapter Five: Water-Particle Interactions in a Photochemically Active System 105

5.00	Introduction	106
5.01	Experiment Method	109
5.01.01	Seawater, Reagents, Organics and Particulates	109
5.01.02	pH and Temperature	111
5.01.03	Experimental Setup	111
5.01.04	Light Spectra	113
5.01.05	Fe(II) Half Life	116
5.02	Experiments	117
5.02.01	Set 1, NMO Experiments	118
5.02.02	NMO Results – Light Phase	121

5.02.03	NMO Results – Particulate Phase	126
5.02.04	Set 2, Humic Acid Experiments	129
5.02.05	Humic Acid Results – Light Phase	132
5.02.06	Humic Acid Results – Particulate Phase	137
5.03	Discussion	139
5.03.01	Light Phase	139
5.03.02	Particulate Phase	142
5.03.03	Organic Material	147
5.04	Conclusions	148

Chapter Six: Effect of Irradiating Regime on Reactive Oxygen Species and Iron in Model Marine Microlayer Systems **151**

6.00	Introduction	152
6.01	Materials and Methods	154
6.02	Numerical Model	155
6.03	Experimental Results	159
6.03.01	Set 1; 0.2 μm Filtered NMO	160
6.03.02	Set 2; 11 % v/v 2.0 μm Filtered <i>Thalassiosira pseudonana</i>	167
6.03.03	Set 3; 1.0 mg L^{-1} Humic Acid at $\sim \text{pH 8.3}$	175
6.03.04	Set 4; 2.0 mg L^{-1} Humic Acid at $\sim \text{pH 7.5}$	182
6.04	Model Discussions	189
6.04.01	NMO Full Spectrum Experiments Kinetics	190
6.04.02	Light Regime Comparisons – k_{CDOM}	195
6.04.03	Light Regime Comparisons – k_{RED}	199
6.04.04	Light Regime Comparisons – k_{RO}	201
6.04.05	Light Regime Comparisons – k_{SOS}	204
6.04.06	Discussion	206
6.05	Conclusions	207

Chapter Seven: Ozone Initiated Cycling of Hydrogen Peroxide and Reduced Iron, in a Batch Reactor Containing Seawater **212**

7.00	Introduction	213
7.01	Materials and Methods	214
7.02	Numerical Model	215
7.03	Experimental Results with Model Fits	218
7.04	Discussion	227
7.05	Conclusions	235

Chapter Eight: Conclusions **236**

Appendices **244**

Chapter One: Appendix	245	
Chapter Four: Appendix	249	
A4.01	Method of calculation for the correction factor for the first three sampling missions of 2008	249
A4.02	Concentrations of trace metals in the 2008 broadwater samples	253
A4.03	Student's t-test comparison of seasonal enrichment factors	255
Chapter Six: Appendix	257	

Bibliography **259**

Figure List

Chapter One	1
Figure 1.01. Conceptual model of the sources and controlling influences of ROS and metals in the surface microlayer	16
Chapter Two	17
Figure 2.01. Schematic of an ICP-MS	23
Figure 2.02. Temporal signal change of a multi-element standard	26
Chapter Three	31
Figure 3.01. Luminol reaction sequence	33
Figure 3.02. FIA, hardware configuration	35
Figure 3.03. King and Croot load /inject valve configurations	36
Figure 3.04. H ₂ O ₂ calibration in aged UPW	39
Figure 3.05. pH sensitivity of luminol reagent for H ₂ O ₂ analysis.	40
Figure 3.06. Repeat calibration curves for iron (II) in UPW	44
Figure 3.07. PCT measured trace of a repeat 10 nM Fe(II) standard	45
Figure 3.08. Dual peak formation during analysis of an acidified Fe(II) standard	46
Figure 3.09. Comparison of UPW and seawater Fe(II) calibrations	47
Figure 3.10. SLRS-4 standard addition calibrations	48
Figure 3.11. CASS-4 standard addition calibration	48
Figure 3.12. Comparison of Chelex-100 cleaned seawater	50
Figure 3.13. PMT trace for Fe(II) in seawater	51
Figure 3.14. Reactivity of luminol reagent for Fe(II) due to reagent pH	52
Figure 3.15. Load/inject valve configuration for dual analysis using a single valve	53
Figure 3.16. Dual analysis seawater trace	54
Chapter Four	55
Figure 4.01. Location of the UEA Broad and mooring position	59
Figure 4.02. Adhesion of the organic acid hydrophobic microlayer to a glass plate	62
Figure 4.03. ETFE screen surface microlayer sampler	62

Figure 4.04. Meteorological data for 30 minutes preceding and during sampling	64
Figure 4.05. Seasonal progression of, temperature, oxygen and pH	65
Figure 4.06. Seasonal progression of chlorophyll-a	68
Figure 4.07. Percentage depth difference from first to second repeat sample	70
Figure 4.08. Comparison of microlayer sampling depths	71
Figure 4.09. 2008 Seasonal progression of dissolved trace metals	74
Figure 4.10. Comparison of broadwater enrichment factors	84
Figure 4.11. Seasonal progression of EFs for elements statistically enriched	87
Figure 4.12. Seasonal progression of EFs for elements statistically depleted	89
Figure 4.13. Seasonal progression of EFs for elements statistically at unity	91

Chapter Five 105

Figure 5.01. Experimental set up.	113
Figure 5.02. Percentage spectral irradiance for each irradiating regime	114
Figure 5.03. Light spectrum fluxes from 280 nm to 750 nm.	115
Figure 5.04. Percentage comparison of experiment irradiating regimes for both UV-R and visible light to modelled 40°N spring noon values from Zepp and Cline (1977).	115
Figure 5.05. Fe(II) oxidation and sorption on to quartz glass at pH 7.4 and 8.	116
Figure 5.06. pH and temperature change for NMO experiments.	120
Figure 5.07. Fe(II) traces from NMO experiments.	123
Figure 5.08. H ₂ O ₂ traces from NMO experiments.	124
Figure 5.09. Mn(II) traces from NMO experiments.	125
Figure 5.10. pH and temperature change for humic acid experiments.	131
Figure 5.11. Fe(II) traces from humic acid experiments.	134
Figure 5.12. H ₂ O ₂ traces from the Humic Acid experiments.	135
Figure 5.13. Mn(II) traces from humic acid experiments.	136

Chapter Six 151

Figure 6.01. Comparison of seawater 10 % irradiance depths for UVB and UVA	154
Figure 6.02. Model of combined cycles of reactive oxygen species and iron	157
Figure 6.03. Stage timings for Full spectrum 0.2 µm NMO experiments	161
Figure 6.04. NMO, Full spectrum incubation experiments with model fits	163
Figure 6.05. pH and temperature change for the 2.0 µm filtered <i>NMO</i> experiments	168

Figure 6.06. 2.0 μm filtered NMO stage times	170
Figure 6.07. 2.0 μm filtered NMO experiments with model fits	172
Figure 6.08. pH and temperature change for the 1.0 mg L^{-1} humic acid experiments	176
Figure 6.09. 1.0 mg L^{-1} humic acid stage times	177
Figure 6.10. Relationship between constant stage apparent H_2O_2 production rates and UVA	178
Figure 6.11. 1.0 mg L^{-1} humic acid experiments with model fits	180
Figure 6.12. pH and temperature change for the 2.0 mg L^{-1} humic acid experiments	183
Figure 6.13. 2.0 mg L^{-1} humic acid stage times	184
Figure 6.14. 2.0 mg L^{-1} humic acid experiments with model fits	187
Figure 6.15. k_{CDOM} rate constants for the 0.2 μm filtered NMO experiments	191
Figure 6.16. k_{RED} rate constants for the 0.2 μm filtered NMO experiments	192
Figure 6.17. k_{RO} rate constants for the 0.2 μm filtered NMO experiments	194
Figure 6.18. k_{SOS} rate constants for the 0.2 μm filtered NMO experiments	195
Figure 6.19. k_{CDOM} (M s^{-1}) light regime comparisons	196
Figure 6.20. k_{RED} (s^{-1}) light regime comparisons	200
Figure 6.21. k_{RO} ($\text{M}^{-1} \text{s}^{-2}$) light regime comparisons	202
Figure 6.22. k_{SOS} ($\text{M}^{-1} \text{s}^{-1}$) light regime comparisons	205

Chapter Seven 212

Figure 7.01. pH and temperature change for experiments	219
Figure 7.02. H_2O_2 and Fe(II) observations with model fits	220
Figure 7.03. Fe(II) observations with model fit	222
Figure 7.04. Comparison of fitting parameter rate constants	226

Appendices 244

Figure A4.01. Linear regression comparisons for aluminium and manganese	249
Figure A4.02. Linear regression comparison for iron	250

Table List

Chapter Two	17
Table 2.01. Concentration of major cations in the broadwater	25
Table 2.02. Analytical blanks and limits of detection	27
Table 2.03. SLRS-4 recoveries	28
Table 2.04. Technique comparison of recovery of manganese from within CASS-4	29
Chapter Three	31
Table 3.01. Measured and calculated concentrations for H ₂ O ₂ standards	38
Chapter Four	55
Table 4.01. Mean percentage error between replicate analysis	72
Table 4.02. Critical values of +/-W for small samples (n<10)	76
Table 4.03. Wilcoxon test results (2)	78
Table 4.04. Wilcoxon test results (3)	78
Table 4.05. Wilcoxon test results (4)	79
Table 4.06. Enrichment factors	81
Table 4.07. Annual average microlayer enrichment factors	86
Table 4.08. Iron concentrations normalised to aluminium average crustal abundance	97
Table 4.09. Comparison of cobalt and copper EF to published values	102
Table 4.10. Summary of the Wilcoxon test relationships	103
Chapter Five	105
Table 5.01. Particulates and LOD for NMO experiments.	118
Table 5.02. Particulates and LOD for humic acid experiments.	130
Chapter Six	151
Table 6.01. Irradiance values for light regime experiments	154
Table 6.02. Model equations	156

Table 6.03. Total iron concentrations of experimental media	159
Table 6.04. NMO experiments H_2O_2 apparent stage rates	162
Table 6.05. 2.0 μm filtered NMO experiments: LODs and H_2O_2 apparent stage rates	170
Table 6.06. 1.0 mg L^{-1} humic acid experiments: LODs and H_2O_2 apparent stage	178
Table 6.07. 2.0 mg L^{-1} humic acid experiments: LODs and H_2O_2 apparent stage rates	185
Table 6.08. Ratio of k_{SOS} : k_{CDOM} for the NMO experiments	204

Chapter Seven **212**

Table 7.01. Total iron concentrations of experimental media	215
Table 7.02. Model equations	217
Table 7.03. Limits of detection for H_2O_2 and Fe(II) analyses for experiments	220
Table 7.04. H_2O_2 apparent production rates	223
Table 7.05. Calculated rate constants for fitting parameter	225
Table 7.06. NOM and O_3 linear and stepwise conceptual decomposition relative rates	227

Appendices **244**

Table A1.01. Published research on trace metals in the surface microlayer	245
Table A4.01. Fisher statistical test results	250
Table A4.02. Original and corrected concentrations for aluminium	251
Table A4.03. Original and corrected concentrations for manganese	251
Table A4.04. Original and corrected concentrations for iron	252
Table A4.05. Concentration of trace metals in the 2008 broadwater samples	253
Table A4.06. Student's t-test comparing sample seasonal EF against unity, 1.0	256
Table A4.07. Student's t-test comparing sample seasonal EF, plate versus screen	256
Table A6.01. Log(10) SSE, H_2O_2 residual fits for NMO repeat experiments	259
Table A6.02. Log(10) SSE, Fe(II) residual fits for NMO repeat experiments	259
Table A6.03. Log(10) SSE, H_2O_2 residual fits for light comparison experiments	259
Table A6.04. Log(10) SSE, Fe(II) residual fits for light comparison experiments	258

Abbreviations and Acronyms

Materials and Methods

ICP-OES	inductively coupled plasma optical emission spectrometer
ICP-MS	inductively coupled plasma mass spectrometer
CCT	collision cell technology
HR	high resolution
KED	kinetic energy discrimination
FIA-Cl	flow injection analysis chemiluminescence
PMT	photon multiplier tube
PCT	photon counting tube
B_E	blank signal attributed to electronic noise
B_W	blank signal attributed to light emission from sample media
B_R	blank signal attributed to light emission from reagent
B_{Sw}	blank signal attributed to light emission from reagent reactions with seawater components other than analytes
S_A	signal attributed to analytes
μ (mu)	mean
σ (sigma)	standard deviation
ρ (rho)	probability
df	degrees of freedom
H_0	null hypothesis
RSD	relative standard deviation
SSE	sum of squares error
NC	none calculated
LOD	limit of detection
ODE	ordinary differential equation
v/v	volume for volume
APDC	ammonium pyrrolidine dithiocarbamate
DDDC	diethylammonium diethyldithiocarbamate
DMP	2,9-dimethyl-1,10-phenanthroline
TETA	tri-ethylene tetramine

qd	quartz distilled
UPW	ultra pure water
AR	analytical reagent
PTFE	polytetrafluoroethylene
PVC	poly-vinyl chloride
CRM	certified reference material
SLRS-4	St. Lawrence River sample 4
CASS-4 or 5	coastal Atlantic seawater sample 4 or 5
TDS	total dissolved solids

Descriptive

SML	surface microlayer
FSML	freshwater-surface microlayer
SSML	sea-surface microlayer
ULW	underlying water
EF	enrichment factor
sw	seawater
chl α	chlorophyll a
DO	dissolved oxygen
CDOM	chromophoric dissolved organic matter
DOM	dissolved organic material
HMW	high molecular weight
LMW	low molecular weight
Fc	<i>Fragilariaopsis cylindrus</i>
mxd	mixed
HA	humic acid
NMO	natural marine organic
NOM	natural organic material
SAS	surface active substances
TEP	transparent exopolymeric particles
c.	circa (relating to time)

ROS	reactive oxygen species
AOP	advanced oxidation processes
APR	apparent production rate
ahhp	alpha-hydroxy-hydroperoxide
L	ligand
LMCT	ligand to metal charge transfer
PAR	photosynthetically active radiation (λ 400 – 700 nm)
UV-R	ultra violet radiation
UVB	ultra violet B (λ 280 – 315 nm)
UVA	ultra violet A (λ 315 – 400 nm)

k kinetic rate of equation

fp fitting parameter

k + subscript

subscripts general to both models

O2 oxygen oxidation of iron (II)

H2O2 hydrogen peroxide oxidation of iron (II)

fitting parameter subscripts specific to light reaction model

RED light induced reduction of iron (III) species

CDOM light induced production of organic radicals leading to the oxidation of oxygen and formation of superoxide

RO superoxide reduction of iron (III) species

SOS superoxide reaction with non-iron species and does not lead to production of hydrogen peroxide

fitting parameter subscripts specific to O₃ reaction model

OHS hydroxide radical sinks

NOM ozone induced production of organic radicals

PSDO catalytic decomposition of superoxide by unknown species leading to the production of hydrogen peroxide

RED ozone induced reduction of iron (III) species

Intentionally Blank

A Study of Trace Metals in the Surface Microlayer

Chapter One

Introduction

1.00 The Surface Microlayer

The surface microlayer is the interface between the ocean and atmosphere. It is through this surface that ocean-atmosphere biogeochemical cycles interact. The modern understanding of the surface microlayer is as a hydrated gelatinous interfacial layer with a complex matrix of dissolved organic matter (Wurl and Holmes, 2008) and as such covers 71 % of the surface of the planet (Hardy, 1982). Studies into the surface microlayer began in 1773 when Benjamin Franklin poured a teaspoon of oil on to a pond and noted the observations, ‘the repulsive force cleared the area of surface material (leaf litter) even when the oil became invisible to the naked eye’. Franklin had deduced through tales from sailors that oil will reside on the surface of water and that when even not visible, affected the properties of the water-air interface.

The modern scientific understanding of the surface microlayer began by showing it to comprise of an upper organic stratum and a lower, water associated, organic stratum (Kjelleberg et al., 1979). The idea of a single hydrated gelatinous layer (Wurl and Holmes, 2008), has since superseded the two-layer model. What modern thinking does agree on is that the surface microlayer is of a variety of complex organic material, (Duce et al., 1972; Garrett, 1967). Based on our understanding of simple hydrophobic organic molecules the theoretical depths range from 10 Å (Garrett, 1967) (1×10^{-4} µm) to 100s Å (Lion and Leckie, 1981). A purely lipid based monomolecular layer will reach to a depth of 30 Å, whereas if there were no organic material present it will be the depth of the upper most water molecule, < 3 Å. Actual microlayer depths have been calculated using proxies; gas transfer rates and molecular diffusion rates. The calculated depths are similar: 62 µm (Broecker and Peng, 1971), 20 µm (Peng et al., 1974), 30 µm (Liss, 1975) and 49 µm (Peng et al., 1979). Inferred depth measurements of the region of physiochemical change give a depth of 50 ± 10 µm (Zhang et al., 2003a).

For operational purposes, so as to encompass all considerations, for example small scale wind mixing and as a habitat for macro-neuston the depth is extended to 1000 µm (Liss and Duce, 1997). The operational depth, 1×10^{-3} m, when considering the system in context with an oceanic water column, $\sim 3.4 \times 10^3$ m, or depth of the atmosphere, $\sim 1 \times 10^5$ m, is negligible in size. Yet, its importance due to the interactions it may control between the ocean and atmosphere is not so negligible. Standard practice in microlayer research is to specify the microlayer depth through the technique used to sample it. To relate the microlayer samples to its underlying water enrichment factors are calculated. Enrichment factors (EF) are the ratio of the concentration of an analyte in the microlayer to the concentration of the analyte in the underlying water (Equation 1.01).

$$EF = \frac{[X]_{SML}}{[X]_{ULW}} \quad \text{Eqn. 1.01}$$

There have been various techniques used to sample the microlayer. A bubble microtome, (Blanchard and Syzdek, 1970; McBain and Humphreys, 1932; Pattenden et al., 1981) will collect from the shallowest microlayer depth, between 0.1 and 1.0 μm . However, with the collection of such shallow microlayers the volume of sample is consequently small. For large volume samples, three main methods have been developed: one which utilises water tension, a screen (Garrett, 1965), and two which acts as absorbers, a glass roller (Harvey, 1966), and a glass plate (Harvey and Burzell, 1972). From within these three techniques, the majority of modern microlayer samples are collected. However, other methods have been applied, such as a floating tray (Hatcher and Parker, 1974), perforated Teflon plate (Larsson et al., 1974), membrane adsorption (Crow et al., 1975), the solidification of liquid PVC (Hamilton and Clifton, 1979), and a cryogenic plate (Turner and Liss, 1989). The main consideration for the sampling device is its suitability for collection of the required sample (Garrett, 1974).

Large volume collection of microlayer material tends to be with a roller, with a hydrophilic drum. However, recoveries of analytes from the microlayer are dependant on the method used. For biological characterisation (chlorophyll- α , pheophytin- α and unsaturated fatty acids) and / or sampling inorganic pollutants a metal screen is the most efficient (Agogue et al., 2004; Garcia-Flor et al., 2005; Momzikoff et al., 2004). The glass plate is more efficient at collecting hydrophobic material, phytoplankton-derived material and fatty acids from bacteria and higher land plants (Momzikoff et al., 2004). For small volumes in relation to bacterial work a polycarbonate filter is the most appropriate (Cunliffe et al., 2009a).

The organically rich, physically stable structure, which is the microlayer, is the first oceanic layer to receive atmospheric deposition (Hardy, 1982). The main body of research on the microlayer has been on the characterisation, fate and enrichment of organic substances. Studies include, for example, the bacterial structure in marine microlayers (Stolle et al., 2009), the presence of semi-volatile organic compounds affecting gas transfer (Guitart et al., 2010) and particularly the presence of organic surface-active substances (Duce et al., 1972; Hunter and Liss, 1981; Wurl et al., 2009). Surface-active substances (SAS (Hunter and Liss, 1981)) are part of a heterogeneous biological exudate (bacterioplankton and/or phytoplankton sourced) and can be responsible for trace metal binding (Strmecki et al., 2010). The presence of SAS suggests that at the surface microlayer there is the potential for an enrichment of trace metals, through stabilisation of atmospherically deposited material and metals by SAS (Hunter, 1980b).

Though not absolute, there has been found to be a difference in particulate matter in the upper and lower microlayers; angular atmospheric particulates in the upper organic layer and round bodied encrusted sediment (lithogenic and biological) in the lower organic layer (Hamilton and Clifton, 1979). The particulate phase ($> 0.45 \mu\text{m}$) or total concentration of trace metals has been shown to be enriched in marine (Barker and Zeitlin, 1972; Cuong et al., 2008; Hamilton and Clifton, 1979; Narvekar and Singbal, 1993), estuarine (Trojanowski and Antonowicz, 2011) and freshwater microlayers (Antonowicz and Trojanowski, 2010). The theory for this is due to the organic stabilisation of the particulate phase at the microlayer (Hunter, 1980b). Measurements of trace metals in the dissolved phase ($< 0.45 \mu\text{m}$) have shown negligible enrichment even after an acid digestion (Brugmann et al., 1992; Cross et al., 1987; Grotti et al., 2001; Hardy et al., 1987; Narvekar and Singbal, 1993; Zhang et al., 2003b). Relative enrichments in the particulate phase for aluminium have been so large compared to negligible enrichment of the dissolved phase that instead total concentrations have been assessed (Narvekar and Singbal, 1993).

The approach generally taken prior to measurement of the dissolved ($<0.45 \mu\text{m}$) fraction of trace metals in the microlayer is through an acid digestion. Only two authors have not used an acid digestion on their samples, these were Hardy and Cleary (1992), who used APDC and DDDC¹ chelated extracts, and Cuong et al. (2008), who conducted a direct ICP-MS analysis of the seawater. Both authors found the dissolved ($<0.45 \mu\text{m}$) fraction EFs to range from 0.9 to 1.5. With respect to the partitioning of metals between their respective size fractions, Brugmann et al. (1992) found that more than 75 % of the iron in a marine microlayer was held in the particulate phase. Any analysis of the dissolved fraction of trace metals in the surface microlayer must include a caveat for contamination during sample collection (Hunter, 1997), which may then lead to a presumption of enrichment when in fact there is none.

Cuong et al. (2008) found trace metal enrichments for nickel, copper, arsenic and lead in a coastal seawater microlayer off Singapore. These enrichments were in both the total and dissolved ($<0.45 \mu\text{m}$) fractions. However, the dissolved trace metal enrichments were less than the particulate phase enrichments and found to be tending towards equality with its underlying water. This in some way is explained by Jickells and Spokes (2001) who suggest that if there is organic complexation of trace metals (specifically iron) then these are potentially being outcompeted by the hydrolysis and precipitation/adsorption reactions and could easily occur in the microlayer even with its enrichment of organic material. This then may lead to greater

¹ APDC – ammonium pyrrolidine dithiocarbamate DDDC – diethylammonium diethyldithiocarbamate

enrichment of trace metals as (hydr)oxides at the surface microlayer. The two sources of trace metals to the microlayer are new material derived from atmospheric deposition and recycled material from within the water column. The biology of the water column will indirectly influence the concentration of trace metals in the microlayer, through the production and subsequent migration to the microlayer, of SAS. The flux of copper to the surface microlayer was seen to increase 50 fold during a spring bloom compared to winter, due to the presence of SAS complexing the copper (Shine and Wallace, 1996). Whilst the presence of copper specific complexing SAS has been shown to be enriched in the surface microlayer (Plavsic et al., 2007).

The pH of a marine microlayer has also been found to be less than that of its underlying water, 0.1 pH unit decrease from 5 to 50 μm (Zhang et al., 2003b), though this degree of change will not be influential on the dissolved fraction of trace metals. At the pH of river water (7.5 – 8.5) and seawater (8.2), the pH is favourable for adsorption of metal ions on to hydrous oxides and organic particles (Stumm and Morgan, 1996).

1.01 The Research

The processes that dissolved trace metals undergo in the surface microlayer are poorly characterised due to the lack of measurements. However, seawater processes are extensively characterised and as such used to infer process occurring on trace metals within the microlayer. This work aims to address this issue by first studying the operationally dissolved fraction (0.2 μm) of iron and other trace metals: aluminium, manganese, copper, cobalt and arsenic, in the surface microlayer and addresses their relationships through the progression of a seasonal cycle in a freshwater lake. Experimental work will then develop further insight into the interactions of Fe(II) and reactive oxygen species (ROS), especially H_2O_2 . The difference between the fieldwork and laboratory work was the use of fresh and marine waters, respectively. The differences in matrix of the samples can have a large affect on the reactivity of free aquo-ions. Of most importance are the organic and inorganic ligands. Within freshwater they are primarily oxides, hydroxides and carbonates whilst in seawater they will also include sulphides and chlorides amongst many others (Millero, 1985; Stumm and Morgan, 1996). Fresh and to some degree coastal waters, are affected by the input of terrestrial organic material that may have very different properties to autochthonous organic material (Blough and Del Vecchio, 2002; Stumm and Morgan, 1996). This work primarily relates its findings to the surface microlayer; however, the results can also be used in the interpretation of the water column. A second important difference is the pH of the water, this can have a direct impact on the speciation and half lives of

soluble metals, freshwater pH can show large ranges, from acidic lakes at pH 5 to a near seawater pH, whilst the pH of seawater is relatively consistent at around pH 8.1.

1.02 The Metals

The primary analytes of interest in the work addressing the seasonal cycle of trace metals in a lacustrine surface microlayer are the dissolved fractions of aluminium, manganese and iron. Aluminium solubility is low at around pH 7 and as such the stable Al(OH)_3 will be the main dissolved fraction of interest. For manganese, it is primarily as Mn(II) aquo-ions (Davison, 1993; Horst and Zabel, 1996). The dissolved phases of iron includes Fe(II) , reactive Fe(III) , colloidal iron and organically complexed Fe(II) and Fe(III) (Bruland and Rue, 2002). The operationally defined dissolved fraction, $< 0.2 \mu\text{m}$ includes both a fine colloidal fraction ($0.02 - 0.2 \mu\text{m}$) and a soluble fraction ($< 0.02 \mu\text{m}$) (Bergquist et al., 2007). The choice of a $0.2 \mu\text{m}$ filtered fraction removes the possibility of the majority of colloidal material being measured.

Aluminium was chosen as it is not metabolically required (Williams, 2002) though phytoplankton can increase their internal concentration through a passive uptake mechanism (Quiroz-Vazquez et al., 2008). In its dissolved fraction in surface waters it can be used as a tool for inferring atmospheric deposition at the surface microlayer (Measures and Vink, 2000). Dissolved aluminium concentrations are also highly dependant of the pH of the water, with a decreasing pH increasing the dissolved fraction and its potential for toxicity (Havens and Heath, 1990). The toxicity of aluminium is not a key factor in seawater with its large buffering capacity but is more likely to occur in fresh waters especially in low oxygen regions of lakes. Aluminium can also form complexes with humic acids in seawater, though complexes will exchange the aluminium for iron if available therefore increasing the free aluminium concentration whilst decreasing the free iron concentration (Yang and van den Berg, 2009). Iron on the other hand is an important trace nutrient, it is biologically available within seawater as dissolved inorganic Fe(II) and Fe(III) (reactive), with greater than 99 % of Fe(III) complexed by organic ligands (Gledhill and van den Berg, 1994; Rue and Bruland, 1995; Wu and Luther, 1995). Some of this organically complexed iron is also available for primary production (Maldonado et al., 2005). The production of Fe(II) from complexed Fe(III) can be influenced by both light (Barbeau, 2006; Barbeau et al., 2001; Faust and Hoigne, 1989; Faust and Zepp, 1993; Waite and Morel, 1984) and pH (Behra and Sigg, 1990).

Manganese is also a biologically required element. The dissolved phase of manganese can be increased through the photochemical reduction of the particulate phase (Spokes and Liss,

1995; Sunda et al., 1983) or reductive dissolution in low oxygen waters. However, unlike iron and also copper, manganese does not easily form organic ligand complexes (Sunda, 1984). The primary loss mechanisms for dissolved Mn(II) are through particle scavenging and precipitation in alkaline conditions (Stumm and Morgan, 1996) or bacterial-mediated oxidation (Emerson et al., 1982; Sunda and Huntsman, 1988). Brugmann et al. (1992) correlated the concentrations of dissolved and particulate fractions of iron and copper in the surface microlayer with that of manganese. The authors indicated that sorption / co-precipitation during the formation of MnO₂ was a major removal process for these metals from a marine microlayer.

Copper is actively complexed by surface active substances (Plavsic et al., 2007; Shine and Wallace, 1996) and coloured dissolved organic matter (CDOM) (Witt et al., 2007) and these ligands and the complexes formed can be photochemically degraded (Witt et al., 2007). When organically complexed, copper is present in its oxidised form Cu (II) (Moffett and Zika, 1983). Indication of enhanced dissolved copper in a microlayer may then infer either a large concentration of organic ligands compared to the underlying water, or an atmospheric source such as fine atmospheric particulate matter (< 2.5 µm), related for example to brake pad dust from cars (Majestic et al., 2009). By comparing manganese and copper one may be able to infer the presence of organic ligands in the microlayer stabilising the copper against the occurrence of sorption / co-precipitation during the formation of MnO₂ (Brugmann et al., 1992). The primary loss mechanism for Fe(II) is rapid oxidation by di-oxygen and/or hydrogen peroxide to Fe(III); where this Fe(III) is uncomplexed it is converted to a non-bioavailable form via precipitation and/or scavenging. Through measuring dissolved arsenic, one may then infer the likelihood that iron is being lost from the system through the formation of particulates (iron (III) oxides) as they scavenge arsenic into their matrix during formation (Burnol and Charlet, 2010).

1.03 Organic Material

The operationally dissolved fraction of trace metals (0.2 µm) contains both a fine colloidal fraction (0.02 – 0.2 µm) and a soluble fraction (<0.02 µm) (Bergquist et al., 2007). The colloidal fraction of natural waters is not well categorised, due to its varied composition. Colloids can include: clays, iron and manganese oxides, viable and unviable biological components (micro-organisms, viruses, biocolloids, fibrils (2 – 10 nm), aggregation of exudates and macromolecular organic matter) and colloidal humic acids (Stumm and Morgan, 1996). Microlayer samples have been found to contain micro-colloids of organic origin (Bigg et al., 2004). With enrichments of SAS (Hunter and Liss, 1981) at the microlayer (Wurl et al., 2009), these organic-based substances can cause a phase change from the dissolved to particulate

(Shine and Wallace, 1996) through coagulation and flocculation. With the chelation of trace metals, there is a neutralisation of electrostatic charges and particles then undergo attraction by Van der Waals's forces. With an increase in free oxidised species there will be higher rates of flocculation as these form organic complexes and (hydr)oxides. On flocculation, the presence of SAS in the system will then increase the size of the flocculent though coagulation, gradually increasing the size of the particles. With the production of a particulate phase, their subsequent aggregation acts as a removal mechanism for trace metals (Mopper et al., 1995; Zhou et al., 1998) through gravitational settling from the microlayer and through the water column.

Within the microlayer and through out the water column, organic complexation is an important factor in the cycling of iron due to the bacterial population. Bacteria produce or excrete iron organic chelators such as siderophores and through their uptake use these to fulfil iron requirements (Trick and Wilhelm, 1995). Bacteria themselves will also reduce iron from within marine aggregates, with the possibility that this processes occurs in all natural waters (Balzano et al., 2009). It is still not proven whether the microlayer is a region of increased bacterial productivity (Aller et al., 2005; Crow et al., 1975; Cunliffe et al., 2009a; Hortnagl et al., 2010; Stolle et al., 2009) or decreased areas of productivity (Cunliffe et al., 2009c; Reinthaler et al., 2008) compared to the underlying waters. The lack of consensus could be attributed to the time at which the microlayer was sampled, as the microlayer bacterial population can show strong diel variability (Santos et al., 2009). Aller et al. (2005) found that much of the bacteria in their surface microlayer samples were either dead or dying.

An example of known SAS are transparent exopolymeric particles (TEP) – phytoplankton excreted polysaccharides (Alldredge et al., 1993). TEP are found to be enriched in the microlayer (Cunliffe et al., 2009b; Wurl and Holmes, 2008); they can also be formed in the water column (Alldredge et al., 1993) and then migrate with other SAS to the microlayer (Wurl et al., 2009). TEP can be produced by resident bacteria, with production occurring under UVB stress, this is either through cell lysis or as a UVB protection (Ortega-Retuerta et al., 2009) suggesting a direct production mechanism in the microlayer due to the presence of increased UVB compared to the underlying water. TEP are produced when dissolved polysaccharides align via a cation bridge (Alldredge et al., 1993). They are relatively stable, however, with an increase in concentration they flocculate to an unsustainable size and will aggregate and sink (Logan et al., 1995). The presence of TEP enrichment in the microlayer may not however be a major removal mechanism for trace metals by aggregation and gravitational settling. As the microlayer has low attenuation of UVB radiation (Plane et al., 1997), TEP (Ortega-Retuerta et

al., 2009) and polysaccharide (Kovac et al. 2000) photolysis rates will increase and as such there is a decreased potential for their aggregation and removal of trace metals.

1.04 Photochemistry

Bacteria are the producers of fluorescent chromophoric dissolved organic material (CDOM) which originates from non-fluorescent organic matter derived from phytoplankton (Rochelle-Newall and Fisher, 2002). CDOM concentrations have been found to be elevated in coastal microlayers (Hortnagl et al., 2010). However, this may have been due to the large input in to coastal and freshwater regions of allochthonous material, high in humic substances from terrestrial sources (Blough and Del Vecchio, 2002). CDOM is important in the redox cycling of iron and manganese as CDOM is the initiating chromophore in the photochemical production of the redox species, superoxide (Micinski et al., 1993; Moffett and Zika, 1983; Petasne and Zika, 1987; Voelker et al., 1997) (Equations 1.02 and 1.03).



Even when comparing between marine visible (slick) and non visible microlayers, carbohydrates are enriched when compared to their underlying water (Garabetian et al., 1993; Sieburth et al., 1976). Lipid enrichments in the microlayer has been seen due to the seasonal affect of biology in the water column (Larsson et al., 1974). Polysaccharides derived from phytoplankton have also shown enrichment in the microlayer (Kuznetsova et al., 2005), a component therefore of the microlayer is in the form of recognisable phytoplankton exudates. Even when a microlayer moves from region to region, i.e. estuary to coastal seawater, the enrichment of phytoplankton-derived sugars is still present (Compiano et al., 1993). Some phytoplankton exudates, hydroxycarboxylic acids (Kuma et al., 1995) and polysaccharides (Steigenberger et al., 2010) have been shown to increase photoreduction of Fe(III). On illumination of natural marine surface waters there can be an immediate production of Fe(II). Of this production, 35 % is due to UVB (300 – 315 nm), 30 % in the far UVA (315 – 360 nm) and 30 % at greater than 360 nm (Laglera and van den Berg, 2007). Within the Gulf of Aquaba surface waters, the point of maximum concentration of Fe(II) also coincided with the point of maximum irradiance (Shaked, 2008).

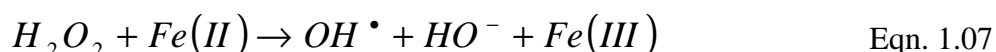
With a depth of ~ 50 μm the attenuation of UVB light in the microlayer of productive waters is around 1 % (Plane et al., 1997). The organic material at the microlayer which absorbs

at 280 to 290 nm is enriched in the microlayer compared to the underlying waters; this organic material has been found to contain dissolved phenolic material (Carlson, 1982). CDOM has been found to contain phenolic moieties (Averett et al., 1989) and the absorption of light in the UV range is the most important for the excitation of organic chromophore (Petasne and Zika, 1987). Following photo excitation of organic chromophores the free electron produced reduces di-oxygen forming superoxide (Equations 1.02 and 1.03) (Micinski et al., 1993; Voelker and Sedlak, 1995). Superoxide will initially react with dissolved metal ions and organic matter and acts as both an oxidant (Equations 1.04) and reductant (Equation 1.05), resulting in the formation of hydrogen peroxide and di-oxygen respectively (Goldstone and Voelker, 2000; Voelker and Sedlak, 1995).



1.05 Oxidation

Redox cycles in seawater have been shown to occur between superoxide and both manganese (Hansard et al., 2011) and iron (Bull et al., 1983; Rush and Bielski, 1985). Manganese and iron are both biologically important elements. However, the manganese reduced form is somewhat kinetically stable in seawater (Glasby and Schulz, 1999), due to its slow oxidation kinetics (Horst and Zabel, 1996; Stone and Morgan, 1984), whereas the dissolved reduced form of iron is less stable with a half life of 2-3 minutes at pH 8. The lifetime of Fe(II) in oxygenated waters is related to its rates of oxidation (Millero et al., 1987) and these rates are variable depending on the ligands present (Millero, 1985). The primary oxidants of Fe(II) are di-oxygen (Equation 1.06) and H₂O₂ (Equation 1.07). Competition occurs between these as too which is the primary Fe(II) oxidant. This competition occurs at temperatures $\sim > 20^{\circ}\text{C}$, oxygen at equilibrium saturation with the atmosphere, and hydrogen peroxide concentrations $\sim > 50$ to 125 nM (Croot and Laan, 2002; Gonzalez-Davila et al., 2006; Millero and Sotolongo, 1989; Moffett and Zika, 1987; Santana-Casiano et al., 2006; Voelker and Sulzberger, 1996). Hydrogen peroxide in seawater has not yet been shown to produce a redox cycle, though hydrogen peroxide reduction of Fe(III) is feasible in seawater if the pH is reduced to approximately pH 7 (Moffett and Zika, 1987). As Equation 1.06 shows the reaction between di-oxygen and Fe(II) leads to further formation of superoxide.

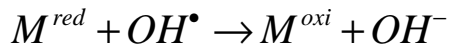


The rates of Equations 1.06 and 1.07 are both temperature and pH dependant, both rates are seen to linearly increase from pH 6 to pH 8 (King et al., 1995; Millero and Sotolongo, 1989; Millero et al., 1987; Moffett and Zika, 1987). An important third oxidant of Fe(II) is the hydroxyl radical, (Rose and Waite, 2001), this has a relatively high rate of reaction, $5.0 \times 10^8 \text{ M}^{-1} \text{ s}^{-1}$ but due to the non-specific reactivity of the hydroxyl radical its concentrations are generally low within aquatic environments.

The oxidation of Fe(II) can be either inhibited (Miles and Brezonik, 1981; Rijkenberg et al., 2008; Shaked et al., 2004; Steigenberger et al., 2010) or enhanced (Santana-Casiano et al., 2000) by organic material. In coastal waters, dissolved concentrations of iron are high due to the proximity of the terrestrial inputs. Humic substances have been shown to reduce Fe(III) (Skogerboe and Wilson, 1981). The dissolved concentration of iron can also remain high in the absence of oxidants, whilst simultaneously complexes between Fe(II) and organic material may have a higher stability and longevity (Rose and Waite, 2003a). Organic material from diatom exudates has been shown to increase the residence time of Fe(II) in oxygenated seawater (Rijkenberg et al., 2008; Steigenberger et al., 2010). The residence time of Fe(II) can also be increased through increased Fe(III) reduction rates in the presence of light. The increased reduction rates are caused by an increased photochemical production of superoxide from those exudates (Steigenberger et al., 2010), or through an increase in the concentration of Fe(II) specific organic ligands (Roy et al., 2008). The presence of biology therefore plays an indirect role in controlling the mechanism of the increased residence time of Fe(II) in surface seawaters and around neutral pH lake waters. At temperatures around 25 °C the half life of Fe(II) in oxygenated waters, low in hydrogen peroxide is expected to be less than 2 minutes (Millero et al., 1987). However, Fe(II) oxidation rates measured in algal-enriched lake water were 30-fold slower than Fe(II) oxidation rates in the water alone, demonstrating the potential for indirect Fe(II) stabilisation by lake phytoplankton exudates (Shaked et al., 2004).

1.06 Reduction

The products of the superoxide reactions are more likely to oxidise reduced metals due to their abundance, with oxidation by di-oxygen itself forming a superoxide. Oxidation of Fe(II) to Fe(III) and also Cu (I) to Cu (II) are through reactions with di-oxygen and hydrogen peroxide (Barb et al., 1951; King et al., 1995; Moffett and Zika, 1987). When a reduced metal reacts, with di-oxygen it will then form the metal oxidised species and superoxide, as seen with iron, Equation 1.06. Hydrogen peroxide oxidation will produce a hydroxyl radical and hydroxide ion (Equation 1.07), with the hydroxyl radical also oxidising a reduced metal (Equation 1.08).



Eqn. 1.08

As well as the mechanism of photochemically produced superoxide in the reduction of oxidised metals, there is also a direct photochemical reaction initiating a ligand to metal charge transfer (LMCT) (Equation 1.09). For iron this can be at either the surface of iron (hydr)oxides (Faust and Zepp, 1993; Waite and Morel, 1984) or in organically complexed Fe(III) (Barbeau, 2006; Barbeau et al., 2003).

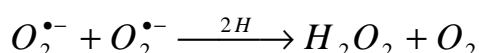


Eqn. 1.09

In waters exposed to light, a decrease in the rate of oxidation of Fe(II) may therefore be due to either a stronger photo reduction of Fe(III) or a stabilisation of Fe(II) by organic compounds. However, certain estuarine Fe(III) binding organic ligands are not susceptible to ultra-violet degradation and as such infer a continued stability of Fe(III) complexes in estuarine and maybe freshwater systems (Rijkenberg et al., 2006).

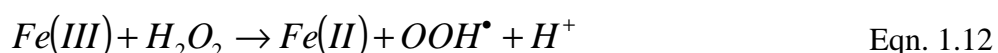
1.07 Hydrogen Peroxide

Hydrogen peroxide is important in the redox cycling of trace metals: Iron – this is termed the Haber-Weiss process (Haber and Weiss, 1932); manganese (Sunda and Huntsman, 1994) and copper (Zafiriou et al., 1998). Within natural waters the main form of production of hydrogen peroxide is through the photo-excitation of an organic chromophore (Equations 1.02) (Petasne and Zika, 1987). The excited chromophore reacts with di-oxygen forming superoxide (Equation 1.03). Superoxide will then disproportionate to form hydrogen peroxide. The disproportionation of superoxide can be catalysed by redox reactive substances, including inorganic (Rush and Bielski, 1985) and organically complexed (Bull et al., 1983) iron; inorganic (Zafiriou et al., 1998) and organically complexed (Voelker et al., 2000) copper, other metals such as manganese (Hansard et al., 2011) and natural organic material (Goldstone and Voelker, 2000). Uncatalysed disproportionation will occur (Equation 1.10, O'Sullivan et al (2005)) though its rate in seawater at pH 8 will be slow (Zafiriou, 1990). If superoxide should eventually attain a sufficiently high steady-state concentration in seawater then it will have a direct effect on reduction and oxidation of metals and set up redox cycles, such as with iron (Miller et al., 1995; Voelker and Sedlak, 1995).



Eqn. 1.10

As well as abiotic production there is also biological production of hydrogen peroxide (Vermilyea et al., 2010; Yuan and Shiller, 2004); this is more important in the dark by keeping a steady state concentration present. From measurements of photochemical production in coastal marine waters, O'Sullivan et al. (2005) found that the majority of hydrogen peroxide production occurred at wavelengths less than 340 nm, the far UVA and UVB range, both of which are minimally attenuated at the microlayer (Plane et al., 1997). Both hydrogen peroxide and superoxide, and their cycling, are primarily initiated photochemically and are involved in the redox cycling of iron (King et al., 1995). The redox reactions between a metal and hydrogen peroxide when used to catalytically oxidise organic compounds are collectively termed Fenton chemistry (Walling, 1975), though this is usually associated with reactions with iron (Equations 1.11 and 1.12).



The rate of reduction of Fe(III) by hydrogen peroxide is slower than the opposing oxidation reaction (Barb et al., 1951). For a systems to attain a semi-equilibrium state the concentration of Fe(III) has to be sufficiently high.

With out a continued source of superoxide the limiting reactions on the oxidation of reduced metals are those with di-oxygen and hydrogen peroxide. Redox cycles are set up with superoxide (Voelker and Sedlak, 1995) and may occur with hydrogen peroxide (Barb et al., 1951) but this is only when the seawater pH is sufficiently low, \sim pH 7 (Moffett and Zika, 1987). The main known pathways for the production of, and increased residence time of, a reduced metal are the direct photochemical reduction through a LMCT and then indirectly by the photochemical production of superoxide.

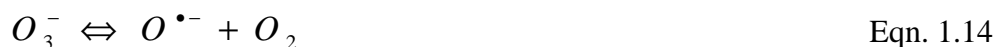
1.08 Ozone

Ozone is an important gas in the higher-atmosphere as it is absorbs UV radiation decreasing the levels received at the surface. Ozone concentrations increase with height and the lowest are seen at the surface, \sim 33 ppbv (Lee et al., 2009), 10 – 15 ppbv (Harvey and Springer-Young, 1988). The primary source of ozone to the microlayer is through dry deposition (Garland et al., 1980). Ozone will not directly oxidise trace metals due to its reactivity with halogens, bromide and chloride (Grguric et al., 1994) and especially iodide (Garland and Curtis, 1981; Thompson and Zafiriou, 1983) and natural organic material (NOM). However, atmospheric concentrations of ozone have been increasing over the last 30 year, between 0.05

and 0.68 ppb per year (Lelieveld et al., 2004), any increase in deposition at the surface microlayer may also increase the redox activity of trace metals. The preferential ozone scavenging in circum-neutral, low ionic waters is by organic material and leads to the oxidation of the organic material and the formation of an ozonide radical (Equation 1.13) (von Gunten, 2003).



Ozone reactivity with the constituents of water becomes inhibited when the resultant products do not liberate further superoxide, resultant products can include fractions of organic material and carbonate/bicarbonate (Buxton et al., 1988). At pH ≈ 8 the ozonide will disassociate to free-oxygen and di-oxygen (Equation 1.14) with the free-oxygen reacting with water to form a hydroxide radical and ion (Equation 1.15) (von Gunten, 2003).



However, the main mechanism of ozone decomposition (initiation reactions) is by hydroxide ion initiated decomposition (Weiss, 1935) leading to the formation of the hydroperoxyl radical and di-oxygen (Equation 1.16).



The hydroperoxyl will then react with an ozone forming the hydroxyl radical, superoxide and di-oxygen (Equation 1.17) (von Gunten, 2003).



The hydroperoxyl conjugate base is superoxide and when they combine they form hydrogen peroxide and di-oxygen (Equation 1.18) (Bielski, 1978; von Gunten, 2003).



Both hydrogen peroxide and superoxide can set up redox cycles with trace metals as shown previously.

These initiation reactions are important in seawater and above neutral lake waters due to the increased pH. The products of ozone decomposition, hydrogen peroxide and its precursor, superoxide, will be involved in redox cycles of trace metals, such as iron. The superoxide is the initiator in the production of hydrogen peroxide, and acts as both an oxidant and reductant in the redox cycling of soluble trace metals. There is a scarcity of information regarding the effect of ozone and the products it forms on the cycling of trace metals within an environmental consideration of marine and fresh waters. To assess the effect of ozone at the surface microlayer

the known photochemical reactions with organic material, leading to the formation of ROS, can be used as a modelling construct. This model can then be used to interpret results from within a laboratory study measuring the production and cycling of ROS and potentially reduced iron.

1.09 The Research Revisited

The body of work relating to trace metals in natural aqueous media is not exhaustive but it is large. Since 1980, there has been less than 23 published works on trace metals in the surface microlayer, some but not all of the measured results are in the Appendices, Table A1.01. This work aims to expand the knowledge of the cycling of ROS and trace metals, especially iron in not only the microlayer but also in the lacustrine and marine environments. Figure 1.01 shows a conceptual model of the sources and controlling influences of ROS and metals in the surface microlayer. Chapter 2 of this work, in part, details the work on the set-up of an inductively coupled plasma mass spectrometer (ICP-MS) for the measurement of the dissolved fraction, from within freshwater samples, with high total dissolved solid loadings, and for the measurement of manganese and total iron from within seawater. The experimental work measures hydrogen peroxide and Fe(II) using a flow injection analysis chemiluminescence system with luminol. The analytes were measured quasi-simultaneously at 22 s intervals using a dual-analyte set up; the development of this method is in Chapter 3.

The fieldwork (Chapter 4) follows the development of dissolved trace metals within the microlayer and underlying water through the seasonal cycle of a lake. As a multi-element approach the analyses of these samples is by the ICP-MS. Both the concentrations and calculated enrichment factors are used to discuss the relationships between the dissolved phases of the relevant metals. The result from this fieldwork is unique in relationship to microlayer research.

The relationship between hydrogen peroxide and Fe(II) within the microlayer is developed further. This work entails three sets of experiments: i) The addition of artificial particulate phases of aluminium, manganese and iron to photochemically active model marine microlayer systems; ii) the effect of different irradiating wavelengths on production and loss of hydrogen peroxide and Fe(II) and iii) the affect of atmospheric ozone concentrations on hydrogen peroxide and Fe(II). Experimental work considers the model marine microlayers over a short-term (< 1 hour).

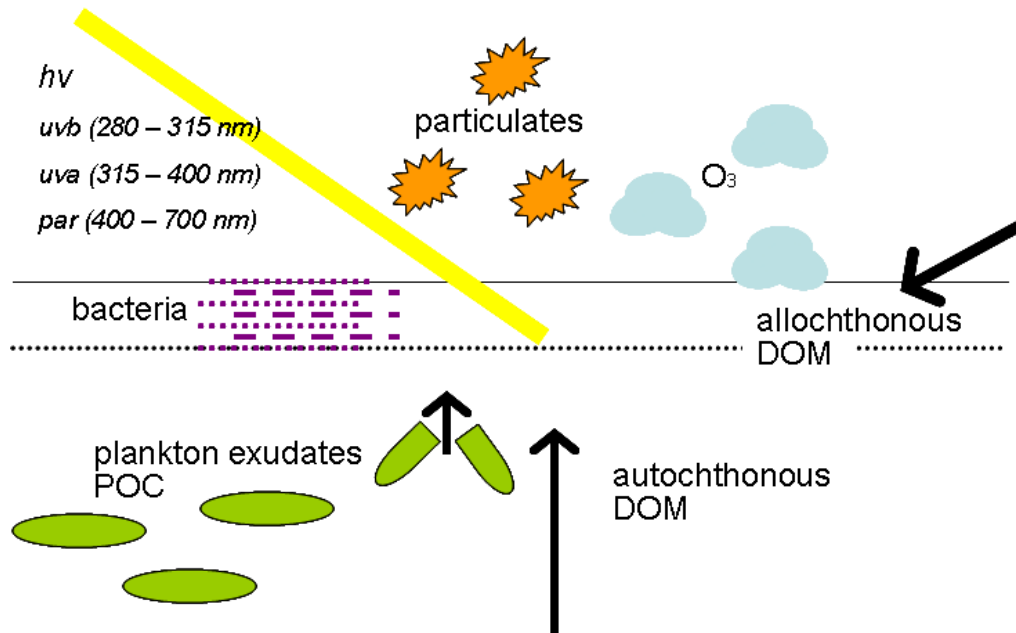


Figure 1.01. Conceptual model of the sources and controlling influences of ROS and metals in the surface microlayer. POC – particulate organic carbon; DOM – dissolved organic matter.

With respect to Figure 1.01 there is one factor which controls the composition of the microlayer, organic material, and three factors which may control the cycling of ROS and dissolved trace metals in the SML, particulates, light and O₃. This thesis will consider each separately under specific working hypotheses: i) Can the seasonal progression of biology in a lake system effect changes to the concentration and enrichments of dissolved trace metals in the SML; ii) Will the addition of an artificial particulate affect the cycling of Fe(II) and ROS in a photochemically active model SML, and will this system act to reduce from the particulate phase soluble ions of iron or manganese; iii) To measure the extent changes in irradiating regime has on the kinetics of Fe(II) and ROS; iv) Does atmospheric O₃ produce and is there a subsequent cycling of, ROS and iron within a model SML.

Chapter Two

General Methods

2.00 Introduction

This chapter introduces the laboratory protocols used during washing and handling equipment. It also describes the inductively coupled plasma (ICP) techniques used for the analysis of fresh (Chapter 4) and seawater (Chapters 5 – 7) samples. It then continues with an explanation of the techniques used for the analysis of ancillary samples for the broadwater work (Chapter 4). The development of the flow injection analysis chemiluminescence (FIA-Cl) system using luminol is described in Chapter 3.

2.01 Trace Metal Equipment, Cleaning and Sample Handling

2.01.01 Equipment Washing

Where trace metal analyses was the ultimate goal all equipment was washed using a specific regime. The majority of equipment for trace metal work was made from high-density polyethylene (HDPE) recommended by Batley and Gardner (1977). The exceptions were borosilicate glass and polytetrafluoroethylene (PTFE) used for the surface microlayer screen and plate samplers, respectively; pure quartz glass used for the seawater photochemical experiment vessel and polypropylene centrifuge tubes. The centrifuge tubes were used to analyse samples by ICP-optical emission spectroscopy (OES) and ICP-mass spectrometry (MS). The four material exceptions still followed the same cleaning regime as HDPE plastic. However, the centrifuge tube caps were cleaned separately in 1 M HCl. A polysulfonate filtration unit was also used for filtration of samples but this was rinsed with 1 M in-house quartz-distilled (qd) HCl later superseded by in-house double qd HNO₃ and then Purtite ultra pure water (UPW).

The cleaning of equipment for trace metal work consisted of three sequential baths; equipment would spend a minimum of 5 days soaking in each. There was an initial cleaning in 5 % Decon 90 to remove excess plasticisers, the equipment was then placed in a 6 M, Fisher AR grade, HCl bath to remove organic based contaminants and a final soak in a 2 M, Fisher AR grade, HNO₃ bath to remove the trace metal contaminants. After each bath, there were at least three rinses in UPW. Following washing, bottles were stored containing UPW acidified to less than pH 2, with qd HCl later superseded by qd HNO₃. Bottles and laboratory equipment were stored double bagged in acid washed, re-sealable polyethylene bags. Sample handling and processing, wherever possible, was undertaken in a class 100 laminar flow hood (Bruland et al., 1979).

2.01.02 Filtration and Storage

Freshwater samples were filtered and acidified within two hours of sampling. The filtration of samples for trace metal analysis was through a polysulfonate vacuum unit; the pvc o-rings were rinsed with 1 M qd HCl followed by UPW before unit and o-rings were left to dry in the laminar flow hood prior to storage. Whatman 0.2 μ m track-etched isopore polycarbonate filters were used to separate the required fraction. The filters were soaked in acid-cleaned polystyrene culture plates containing 1.0 M qd HCl, for five days, before storage in UPW, similar to Planquette et al. (2007). Vacuum filtration of all samples was undertaken at -15 kPa. The low suction pressure prevents the rupture of phytoplankton cells which, either release their trace metals or increase the dissolved organic material (DOM) fraction. Using a 0.2 μ m filter will also remove most bacteria and other organisms (except viruses). Samples were acidified to less than pH 2, in order to prevent metal sorption to container walls. Bottles were finally stored double bagged.

2.01.03 Dilution and Standard Additions

Sample dilutions and the additions of standards for ICP-OES and ICP-MS work were undertaken using a Varian SP55 autodilutor, which is coupled to the ICP-OES. For FIA-CL work they were undertaken manually. Standard additions are a form of calibration where a known quantity of an analyte is added to a sample and the measured response is compared to a sample with no addition. The internal calibration method was used on those samples where a rotational matrix effect occurs; rotational effect arises when the size of the signal derived from a fixed concentration of the analyte is affected by other constituents of the test solution (Ellison and Thompson, 2008). In terms of the calibration the slope is affected rather than the intercept. ICP work was carried out using a suite of additions with a repeated zero addition sample. Blanks were calculated through the measurement of the concentration of the dilutant (this was then corrected for volume of the addition to the sample) and a repeat measurement of UPW and a standard addition for the addition blank (this was then corrected by the number of counts for UPW measurement). With respect to the standard additions, a blank can be more easily calculated by repeating the lowest addition standard.

The calculation of the concentration, sample error (Equation 2.01) and limit of detection (LOD) (equation 2.02), were taken from Miller and Miller (1993); the concentration is given by the ratio a/b ; intercept (a) to the slope (b) taken from the linear calibration.

$$S_{xE} = \frac{S_{y/x}}{b} \left\{ \frac{1}{n} + \frac{\bar{y}^2}{b^2 \sum_i (x_i - \bar{x})^2} \right\}^{\frac{1}{2}} \quad \text{Eqn. 2.01}$$

$S_{y/x}$ is the sum of squares of the y-residuals, the difference between the measured y_i and the calculated values \hat{y}_i using the regression line.

$$S_{y/x} = \left\{ \frac{\sum_i (y_i - \hat{y}_i)^2}{n-2} \right\}^{\frac{1}{2}} \quad \text{Eqn. 2.02}$$

n is the number standard additions made, including zero additions, \bar{y} is the mean of the machine output values for the standard additions, x is the concentration of each standard addition, \bar{x} is the mean of the concentration values. The LOD is three times the error of the zero addition standard as calculated by $S_{y/x}$.

2.02 Broadwater Chlorophyll-a

Chlorophyll-a (chl α) samples were collected using a niskin bottle on a hand winch and stored in 2 L polycarbonate bottles; for approximately two hours prior to filtration. chl α analysis was of known volumes filtered through a GF/F filter at low vacuum (3 replicates). The GF/F was then wrapped in aluminium foil and stored at -80°C. 24 hrs prior to analyses scintillation vials were rinsed with 90 % acetone, then a further 20 mL of 90 % acetone was added. Sample filters were removed from the freezer in groups of 10 and placed directly into the acetone, the caps were replaced and the samples lightly shaken. The pigments were left to extract from the sample for 24 hrs at 4°C in the dark. After 24 hrs the samples were analysed in batches of 10 at a dilution factor of 100. Phaeo-pigments were analysed in the broadwater samples by adding 2 drops 10 % HCl, which knocks out the central magnesium atom in the active chlorophyll-a. A Turner Machines 10AU fluorometer was calibrated using dilutions of pure 1 mg L $^{-1}$ chl α standard (Sigma). Measurements were taken at 630, 645, 665 and 750 nm, and at 665 and 750 nm following acidification, the reading at 750 nm was used as the blank for both the direct chl α and phaeo-pigment measurements. The mean relative standard deviation (RSD) of replicate samples was 7 % (range 1 – 18 %). The calculation (Equation 2.03) for the chl α concentration was based around that of Lorenzen (1967).

$$chl \alpha = Fd \ Z (U - A) \frac{v}{V} d \quad \text{Eqn. 2.03}$$

where

Fd is the \bar{x} of $\left(\frac{[\text{standard}]_i}{\text{abs } A_i} \right) \cdot l$

$Z = \frac{Y}{Y-1}$ where, Y is the \bar{x} of $\left(\frac{\text{abs } U_i}{\text{abs } A_i} \right)$

U is the absorbance of the unacidified sample at 665 nm corrected for the blank at 750 nm and A is the absorbance of the acidified sample at 665 nm corrected for the blank at 750 nm, l is the pathlength of the cell (cm). v is the volume (mL) of 90 % acetone used and V is the volume (mL) of the filtered sample, d is a correction for the dilution of the filtered sample.

2.03 Metal/Species Specific Analytical Techniques

Two techniques were trialled to allow for a corroboration of ICP-MS results from samples derived from experimental work (Chapters 5 – 7), for the measurement of Mn(II) and aluminium, however, these were not used. A spectrophotometric technique for the analysis of Mn(II) (Ji et al., 2009) was not found to be sensitive enough. The spectrofluorometric analysis of a micelle enhanced aluminium-lumogallion complex was not implemented during the course of running the experiments due to time constraints.

2.04 Inductively Coupled Plasma Mass Spectrometry

The potential for analysis of trace nutrients in aqueous solutions by inductively coupled plasma mass spectrometry (ICP-MS) was first successfully realised by Houk et al. (1980). The ability of the technique to undertake rapid multi-element analysis to sub-nanomolar / ppt levels has been its most important contribution. Seawater and high ionic matrix freshwaters have however been difficult to measure on the ICP-MS due to potential low concentrations and the formation of polyatomic interferences; formed from precursors in the plasma gas, entrained atmospheric gases, water, acids and sample matrix (Evans and Giglio, 1993). Techniques have been developed to overcome interferences; the main method has usually been through the pre-concentration and subsequent matrix elimination with columns containing, for example, 8-hydroquinoline immobilised on a silica stationary phase (Sturgeon et al., 1981). The pre-concentration technique was first applied in ICP-MS analysis by McLaren et al. (1985).

Another sample manipulation method of note for trace metal analysis by ICP-MS has been co-precipitation and isotope dilution with Mg(OH)₂ (Wu and Boyle, 1997).

Developments to the ICP-MS hardware itself have also been used to remove polyatomic interferences allowing for the analysis of high matrix samples. The techniques include: using a high-resolution (HR) mass spectrometer (Feldmann et al., 1994; Giessmann and Greb, 1994); a gas to promote collisions on larger polyatomic ions (Eiden et al., 1997); a reaction gas (Louie et al., 2002) and kinetic energy discrimination (KED) (Yamada et al., 2002). The available ICP-MS has a quadrupole, which can be used in a semi-HR mode (it is not a true high resolution instrument) whilst using collision cell technology (CCT). The CCT can utilise both reaction and collision cell gases and can produce a KED bias between the collision cell and the quadrupole. With the ICP-MS able to use these techniques, (as yet un-trialled at the university), an expected large number of samples without a sufficiently large clean area in which to either chemically remove the matrix or concentrate the analytes, the alterations to the machine configuration were favoured to reduce the effect of interference ions.

2.04.01 Inductively Coupled Plasma Multi-Element Techniques

Two multi-element ICP techniques were used to analyse fresh and seawater samples: the instruments used were a Varian Vista-Pro, ICP-OES and a Thermo X-Series 1, ICP-MS. Both techniques use a similar sample input method prior to ionisation. An auto sampler with a Teflon coated probe selects the sample, which is then transferred by means of a peristaltic pump, with Accu-rated PVC tubing. For the ICP-OES the sample injects through a sea-spray nebuliser (2 mL min^{-1}) into a cyclonic spray chamber (50 mL volume) before the suction from the plasma draws the finer mist particles in. The ICP-MS injects sample through a micro-mist nebuliser (0.14 mL min^{-1}) into a cryogenically temperature controlled impact bead nebuliser before the suction from the plasma draws the finer mist particles in.

To form an ion requires that at first plasma is produced with which to ionise it. The plasma used is an ionised argon gas. The ionisation process commences by arcing an electrical discharge, from a tesla unit, through the gas. To ensure constant plasma, an electromagnetic field is used to continually charge particles which then collide with those formed during the initial ionisation process. A radio frequency (RF) generator is used to produce the electromagnetic field. The RF generator runs either at 40 MHz (ICP-OES) or 27 MHz (ICP-MS) around the end of a silica glass torch. As the sample is directed into the centre of the plasma from behind it initially desolvates, then is vaporised, atomised and finally electrons are

stripped in the ionisation of the analyte. The two measurement techniques used during this work consider very different specific properties of an ion. ICP-OES measures the intensity of the light emitted at a specific wavelength, produced during ionisation. To measure the concentration of an analyte the ICP-OES uses an array of semiconducting photodetector charged coupled devices to read the light formed during the ionisation of an element. The intensity of the light is related proportionally to the concentration of the element based on the calibration. ICP-MS uses a quadrupole mass spectrometer to select an ion based on its mass to charge ratio (m/z).

The ICP-MS (Figure 2.01) ion beam on leaving the torch is accelerated, narrowed and focused before reaching the quadrupole. The beam is narrowed by a set of nickel cones, skimmer and sampler cones. The beam is then focused and accelerated by a sequence of magnetic lenses acting on the ion beam. A collision / reaction cell can be fitted at the interface between the lenses and the quadrupole. The cell can be set so that a flow of a specific gas in and around the ion beam induces collisions (hydrogen/helium mix) or reactions (ammonia). The mass spectrometer uses an oscillating RF running along and between four rods (quadrupole) which focus the ion beam to a specific m/z. Ions which are not supported by the oscillating radio frequency do not run true through the quadrupole, and fly away from the ion beam and therefore do not reach the collector (nickel, electron multiplier detector). Each collision registers a count, a time integrated value is then transferred to the PC running the control and display software.

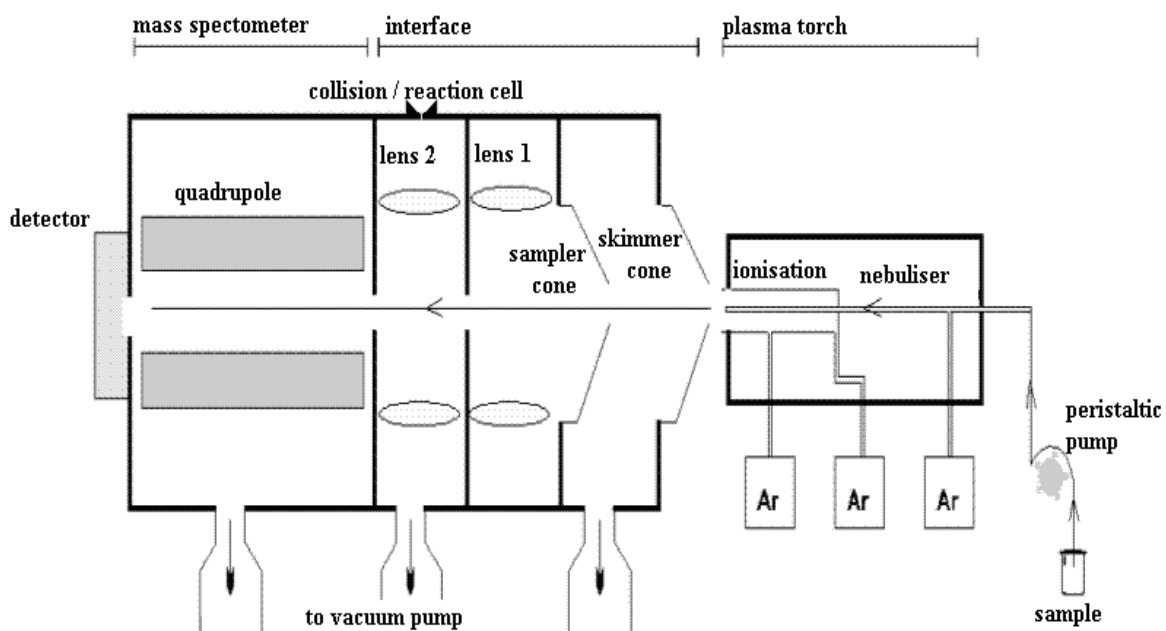


Figure 2.01. Schematic of an ICP-MS, adapted from http://iramis.cea.fr/Images/astImg/886_2.gif

All samples for ICP-MS analysis were sampled through a Cetec 500 auto-sampler. The auto-sampler removed a sample from either Grenier or Corning 15 mL polypropylene centrifuge tubes. For multi-element analyses, whether using standard calibrations or when undertaking method development with standard additions, the standards were taken from diluted Spectrosol and BDH certified standards. For dual / tri element method development and sample analyses, the aluminium, iron and manganese standards were produced from serial dilutions of their respective sulphate salts, $\text{AlKO}_8\text{S}_2 \cdot 12\text{H}_2\text{O}$, $\text{FeSO}_4 \cdot 7\text{H}_2\text{O}$ and $\text{MnSO}_4 \cdot \text{H}_2\text{O}$ (99+% Acros Organics) into pH 1.6 UPW (acidified with double qd HNO_3). In retrospect, soluble nitrate salts should have been used as these have lower polyatomic interferences than sulphate ions (Louie et al., 2002).

2.04.02 ICP-MS

The ICP-MS was used to measure freshwater samples taken from the UEA Broad, and seawater samples taken during a series of seawater experiments. During the analysis of the freshwater samples, the analytical methodology had been continually improved. This work entailed comparisons of high and standard resolution at the quadrupole and variations in the flow rate and type of gas used in the collision cell. Due to these changes, only those samples analysed with an accurate method, based on the recoveries of certified reference material (CRM) from the National Research Council Canada, were used in further work.

2.04.03 Stability

The stability of an ICP-MS can be affected by both the matrix of the samples being analysed and the environmental factors within the room housing the ICP-MS. Following analyses of a suite of broadwater samples, the skimmer and sampler cones were visually inspected, a deposit of material was found around the orifices of the cone. Deposition on the cones can lead to a deterioration in stability, with between 5 and 25 % signal loss occurring within the first 50 minutes, (Williams and Gray, 1988); one multi-element analysis takes around 6 minutes. Extended wash phases between samples removes some deposits (Williams and Gray, 1988); however, there is still a cumulative effect over extended runs. The majority of machine runs involved 60 or more samples and could last from 12 to 24 hours. The formation of precipitates is due to the concentrations of the total dissolved solids (TDS) (Jarvis et al., 1997) and especially the elevated concentrations of cations (Wright, 2002). High concentrations of alkaline earth cations were found following ICP-OES analysis of the broadwater (Table 2.01).

Table 2.01. Concentration of major cations in the broadwater, measured by ICP-OES

	mg L ⁻¹	mM
calcium	84 +/- 3	2.1 +/- 0.07
potassium	2.8 +/- 0.16	0.07 +/- 0.004
magnesium	3.3 +/- 0.12	0.13 +/- 0.005
sodium	28 +/- 1.2	1.2 +/- 0.05
strontium	620 +/- 29	7.1 +/- 0.3

The TDS loading, attributable to the major cations, is ~ 750 mg L⁻¹. The major ion TDS level, though not as high as that advised by Jarvis et al. (1997) as a safe working limit of 1000 mg L⁻¹, may still pose a problem if minor ions (transition metals) and also organic material were also included within the TDS. A 1:10 dilution was initially chosen for further analyses of subsequent broadwater samples. This dilution is in line with work by Louie et al. (2002) who successfully analysed the complex matrix of seawater at this dilution; the dilution would bring the TDS concentration to ~ 100 mg L⁻¹.

The stability of the ICP-MS was also investigated over long (> 4 hours) analytical runs (Figure 2.02). Whether the instability is due to the continued deposition of TDS even with diluted samples or due to the environmental conditions within the room housing the ICP-MS is unknown. Though the use of a repeat standard (analysed every sixth sample, ~ 30 minutes) did allow for a correction to the signal, the range of the change, $\pm > 25$ % and the circumstances affecting the ICP-MS stability, location, matrix effects and deposition of TDS were still considered too detrimental to analytical work until. To enable a recalibration of the instrument during the analyses of each sample and allow for the affect of matrix interference the standard addition technique was employed. The use of standard additions was combined with changes to the instrument configuration which helped mitigate the effect of polyatomic and isobaric interferences.

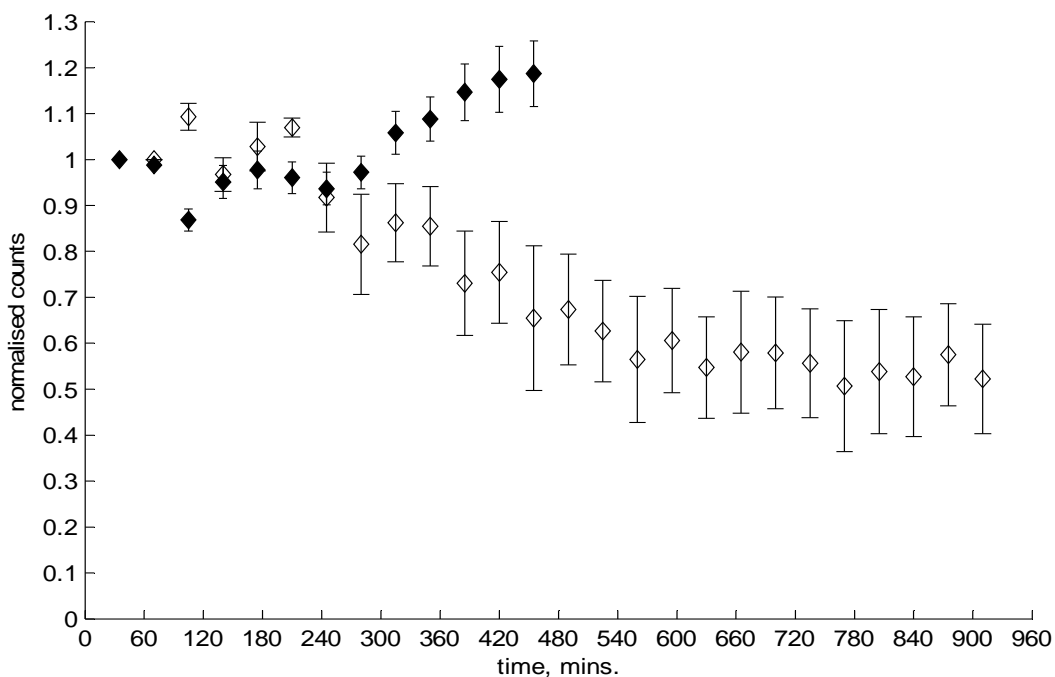


Figure 2.02. Temporal signal change of a multi-element standard. The closed (analysed 15th March 2008, day time) and open (analysed 01st December 2008, evening to night) diamonds represents a composite of the mean counts for all elements normalised to their initial values with the error bars the standard deviation of these composites.

2.04.04 ICP-MS Signal Interference Mitigation

The Thermo X-Series mass spectrometer usually runs with a quadrupole resolution of 0.8 m/z units, the instrument has the capability of increasing the quadrupole resolution to 0.02 m/z, though this has a detrimental affect on the total number of counts. CCT is a mechanism whereby polyatomic and isobaric interference ions are removed from the ion beam. The polyatomic interference ions are recombinations of either the components of the argon gas and / or elements within the matrix. Recombined ions are larger than the pure (single) ions and have a subsequent higher mass to charge (m/z) ratio. The CCT gases act on both the difference in size and mass to charge ratio when removing the polyatomic interferences. CCT gas flow can be controlled through the cell; gases available were a helium / hydrogen mix or a 7 % ammonia gas. The two gases work in different ways. The hydrogen / helium mix acts to remove energy from polyatomic interferences through multiple collisions with the larger interference ions. The collisions remove energy; this then prevents the interference ions traversing the quadrupole by spinning out of the ion beam. The ammonia gas is a reaction gas, on its dissociation in the ion beam the protons can combine with polyatomic interferences removing them from the m/z ratio of interest. As well as removing them from the m/z window, they can also act to displace the interference ions whilst the ion beam is traversing the quadrupole. The Varian X-series ICP-MS

is fitted with a kinetic energy discrimination (KED) jump, the KED jump is a negative bias between the collision cell and quadrupole mass spectrometer. Recombined interference ions with lower energy (higher m/z ratio) than pure (single) ions do not have the impetus to pass the KED bias. These tools, high resolution, a collision gas, 7% He/H₂ at a flow rate of 6.5 mL min⁻¹ and the KED, were applied to the ICP-MS configuration to enable analysis of broadwater freshwater samples. Combined with these configuration changes were a 1:2 dilution of the freshwater samples and a 1:20 and 1:40 dilution of the seawater samples.

2.04.05 Analytical Blank

The analytical blank for the analysis of the diluted samples is a standard addition series based in ultra pure water (UPW) acidified to ~pH 1.8; this signal incorporates that from the UPW dilutant, the acid and the background signal. Initial work was undertaken using a non-specific cleaned container and AR grade HNO₃, used to bring the dilutant to ~pH 1.8. This was subsequently changed to a trace metal cleaned vessel and double quartz-distilled HNO₃. The reason for the change in protocol was highlighted following an analysis of a 10 and 0.1 ppb spiked broadwater and also SLRS-4 which showed high blank values (analytical set up, He/H₂ CCT gas at 3.5 mL min⁻¹ in HR mode). The results for the blank signal using the clean container and the subsequent calculated limits of detection (LOD) are shown in Table 2.02. The blanks and LOD were measured in HR mode with H/He CCT gas at 6.5 mL min⁻¹ and the KED bias in place. LOD were calculated for UPW diluted with the acidified UPW (dilutant).

Table 2.02. Analytical blanks and limits of detection

	blank	RSD	LOD
	nM	% (n=6)	nM
Al	140 ± 42	30	126
V	21 ± 17	80	50
Mn	0.5 ± 0.3	60	0.9
⁵⁶ Fe	24 ± 3	13	9.4
⁵⁴ Fe	26 ± 3	12	9.6
Ni	14 ± 2	18	7.3
Co	0.1 ± 0.03	28	0.1
⁶⁵ Cu	9 ± 2	20	5.6
⁶³ Cu	11 ± 3	23	8.0
As	0.9 ± 0.3	31	0.8
¹¹⁴ Cd	0.7 ± 0.05	8	0.15
¹¹² Cd	0.6 ± 0.06	9	0.18
²⁰⁸ Pb	4 ± 0.4	9	1.1
²⁰⁶ Pb	4 ± 0.5	13	1.6

2.04.06 ICP-MS Accuracy – CRM Recovery

The result for a repeated analysis of SLRS-4 with the configuration which was applied to the broadwater samples is shown in Table 2.03. This configuration used the quadrupole in high resolution with H/He CCT gas at 6.5 mL min^{-1} and a KED bias between the CCT cell and the quadrupole. Samples were diluted to factor of 1:2. Four elements were unable to be accurately measured, these were vanadium, nickel, cadmium and lead. The recoveries for aluminium, manganese and arsenic were within 10% of the certified values, with less than 10% RSD ($n = 3$). Copper and iron using two isotopes were within 15% of the certified values with the RSD on the iron analysis less than 10% and on the copper analysis 15%. Cobalt measurements were within range when the error is factored in, however, the recovery was high, 140%, also the RSD was poor $>40\%$; results should be handled with caution as they are affected by noise within the ICP-MS. All elements successfully recovered have their respective LOD, calculated as three times the standard deviation of an acidified UPW sample (blank), below the certified concentration in SLRS-4.

Table 2.03. SLRS-4 results from final instrument configuration. Only those elements in black (successful recoveries) were considered for further work, those in grey were not used.

	certified	measured	recovery	RSD	blank	LOD
	nM	nM	%	% ($n=3$)	nM	nM
Al	2001 ± 150	1892 ± 135	106	7	140	126
V	6 ± 1	12 ± 11	193	96	21	50
Mn	61 ± 3	64 ± 4	105	6	0.5	0.9
^{56}Fe	1844 ± 90	2123 ± 187	115	9	24	9
^{54}Fe	1844 ± 90	2141 ± 195	114	9	26	10
Ni	11 ± 1	32 ± 7	292	21	14	7
Co	0.6 ± 0.1	0.8 ± 0.3	140	41	0.1	0.1
^{65}Cu	29 ± 1	25 ± 4	88	15	9	6
^{63}Cu	29 ± 1	29 ± 1	101	14	11	8
As	9 ± 1	8 ± 0.3	90	3	0.9	0.8
^{114}Cd	0.1 ± 0.01	0.3 ± 0.1	337	36	0.7	0.1
^{112}Cd	0.1 ± 0.01	0.8 ± 0.1	758	15	0.6	0.2
^{208}Pb	0.4 ± 0.01	20 ± 2	5040	15	4	1.1
^{206}Pb	0.4 ± 0.01	18 ± 4	4562	20	4	1.6

2.04.07 CRM Recoveries as Correction Factors

A small suite of earlier broadwater samples were able to have their measured concentrations corrected through a second analyses of a series of samples collected on the 19th March 2008. These samples had been analysed under two ICP-MS configurations; initially

analysed as a 1:10 diluted sample with an external calibration and again analysed as a 1:2 diluted sample with the H/He CCT gas at 6.5 mL min^{-1} , HR mode and KED jump, as per the successful recovery of the CRM, SLRS-4. The measured concentrations were compared through a one-tailed Fisher F-test, with the null hypothesis (H_0) indicating the results are due to random scatter. The H_1 was true for aluminium $f = 268$ ($p > 0.99$), manganese $f = 71$ ($p > 0.99$), and ^{56}Fe , $f = 81.7$ ($p > 0.99$). Further information on the calculation of the correction is given in the Appendices, Section A4.01.

2.04.08 Method for Seawater Experimental Samples

The analysis of seawater following experimental work initially attempted to analyse for all dissolved elements as in the freshwater analyses. However, low limits of detections and good sensitivity were essential in the work to be able to measure changes in the soluble fraction (0.2 μm filtered) due to the chemistry. The method therefore concentrated on aluminium and manganese as initial experimental trials were to be conducted with the addition of particulate phases of aluminium, manganese and iron; reduced iron was to be measured on a FIA-Cl system (Chapter 3), though total iron values for each experiment were to be measured on the ICP-MS with expected high concentrations. Aluminium though not certified in the CRM CASS-4 was measured with the aim of measuring a precise value; however, this was not achieved so therefore only manganese was measured from experimental samples.

Comparing between the ICP-MS using NH_3 and H/He CCT gas (1:20 sample dilution) and ICP-OES (1:10 sample dilution) measuring diluted CASS-4 using standard additions shows that the best method would be to use the ICP-MS with H/He CCT gas at $\sim 6.5 \text{ mL min}^{-1}$ in HR mode and incorporating the KED to aid in the removal of interference ions to measure the manganese (Table 2.04). The method provides the lowest blank and a comparable LOD to the NH_3 gas whilst the accuracy and precision were better than the NH_3 gas.

Table 2.04. Comparison of techniques for recovery of manganese from within CASS-4

	certified nM	measured nM	recovery %	RSD %	blank nM	LOD nM	dilution factor
H/He CCT gas	50.6 ± 3.5	51 ± 3	101 (n = 4)	6	0.2	1.3	20
NH_3 CCT gas	50.6 ± 3.5	62 ± 11	123 (n = 5)	18	1.4	0.9	20
OES	50.6 ± 3.5	52 ± 9	103 (n = 5)	17	2.2	6	10

The analysis of seawater samples for total iron was undertaken on an ICP-MS using 1:40 dilutions and standard additions. The corresponding recovery of the National Research Council

of Canada, certified reference material, CASS-5, specified concentration, 25.8 ± 2.0 nM, was, following the blank correction, 106% and was measured at 28 ± 4 nM ($n = 3$), 15 % RSD. The blank was measured at 14.8 ± 0.09 nM with a corresponding limit of detection ($3 \times \sigma$ of 3 ultra pure waters) of 0.3 nM.

2.04.08 ICP-MS Final Configurations

For both multi-element freshwater analysis and for manganese total iron for the seawater experiments the ICP-MS was used in HR mode. The CCT had a 7% H/He collision gas at flow rates of ~ 6.5 mL min $^{-1}$ and between the CCT cell and quadrupole a negative KED bias was set. The freshwater samples were diluted to a 1:2 whilst seawater samples were diluted to 1:20 (manganese) and 1:40 (total iron).

Chapter Three

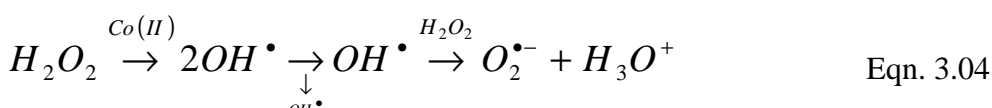
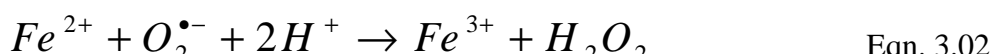
Flow Injection Analysis Method Development

3.00 Introduction

The flow injection analysis of luminol chemiluminescence has been used for many years, since Seitz and Hercules (1972), for the measurement of soluble iron (II). The system's ability to measure in real time makes it a good analytical tool for short-term (< 1 h) experiments. This chapter details the work involved in compiling the equipment and enabling it to measure, quasi-simultaneously, two analytes, hydrogen peroxide and Fe(II).

3.01 Flow Injection Analysis - Chemiluminescence with Luminol

The FIA-Cl method utilises the chemiluminescence of luminol as the means of measuring the concentration of hydrogen peroxide and iron (II) in aqueous media. FIA-Cl can measure a range of analytes, especially the reduced species of transition metals; chemiluminescence occurs when the reduced form of a redox pair is oxidised, (Cu(I) / Cu(II) (Coale et al., 1992), Co(II) / Co(III) (Sakamoto-Arnold and Johnson, 1987), Fe(II) / Fe(III) (Seitz and Hercules, 1972), Mn(II) / Mn(IV) (Doi et al., 2004)). In order to induce luminol chemiluminescence, a reduced metal e.g. Fe(II) (Equations 3.01 to 3.03) or for H₂O₂ analysis Co(II) (Equation 3.04) (held in the luminol reagent) is oxidised. These oxidation reactions produce hydroxyl and superoxide radicals. Fe(II) will oxidise when mixed with the luminol reagent within several hundred milliseconds (King et al., 1995; Rose and Waite, 2001).



The following luminol reaction sequence (Figure 3.01) is adapted from Rose and Waite, (2001) and Merenyi et al. (1990). The radicals produced from the metal oxidation react with the luminol negative ion, held in an alkaline medium, forming a luminol negative radical; either through primary or one electron oxidation (Figure 3.01, stage 1).

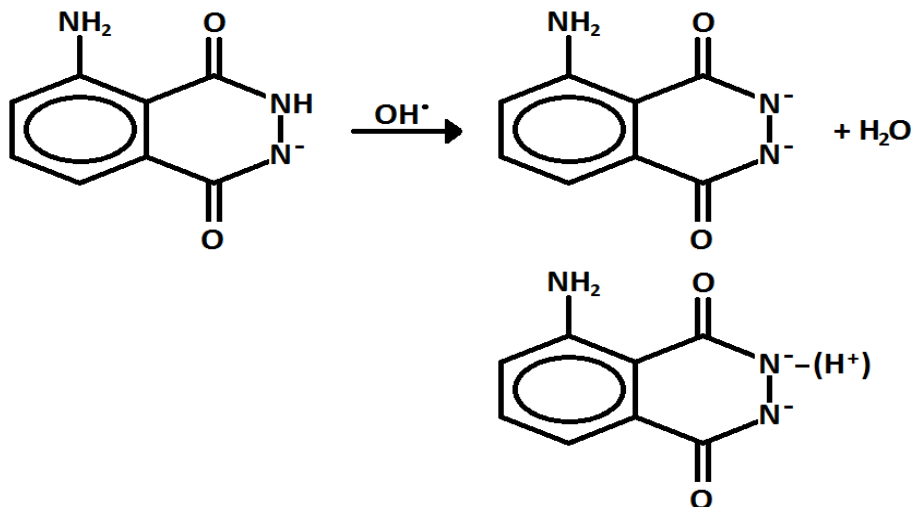


Figure 3.01, stage 1

The luminol negative radicals, ($L^{\bullet-}$, LH^{\bullet}) can then pass through one of two mechanisms to form the alpha-hydroxy-hydroperoxide (α hhp) intermediate. The first pathway (Figure 3.01, stage 2a) occurs for luminol that is present as a monoanion ($L^{\bullet-}$), and involves the oxidation by superoxide to the α hhp intermediate.

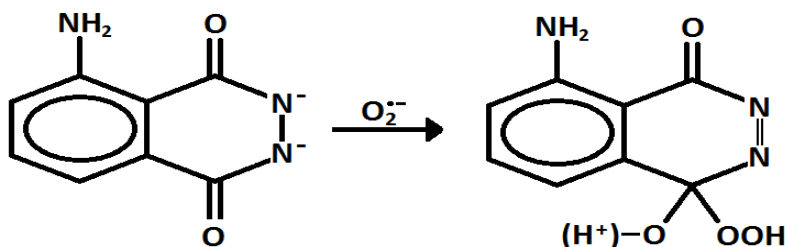


Figure 3.01, stage 2a

The second pathway (Figure 3.01, stage 2b) can act on both the monoanion and undissociated forms of the luminol negative radical and requires a secondary oxidant, again for instance OH^{\bullet} . The diazaquinone (L) forms by either rapid recombination of the luminol radicals ($L^{\bullet-}$, LH^{\bullet}) or more slowly from the reaction of the luminol monoanion with molecular oxygen (Merenyi et al., 1990). Diazaquinone then reacts with monodissociated hydrogen peroxide (HO_2^-) to form the α hhp intermediate.

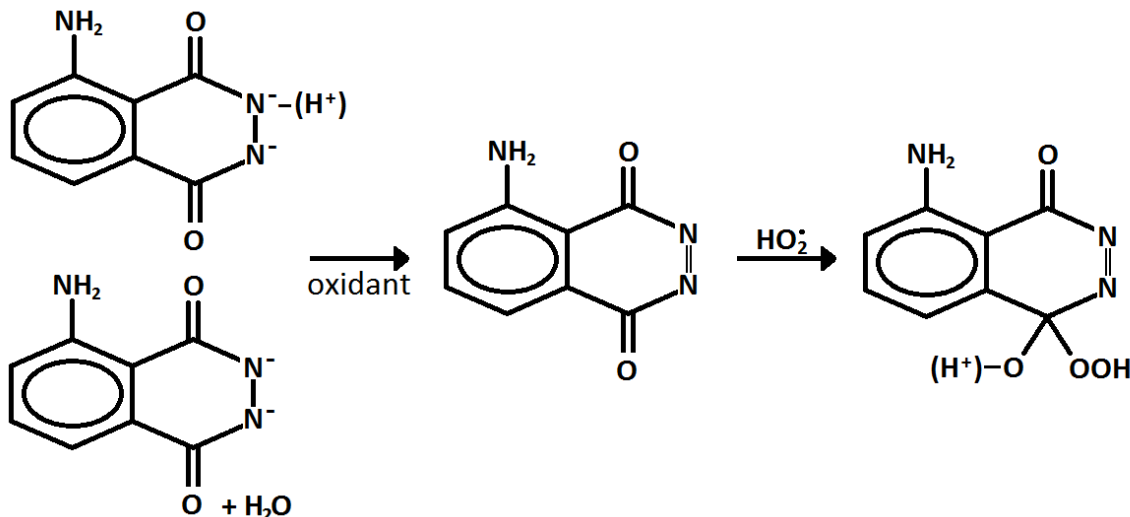


Figure 3.01, stage 2b

The formation of the α hhp is the key stage in luminol chemiluminescence (Merenyi et al., 1990). The α hhp intermediate deprotonates to either an undissociated or monoanion forms. These forms then decompose to aminophthalate and N_2 gas (Figure 3.01, stage 3). However, it is only the decomposition of the monoanion to its ground state which leads to the excitation and chemiluminescence (Eriksen et al., 1981; Merenyi et al., 1990; Uchida et al., 2004).

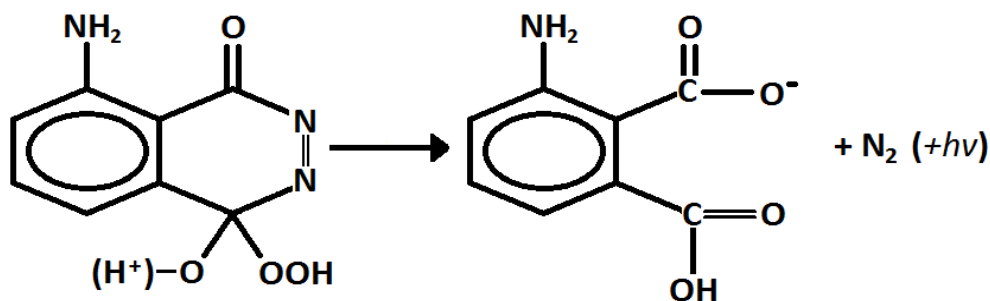


Figure 3.01, stage 3

3.01.01 Hardware Configuration

Intensity of luminol chemiluminescence measurements were measured on either a Hamamatsu (Iwata City, Japan) 124-06 photon multiplier tube or a Hamamatsu 135-11 photon counting tube. The photon multiplier tube (PMT) measures the luminescence as a change in voltage; photons captured on an electrified grid impart energy to that grid, the subsequent increase in voltage is then measured. The voltage passes to a DGH D1000 interface module (DGH) (New Hampshire, USA) this converts the voltage to an ASCII readable format for the pc

running Windows XP. The photon counting tube (PCT) counts the number of photons and passes this directly to the control pc through an RS232 port. The sensitivity of the PMT is set manually; the constant voltage across the grid can be from 1 to 1250 mV. The control software was written by the computing support staff in the school of Environmental Science at the University of East Anglia; coding was in Microsoft's Visual Basic 2008. Peak heights were used during the initial system testing and development. When the system was operational and understood and the software had undergone further development, work continued using peak area. Peak area is less sensitive to the system spiking and changes to the peak form due to aging of peristaltic pump tubing. It is therefore a more robust indication of the chemical reaction.

The photon tube housing is a solid uPVC block; this holds the tube perpendicular to a glass spiral flow-cell. To prevent light contamination a black plastic (photographic plate) bag surrounds the block and tube. The lower half of the bag and where the two inlet and single outlets enter the bag are covered with black gaffer tape for approximately 20 cm. 1 mm id Teflon tubing is used throughout the flow injection system except on the waste outlet, which is of 3 mm id. Connectors are PTFE and supplied by Omnifit (Diba industries, Cambridge, GBR). Reagent, sample and carrier pump tubes are made from Tygon ST, Upchurch Scientific (Washington State, USA) and their flow rates are controlled by a Rainin 8 channel peristaltic pump (California, USA). The switching valve is a VICI - Valco Instruments Co. Inc. (Texas, USA) 10 way cheminert microelectric valve actuator with control module. The FIA-CL hardware set up for the dual analysis of analytes with a reagent carrier (Figure 3.02) is based on that of King (2000).

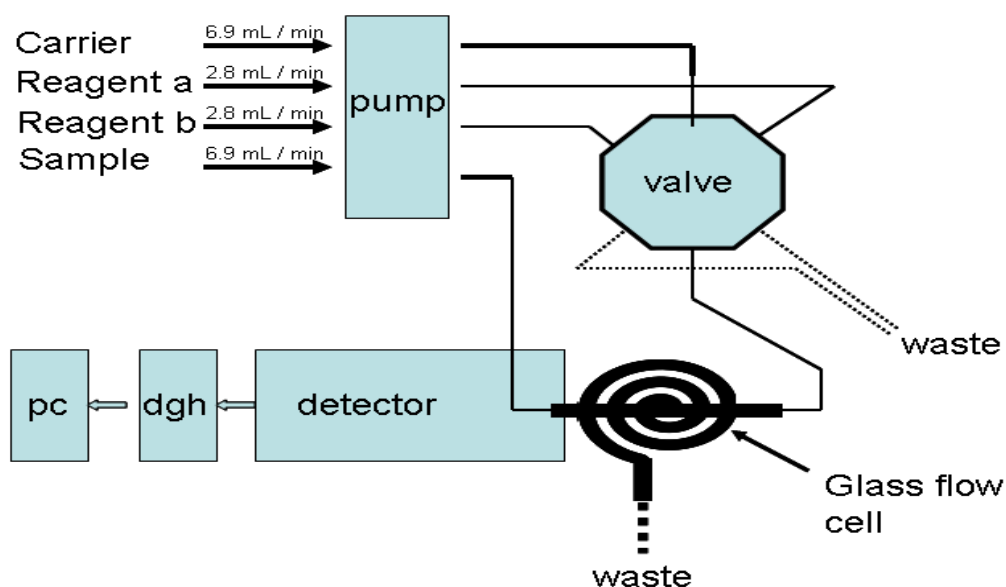


Figure 3.02. FIA, hardware configuration

3.01.02 Valve Configuration

Analysing single analytes on the FIA-Cl system allows two plumbing configurations on the VICI load / inject valve. The configurations (Figure 3.03) are that of King et al. (1995), and that demonstrated at IFM-GEOMAR (COST735 funded STSM) by Dr. Peter Croot, based on the set up for H₂O₂ analysis by Yuan and Shiller (1999), except with an increased holding loop. The difference between configurations is where the sample and reagent mix. The fast kinetics of Fe(II) oxidation when encountering the high pH luminol reagent suggest favouring the King over the Croot set up. This is as mixing within the flow cell occurs directly under the PMT, where as with the Croot set up mixing commences prior to the flow cell. However, if a sufficiently large volume of reagent / sample (approximately 700 µL) is used for iron (II) analysis then this negates the problem of the early reagent sample mixing and the loss of some signal which could be encountered with the Croot set up. The King configuration mixes sample and reagent within the flow cell. In the Croot configuration the reagent passes into the sample flow stream prior to full mixing in the flow cell. The Croot configuration has more flexibility than the King system because either an aliquot of reagent passes into a sample flow stream or the sample passes into a reagent flow stream. This flexibility is useful if there are only small quantities of sample available. The configuration of the valves does have some relationship to the analyte under consideration. The formation of the hydroxide radical during iron (II) oxidation has millisecond kinetics at the pH of the luminol reagent, pH > 10, (King, 2000).

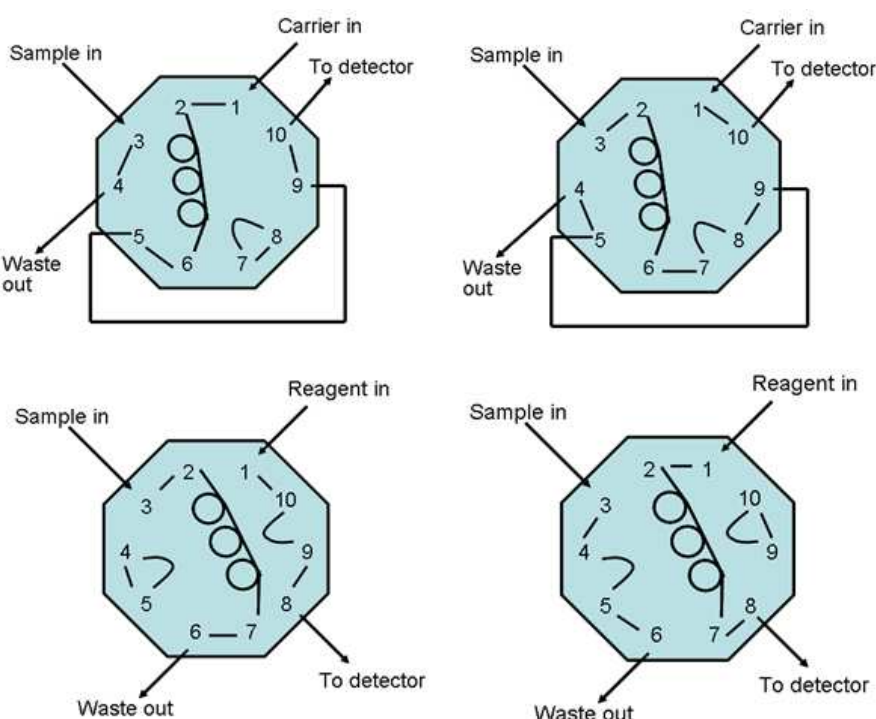


Figure 3.03. King et al. (1995) (top) and Croot load (left) /inject (right) valve configurations.

3.01.03 Luminol Recipe

The luminol reagent requires an alkaline buffer. Various buffers have been used, KOH – H₃BO₃ (King et al., 1995; O'Sullivan et al., 1995; Seitz and Hercules, 1972), NaOH (de Jong et al., 1998), NH₄OH (King, 2000; Rose and Waite, 2001), Na₂CO₃ (Bowie et al., 1998) and K₂CO₃ (Croot and Laan, 2002). The main buffer used in this work was K₂CO₃ (Croot and Laan, 2002) with some tests carried out using a NH₄OH buffer (King, 2000). The key to obtaining interference-free fluorescence is optimisation of the pH when the luminol reagent and sample are mixed. Optimum fluorescence of the mixed sample and reagent occur at approximately pH 10.5 to 11.0 for fresh water (O'Sullivan et al., 1995; Seitz and Hercules, 1972) and for seawater at pH 9.9 (O'Sullivan et al., 1995), though this is also dependant on the valve set up.

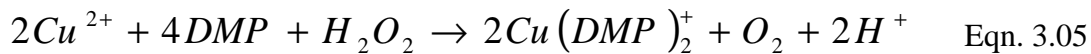
3.02 Hydrogen Peroxide Analysis

The analysis of H₂O₂ compared to iron (II) is less susceptible to contamination and standards are relatively stable. For these reasons, H₂O₂ analyses were used whilst developing the FIA-Cl system and understanding how the system worked with trials on both the PMT and the PCT. The FIA-Cl method for measuring H₂O₂ with luminol is based on H₂O₂ oxidising cobalt (II) which is held in the alkaline luminol solution. The oxidation of Co(II) by hydrogen peroxide (see Section 3.01 Eqn. 3.04) produces hydroxide and superoxide radicals which then cause the oxidation of the luminol (Figure 3.01). Cobalt (II) is used as this is the most sensitive reduced species in a redox pairing to H₂O₂, the method was first applied to seawater by Yuan and Shiller (1999). Their luminol reagent consisted of 0.65 mM Luminol in 0.1 M NaCO₃ adjusted to pH 10.15 with 2 M HCl. A Co(II) solution produced from its sulphate salt was added to the luminol reagent to achieve a final concentration of 60 µM.

3.02.01 H₂O₂ Standards

The H₂O₂ stock and sodium thiosulphate for its standardisation were measured titrimetrically as per Vogel (1989). The concentration of the 6 % H₂O₂ stock was 2.63 M. Primary and working standards were produced through serial dilutions into weighed, dark aged, UPW. The primary standard was stored in a brown polyethylene bottle at 4°C for up to one week. Working standards were produced on the day of use. During development H₂O₂ standards were periodically checked. The technique follows that of Baga et al. (1988) where H₂O₂ is used to reduce copper (II) in the presence of excess 2,9-dimethyl-1,10-phenanthroline (DMP) (Equation 3.05) with the addition of 0.1 M phosphate buffer to the samples as suggested

by Kosaka et al. (1998). The copper (I)-DMP complex is determined spectrophotometrically at 454 nm.



The DMP solution is made by dissolving 1 g of DMP in 100 mL ethanol; this is stored in an amber glass bottle at 4°C. A 0.01 M Cu(II)SO₄ solution was made by dissolving copper(II) sulphate pentahydrate in ultra pure water (UPW). The 0.1 M phosphate buffer was made by combining K₂HPO₄ and NaH₂PO₄ in equal molar quantities and titrating with either 0.5 M H₂SO₄ or 1 M NaOH to achieve pH 7. The method involves combining 1 mL of 0.01 M Cu(II)SO₄ and 1 mL of the ethanoic DMP solution in a 10 mL volumetric flask, these are then followed by 1 mL of 0.1 M phosphate buffer and a volume of H₂O₂ primary standard, volume made up with UPW.

A comparisons between Baga et al. (1988) (Equation 3.06) the adapted phosphate buffer version of Kosaka et al. (1998) (Equation 3.07) and through the serial dilution of the stock (Table 3.01) showed results were within 3 %. This result suggests that the serial dilutions were accurate with an operational error of ~3 % during dilutions and that this method can be used for the production of working standards with out the requirement for permanent checks.

$$[H_2O_2] = \Delta A_{454} / 1500V \quad \text{Eqn. 3.06}$$

$$\Delta A_{454} = \epsilon [H_2O_2] (V / 100) \quad \text{Eqn. 3.07}$$

ΔA_{454} is the difference between the absorbance of the blank and the sample, V is the volume of working standard, ϵ , the molar extinction coefficient - calculated as the slope of the calibration based on the volumes of working standard used and their absorbance. The Baga et al. (1988) equation has ϵ as 1500.mol⁻¹.cm⁻¹ implicit within its calculation.

Table 3.01. Measured and calculated concentrations for H₂O₂ working standards

	measured	RSD
	μ M	%
Baga et al., 1988	97.6	0.41
Kosaka et al., 1998	100.4	0.4
serial dilutions	102.5	0.39

3.02.02 H₂O₂ Development

Production of a first calibration curve was aimed at H₂O₂ seawater concentrations, Atlantic surface waters, < 30 – 123 nM, (Steigenberger and Croot, 2008). Figure 3.04 shows an example trace produced from the PMT, with the inset showing the calibration curve obtained (based on linear response). The standard range and correlation indicate that the basic system was capable of measuring H₂O₂ concentrations between the 10 s to 100 s nM.

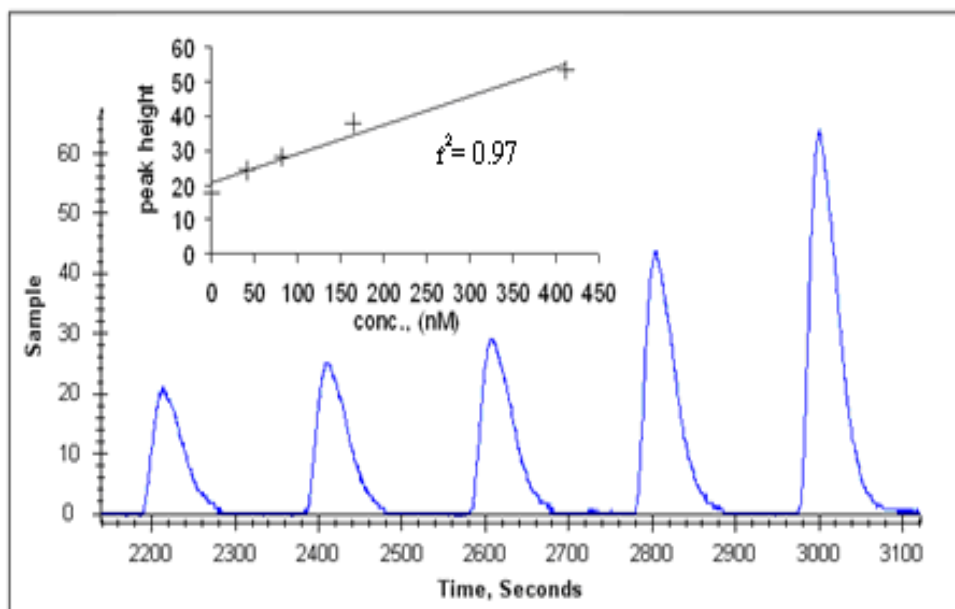


Figure 3.04. H₂O₂ calibration in aged UPW; standards 0, 41, 82, 165 and 412 nM. PMT trace using Croot plumbing, (trace lifted directly from the software). Sample and reagent flow rates 1.1 mL min⁻¹, sensitivity 1250 mV, call rate 500 ms

Within the H₂O₂ calibration the sensitivity between UPW based standards and the blank was low. Following Yuan and Shiller (1999) and Croot and Laan (2002) the luminol reagent was held at a pH of 10.2. However, the optimum pH for the luminol in the analysis of H₂O₂, as it follows the same mechanism as that for the analysis of iron (II) is approximately pH 11 (Seitz and Hercules, 1972). When the luminol reagent mixes with a pH 8 medium sample its pH will decrease. Therefore, the pH of the luminol reagent should be sufficiently high that when it mixes with seawater the decrease should bring the pH to that for optimum chemiluminescence, pH 11. Figure 3.05 shows how chemiluminescence increases for a 60 nM H₂O₂ seawater standard as the pH of the luminol reagent increases. Standards measured at pH < 10.6 were affected most by fluctuations in the PMT baseline (0.96 ± 0.32), suggesting the sensitivity was poor. At pH > 11.2, the peaks tended to merge with one another. pH 11.2 reagent gave the

highest sensitivity without the merging of the peaks. Standards in aged seawater produced chemiluminescence signals an order of magnitude lower than those in aged UPW.

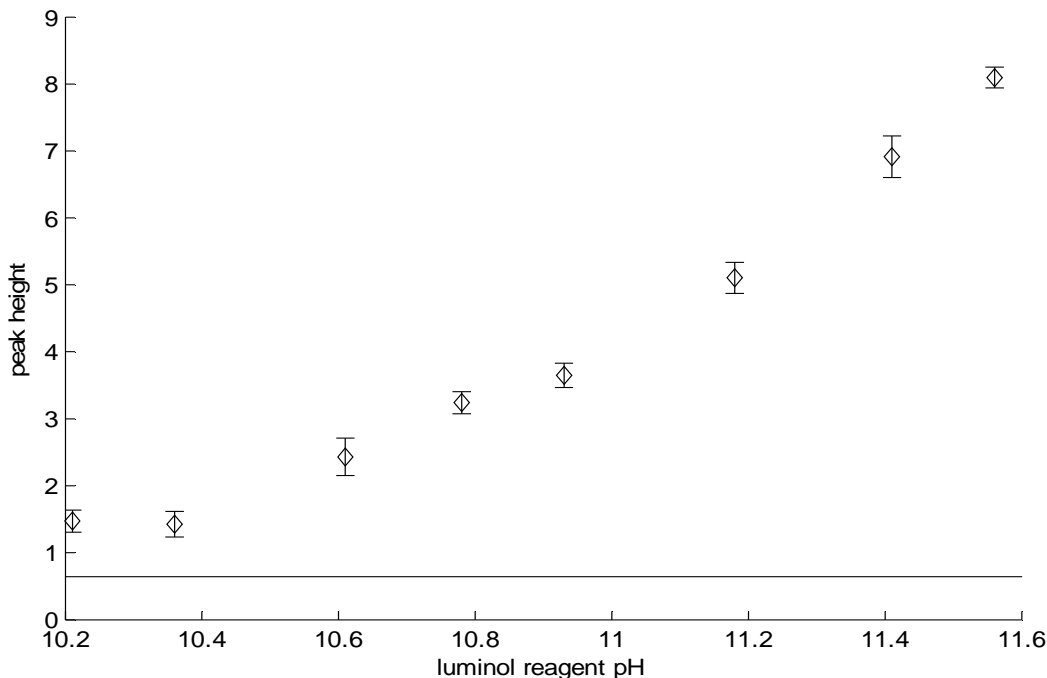


Figure 3.05. pH sensitivity of luminol reagent for H_2O_2 analysis. Error bars are the standard deviations of 8 repeat samples. Solid horizontal line is the mean baseline for the analyses.

Yuan and Shiller (1999) measured a concentration of 30 nM H_2O_2 in fresh Milli-Q water, when left in the dark overnight oxidation reactions lead to the decay of this hydrogen peroxide. When operational, the system attempted to measure H_2O_2 in dark aged UPW and North Sea seawater via standard additions. For both attempts, measurements were below the limit of detections (LOD), 1.3 nM and 2.3 nM respectively. Limits of detection as calculated from 3σ of the blank signal are dependant on the luminol reagent, strength and pH, and the matrix of the analyte and are therefore specific to each batch of luminol produced and the medium under consideration.

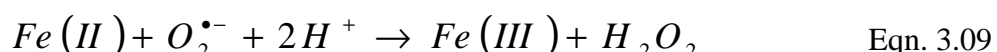
3.02.03 Blank Signal

The FIA-Cl signal is made up of five parts (Croot and Laan, 2002; Yuan and Shiller, 1999): Electronic noise (B_E), light emission from sample media (B_w), light emission from reagent (B_R), light emission from reagent reactions with seawater components (B_{sw}) other than analytes and the signal attributed to analytes (S_A). The baseline comprises of $B_E + B_w$, with the PMT this is dependant on the sensitivity set by the voltage. For example the baseline reading

was around 0.96 ± 0.32 counts per 0.5 seconds, this signal is constant for standards and samples. The blank signal $B_R + B_{SW}$ is specific to each reagent batch, sample medium and plumbing configuration (external or internal flow cell mixing), this is given as a fluorescence count above the baseline; S_A is corrected for this value. The blank is therefore the fluorescence caused through a combination of the experimental media (without addition of analytes, though there may be some latent concentration) and the luminol reagent. The blank signal can be measured for every standard analysed ($n=2$ for five standards during calibrations in experimental work) and also as a blank value itself through a continued analysis of the sample medium. The standard deviation of the repeated analyses of the blank signal is that used to calculate the LOD. As the LOD and blank are media specific they can only be given for each experiment (Chapters 5 – 7).

3.03 Iron (II) Analysis

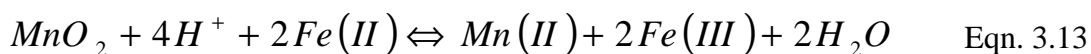
The iron (II) luminol chemiluminescence measures the soluble (aquo) and organically complexed iron (II) (Rose and Waite, 2002). Organically complexed iron (II) should be present in the system for longer due to its slower oxidation rates (Emmenegger et al., 1998), however, it is not totally clear whether the total proportion of iron (II) which is organically complexed (King, 1998) is also being measured. The primary mechanism by which luminol chemiluminescence is produced in the presence of iron (II) is due to its oxidation by oxygen, following the Haber-Weiss mechanism (Equations 3.08 to 3.11), as proposed by King et al. (1995). The by-products of the iron (II) oxidation, the hydroxide radical and the superoxide ion, are those that act on the luminol to produce its eventual chemiluminescence and not the iron (II) itself.



3.03.01 Iron (II) Interferences

Primary transition metal cations which can interfere with the Fe(II) – luminol luminescence are; Co(II), Cu(I), Mn(II), Ti(II), V(IV), Zn(II) (Klopf and Nieman, 1983; O'Sullivan et al., 1995; Seitz and Hercules, 1972). With a mixed sample / reagent pH greater

than pH 9 this favours the iron (II) – luminol luminescence over other reduced metals, Co(II) and Mn(II) (O'Sullivan et al., 1995; Xiao et al., 2002). Ussher et al. (2009) found that it is Co(II) and V(IV) which are the main interferences. However, the concentration of cobalt is generally low enough in seawater not to be problematic, average concentration 0.02 nmol kg⁻¹ (Bruland, 1983). A concentration of 1 µM Co(II) would produce an equivalent Fe(II) concentration of 45 nM. V(IV) which has a seawater concentration, 30 – 40 nM (Jeandel et al., 1987) would be included in the blank signal (Bsw). Increasing the concentration of luminol, to greater than 1 mM allows it to compete more effectively for the iron (II) which is being oxidised by copper (II) (Equation 3.12) and MnO₂ (Equation 3.13) (O'Sullivan et al., 1995) which forms and precipitates at seawater pH > 9.5; this concentration of luminol was applied by Hansard and Landing (2009).



King (2000) found that the relationship between iron (II) concentration and chemiluminescence intensity was attributed solely to iron (II) concentrations from 1 nM to 1 µM. Whilst Rose and Waite (2002) found that chemiluminescence solely due to iron (II) concentration could only be wholly attributed to iron (II) concentrations from 1 to 32 nM. Organic material can affect luminol chemiluminescence by adsorption of the luminescent signal, competing for radical intermediates and complexing the iron (II) (O'Sullivan et al., 1995). However, slopes of seawater calibrations with and without organic material were still the same (O'Sullivan et al., 1995). King et al. (1995) found no effect of hydrogen peroxide at concentrations up to 1 µM, whilst Rose and Waite (2001) found that hydrogen peroxide concentrations greater than 100 nM affected iron (II)-luminol luminescence.

The concentration of the luminol reagent for iron (II) analyses was set to 1.5 mM. This concentration is three times the concentration of Yuan and Shiller (1999) and King et al. (1995) and twice that of Croot and Laan (2002), but closer to that of Hansard and Landing (2009), 1 mM. Seitz and Hercules (1972) used 0.4 mM luminol but state that 5 mM luminol gave the best response. The reason for the increased concentration of luminol was work by O'Sullivan et al. (1995) suggesting that at higher (> 1.0 mM) luminol concentrations there is less effect in measuring H₂O₂ and as such can be used to measure iron (II) in higher peroxide waters.

3.03.02 Iron (II) Analysis in Acidified UPW

Measurements of pre-acidified (in-house double quart-distilled HNO_3) iron (II) in UPW commenced with the plumbing following that of King (2000) (Figure 3.03). The iron (II) standards were produced from dilutions into UPW at pH 1.6 from an iron (II) sulphate stock solution produced by weighing the appropriate amount and combining with pH 1.6 UPW. At pH 1.6 the iron (II) will remain in this reduced form whilst in solution, however, new stocks were produced monthly. The initial luminol reagent recipe followed that of Dr. Peter Croot, 0.07 mM luminol in 0.05 mM K_2CO_3 except with no addition of tri-ethylene tetramine (TETA) which is used for the removal of Fe(II) during Fe(III) analysis; this recipe was provided whilst undertaking a COST735 sponsored visit at IFM-GEOMAR. Following the work of O'Sullivan et al. (1995) the concentration of the luminol reagent was subsequently increased to 1.5 mM to prevent chemiluminescence from residual redox pairs, hydrogen peroxide and to allow it to out compete $\text{Mg}(\text{OH})_2$ for iron (II) during its precipitation at pH > 9.5. The initial pH of the reagent was 9.3 and the standards at pH 1.6 before buffering to pH 4.6 (Fe(II) half-life >7days) with 2 M ammonium acetate (trace metal clean, Fisher, Seastar).

Calibration curves for iron (II) in UPW buffered to pH 4.6 were produced using batches of luminol reagent aged for different lengths of time (Figure 3.06), and measured on the PCT. The calibration curves distinctly show the non linear response for calibrations over extended calibration ranges (0–100 nM) compared to those over shorter ranges (0–25 nM) (Croot and Laan, 2002; King et al., 1995). The plots also show how luminol chemiluminescence varies between similar batches, this has also been attributed to differently aged luminol (Hansard and Landing, 2009; Rose and Waite, 2003a; Yuan and Shiller, 1999). Croot (personal communiqué) suggested leaving the reagent for 24 hrs prior to use and this time frame was used in future works.

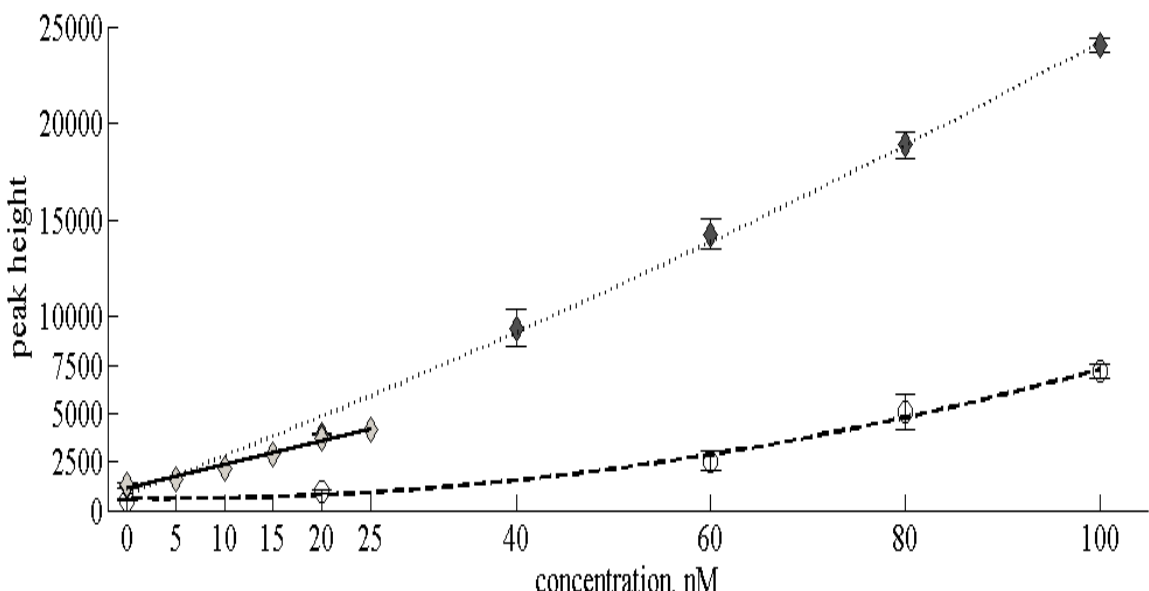


Figure 3.06. Repeat calibration curves for iron (II) in UPW. Diamonds were analysed using the same luminol reagent (aged 1 week) whereas circles were measured using a newer (aged 24 hrs) luminol reagent. The error bars are the standard deviations of 4 repeat analyses.

The iron (II) calibrations, Figure 3.06, show a change of slope from the 0 – 25 nM range to the 0 – 100 nM range. The change in slope between calibration ranges suggest as earlier with the H_2O_2 that the response is non-linear and is so for Fe(II) from $\sim > 20$ nM. R^2 values for the linear and curve-linear 0 – 25 nM calibration are 0.978 and 0.983 respectively. The curve-linear results agree with King et al. (1995), linear response up to approximately 12 nM and also Rose and Waite (2001) and Seitz and Hercules (1972). Croot and Laan (2002) undertook real time analysis of Antarctic seawater, due to the non linearity of the iron (II) calibration they kept their calibration range as small as possible to allow for a liner correlation. Yuan and Shiller (1999), King et al. (1995) and Croot (personal communiqué) suggest that calibrations are generally non linear unless there is a small range in the standards. Yuan and Shiller (1999) had linearity in their H_2O_2 system up to 300 nM. The differences in the range of the linear response may also be attributed to the experimental set-up used; the photon counter, flow cell and dynamics and point of mixing of the reagent and sample.

The rate at which data were logged at the pc was far less than that used by Croot. On this computational side the FIA software was obtaining data from the PCT at c.500 ms. The Croot set up would obtain data every 50 ms, the fastest at which the PCT undertakes data acquisition. The faster acquisition provides better analytical reproducibility through an increase in the accuracy of the peak form. Enhanced reproducibility lends itself to greater precision in the calibrations. The reproducibility was questioned on closer inspection of the peak form, which shows intense shoulders on each peak (Figure 3.07). The PMT minimum call rate is

500 ms and it was due to this limit that the rate remained at 500 ms which detracted from the sensitivity of the peak form, however, the smoothing effect removed the peak shoulders.

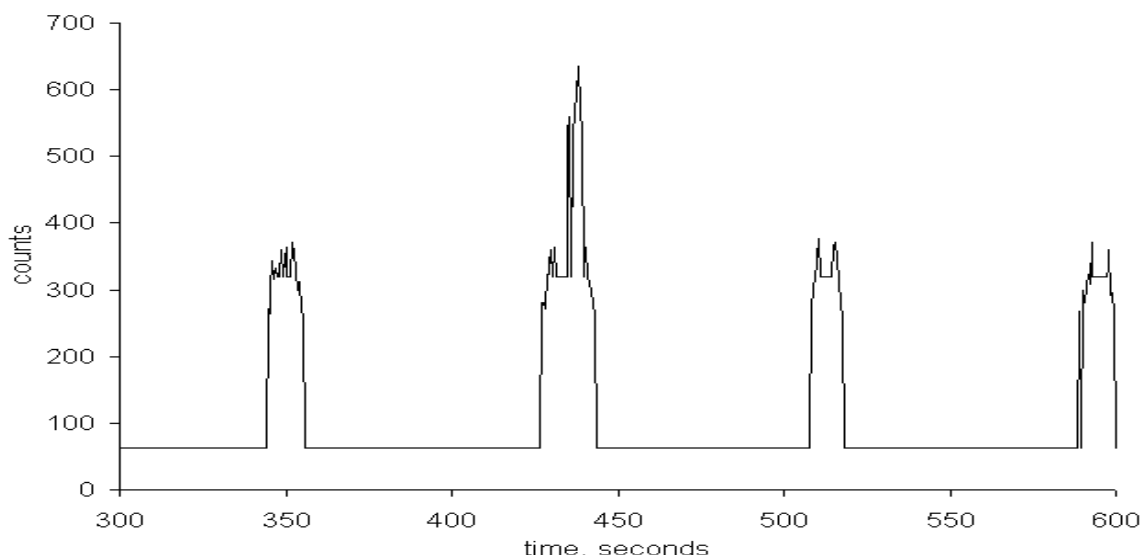


Figure 3.07. PCT measured trace of a repeat 10 nM Fe(II) standard. The trace sample shows intense shoulders on the peak.

Measuring iron (II) standards buffered to pH 4.6 had precisions > 10% RSD. The poor precision was due to a dual peak forming (Figure 3.08); for each analysis a sharp intense peak developed followed by a smaller but broader peak. The dual peaks were not considered problematic, their magnitude was. The Croot iron (II) analysis also exhibited a distinct fore peak before a much larger second peak attributed to the iron. The trough between the two peaks in the Croot lab was negative whereas the FIA-Cl system here stayed positive. The fore peak was due to the production of CO₂ when the alkaline luminol reagent aliquot mixes with the acidic sample; the change in pH produces CO₂ from the carbonate present in the system. The chemiluminescence of luminol by CO₂ has been seen by Xiao et al. (2002).

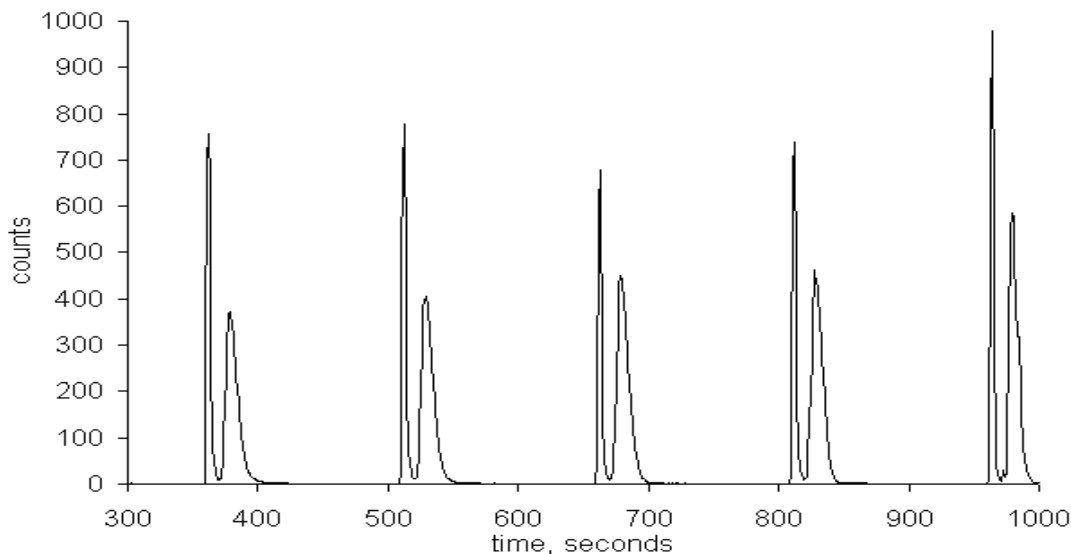


Figure 3.08. Dual peak formation during analysis of an acidified Fe(II) standard.

Configuration changes, reagent loop volume, load and inject timings, and pump speed, and altering the plumbing from reagent injection (Croot) to a carrier system (King, 2000), did not affect the formation of a pre peak nor its magnitude. To prevent the dual peaks the sample analyses pH was elevated so there was less CO₂ formation at the reagent-sample interface. Using pH 6 (Fe(II) half-life 7 days) buffered seawater standards the relative size of the pre peak dropped to a similar height as the aft peak. Therefore, as sample pH increases the pre-peak decreases, however, above a certain pH the Fe(II) would oxidise to Fe(III) too quickly to be analysed.

Calibrations in pH 6, UPW and seawater from 0 – 100 nM at 20 nM increments (Figure 3.09) resulted in expected non-linear response, therefore a second order polynomial was fitted (Hopkinson and Barbeau, 2007; Rose and Waite, 2001) using information derived from the aft peak. When the system was applied to seawater the double peaks were not present. This would suggest that a residual radical within the processing of ultra pure water causes or enhances this pre-peak or that the seawater buffering capacity itself helps prevent the formation of CO₂.

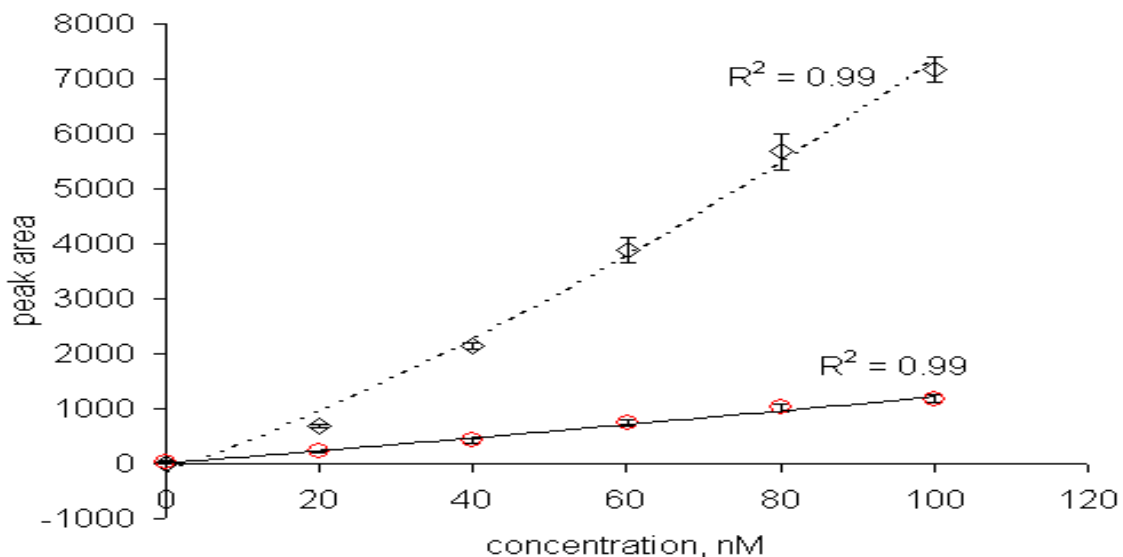


Figure 3.09. Comparison of UPW (diamonds, dotted line) and seawater (circles, constant line) Fe(II) calibrations. Error bars are the standard deviations of five continuous analyses of the standard.

One caveat with a curve-linear fit for a standard addition calibration is that a calculation of the LOD is based on $3 \times \sigma$ of the calculated error on the zero addition standard as if the fit was linear (Miller and Miller, 1993). The LOD (Figure 3.09) thus calculated for UPW was 13 nM and for seawater, 11 nM, RSD 7%. The comparison in Figure 3.09 also shows that artefacts within seawater and or differences in the pH reduced sensitivity to approximately a fifth, a phenomenon also seen with the analysis of H_2O_2 . With respect to the seawater matrix the change can be either through a suppression of the signal or an increase in the non-light producing luminol chemiluminescence, greater formation of the undissociated αhhp intermediate (Rose and Waite, 2001). The effect seawater and its constituents has is incorporated into components of the blank signal (Section 3.02.03).

3.03.03 Discrete Iron (II) Measurement

With no certified reference material (CRM) available for iron (II), analysis was undertaken on samples with specified total iron concentrations held at pH 1.6. Due to the effect of matrix and previous history of the sample (Rose and Waite, 2003a; Rose and Waite, 2001) standard additions must be used (Croot and Laan, 2002; Hopkinson and Barbeau, 2007; Rose and Waite, 2002). The National Research Council of Canada CRMs, are held at pH 1.6 using ultra pure HNO_3 . The freshwater CRM is SLRS-4, it has a total iron concentration 1844 ± 90 nM, this was diluted 100-fold into UPW buffered to pH 6. From three replicate analyses the measured concentration was 1618 ± 128 nM giving an 88 ± 7 % recovery,

assuming a linear response (Figure 3.10). The reason for this relatively low recovery is that even at pH 1.6, the 0.2 μm filtered CRM can still contain a highly refractory proportion of iron, held inside fine clays and as stable Fe(III) solids, which would not be measured by FIA-Cl (de Jong et al., 1998).

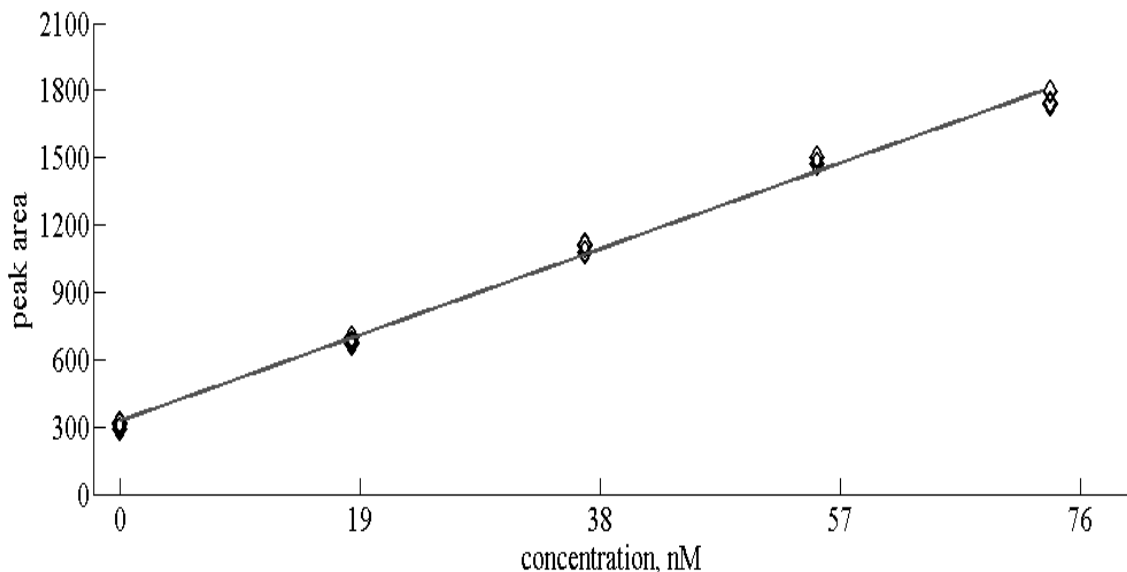


Figure 3.10. SLRS-4 standard addition calibrations. The subsequent concentration achieved was $1618 \pm 128 \text{ nM}$.

The standard addition method was successful for the SLRS-4 and was applied to the seawater CRM, CASS-4, total iron, $12.8 \pm 1.0 \text{ nM}$. The CASS-4 was analysed undiluted. The concentration obtained was $11.8 \pm 2 \text{ nM}$ giving a $92 \pm 16 \%$ recovery (Figure 3.11).

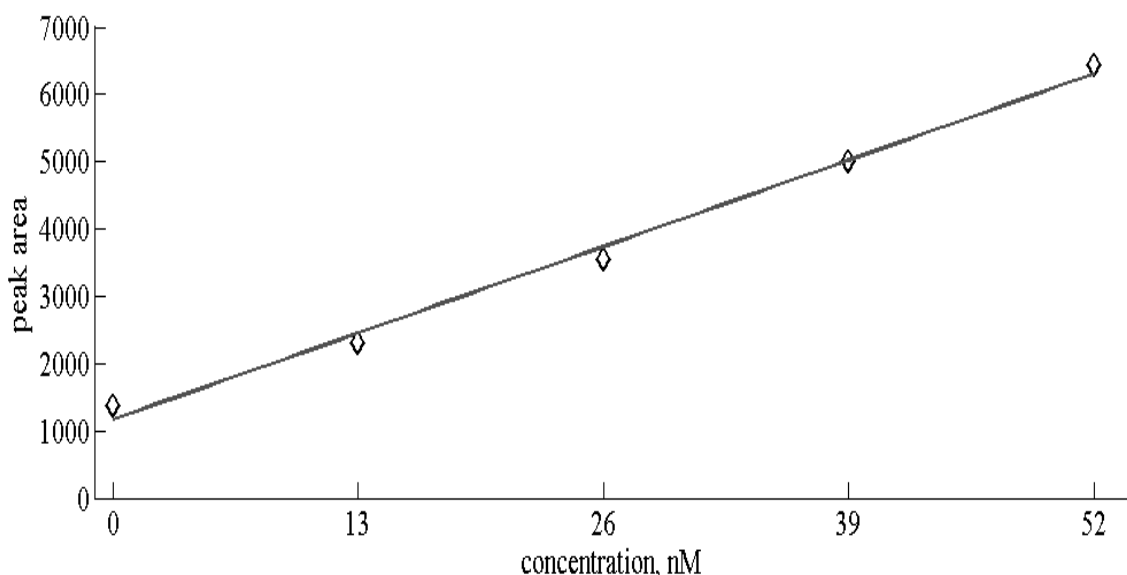


Figure 3.11. CASS-4 standard addition calibration. The subsequent concentration achieved was $11.8 \pm 2 \text{ nM}$.

FIA-Cl can only analyse discrete samples using standard additions, when it is used as a tool for total iron analyses. The reasons that standard additions are required are: Differences in the pH of the sample and standard; the latent ability of the sample to cause fluorescence (this is through the composition of the sample prior to acidification and the changes which occur with respect to production of, especially superoxide, when the sample pH is altered) (Rose and Waite, 2001); direct matrix effects between sample and standard for example calcium and magnesium ions at seawater concentrations suppressing chemiluminescence (Bowie et al., 1998), and that a portion of the iron is still refractory (de Jong et al., 1998). To overcome the refractory element of the iron the analysis must be combined with the sulphite reduction method (Bowie et al., 1998). A blank was not calculated during the analysis of the CRMs, however, should this be repeated the signal attributed to the blank can be calculated by repeating the lowest concentration standard addition and using this standard deviation as an assessment of the blank.

3.03.04 Chelex-100 Cleaned Seawater

The aged North Sea seawater being used would produce a signal (measured through standard additions) of 7 nM. To see if this signal was due to latent iron (II) or other potential interfering metal redox pairs the water was passed through a Na^+ form Chelex-100 column. Figure 3.12 compares aged 0.22 μm filtered seawater (control) with the same water that has both freshly passed through a Chelex-100 column and one which had been aged (24 h) after passage through a column. The freshly exchanged seawater produced the greatest signal – removal of weakly bound divalent ions can have the effect of altering the redox potential of the medium with an increase in relatively short lived oxidants which could potentially cause luminol chemiluminescence. Comparing the control and the 24 h aged exchanged seawater there is a 12 % decrease in the signal, though they do agree within error ($n=4$). The change in equivalent Fe(II) equated to ~ 0.9 nM. Due to the large volumes required for experiments and subsequent treatments with humic materials and waste culture water the small relative change in the blank due to the cleaning of the seawater was acceptable and therefore there was no continuation of the cleaning of the seawater.

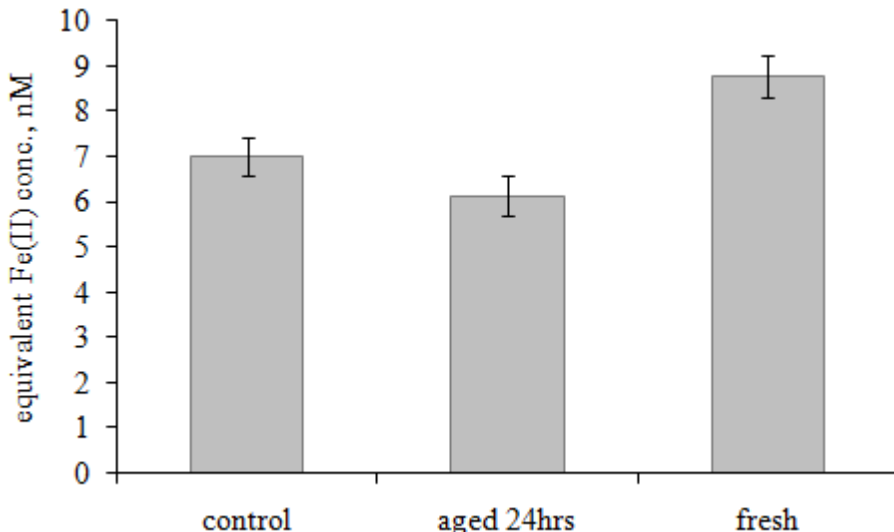


Figure 3.12. Comparison of Chelex-100 cleaned seawater. Error bars are the standard deviation of 4 repeat samples.

3.03.05 Real Time Iron (II) Calibrations

To quantify real time measurements accurately the sample and standard would have to be at the same pH and from within the same medium. As future experiments were to be conducted at natural seawater pH, the production of an iron (II) calibration curve would be at approximately pH 8.1, $\sim 25^\circ\text{C}$, giving a half-life of iron (II) of around 2 minutes (Millero et al., 1987). Calibrations needed to be undertaken to minimise the time between injection of iron to the standard media and analysis of the standard and incorporate the fact that during transit time (standard to luminescence) there is iron (II) oxidation. The second problem was solved as the Teflon tubing and pump speeds were the same as those within the experiment therefore a calibration would take into account the loss of iron (II) through oxidation over the transit time.

The transit time from the sample bottle, containing seawater, to the FIA-Cl mixing cell, at a flow rate of $0.13 \pm 0.01 \text{ ml s}^{-1}$, was 19 s. Calibrations for real time iron required that a chemiluminescence peak appear at a set point in the analytical cycle and that it was repeatable. One analytical cycle took 44 s, the iron (II) measurement commenced 22 s into a cycle, the iron peaks on a signal trace would then appear at $22 + (44 * n)$ s, example shown in Figure 3.13. Work on measuring the appearance of the most prominent Fe(II) peak started by injecting small volume additions, $5 - 20 \mu\text{L}$, of a working standard into the bottle containing seawater. A constant stream of seawater was being removed from the bottle and sent to the FIA-Cl mixing cell. The volume of the sample residing in the bottle at the point of working standard addition was required to calculate the concentration of the actual standard; this volume was calculated through the flow rate of the peristaltic pump. At 19 s (transit time) prior to mixing of the

standard and luminol reagent in the mixing cell the highest peaks formed were those second and third post injection. This indicated that insufficient mixing time was allowed in the standard bottle to achieve an equilibrium Fe(II) concentration. By using the 19 s prior to mixing of the sample and reagent as the bench mark, working standards were injected 19 ± 10 s prior to mixing. At 24 s prior to mixing of standard and reagents all first peaks were consistently greater in area and height than the second peaks indicating that this was the optimum point for injection of the standard. If the point of injection was greater than 24 s prior to mixing then there would have been greater oxidation of Fe(II) in the standard. Repeat measurements of a 10.4 nM standard for precision gave an RSD of 6 % ($n = 5$). The time for injection prior to analyses was set at 24 s. This timing was true for both the reagent injection following the method of Croot and also using a carrier solution as with the method of King.

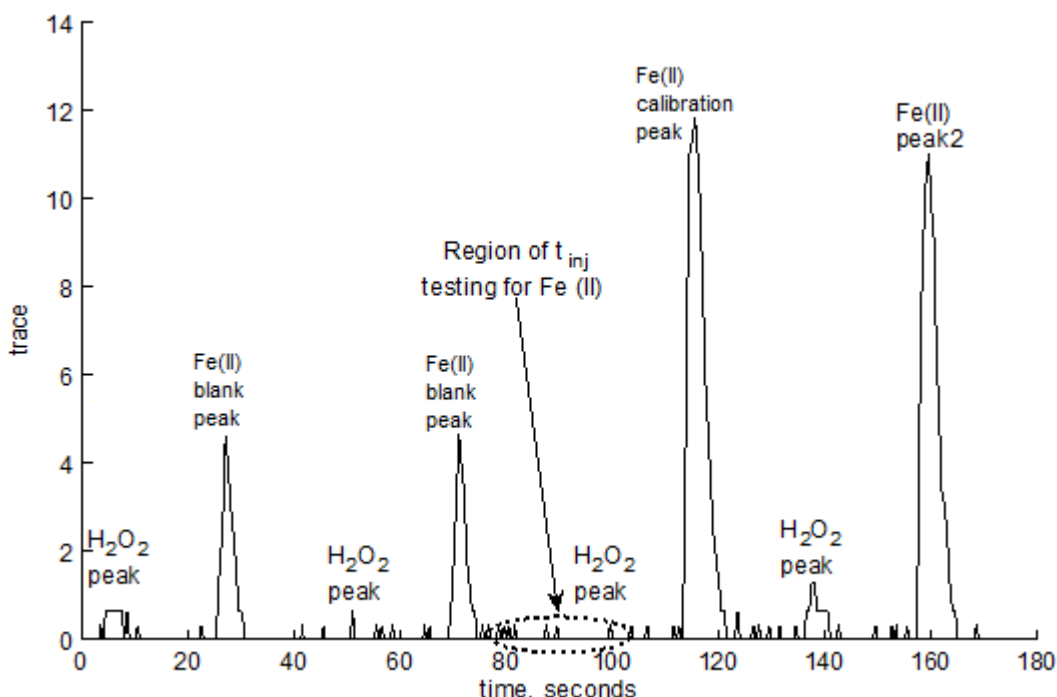


Figure 3.13. PMT trace for Fe(II) in seawater. The standard injection is of 9.9 nM at 86 s. t_{inj} indicates the time at which the iron (II) standard is spiked.

3.03.06 Iron (II) Sensitivity

The FIA-Cl could analyse continuous samples in seawater though signals were low. A strong signal needed to be robust against fluctuations in the baseline and show the highest sensitivity from the zero addition standard to the peak following addition of Fe(II). Measurements of real time Fe(II) have been conducted with the pH of the mixed luminol reagent at 10.3 (Rose and Waite, 2001), 10.2 (King et al., 1995) or 10.1 (Croot and Laan, 2002). Bowie et al., (1998) worked with a reagent at pH 12.2, samples at pH 5 and a reaction pH of 10.4;

Klopf and Nieman (1983) worked with a reaction pH of 10.3, Ussher et al. (2009) used a pH 11.8 reagent. Work by Seitz and Hercules (1972) showed that the optimum pH of the luminol for iron (II) analysis is pH 11. A 5 nM iron (II) standard was measured with changes to the 1.5 mM luminol reagent from pH 10.2 – 11.9, Figure 3.14. pH 10.2 reagents failed to produce a peak greater than the 0 nM standard, indicating the mixed sample reagent pH was to low. What was required was an appreciable signal above the baseline and which had the highest sensitivity over the blank and did not bring the mixed reagent sample to a point where there was large potential for $Mg(OH)_2$ precipitation. At pH 11.2 the signal was sufficiently large, that the baseline accounted for less than 2 % of the signal and the percentage change from the 0 nM standard to the 5 nM standard is in the region of a 150 % increase. Reagents at pH 10.8 / 11 had slightly better sensitivity but > 3 % of their signal was the baseline and fluctuations there in. Reagents at a pH between 11.2 and 11.6 showed similar sensitivities to the pH 11.2 reagent, and above 11.6 the sensitivity decreased. The decrease in sensitivity would indicate that a mechanism within the mixed sample reagent is decreasing the chemiluminescence, potentially the affect of $Mg(OH)_2$ precipitation. As the sensitivities were similar from pH 11.2 to 11.6, a pH 11.2 reagent was chosen as this would produce the lowest pH of the mixed sample and reagent with the lowest potential for precipitation.

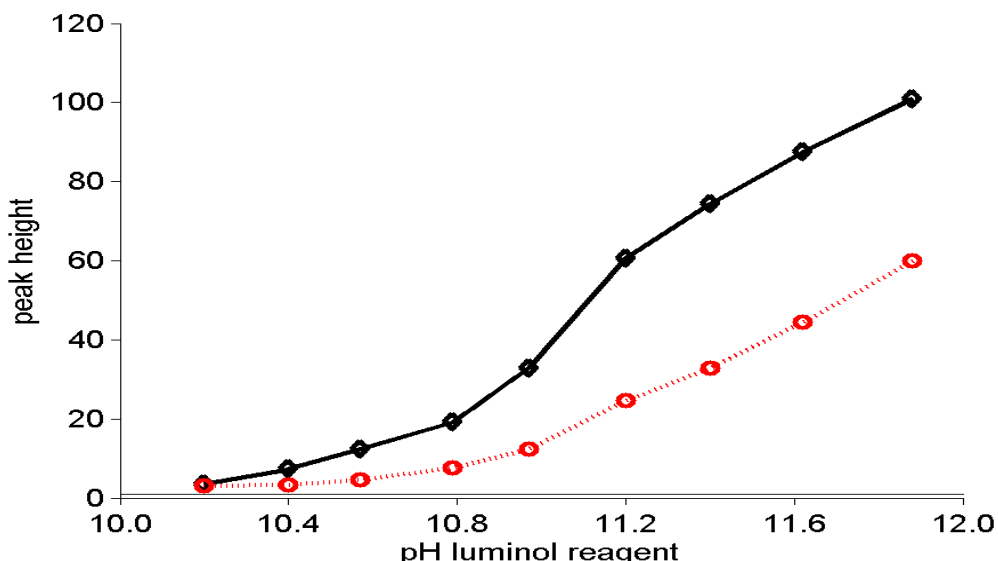


Figure 3.14. Reactivity of luminol reagent for Fe(II) due to reagent pH. Signal is due to mixing with a 5 nM iron (II) seawater standard. Black diamonds and solid line show the peak height achieved following an addition of 5 nM iron (II) to seawater. Red circles with dotted line show the peak height of the 0 nM standard. The black line is the baseline reading, 0.96 counts.

The FIA-Cl system could measure both hydrogen peroxide and iron (II) in seawater; further development went on to test its ability to quasi-simultaneously analyse these analytes. The key factor was the change in the plumbing configuration of the load – inject valve, shown in Figure 3.15. The system still allowed a choice of methods to enable analysis, either that followed by King et al. (1995), using a carrier to mix the sample and reagent directly in the flow cell, or as with Croot, the reagent is passed into the sample flow stream prior to arrival at the flow cell. With the change in valve plumbing a series of tests were conducted to enable the optimum analyses without interference from the previous sample. The valve switch timing was altered in line with changes in the peristaltic pump speed, changes to the peristaltic pump tubing to smaller sample and larger reagent internal diameters (id) and changes in the reagent volume injected (valve loop size) into the carrier / sample stream. The final configuration was a valve switching of 22 s between each analysis at a pump speed of 16 rpm. Tygon ST pump tubing (Upchurch Scientific, Washington State, USA) was used for the sample / carrier and had an id of 2.79 mm and a flow rate of 6.9 ml min^{-1} at 16 rpm. The reagent tubing had an id of 1.52 mm giving a flow rate of 2.7 ml min^{-1} . Figure 3.16 shows a quasi-simultaneous, blank trace for hydrogen peroxide and iron (II) from within seawater.

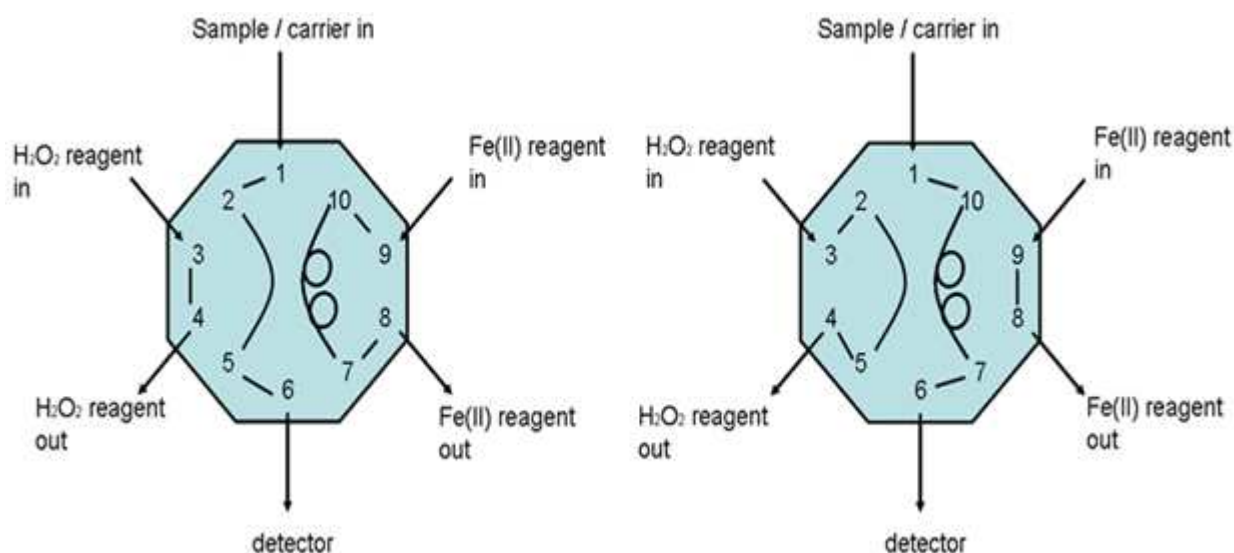


Figure 3.15. Load/inject valve configuration for dual analysis using a single valve. Left - iron (II) luminol reagent injection into a carrier or sample stream and right - H₂O₂ luminol reagent injection into carrier or sample stream.

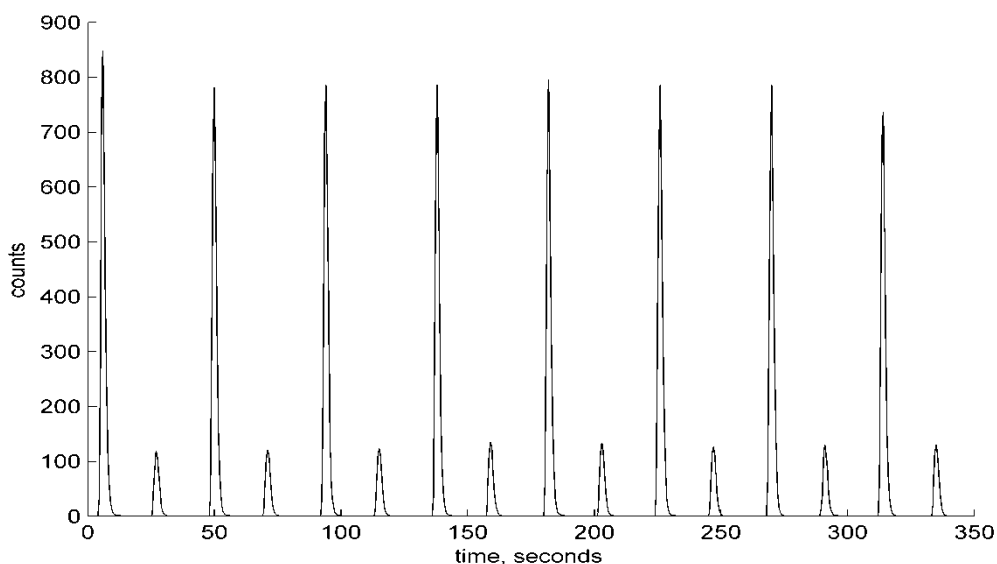


Figure 3.16. Dual analysis seawater trace. Taller peaks are due to H_2O_2 and the shorter peaks are for iron (II). The first hydrogen peroxide peak is larger than the rest due to luminol reagent activation by external light sources as it sits in the valve loop before analysis starts.

For the real time measurements, standard calibrations were to be used for both hydrogen peroxide and Fe(II). The matrix of the sample and standards were to be the same and therefore did not require the use of standard additions. The Fe(II) could be calibrated following the method developed based on the timing of the sample injection. H_2O_2 standards are stable over hour time scales; however, for consistency the same calibration method based on the timings for both Fe(II) and H_2O_2 was used. With the system able to analyse quasi simultaneously and the output could be calibrated it was then used as an analytical tool for real time measurements. Blank and LOD measurements are dependant on the matrix of the sample and all calibrations for experiments were undertaken in the same medium as the experiment. The 1.5 mM luminol (Sigma Aldrich, Luminol 98 %) solution was buffered with 0.08 M K_2CO_3 (Fisher), sonicated for 5 minutes, and aged for 24 hours at 4°C. After 24 hours the pH is adjusted to 11.2 with 2 M HCl (Fisher), the luminol reagent for H_2O_2 analysis is spiked to 6 μM with Co(II) and the reagents are placed in a water bath to speed their equilibrium to the laboratory ambient air temperature. The luminol reagent was produced by combining ~0.203 g luminol with ~8.25 g of K_2CO_3 into a brown polypropylene container and adding 750 mL UPW.

Chapter Four

Time Series of Trace Metals in a Lacustrine Surface Microlayer

4.00 Introduction

In Chapter Four work carried out on a seasonal sampling of a freshwater surface microlayer (FSML) for nominally ‘dissolved’ trace metals is presented. This is the first known work to measure through a seasonal progression the concentrations of dissolved trace metals in the surface microlayer of an aquatic system and relate these to the underlying water through the calculation of enrichment factors. The $<0.2\text{ }\mu\text{m}$ filtered fraction will compose of: Free metal ions, inorganic ion pairs, complexes and organo-metallic compounds, chelated organic compounds, metal species in highly dispersed colloids and metal species adsorbed onto colloids; whereas the $>0.2\text{ }\mu\text{m}$ fraction should contain precipitates, organic particles and in situ detrital material (Stumm and Morgan, 1996).

The particulate phase ($>0.45\text{ }\mu\text{m}$) of trace metals has been shown to be enriched in marine (Barker and Zeitlin, 1972; Brugmann et al., 1992; Cuong et al., 2008; Grotti et al., 2001; Hamilton and Clifton, 1979; Narvekar and Singbal, 1993), estuarine (Trojanowski and Antonowicz, 2011) and freshwater microlayers (Antonowicz and Trojanowski, 2010). However, enrichment factors in the dissolved fraction ($<0.45\text{ }\mu\text{m}$) (collected by roller) suggest that this fraction is potentially at the same concentration as in the underlying water (ULW) (Cuong et al., 2008) or enriched for manganese, iron and cobalt (Brugmann et al., 1992). The surface microlayer has been described as a gelatinous layer (Wurl and Holmes, 2008) made up of organic surface active substances (SAS) (Hunter and Liss, 1981) that are stable at the microlayer. SAS comprises various organic compounds derived from cell death and can act to bind trace metals (Strmecki et al., 2010). With the formation of complexes and the migration of SAS through the water column there can also be a flux of trace metals, for instance copper, to the microlayer (Plavsic et al., 2007; Shine and Wallace, 1996). As productivity increases so to does the concentration of coloured dissolved organic matter (CDOM). CDOM is formed by bacterial reworking of dissolved organic carbon which can be both allochthonous and autochthonous (Blough and Del Vecchio, 2002). CDOM is the initial point of photochemical production of superoxide (Voelker et al., 1997) which is involved in the redox cycling of trace metals. Therefore, with an increase in CDOM in the microlayer (Hortnagl et al., 2010) which absorbs at $>280\text{ nm}$ (Carlson, 1982) the surface microlayer could theoretically be an enhanced region of redox activity compared to the ULW.

With an enriched particulate phase and little attenuation of UV light ($<0.1\%$ absorption) at the microlayer (Plane et al., 1997), combined with an increase in the concentrations of organic material e.g. Duce et al. (1972) and Wurl et al. (2009), the possibility exists of a reduction of

trace metals into the soluble phase through the photochemical excitation of the elevated concentrations of organic material. Subsequent cycling of metals into the colloidal phase through sorption by organic material (Hunter, 1980a) and there release by a photochemical ligand to metal charge transfer from for example iron (hydr)oxides (Faust and Zepp, 1993; Waite and Morel, 1984) or organically complexed, e.g. Fe(III) (Barbeau, 2006; Barbeau et al., 2001) could sustain an enrichment in the microlayer in the $< 0.2 \mu\text{m}$ filtered fraction. These processes, in order to produce a net effect of enrichment, must be faster than the transformation or loss of material, primarily through redox reactions, e.g. re-oxidation of Fe(II) to an Fe(III) solid phase. With the production of a particulate phase, its subsequent aggregation acts as a removal mechanism for trace metals (Mopper et al., 1995; Zhou et al., 1998) through gravitational settling from the microlayer.

4.01 Sampling Devices

Two sampling materials were chosen for their characteristic hydrophobicity which should reflect the organic gelatinous microlayer. These were a borosilicate glass (plate sampler) and a Teflon® derivative (screen sampler – polytetrafluoroethylene (PTFE) frame and ethylenetetrafluoroethylene (ETFE) mesh). The aim of the study is to measure the dissolved fraction. Within this fraction there is the potential for metals to adsorb onto a glass surface and be retained in the microporous surface; this dependence is based on the ability of the metal to be hydrolysed (Batley and Gardner, 1977). Teflon will also adsorb inorganic metal-ligand complexes, primarily oxy-hydroxides (Belzile et al., 1989). This is due probably to the existence of a negative surface charge, comprising hydroxyl ions sorbed by either Van der Waals forces or hydrogen bonding (Batley and Gardner, 1977). Belzile et al. (1989) suggest that this can occur for both iron and manganese. It should be noted that the results of Belzile et al. (1989) were based on a Teflon® plate left for 10 weeks in lake sediments to allow for a measurable quantity to be collected. Teflon is not known to be appreciably contaminated by trace metals and will not truly adsorb dissolved species (Ashton and Chan, 1987).

The glass plate has been shown to have an affinity for hydrophobic amino acids, phytoplankton derived detrital matter, fatty acids from bacteria and higher land plants and dissolved carbohydrates (Harvey and Burzell, 1972; Momzikoff et al., 2004). Work with a Teflon plate has shown that this material is suitable for lipids (Kjelleberg et al., 1979) and should therefore have similar organic sampling characteristics as the glass plate. Conversely a Teflon screen used to sample an artificial laboratory microlayer was found to show poor recoveries for organic material (fatty acid, oleic acid) based on ^{14}C or ^3H activity (van Vleet and

Williams, 1980); the authors used a methanol rinse to remove the sample. The rinse, to remove / clean the plate between samples, is important for organic material as residual left between each dip may affect subsequent samples. The effect of the build-up of either hydrophobic or hydrophilic material on the sampler and the effect these have on the collected sample is partially limited by the mechanical aspect of each sampler. Plate samples after continuous dips will build up layers of residual material. The physical removal mechanism of scraping the surface with a Teflon strip will remove some of this retained sample but at the molecular level will have no affect. Using a methanol rinse to remove the sample requires an extra step in the sampling protocol, increasing the potential to contaminate the sample in the field. With a methanol rinse the sorption sites are re-exposed and hence there would be a requirement to recondition the sampler. The screen sampler uses surface tension to capture sample within the voids of the mesh, held by surface tension. The release of sample is through a gentle agitation to the screen. As long as the surface tension of the sample is not drastically compromised, which may happen with large concentrations of SAS, then that sample collected should be representative of the microlayer. If there is loss onto adsorption sites on the large surface area of the screen, this loss should be minimal as the screen is immersed in the water first and pulled through the microlayer hence these sorption sites will be filled when in the water.

Carlson (1982) suggest that inter-comparisons of surface microlayer data collected separately by two methods, e.g. plate and screen, was inadvisable as the thickness of the microlayer collected would be different. However, the authors also found that the composition of a variety of organic constituents (DOC, dissolved UV-absorbing phenolic materials, chlorophyll-a (chl α), adenosine tri-phosphate and POC and PON) did not show a bias to the sampling device and differences could be explained by depth of sample taken. Over the integrated depths, the plate sampler has traditionally been shown to retrieve a shallower sample than a screen sampler.

The act of conditioning, repeated use of the sampler prior to retrieval of the first sample should decrease the loss of sample through adsorption onto the sampling material. Considering the effect of the loss of ferric ions to (non-equilibrated) different materials it was found that on glass there was a loss of ~8% in 1 hour and for PTFE it was ~15% in 1 hour following an addition of 1.34 nM Fe_{tot} of which 0.7 nM was the ^{55}Fe radioisotope (Fischer et al., 2007). This rate of loss for a readily hydrolysable ion on the two sampler materials, which were unconditioned, was low enough in the first hour so that with a conditioning of the material and retention times of the sample on the sampler in the order of 30s the losses should be negligible.

4.02 Methods

4.02.01 Sample Site

The collection of surface microlayer samples was undertaken within a series of collaborations examining the UEA broad. The UEA Broad (Figure 4.01) is a manmade (quarry) temperate lake, which measures approximately 700 m long and between 70 and 150 m wide. The littoral zone extends for about 1 m before the bottom sharply drops to a depth of between 4 to 6 m. It is in close proximity to the River Yare but is not directly affected by the river other than by fluctuations in the ground water and as an overflow reservoir (Jamie Kettle, personal communiqué). There is a culvert on the western end of the lake, which is a point source of water, mainly used to allow the lake to become the overflow reservoir from wetlands at that end of the lake. There is also a small inlet pipe at the eastern end of the lake, which receives surface run off from a nearby road. The water sources to the lake are; these point sources, precipitation, and overland and ground water flow. The ground water flow is the major flux during most of the year, (Kettle et al. in press).



Figure 4.01. Location of the UEA Broad and mooring position (grey cross and circle). Grey areas are university buildings and green areas are vegetation.

To the north of the lake there are large concrete structures, which comprise the accommodation and teaching facilities of the University of East Anglia. Run-off from these buildings is directed through drains. Any surface run off would not reach the lake as it would

instead be taken as groundwater recharge as it flows over the greater than 300 m of grassed soil between structures and the lake. The near surrounding land to the east, south and west are woodlands, whilst it is primarily grass to the north. The shoreline of the lake is a surround of trees. This lake was chosen as a study site due to ease of access from the university. Sampling was initially undertaken at the north shore. Following integration of the project with other work sampling was from a small dinghy, the position of which is shown in Figure 4.01. The mooring location of the sample site is 30 m from the shoreline, with a water depth of approximately 5.2 m.

4.02.02 Sampling

Nine sampling missions for trace metals were undertaken from January through to August 2008. Microlayer samples were collected using a glass plate and a Teflon screen. ULW samples were taken from a depth of 10 cm directly into a bottle whilst wearing powder free PVC gloves. When possible microlayer sampling was usually conducted at approximately the same time on each mission, this was between 11:00 and 13:00. Only the last six sampling missions had a corroboration of their measurements through the measurement of a fresh water certified reference material from the Natural Research Council Canada, SLRS-4 (see Section 5.04); the results from the first three sampling missions were calculated through an application of a correction factor between results from the fourth sampling mission, which was analysed under two different ICP-MS analytical set-ups, see Appendices, A4.01.

Surface microlayer samples were collected by the glass plate (Harvey and Burzell, 1972), Figure 4.02, and screen (Garrett, 1965), Figure 4.03. All samples were collected windward of the dinghy; this prevented contamination from the dinghy itself and allowed for a quicker reformation of the microlayer at the point of sampling. The glass plate is passed through the microlayer at an acute angle towards the underlying water; it is then turned perpendicular to the microlayer and withdrawn back through it. The plate is held in the air to allow retained water to drain off. The rate of removal of the plate and time of drain are user selective. On average, removal time was around 2s, giving a withdrawal rate of 0.15 m s^{-1} for the 30 cm section of the plate used. Drain time for the plate was 10 s. A Teflon squeegee was used to remove the microlayer adhering to the plate. A PTFE plate was trialled in place of the glass plate. However, the quantity of sample collected, approximately 2 mL or less per dip, meant it was not feasible due to the time required to collect a reasonable size of sample, 100 mL or more. With the glass plate it would take approximately 40 minutes to collect two 140 mL samples.

The screen sampler device (Figure 4.03) was adapted from that of Garrett (1965): the frame and handles were made from PTFE whilst the mesh was made from ETFE, with nylon bolts (recessed into the frame) holding the sections together (PTFE and ETFE supplied by Plastok Ltd, Birkenhead, UK). The ETFE 230 mesh, with 36 μm diameter thread, 75 μm aperture with 45.7% open space, was built into the 394.5 by 340.5 mm, PTFE frame. When sampling the screen was inserted at an acute angle to the surface; it was then withdrawn slowly through and parallel to the microlayer. The screen would then be turned to approximately 60° for 10 s to allow water sitting on the mesh and around the fame to drain. The screen was then positioned over the waiting vessel and sample allowed to drain from the screen.

For both microlayer sampling techniques the depth of the microlayer sample collected is calculated by: (i) volume collected, (mm^3) (obtained by weighing the sample) divided by the surface area of the plate (mm^2) to provide the depth or (ii) volume collected (mm^3) divided by the internal surface area of the screen corrected for its available open space (mm^2). Organic material can affect the density of the sample collected however the change in density due to this affect was considered minimal and not incorporated into the change from weight to volume. Enrichment factors of dissolved organic carbon (DOC) in a marine SML range can range from 1.2 to 1.9 (Gasparovic et al., 1998). The actual measured concentrations in the SML for these EF were from 1.67 to 2.83 mg L^{-1} with their corresponding ULW DOC concentrations ranging from 1.21 to 1.85 mg L^{-1} in a non slick SML (Gasparovic et al., 1998). DOC in non slick SML samples is generally four times the concentration of particulate organic carbon (POC) (Gasparovic et al., 1998; Stolle et al., 2010; Williams et al., 1986). Higher enrichments have been seen in slick specific sites (Stolle et al., 2010) with slicks also tending to have higher POC concentrations to DOC concentrations (Stolle et al., 2010). In general, DOC EF are < 2 , (Gasparovic et al., 1998; Stolle et al., 2010; Williams et al., 1986) . Assuming SML maximum concentrations of DOC at 10 mg L^{-1} then in a 100 mL of sample there would be $\sim 1 \times 10^{-6}$ g per 100 g of sample. The conversion from weight to volume involving a difference in density due to DOC in the SML would then be small with respect to the actual physical sampling of the microlayer.

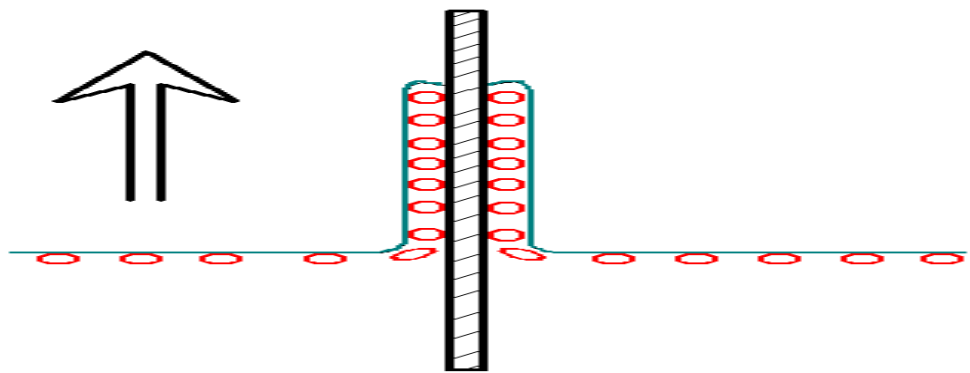


Figure 4.02. Adhesion of the organic acid hydrophobic microlayer (red spheres) to a glass plate (black oblong with diagonal lines)

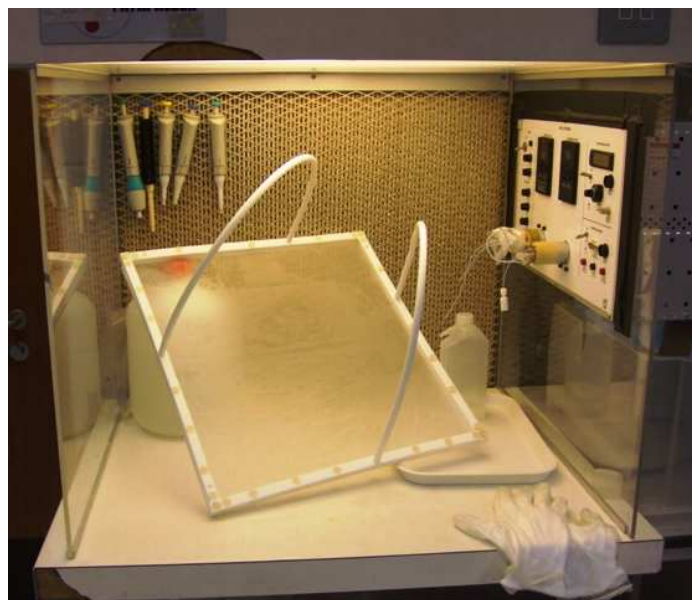


Figure 4.03. ETFE screen surface microlayer sampler

4.03 Ancillary Parameters

Meteorological data originated from the website www.wunderground.com; the nearest weather station is 2.7 km NNW (latitude N 52.643 °, longitude: E 1.236 °) of the sample site. During sampling, ancillary data were gathered to characterise the water column. The water column was profiled for temperature, oxygen and pH using a YSI 556 multi-probe system, (YSI Inc., Ohio, USA). Measurements were taken from the surface, ~0.1 m, and every 0.5 m to the lake bed. The dissolved oxygen (DO) and pH were calibrated prior to each sampling mission: DO with air saturated ultra pure water and the pH using standard NIST buffers at pH 4.02 and 7.00. The specified sensitivity of the YSI 556 is:

Dissolved oxygen, (mg L^{-1}) 0 – 20 $\text{mg L}^{-1} \pm 2 \%$, with a resolution of 0.01 mg L^{-1} .

Temperature is accurate from -5 to 45 °C, $\pm 0.15 \text{ }^{\circ}\text{C}$ with a resolution of $0.1 \text{ }^{\circ}\text{C}$.

pH, range 0 to 14 with an accuracy of 0.2 and a resolution of 0.01. Accompanying these data were water samples collected from 1, 2, 3 and 4 m deep, taken by means of a Niskin bottle on a line, and analysed for nutrients, chl α and CDOM.

4.03.01 Meteorological Data

The meteorological data: insolation, temperature, wind speed and wind direction are shown in Figure 4.04. There is a caveat within the meteorological data that the conditions recorded at the weather station may not have been those at the sampling site. Although meteorological data were available at 15 minute intervals, only those which coincided with the 30 minutes prior to and during microlayer sampling are used. The interval used is based on work by Hunter (1980b) who adopted a residence time of 10 minutes for particulate matter in a North Sea microlayer.

Insolation and temperature (Figure 4.04) are important factors in controlling stratification and the subsequent affect this may have on the biology of the system. From January to April the insolation is relatively low ($150 - 470 \text{ W m}^{-2}$) combined with low air temperatures ($6 - 10^\circ\text{C}$). Insolation increases from April to May, $210 - 960 \text{ W m}^{-2}$ whilst air temperature increases from 9 to 25°C . From May until July the mean insolation decreases for the sampling period. However, the range bars in late May, June and August indicate heavy passing cloud cover. Maximum air temperature in May then decreases to mid July, showing a summer minimum of 15°C , and then increases by $\sim 5^\circ\text{C}$ in August. Temperature can have a physical affect on the structure of the microlayer, a drop of 4°C can see an increase in the thickness of the microlayer by some 12 % (Harvey, 1966).

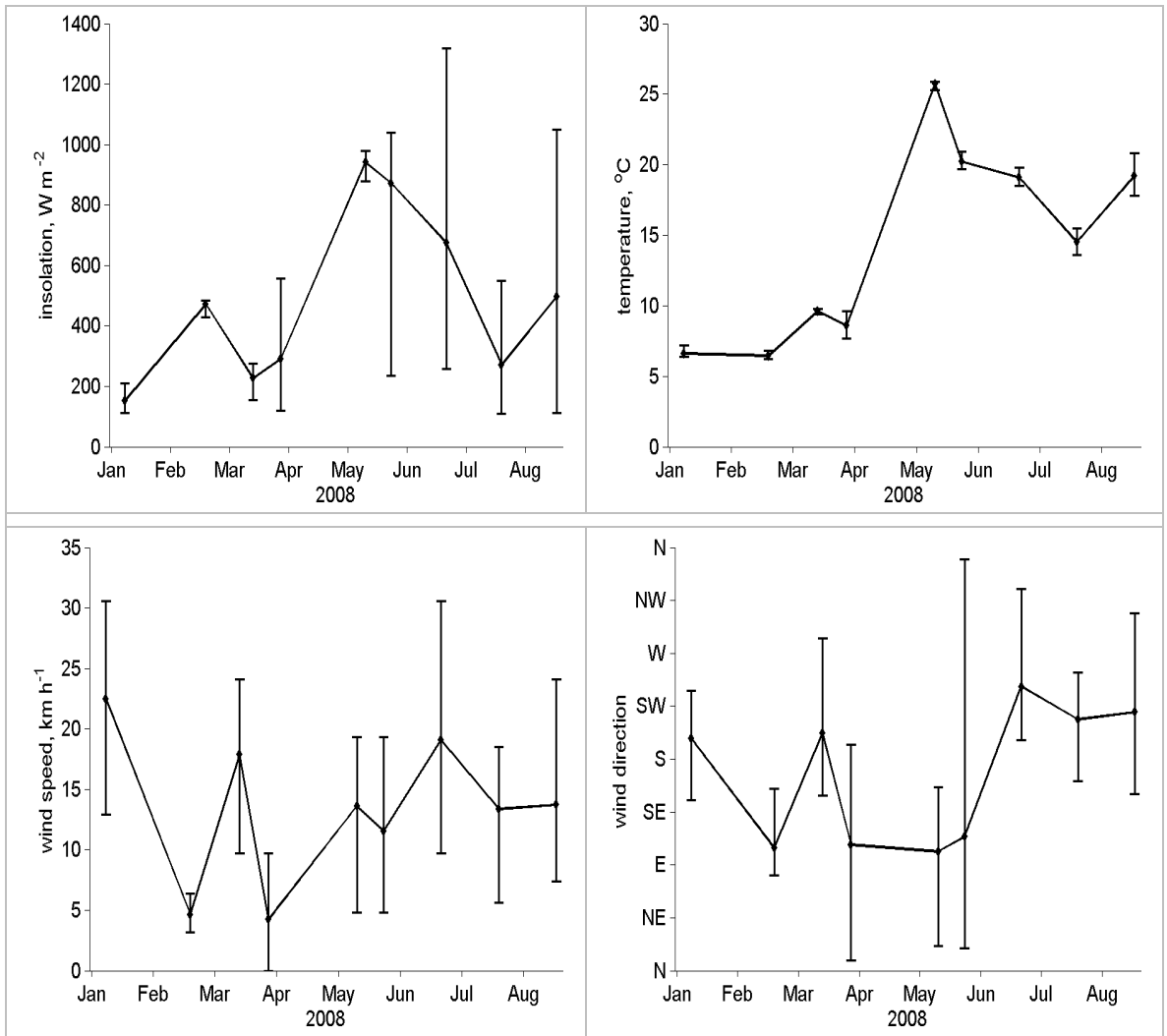


Figure 4.04. Meteorological conditions for the 30 minutes preceding and during sampling. The graphs show the mean and ranges of the data.

The wind speeds for the sampling missions are in Figure 4.04. The mean wind speed was 13.4 km h^{-1} . The UEA Broad is sheltered and therefore wind speed may not have an adverse affect on the formation of the microlayer, though it has been noted that wind speeds greater than 10.8 km h^{-1} can limit the formation of slicks (Liss and Duce, 1997). On only two occasions were the average wind speeds during sampling less than 10.8 km h^{-1} , these were in February and March, both 5 km h^{-1} . Due to the surroundings and shape of the lake a wind shadow (3 – 5 times greater than the height of the trees, assuming tree height of $\sim 10 \text{ m}$) should prevent winds from the north and south affecting the lake. From April through to June the wind is predominantly from the east (Figure 4.04) with average wind speeds lower than the mean, 13.4 km h^{-1} ; from June the wind is predominantly from the south-south-west (Figure 4.04) with average winds speeds around the mean. From June onwards there is the potential that the combination of direction and speed may have an adverse effect on the formation of the microlayer.

4.03.02 Physiochemical Parameters

As with the meteorological data there is a higher temporal sampling resolution for the temperature, dissolved oxygen and pH, approximately fortnightly in this case, however, consideration is only given to those data which coincided with the microlayer sampling missions. The in situ data are presented in Figure 4.05.

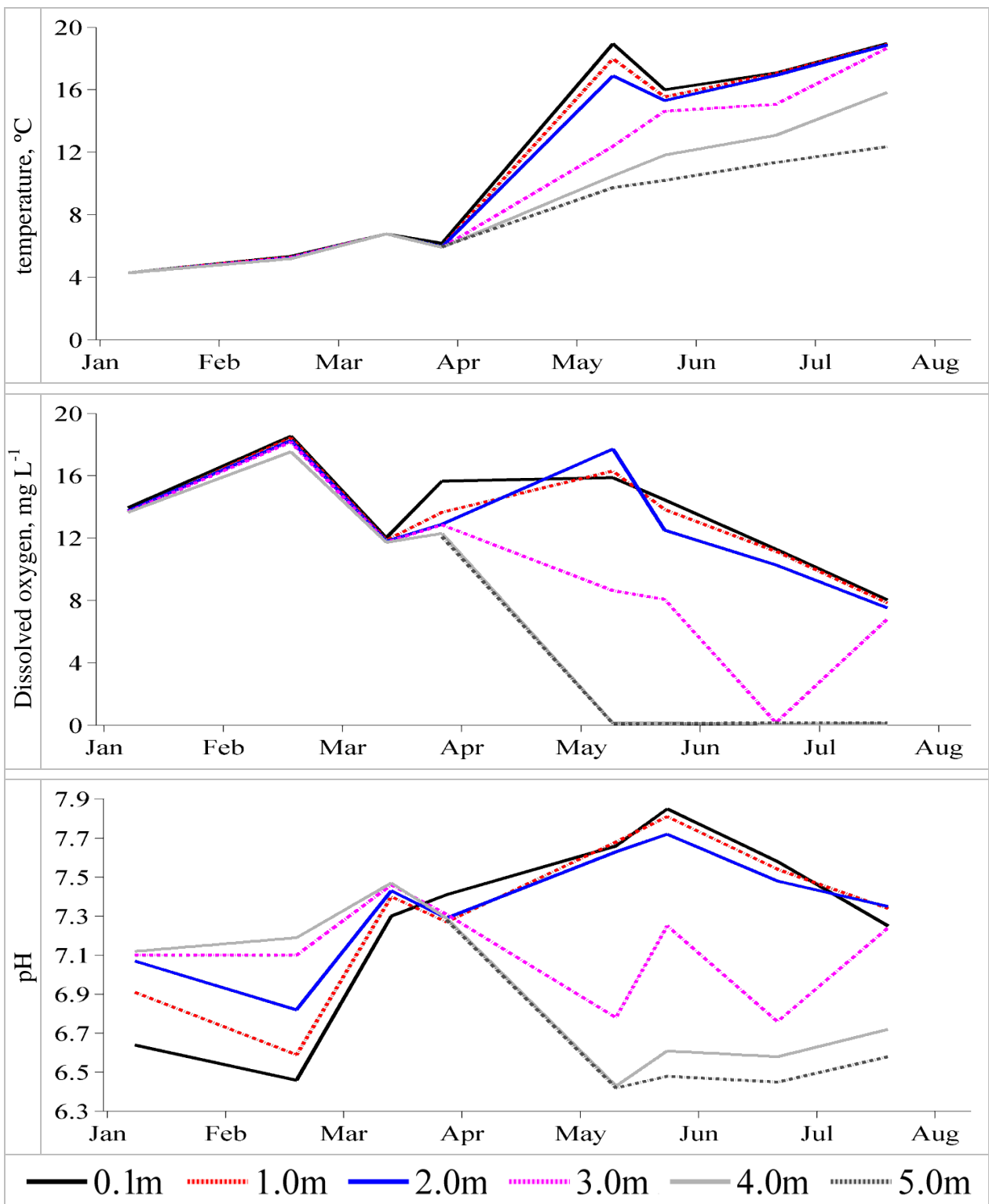


Figure 4.05. Seasonal progression of, temperature, oxygen and pH, at depths, 0.1 – 5 m, through the water column

January to late March shows a mixed water column (no stratification), with temperatures between 4 and 7 °C (Figure 4.05). The mixing can be attributed to cool day time air temperatures (6 – 10 °C) combined with the influx of ground water at ~ 5 °C (Kettle et al. in press). From late March temperature stratification begins and continues through to July. The greatest difference between surface and deep waters is in May (~ 10 °C), from warm surface waters at 0.1 - 2 m depth (20 °C) to cool bottom waters at 5 m depth (10 °C). From late May until July there is an increase in temperature of the water at all depths, with the difference in temperature from the surface waters to 4 m decreasing over this time.

DO from January through to early March exhibits little variation with depth (Figure 4.05). The lake system shows an increase in the DO concentration (14 – 18 mg L⁻¹) and subsequent decline (18 – 11 mg L⁻¹) over the remainder of the sampling period for surface depths, \leq 2m. The onset of stratification in late March has DO concentrations in the deep waters > 2 m diverging, with concentrations decreasing with depth. At the point of maximum temperature stratification, (May, maximum air temperature, 25 °C), there is a large divergence between surface and deep water with 4 and 5 m depths exhibiting anoxia. At this point there is also an increase in concentration of the 1 and 2 m deep above that in the surface water (0.1 m). From late March through to June, there is a super-saturation (> 100 % oxygen) occurring in the surface layers (< 2m), with a maximum of 176 % in May, on occasions levels were measured at over 200 % saturation (data not shown). Similar super-saturations have been recorded in surface waters of Lake Kinneret in Israel, these were attributed to high phytoplankton standing stock and low wind driven turbulence (Yacobi et al., 1993). From May onwards there is a decrease in the DO concentration in the Broadwater at all depths, coinciding with cooler air temperatures (15 – 20 °C). Over this period there is a gradient of decreasing oxygen with depth; 0.1 – 2m, show a difference of ~ 2 mg L⁻¹, with water at 3m depth attaining anoxia in June. The system then converges for depths shallower than 3m to around 8 mg L⁻¹ in July from the high of 18 mg L⁻¹ in May.

The changes in concentration of DO can be attributed to three affects. Temperature controls the solubility of oxygen, as temperature increases solubility decreases so therefore those waters in contact with the atmosphere will have higher oxygen concentrations in winter than in summer. This can be seen when comparing winter (January to early March) to summer surface concentrations (late May to July). Within the temperature seasonal controlled cycle there are the underlying effects of photosynthesis increasing concentration as phytoplankton standing stock increases and respiration decreasing concentration through the biological oxygen demand (BOD). The change in DO over the winter (January to early March) when air temperatures are

relatively stable ~ 7°C could be attributed to a bloom of phytoplankton which is then removed by an oxygen consuming organism. The effect of the BOD outstripping the production of oxygen is seen from April onwards in deep waters ≥ 3 m which have low and anoxic levels of DO compared to the surface waters. With roughly stable surface water temperatures the DO decrease from June onwards, this decrease can be suggestive of a gradual loss in the oxygen production mechanism or that there is an increase in the BOD in these waters.

In January and February there is a decreasing gradient of pH with depth (Figure 4.05). The difference with depth over this period reaches a maximum in February coinciding with the DO maximum (~18 mg L-1). During March the water column pH converges to around pH 7.3 and subsequently the pH at depths are lower than the surface pH. Surface (0.1 – 2 m) pH shows a difference of around 0.1 pH units, and these depths have an increase in pH from pH 7.3 to 7.7 from April to late May and then decrease back to pH 7.3 in July. Bottom waters, < 4 m have a decrease from pH 7.3 to 6.4, and subsequently increase through to July (pH 6.7) with a difference of ~-0.2 pH units between 4 and 5 m. At 3 m the pH is variable and fluctuates by ~0.2 units around pH 7.

One of the main controlling factors of the pH of water is the concentration of CO₂. Like oxygen, CO₂ solubility decreases with temperature. Due to the atmospheric concentration of CO₂ unbuffered water at equilibrium with the atmosphere will be at around pH 5. In the Broadwater from January to early March the decreasing gradient with depth of pH can be attributed to the atmospheric CO₂ dissolving in the surface waters. Over this period the water column is not stratified so therefore there is a mechanism in the deeper waters utilising CO₂ and hence increasing the pH. From May onwards the difference between shallow < 2 m and deep waters > 4 m can be attributed to the affect of biology. Surface stratified waters contain phytoplankton (Figure 4.06) which consumes CO₂ during photosynthesis, resulting in an increase in the pH and deep waters with increased BOD producing CO₂ through bacterial respiration, with lower phytoplankton standing stock and a decrease in the pH.

4.03.03 Chlorophyll-a

The chl α seasonal depth profiles are shown in Figure 4.06. The chl α concentrations are the calculated mean of three separate extractions (300 mL each) of one sample (1 L) taken at each depth.

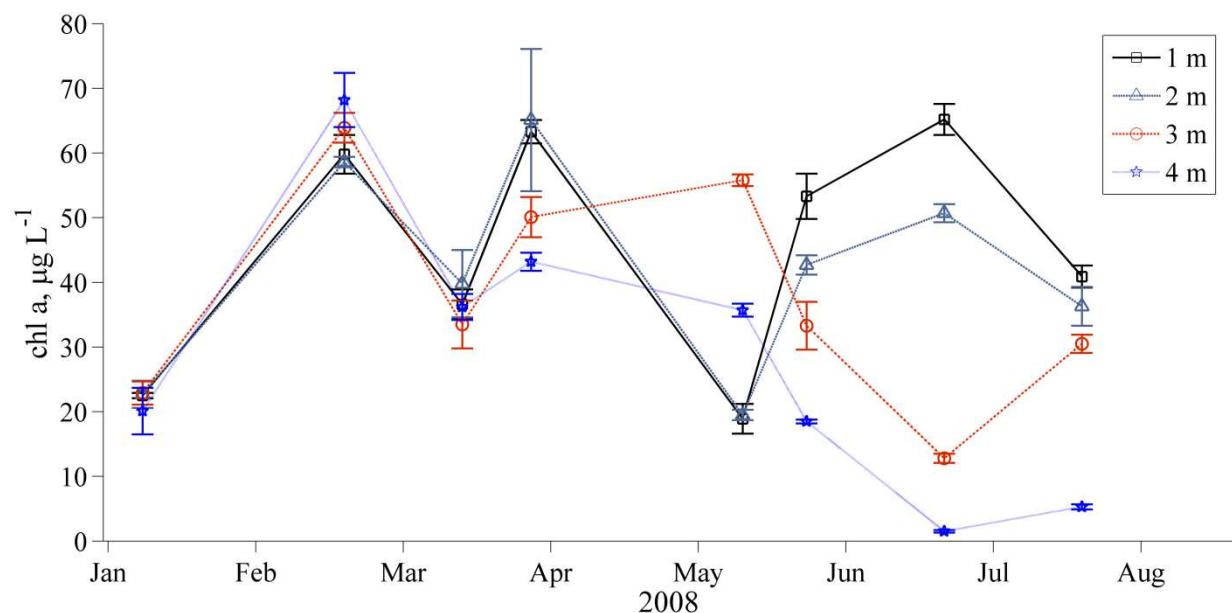


Figure 4.06. Seasonal progression of chl α at depths, 1 – 4 m, through the water column. Error bars are the standard deviation of three repeat samples.

From January to February, there is an increase in chl α of $\sim 50 \mu\text{g L}^{-1}$, for all depths. This subsequently decreases by $\sim 30 \mu\text{g L}^{-1}$ into early March. Late March with the onset of stratification surface waters (1 and 2 m) have higher concentrations of chl α than deeper waters. Early May shows a surface water mixing event in the oxygen profile (Figure 4.05) with a concurrent turn over in the chl α ; concentrations at 3 and 4 m were greater than at 1 and 2 m. This mixing is not seen in the temperature profile (Figure 4.05) instead it shows the point of greatest stratification between surface and deep waters. This would suggest that the phytoplankton which was at 1 and 2 m were either, removed between March and May; a primary loss mechanism for phytoplankton is through its grazing by zooplankton or migrated to the slightly deeper water due to the higher insolation (Figure 4.04). At 3 and 4 m chl α was not significantly altered over this period. From late March onwards, over the shallow water mixing event and through the remainder of the year, water at 3 m has higher chl α than 4 m water by around $10 \mu\text{g L}^{-1}$.

Following the mixing, in late May chl α tends to decrease with depth. June shows a large difference between surface and bottom waters before an event in July decreases surface water concentrations whilst increasing bottom water concentrations. A personal communiqué from Dr Claire Hughes provided some insight into the speciation of the phytoplankton of the broad through the year. During the first third of the time series there was a diatom bloom, which was rapidly grazed down. This bloom coincides with the decreasing gradient of pH with depth (Figure 4.05). Following the diatom bloom the blue-green algae become the dominant species (late May to August). The broad as a whole is phosphate limited (Dr Claire Hughes personal communiqué) and this has the affect of low growth rates in the blue-green algae. In the broad it is the combination of stratification, light limitation and anoxia which influence the chl α distribution.

The switch in the gradient to higher pH in surface waters corresponds to the end of the diatom bloom and the beginning of temperature induced stratification. With the diatom bloom the photosynthetic biomass was greater in the deeper waters with photosynthesis greater than respiration whereas surface waters were equilibrating with atmospheric CO₂. From March onwards the deep waters have a low photosynthetic biomass, BOD increases with the fall out of detrital material into the stratified waters with the subsequent decrease in pH due to bacterial respiration.

4.03.04 SML Depth

The average thickness of the microlayer sample for the plate and screen samples were, respectively 58 ± 9 (n = 18) μm (range 43 – 76 μm) and 338 ± 59 (n = 18) μm (range 257 – 564 μm), with 45.7% void space in the mesh. On average, each plate dip recovered ~10 mL whilst the screen recovered ~21 mL of microlayer sample. Screen samples recovered on average a depth of microlayer 4.5 times greater than the plate. During plate sampling the repeat sample collected a microlayer 9 to 18 % thinner than the first sample. The screen repeat sample was not as consistent with the difference in the depth of the repeat sample from 18 % thinner to 29 % thicker. Figure 4.07 shows the percentage difference from repeat one to two for both samplers. With microlayer work the thinner the sample collected the more representative this sample should be of the microlayer. A specific point of interest is that in early May. During this sampling mission the chl α was at its lowest concentrations in 1 and 2 m samples, 18 mg L⁻¹, correspondingly both the plate and screen replicate samples showed the greatest difference for thinner repeat samples, ~18% thinner. It must also be noted that the variation in the replicate

screen sample may also be due to operator. Screen samples were collected by the second person in the dinghy, whilst all plate samples were collected by the author of this work.

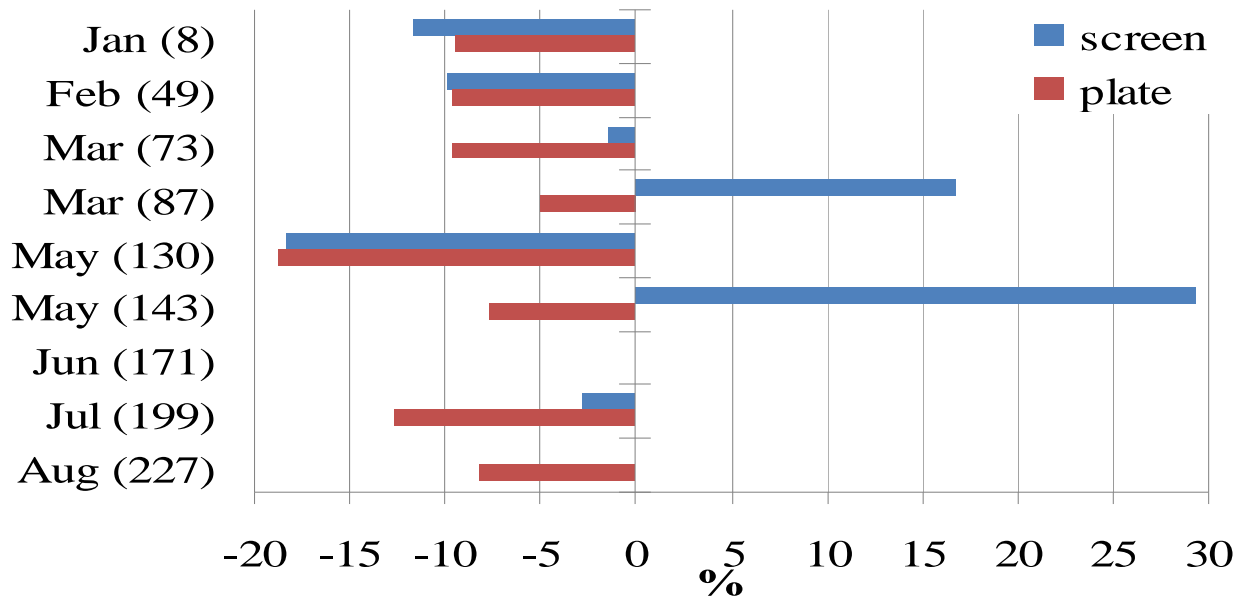


Figure 4.07. Percentage depth difference from first to second repeat sample. Number in brackets refers to the 2008 Julian day.

Figure 4.08 shows a visual comparison of the thickness of the microlayer sampled. The comparison is by means of a box plot; this introduces four sets of statistics. The median value is represented by the central horizontal line within the inter-quartile range (25th – 75th percentile) as the black box; the mean value is represented by the black cross. The extent of the data that lies within ± 2.7 standard deviations ($p = 99.3\%$) are encompassed by the error bars; error bars end at the minimum / maximum value within 2.7σ . Outliers, $> \pm 2.7\sigma$, are represented by the red crosses.

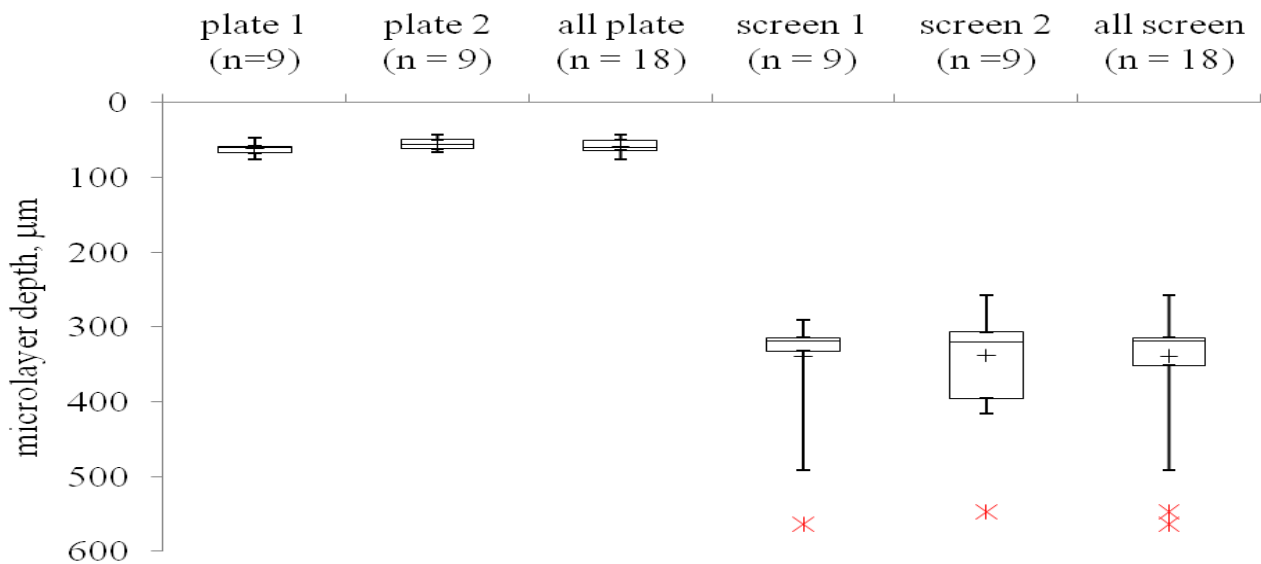


Figure 4.08. Comparison of microlayer sampling depths for replicates and the combine data. See text for explanation of the variables shown in the plot.

The depths of the microlayer samples are consistent with previous works studying trace metals in the particulate phase, though in the marine environment. Depths collected using the plate and screen techniques were: nylon screen: 250 – 450 μm (Brugmann et al., 1992), 200 – 400 μm (Hardy and Cleary, 1992), 440 μm (Mignon and Nicolas, 1998); acrylic and polythene screen 212 μm (Narvekar and Singbal, 1993); glass plates have sampled depths 30 – 55 μm (Hardy and Cleary, 1992) and 30 – 60 μm (Hardy et al., 1987).

4.04 Trace Metals Analysis

Of the sampling missions only the last six missions had a validation of the ICP-MS analytical technique for aluminium, manganese, iron, copper, cobalt and arsenic, through a successful recovery of the certified reference material SLRS-4 (see Chapter 2, Table 2.03, analytes highlighted on black). Before analysis sample containers were weighed to derive the volume of sample collected from each microlayer technique. Samples were then filtered through an acid washed 0.2 μm Whatman nucleopore polycarbonate filter held in a polysulfonate filtration unit. The first ~ 30 mL of each sample was used to rinse the filtration unit and condition the filter before being discarded. Between samples the filtration unit was rinsed three times with ultra pure water. The remaining filtrate was then stored acidified (< pH 2) with double distilled HNO₃ in the dark prior to analyses on the ICP-MS at a 1:2 dilution with calibration by means of standard additions; for each standard addition the actual sample was analysed twice. During each measurement of the sample on the ICP-MS the actual zero addition standard was measured twice, once at the beginning and once at the end of the standard addition series. The mean

percentage difference between these duplicate analyses based on the counts achieved at the ICP-MS detector is given in Table 4.01; on occasions there are large differences between the duplicate analyses and this was due to low concentration samples. As both analyses were used in the fitting of the standard addition calibration this difference is incorporated into the calculated analytical error of the measurement based on the fit of the standard addition calibration as per Miller and Miller (1993). Except for the dilutions, standard additions and ICP-MS sampling of samples all handling of samples was carried out in a class 100 laminar flow cupboard.

Table 4.01. Mean percentage difference between all duplicate analyses of broadwater samples.

	mean	minimum	maximum
Al	1.1	0.01	9.5
Mn	1.0	0.03	6.9
⁵⁶ Fe	1.9	0.02	26
Co	2.8	0.1	32
⁶³ Cu	1.9	0.03	8.7
As	1.3	0.01	6.3

4.05 Results

The concentrations for the dissolved: aluminium, manganese, iron, cobalt, copper and arsenic, for all samples are given in the Appendices, section A4.02, Table A4.05. The error on the measurements is derived from the fit of the standard addition calibration series for each sample. For the first three sampling missions the concentrations for aluminium, manganese and iron were calculated through a correction based on the repeat analysis of one set of samples through two different ICP-MS analytical protocols, the description of this correction is given in the Appendices section A4.01.

4.05.01 Temporal Progression of Dissolved Trace Metals

The seasonal progression of the measured concentrations of the dissolved fractions from plate and screen sampled microlayer and the ULW are presented in Figure 4.09. The variation in the location and nature of lakes do not easily allow for a comparison of the concentrations of trace metals. Due to the unique suite of measurements there are also no directly comparable surface microlayer data sets. Where possible the concentrations of the samples have been compared to an appropriate depth (< ~ 0.2 m) freshwater sample also measuring the dissolved fraction using an ICP-MS; these were taken from Lake Biwa, Japan (Sugiyama et al., 2005). If

values are not available then the samples are compared to appropriate marine surface microlayer concentrations again measured as a ‘dissolved’ fraction on an ICP-MS (Cuong et al., 2008).

Aluminium (Figure 4.09) sample concentrations range between 200 and 700 nM. Significant features (though not represented by all samples at once) include a weak increase in concentrations until late March. All samples then decrease to a low in early May before showing a recovery in their concentrations until June/July followed by an overall decrease in concentration into August.

The manganese (Figure 4.09) samples have elevated concentrations in January 2008 at all depths. As the year progresses the concentration in all samples tends to decrease; ULW, 92 down to 5 nM; plate 41 down to 2 nM and screen 29 down to 5 nM. The low end and overall range of the manganese results are similar to the Lake Biwa freshwater dissolved fraction, manganese mean, 4.3 nM, range 0.7 – 710 nM (Sugiyama et al., 2005). The Broadwater samples collected in August show slightly increased concentrations over those from the preceding two months. With respect to the measurement of total Manganese, across a seasonal range of surface microlayer and ULW concentrations from Lake Jasień, Northern Poland, are between 273 – 5880 nM (15 and 323 $\mu\text{g dm}^{-3}$ (Antonowicz and Trojanowski, 2010)).

Iron concentrations (Figure 4.09) range between 30 and 550 nM, with the lowest concentrations tending to be derived from plate samples. The ULW sample from February measured at 556 nM, compared with its corresponding SML samples measuring below 100 nM. Though not statistically proven as an outlier, due to the concentration range of iron in all the ULW samples, this ULW sample shows all the characteristics of being contaminated, especially when assessed against the concentration of iron in its corresponding SML samples. The difference in concentrations may be an artefact of contamination due to the magnitude of the difference in relation to other sample pairs, though this sample has not been shown to be an outlier. These results show higher concentrations in the dissolved fraction than those from Lake Biwa, Japan (Sugiyama et al., 2005), mean 44.7 nM, range 4 – 68 nM. From January to February microlayer samples decrease in concentration whilst the ULW sample increase in concentration. From May onwards all samples show a similar pattern, an increase in their concentrations from early to late May, then a decrease until July, before concentrations increase into August.

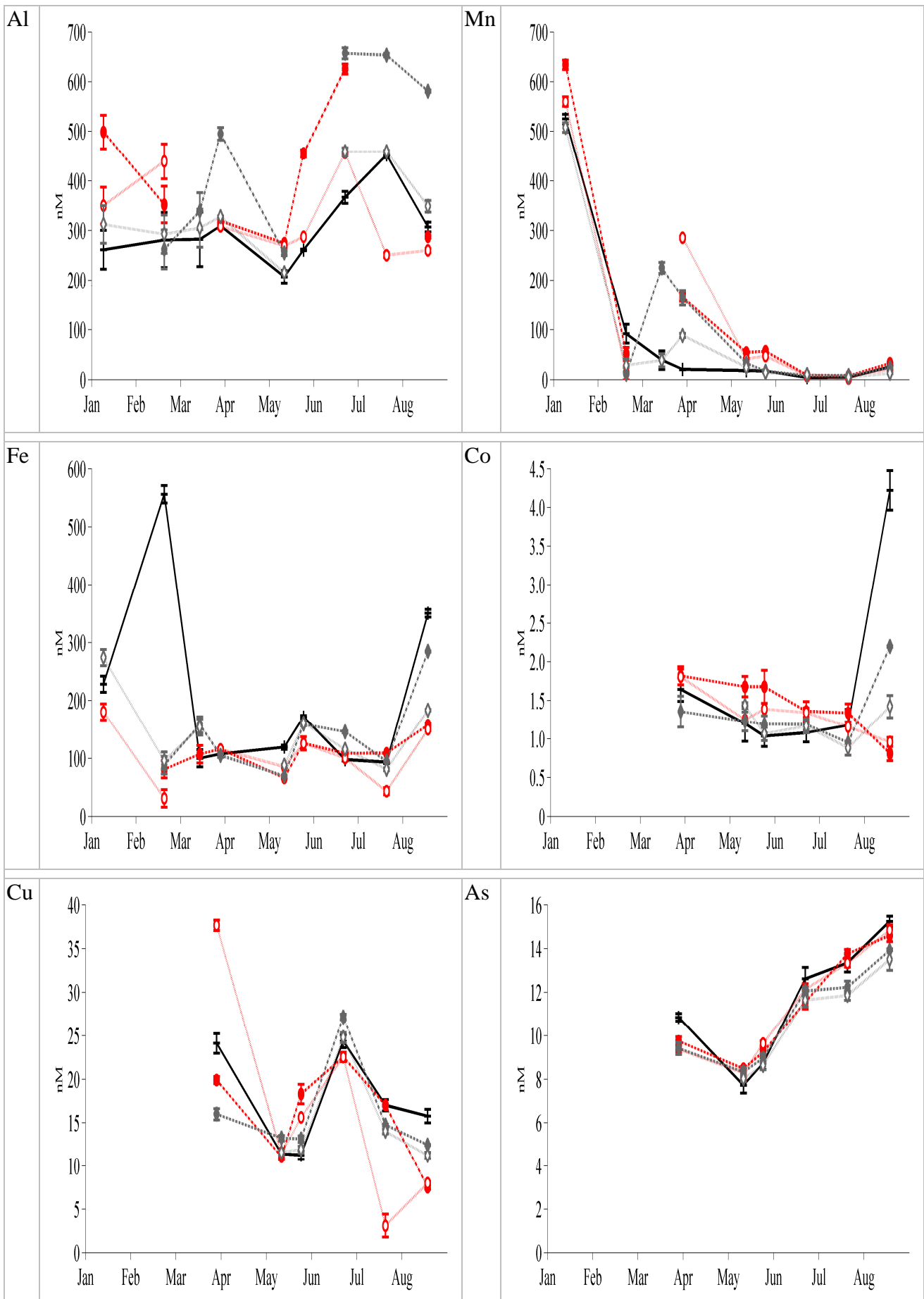


Figure 4.09. 2008 Seasonal progression of 'dissolved' trace metals. ULW – black line with crosses, plate 1 – red (dash-dot) line and shaded circles, plate 2 – red (dotted) line and open circles, screen 1 – grey (dash-dot) line and shaded diamonds, and screen 2 – grey (dotted) line and open diamonds.

Cobalt concentrations generally decrease in all samples from April through to July, < 2 nM to ~ 1 nM. Screen samples continue to decrease to 0.9 nM in August whilst ULW and plate samples show a marked increase in concentration, maximum measured concentration of 4.2 nM in the ULW in August.

Copper (Figure 4.09) concentrations range between 3 and 38 nM. These samples are slightly elevated with respect to those from Lake Biwa, average 9 nM, range of all samples 6 – 15 nM (Sugiyama et al., 2005). The low end of these concentrations are similar to work carried out on a coastal marine microlayer with a glass roller (n=2, 2 replicates) 4.2 – 11.3 nM (Cuong et al., 2008). The time series pattern shows elevated concentrations in March, which then decrease in May before increasing in concentration to a high in June. From June onwards the concentrations in all samples tend to decrease.

Arsenic (Figure 4.09) values range between 8 and 15 nM, these values are similar to those measured by Cuong et al. (2008), 4.5 – 15.9 nM, in a coastal marine microlayer. The concentrations decrease from April to May and then at all depths show an increase in concentration as the year proceeds.

4.05.02 Wilcoxon Test

A Wilcoxon signed rank test (Wilcoxon, 1945) was used to assess whether there was statistical significance between the sample groups and therefore allow for a reliable assessment of the degree to which there is potential enrichment within the microlayer. The test is non-parametric and therefore no underlying assumption is required about the population, though it is expected to show a normal distribution. The assumption of normal distribution is required to take the Wilcoxon test one stage further and statistically relate the differences between the population means. However, the Wilcoxon test itself, due to the ranking of the pairs does not require a normal distribution as it is based on the ranking of pairs and as long as both data show the same population distribution then this distribution is not problematic.

The test was applied as non-directional as no assumption was made as to implicit differences in either the sampling technique or the samples. Using the null hypothesis that the difference between the groups is random a series of tests were applied:

1. Between replicate microlayer samples taken with the same technique – can the replicates be combined? i.e. sample one and two show random changes in concentration and therefore they are in fact a repeat sample.

2. Between combined replicate plate and screen samples – indicating either differences between sample depth or technique.

3. Between the ULW and combined replicate samples – assessment of enrichment of the microlayer.

4. Finally, between the ULW and separately the first and second replicate plate and screen samples.

A calculation for the test involves first finding the difference between pairs in population A and B; absolute difference is then ranked and those ranks are multiplied by the sign of the difference. The sum of the signed difference then provides the Wilcoxon rank-sum test statistic, W. A z-ratio, z, can then be calculated and this will indicate how significant the difference from the mean, W is. Populations with $n < 10$ can not be used to calculate the z-ratio as the distribution is too small to allow an approximation to a normal distribution. As such, the values of W for $n < 10$ were compared to Table 4.02.

Table 4.02. Critical values of $+/‐W$ for small samples ($n < 10$) using a non-directional test (<http://faculty.vassar.edu/lowry/ch12a.html> (26th January 2011)).

α	0.05	0.02	0.01
n	--	--	--
5	15	--	--
6	17	21	--
7	22	24	28
8	26	30	34
9	29	35	39
			43

The calculation of z (populations, $n > 10$) requires a calculation of the standard deviation of W (Equation 4.01). There is also the assumption that the mean of the signed differences (μ_w), should the null hypothesis be correct, equals zero, i.e. if the differences between the ranks is random, then there is an equal quantity of negative and positive values and these are normally distributed so when summed equal zero. The calculation of z is shown in Equation 4.02. A ± 0.5 correction is applied as there could be a tied rank within the calculation of W and the test uses whole integers.

$$\sigma_w = \sqrt{\left(\frac{n(n+1)(2n+1)}{6} \right)} \quad \text{Eqn. 4.01}$$

z is then calculated using

$$z = \frac{(W - \mu_w) \pm 0.5}{\sigma_w} \quad \text{Eqn. 4.02}$$

z is compared against a table of critical values to provide the appropriate probability that the differences between samples A and B are random. The comparison was made to an online table - <http://faculty.vassar.edu/lowry/wilcoxon.html> which also provided the resultant probability, p , for the null hypothesis. All tests were conducted following the removal of concentration outliers (highlighted in red in Table A4.05).

4.05.02.01 Wilcoxon Test Results

The first test compared replicate microlayer samples taken by the same sampling device. Two elements from different samplers indicated through the test that their differences were statistically a non-random difference. These were the aluminium screen samples $W = 26$, $n = 7$, $p = 0.02$, and manganese plate samples $W = 28$, $n = 7$, $p = 0.02$. All other analytes using the same sampling technique indicated a random spread of results between repeat samples.

The second test was between combined repeat microlayer samples. This test was also conducted using aluminium measurements as sampled with the screen and manganese measurements as sampled with the plate, even though the previous statistical test suggested that these were different. The reason for using both sets of repeat data then provides a higher number of data points (two per sample) allowing for a more robust test of the data as the number of values used is doubled allowing for a better approximation to a normal distribution. The results from these tests are shown in Table 4.03. The sign of W indicates the direction of the difference. If W is positive then group A values are greater than group B values, in this case plate samples would tend to have higher concentration than screen samples. Should W be negative then in this case plate samples would tend to have lower concentrations than screen samples. Those elements which showed a high probability that their differences in concentration were not random and that the plate samples measured higher than the screen samples were manganese (96%) and arsenic (98%). Iron shows a high probability (99 %) that the differences between the samplers are not random and that the screen samples have a higher concentration than the plate samples. Aluminium and copper both have a greater than 50 % chance that the samples are random and as such do not show either a preference for the sampler or depth of microlayer collected. As the number of samples is small and from an environmental context an assumption may be made that there is a difference between cobalt concentrations as sampled by each sampler, though this probability is only 66%, and that cobalt is enriched in plate samples compared to screen samples.

Table 4.03. Wilcoxon test results (2) for all plate and screen samples. The table shows the Wilcoxon value, +/-W and test statistic, z and probability of random/non random association.

		W	z	n	p random	% probability non-random
Al	plate vs screen	-16	-0.65	12	0.54	46
Mn	plate vs screen	67	2.09	14	0.04	96
Fe	plate vs screen	-87	-2.75	14	0.01	99
Co	plate vs screen	22	0.96	11	0.34	66
Cu	plate vs screen	-12	-0.56	11	0.61	39
As	plate vs screen	54	2.38	11	0.02	98

The third test measured differences between combined replicate microlayer sampler samples and the ULW, Table 4.04. Aluminium plate and screen and manganese plate samples indicate that these concentrations are higher in the microlayer samples than the ULW and would be enriched. The only other analytes to show strong statistically significant relationships are iron, plate collected samples and arsenic, screen collected samples, which indicate a depletion of each in the microlayer.

Table 4.04. Wilcoxon test results (3) for a comparison between ULW and combined replicate microlayer samples.

		W	z	n	p random	% probability non-random
Al	ULW vs plate	-76	2.14	15	0.03	97
	ULW vs screen	-112	3.17	15	0.03	97
Mn	ULW vs plate	-74	1.90	16	0.06	94
	ULW vs screen	-18	0.50	15	0.64	36
Fe	ULW vs plate	90	2.54	15	0.01	99
	ULW vs screen	46	1.18	16	0.24	76
Co	ULW vs plate	-28	1.08	12	0.28	72
	ULW vs screen	26	1.13	11	0.26	74
Cu	ULW vs plate	20	0.76	12	0.45	55
	ULW vs screen	22	0.96	11	0.34	66
As	ULW vs plate	16	0.61	12	0.54	46
	ULW vs screen	46	2.02	11	0.04	96

Again, due to the small sample sizes and the fact these are environmental samples, iron screen samples indicate that they are depleted in the microlayer, with a probability that these results are not random > 76%. The sign of W for this test corroborates the results from the test with the plate and ULW comparison. Cobalt results are the most difficult to interpret as the

chance that the differences between microlayer samples and ULW is not random is $> 72\%$, however, plate samples would indicate enrichment whilst screen samples would indicate depletion. The cobalt statistics could therefore be used as an indication that a probability of $> \sim 75\%$ is required to provide a higher chance of a definitive result, though from the second test the cobalt from plate samples is also enriched compared to the screen samples (Table 4.03). Except for the cobalt statistics all other elements have a W of the same sign for both sampling devices. The sign of W if in agreement with a statistically proven difference in the same metal from the microlayer maybe used as a reassurance factor that the test does show that there is a potential for enrichment or depletion even if the probability is not as significant.

The Wilcoxon test suggests that there is an enrichment of aluminium (both) and manganese (plate) and a depletion of iron (both) and arsenic (screen) in the microlayer and as such allows for the data to be used in the calculation of enrichment factors. This test has shown statistically that there is, on a seasonal scale, either enrichment or not of the dissolved fraction of the specified trace metals. What the test does not provide and actually hides is the variation of the concentrations of the metals through the season and when certain metals maybe enriched or depleted and this being due to the environmental circumstances.

The final test was an exercise in whether the results could be de-constructed into a specific microlayer sample repeat. These tests were again conducted on small populations $n < 10$; results are shown in Table 4.05. Only aluminium was able to show conclusively that repeat samples taken with the screen showed enrichment in the microlayer. Iron though not showing depletion in both samples does show that the second plate sample has better correlation than the first and it would be this sample that contributes most strongly when the replicates were combined in the third test, Table 4.04.

Table 4.05. Wilcoxon test results (4) for a comparison between ULW and replicate microlayer samples

		W	n	α
Al	ULW vs plate 1	-24	7	0.05
	ULW vs plate 2	-12	8	X
	ULW vs screen 1	-26	7	0.02
	ULW vs screen 2	-36	8	0.01
Fe	ULW vs plate 1	16	7	X
	ULW vs plate 2	30	8	0.05
	ULW vs screen 1	16	8	X
	ULW vs screen 2	8	8	X

4.05.03 Enrichment Factors

An enrichment factor (EF) is the ratio of the concentration of an analyte in the SML to that in the ULW, Equation 4.03.

$$EF = \frac{[X]_{SML}}{[X]_{ULW}}$$

Eqn. 4.03

Values above one will indicate enrichment of that analyte in the SML, a value of one indicates unity and less than one indicates depletion. Table 4.06 shows the calculated enrichment factors.

Table 4.06. Enrichment factors, broken down into replicate samples. Manganese data highlighted in red (sampled on 2008 Julian Day 87) were further calculated to represent EF outliers ($\pm 2.7 \sigma$) based on the analysis of combined replicate manganese data.

2008 Julian Day		8	49	73	87	130	143	171	199	227	mean	sigma	median	min	max	n
Al	plate 1	1.91	1.25		1.03	1.33	1.74	1.71		0.94	1.42	0.38	1.33	0.94	1.91	7
	plate 2	1.34	1.56		1	1.3	1.1	1.24	0.55	0.85	1.12	0.32	1.17	0.55	1.56	8
	screen 1		0.93	1.2	1.6	1.23		1.79	1.44	1.89	1.44	0.34	1.44	0.93	1.89	7
	screen 2	1.19	1.04	1.08	1.06	1.04		1.25	1.01	1.13	1.1	0.08	1.07	1.01	1.25	8
Mn	plate 1	1.21	0.56		X	3	3.24	2.05	1.54	1.29	1.84	0.98	1.54	0.56	3.24	7
	plate 2	1.07	0.14		X	2.27	2.69	1.67	0.5	0.81	1.3	0.94	1.07	0.14	2.69	7
	screen 1		0.12		X	1.82	0.96	1.88	1.73	0.94	1.24	0.69	1.35	0.12	1.88	6
	screen 2	0.97	0.31	0.99	X	1.35	0.79	2.35	1.03	0.5	1.03	0.62	0.98	0.31	2.35	8
Fe	plate 1		0.16		1.07	0.55	0.73	1.11	1.17	0.45	0.75	0.38	0.73	0.16	1.17	7
	plate 2	0.8	0.07		1.07	0.72	0.73	1.03	0.46	0.43	0.66	0.33	0.72	0.07	1.07	8
	screen 1		0.17	1.52	0.98	0.58	0.93	1.49	1.02	0.81	0.94	0.44	0.95	0.17	1.52	8
	screen 2	1.19	0.19	1.49		0.74	0.94	1.18	0.87	0.52	0.89	0.41	0.9	0.19	1.49	8

Table 4.06 continued.

2008 Julian Day		8	49	73	87	130	143	171	199	227	mean	sigma	median	min	max	n
Co	plate 1			1.11	1.35	1.62	1.26	1.14	0.19	1.11	0.49	1.2	0.19	1.62	6	
	plate 2		1.1	1	1.34	1.24	0.99	0.23	0.98	0.39	1.05	0.23	1.34	6		
	screen 1		0.83	0.99	1.15	1.1	0.81	0.52	0.9	0.23	0.91	0.52	1.15	6		
	screen 2			1.15	1.03	1.08	0.75	0.34	0.87	0.33	1.03	0.34	1.15	5		
Cu	plate 1			0.82	0.97	1.62	0.93	1	0.48	0.97	0.37	0.95	0.48	1.62	6	
	plate 2		1.56	1	1.38	0.93	0.18	0.51	0.93	0.52	0.96	0.18	1.56	6		
	screen 1		0.66	1.16	1.17	1.11	0.87	0.79	0.96	0.22	0.99	0.66	1.17	6		
	screen 2			1.02	1.06	1.02	0.82	0.71	0.93	0.15	1.02	0.71	1.06	5		
As	plate 1		0.9	1.1	1.06	0.92	1.03	0.96	0.99	0.08	0.99	0.9	1.1	6		
	plate 2		0.86	1.07	1.11	0.96	1	0.97	1	0.09	0.99	0.86	1.11	6		
	screen 1		0.87	1.08	1.03	0.96	0.92	0.91	0.96	0.08	0.94	0.87	1.08	6		
	screen 2			1.04	0.99	0.92	0.89	0.89	0.94	0.07	0.92	0.89	1.04	5		

Results from the first Wilcoxon test suggest that repeat data from each sampler for each sampling mission can be combined. Combining data does not calculate the mean of repeat one and two, but instead calculates the enrichments separately using the same ULW sample, therefore a repeat sample. The enrichment factors for the combined replicate samples are shown initially introduced through a series of boxplots, Figure 4.10. These plots show a simple comparison of the screen and plate enrichments compared to unity (the explanation of the statistics shown for the boxplot was given earlier, section 4.03.04).

Aluminium (Figure 4.10) in the microlayer is enriched in both the plate and screen samples, indicated by the mean and median from both techniques. The interquartile ranges for both samplers also lie above the unity line, with the mean and median values comparatively central within the range. The range of the data for both samplers does however extend below the unity line. These results for combined replicate data agree with the Wilcoxon test (3) that there is significant enrichment of aluminium in the microlayer.

The plate sampled microlayer mean and median values for manganese (Figure 4.10) also indicate enrichment, or at least unity (screen median value). However, the plate and screen interquartile ranges cross unity, though mean and median values are relatively central within the range. The screen interquartile range is slightly skewed towards enrichment. The visual representation appears in agreement with the Wilcoxon test (3) which indicated significant enrichment of the plate samples but no enrichment of the screen samples.

Plate and screen iron (Figure 4.10) median and mean values indicate depletion in the microlayer. The interquartile range does however cross unity for both samplers, more so with screen samples. With both samples the mean and median are relatively central indicating a normal distribution. These results agree with the Wilcoxon test, that the plate is depleted and that the screen is also depleted but that due to the range of the screen data it is not as significant.

Cobalt (Figure 4.10) sampled from within the microlayer shows contradictory results in the boxplot when comparing between samplers. Plate sample EFs suggest enrichment with the mean, median and the interquartile range in agreement. However, due to high depletion factors for some samples (August, Figure 4.09) the range of the data extends well below unity. Both the screen sampled mean (depletion) and median (unity) and extent of the interquartile range tending to depletion suggest that these samples may be depleted but, as with the Wilcoxon test, there is not enough evidence to suggest that this is significant or that should it be occurring because the number of times it does occur is limited.

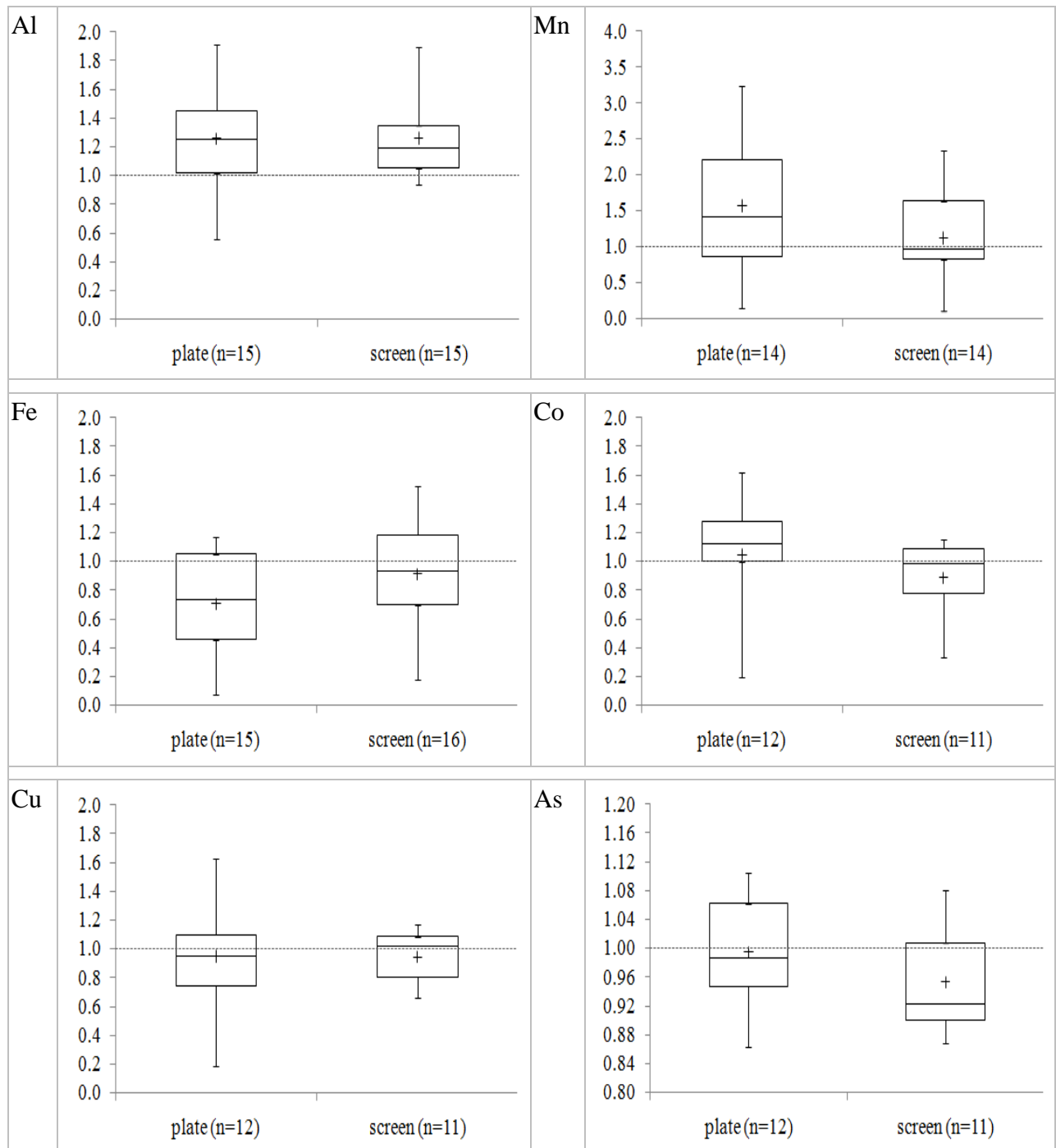


Figure 4.10. Comparison of broadwater enrichment factors for combined plate and combined screen samples. Unity with the ULW is indicated by the continuous horizontal line. See text for explanation of the variables shown in the plots.

The copper from within microlayer plate samples (Figure 4.10) would indicate depletion with the mean and median central of the interquartile range lying below unity. Screen samples as with cobalt are less constrained, with the median lying above unity and the mean below thus suggesting that there is little or no difference between these samples and the underlying water. The range of the plate data and unconstrained nature of the screen data agree with the low probability measured by the Wilcoxon test of non-random differences < 66 %.

The microlayer samples containing arsenic (Figure 4.10) have mean and medians values indicating depletion of their samples compared to the ULW concentration. The plate interquartile range tends towards enrichment whereas the screen sample interquartile range generally lies below unity, indicating the majority of samples do show depletion. These agree with the Wilcoxon test that the screen is depleted but the range of the data for the plate does not allow for a significant relationship to be assessed. Within the arsenic data it should also be noted that the interquartile range of enrichment factors is small, ± 0.08 .

Using the comparisons from Figure 4.10 combined with the Wilcoxon test results has allowed for the suggestion that certain trace metals in their dissolved fraction show enrichment (aluminium and manganese) or depletion (iron and arsenic) in the microlayer. The box plots indicate that there is also an argument for using a significance of more than 75 % to indicate enrichment or depletion, as there needs to be an appreciable shift in both the mean and median values from unity. The box plots also highlight how the depth of microlayer recovered will affect the enrichment. If the assumption is valid that the thinner the sample collected the more representative of the microlayer it is, for dissolved metals, then screen samples should tend more towards unity than plate samples. This would appear valid for manganese, iron, cobalt and copper with screen mean and median values closer to unity than plate samples, with aluminium tending to show a greater deviation from unity with a shallower microlayer sample. Also, the enrichment factors should fall within a smaller range due to the increased dilution factor narrowing the interquartile range. This is shown by aluminium, manganese, iron and copper.

4.05.03.01 Annual Average EF

Variability is present through the year, as evidenced by the changes in the difference between the concentrations of the trace metals in the microlayer and ULW. However, when the EFs were averaged over the year, Table 4.07, this potential variability is lost and the microlayer tends to unity with its ULW. For all analytes, combining their microlayer replicate samples for each sampling device indicates that unity is within one standard deviation of both the mean and median values of these combined samples. This then suggests that over a time integrated period the dissolved fraction of the specified trace metals resolves to unity with the ULW. The data in this simple form may be over simplified and ignore the implications of the variability due to the temporal progression of the water body. If there is depletion/enrichment within the microlayer then for the dissolved fraction of aluminium, manganese, iron, cobalt copper and arsenic this occurs within a small range and only on specific occasions would significant ($> \pm 1 \sigma$) enrichment occur.

Table 4.07. Annual average microlayer enrichment factors for combined replicate samples through 2008. * calculation of the manganese enrichments has the outliers (day 87) removed.

	mean	median	min	max	n
plate					
aluminium	1.3 ± 0.4	1.3	0.55	1.91	15
manganese*	1.6 ± 1.0	1.4	0.14	3.24	14
iron	0.7 ± 0.4	0.7	0.07	1.17	15
cobalt	1.1 ± 0.4	1.1	0.19	1.62	12
copper	1.0 ± 0.4	1.0	0.18	1.62	12
arsenic	1.0 ± 0.08	1.0	0.86	1.11	12
screen					
aluminium	1.3 ± 0.3	1.2	0.93	1.89	15
manganese*	1.1 ± 0.6	1.0	0.12	2.35	14
iron	0.9 ± 0.4	0.9	0.17	1.52	16
cobalt	0.9 ± 0.3	1.0	0.34	1.15	11
copper	0.9 ± 0.2	1.0	0.66	1.17	11
arsenic	1.0 ± 0.07	0.9	0.87	1.08	11

Based on the information in Table 4.07 a Student's t-test was used to provide an idea of which elements in there dissolved phase have: i) statistically different mean values from unity, EF = 1.0; and ii) which samples have statistically different mean SML sample enrichments or depletions. The equations and results from these tests are in the Appendix, section A4.03.

Those elements that show significant enrichment in the plate sampled microlayer are:

Al, $p = 99\%$, $t = 2.7$, $df = 14$ and Mn, $p = 97.5\%$, $t = 2.2$, $df = 13$.

Only aluminium shows significant enrichment in the screen sampled microlayer:

Al, $p = 99.5\%$, $t = 3.5$, $df = 14$.

Iron is the only element to show significant depletion of the plate sample relative to the ULW: Fe, $p = 99.5\%$, $t = -3.3$, $df = 14$.

Cobalt and arsenic in the screen sampled microlayer also shows significant depletion relative to the ULW: Co, $p = 90\%$, $t = -1.4$, $df = 11$ and As, $p = 95\%$, $t = -2.2$, $df = 10$.

With respect to whether there is a significant difference between the plate and screen sampled microlayers, only two elements show a significant difference: Manganese is enriched, $p = 90\%$, $t = 1.39$, $df = 26$ and iron is depleted, $p = 90\%$, $t = -1.52$, $df = 30$. As these results do not deviate from the assessment using the Wilcoxon test further discussions concentrate on those results from the Wilcoxon tests.

4.05.04 Temporal Progression of Enrichment Factors

Based on the Wilcoxon test (3) results (Table 4.04), of the six analytes only aluminium and manganese are statistically enriched with respect to ULW at 0.1 m in their nominally dissolved fraction. Those analytes which, based on their Wilcoxon test (3) results are depleted, are iron and arsenic, whilst cobalt and copper results suggest that they are tending towards unity with the ULW. Work by Cuong et al. (2008) found that the enrichment factors for dissolved ($<0.45\text{ }\mu\text{m}$) copper and arsenic in a coastal marine microlayer ($\sim 50\text{ }\mu\text{m}$) were close to unity, an EF of 1.0, their results were, copper, $\text{EF} = 0.9 - 1.2$, and arsenic, $\text{EF} = 0.9 - 1.1$, ($n=2$ with 2 replicates). For the Broadwater samples, the seasonal progression of surface microlayer EF of the enriched trace metals, aluminium and manganese, is shown in Figure 4.11. Plate samples are presented in black and screen samples in red, repeat one is a solid line whilst repeat two is a dashed line. Mean of the combined repeat data is represented by a thin light grey line, whilst the grey box represents $\pm 1\sigma$ from this mean. Error bars are the relative standard deviation.

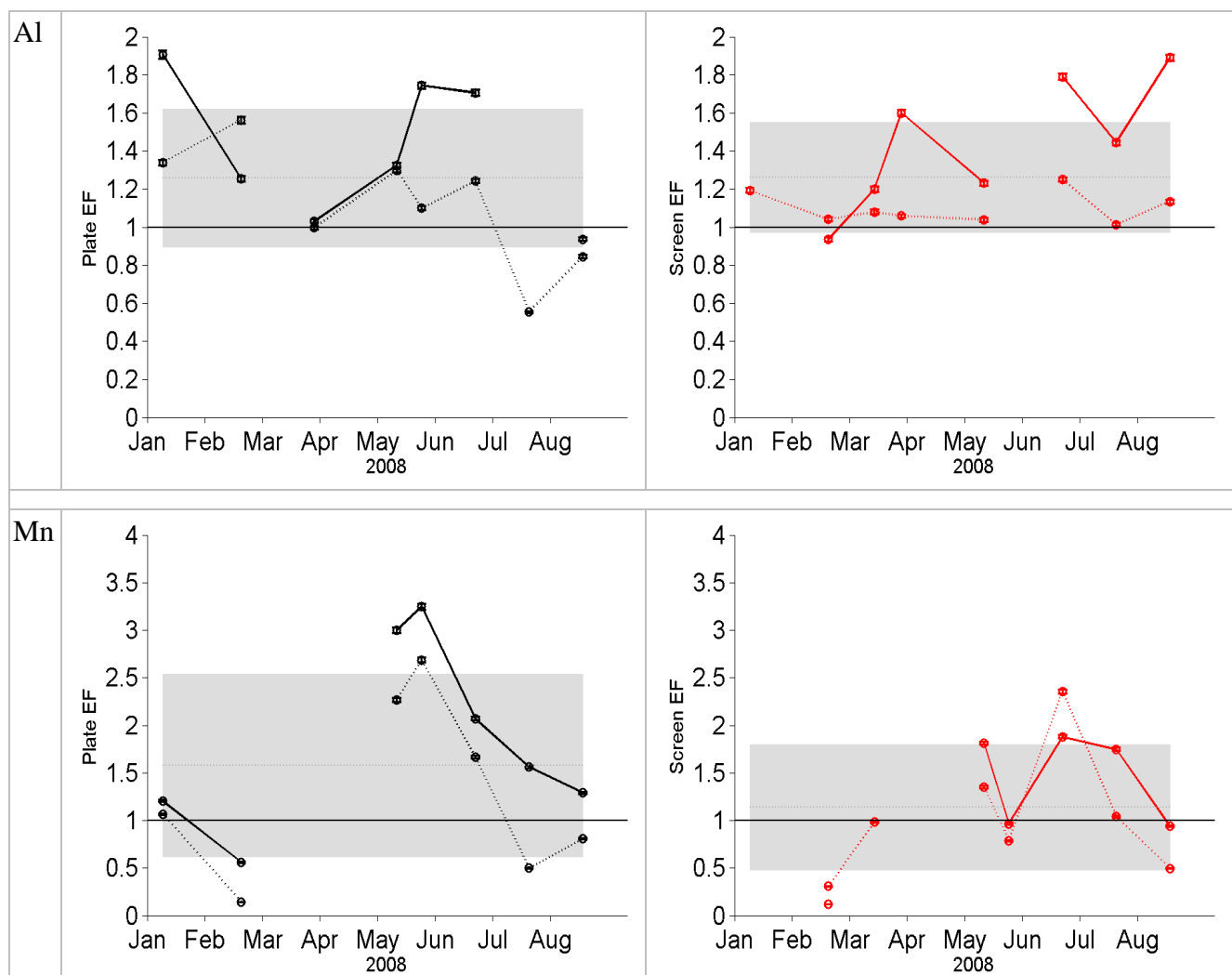


Figure 4.11. Seasonal progression of EFs for dissolved elements statistically said to be enriched in the surface microlayer. See text for description of figure.

Of the enriched analytes the only discernable trend in EF is that of manganese plate samples from early May through to August. This is an increase in the EF in May followed by a steady decline through the remainder of the year, tending towards unity as the season progresses. This coincides with the blue green algae bloom, with the manganese enrichment peaking during the initial growth of the blue green algae at 1 and 2 m, chl α increases from 20 to 55 $\mu\text{g L}^{-1}$. As the cyanobacteria population stabilises, (chl α 55 – 65 $\mu\text{g L}^{-1}$) and then declines (chl α 65 to 40 $\mu\text{g L}^{-1}$) the enrichment of Mn in the microlayer decreases. The steady decline in enrichments is also seen in the screen samples from June onwards. There is also a consistent difference between plate sampled replicate one and two, and screen sampled replicate one and two (except in June) with two measuring lower than one. This is also true for aluminium screen and plate samples with one exception, those calculated for February. This may suggest that a dilution of the microlayer is occurring from replicate one to two as the microlayer is removed from the sample site.

Results from Wilcoxon test (3) results (Table 4.04) indicate that iron (plate 99% and screen 76% probability) and arsenic (plate 46% and screen 96% probability) are depleted in the microlayer. The seasonal progression of their EF show that there are times of both enrichment and depletion (Figure 4.12) therefore the statistical analysis is masking this seasonal variability.

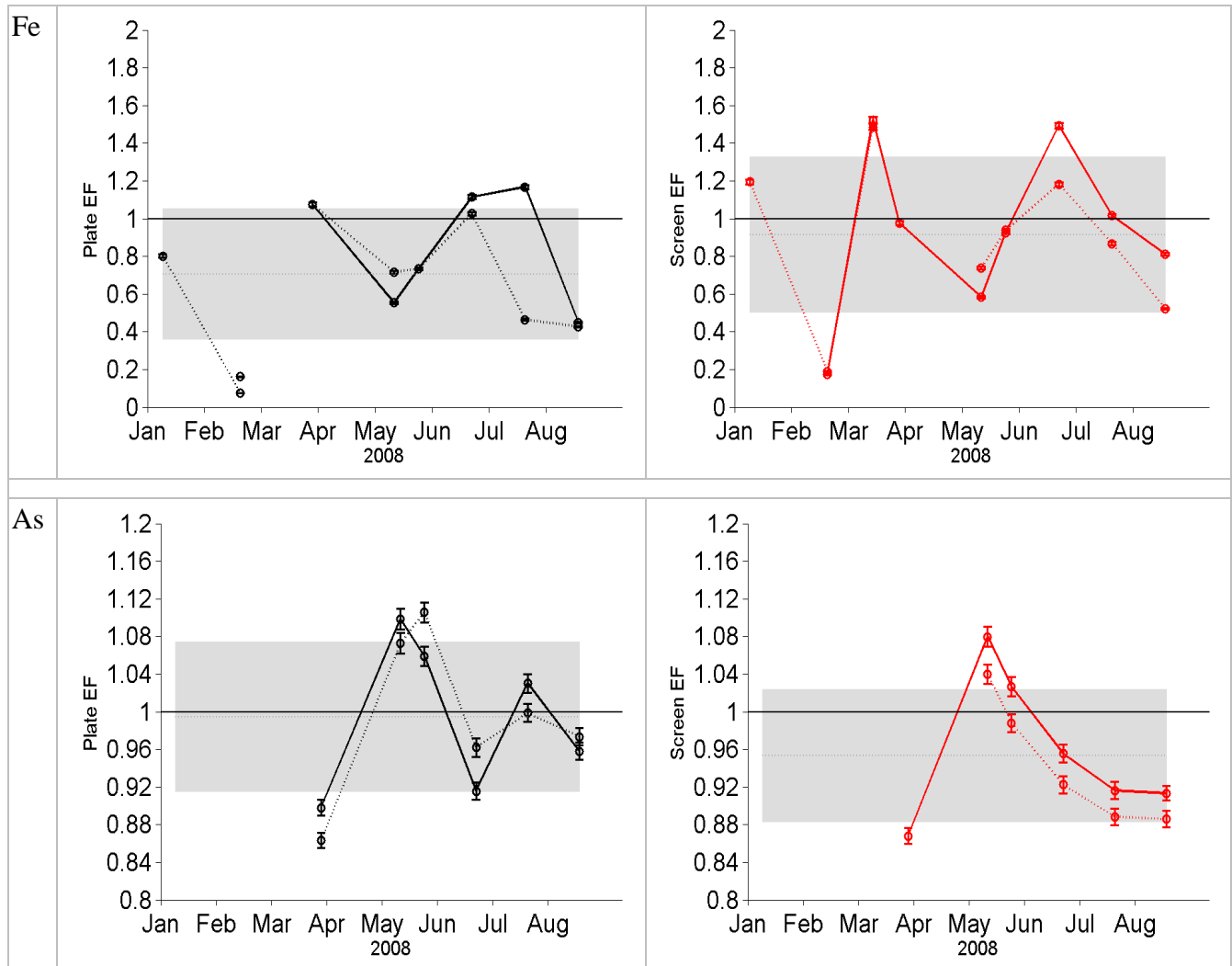


Figure 4.12. Seasonal progression of EFs for dissolved elements statistically said to be depleted in the surface microlayer. See text for description of figure.

Iron EF for both the plate and screen show similarities in their temporal pattern. Using the progression of the screen samples for the seasonal description; between January (EF 1.2) and March (EF 1.5) there was a large decrease in EF, down to 0.2. This decrease in EF corresponds with the diatom bloom in the beginning of the year (maximum chl α in deep waters and concentrations increase with depth) then as this is grazed down in March the EF for iron indicates enrichment in the microlayer. Progression of the time series shows a decrease in the iron EF, close to unity, as there is the second phytoplankton bloom (blue green algae) in late March, with maximum chl α ($\sim 60 \mu\text{g L}^{-1}$) occurring at 1 and 2 m. To early May, the iron shows depletion within the microlayer with chl α highest in the deep waters and lowest ($\sim 20 \mu\text{g L}^{-1}$) in the surface waters. As the cyanobacteria bloom takes off in the surface waters the EF for iron increase and these show a point of maximum enrichment occurring in June as the cyanobacteria standing stock is at its highest. There are three pronounced times of depletion of iron in the microlayer: the first, in February, coincides with the diatom bloom; the second in May coincides with the chl α at 3 and 4 m being greater than that at 1 and 2 m. The third point occurs at the end

of the time series as the blue green algae bloom is declining and chl α at 1 – 3 m are tending towards a similar concentration. The calculated EF for the plate samples during times of depletion is similar to those of the screen. However, the screen samples indicate higher levels of enrichment suggesting that changes in iron within the microlayer, with respect to its enrichment, are also dependant on the depth of the sample retrieved. The points of maximum EFs in late March and June coincides with the grazing down of the diatom bloom and the point of maximum chl α at 1m attributed to the slow growing, blue green algae bloom. The second point of strong depletion in iron (May) in the microlayer coincides with the time manganese indicates a strong enrichment in the microlayer.

Arsenic plate EFs show two points of increased enrichment, the first is during May whilst the second is in July. The point of maximum enrichment in May is also represented in the screen samples. This point corresponds to a depletion of iron and the point of maximum enrichment in manganese plate samples. During these times the water column has a progression from one phytoplankton species to another and the subsequent decline of the second species, respectively. The screen samples from the period of enrichment in May gradually decrease through the rest of the year with replicate one always greater than replicate two. The gradual decrease in the enrichments is similar to that in manganese samples over the same period, though the arsenic decline precedes that of the manganese. Plate samples do not show a bias between the first and second repeats, whereas the screen samples did, suggesting that this depth is being diluted on removal of the microlayer.

Cobalt and copper concentrations when compared using the Wilcoxon test (3), Table 4.04, did not exhibit a significant tendency toward either depletion or enrichment and as such are being termed as at unity with the ULW. The seasonal progression of the microlayer EFs are shown in Figure 4.13 and highlights how the statistical test, with a smaller population does not provide a robust result.

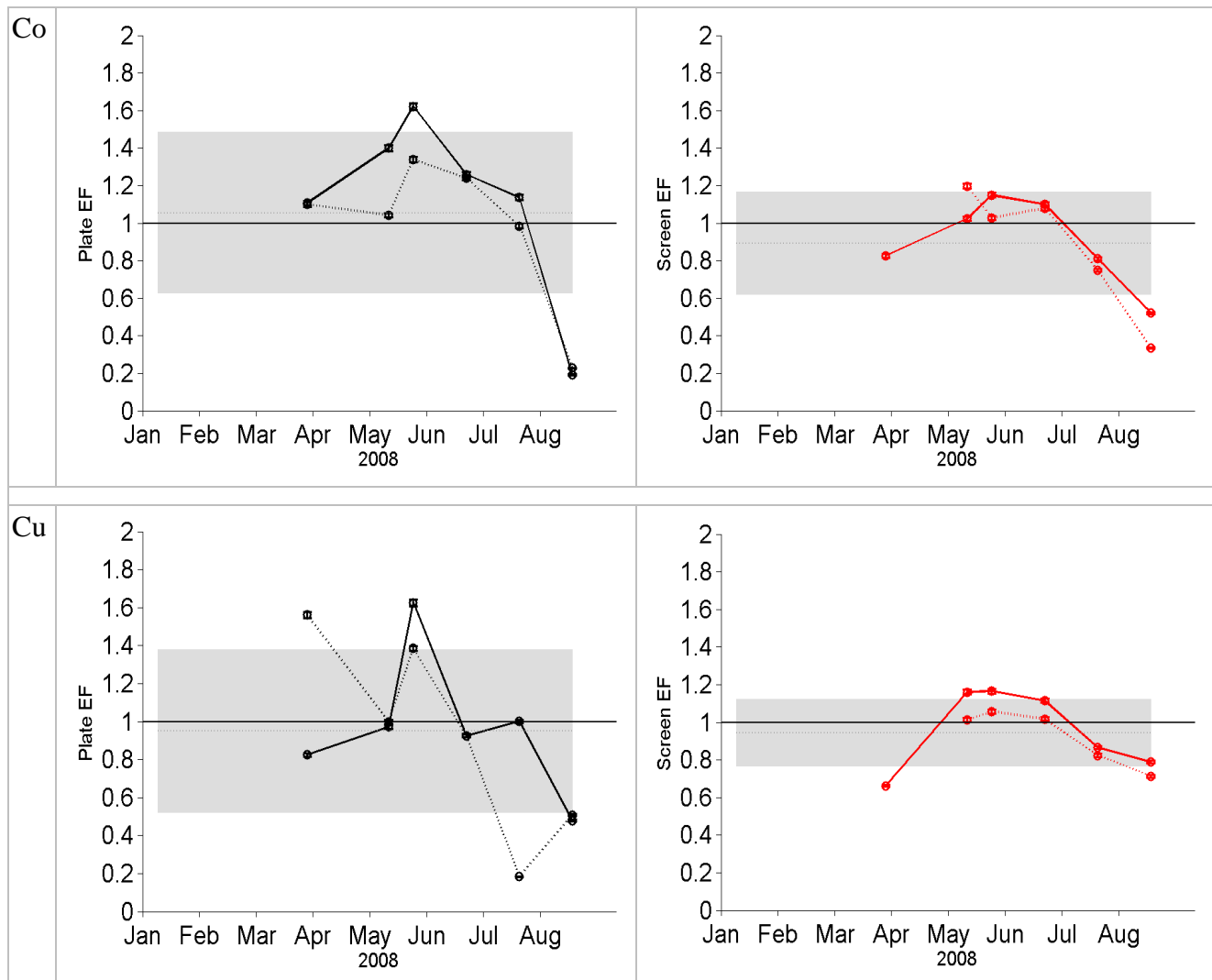


Figure 4.13. Seasonal progression of EFs for elements statistically said to be at unity with the ULW. See text for description of figure.

Cobalt measured from within the microlayer sampled by the plate is enriched or close to unity, except for that in August. The point of maximum enrichment occurs in late May during the growth phase of the blue green algae. Cobalt from within a shallower microlayer (plate samples) like aluminium shows a continued enrichment in the microlayer during April and May, when there are large changes in the speciation of phytoplankton in the Broad. For all, except the August plate sample, enrichments in the first replicate are greater than in the second, however, none of the two previous statements could be statistically corroborated due to small data sets ($n = 6$). EF and the degree of depletion are generally lower in the screen sampled microlayer. The screen sampled microlayer does show a period of enrichment which occurs during the growth and stabilisation of the blue green algae, May to June. Using the first replicate sample in both the plate and screen sampled microlayer cobalt EF increase from March to late May. EFs then show a gradual decrease as the season progresses.

Copper EFs for both screen and plate (disregarding plate, replicate two, late March sample) have a point of maximum enrichment occurring in late May, during the growth stage for the blue green algae. From this point of maximum enrichment, EFs tend to decrease as the season progresses. For screen samples the first replicate EF is always greater than the second replicate. The difference between plate replicates is not as clear as on three occasions, early May, June and August, the calculated EF are similar, whereas other times there is no discernable bias.

What the seasonal progressions of EF do show is that within the $\pm 1\sigma$ of the mean of the combined enrichments there is variability and that the direction of change can be consistent. This is shown, for example, in the decrease in EFs from a maximum occurring in May for manganese, arsenic, cobalt and copper. This form coincides with the succession of the blue green algae bloom. There are points of reference that occur, such as the high in enrichment factors occurring in May, for manganese (plate), arsenic (both) and copper and cobalt (both) whilst there is depleted iron. In May the chl α is low in the surface (1 and 2 m) concentrations, $\sim 20 \mu\text{g L}^{-1}$ whilst at 3 and 4 m it is 55 and $35 \mu\text{g L}^{-1}$ respectively. The water column is also at its stage of maximum thermal stratification, prior to the formation of the blue-green algae bloom. Manganese (screen), aluminium (screen) and iron (both) have a high point in enrichment occurring in June during the blue green algae bloom. Chl α concentrations at 1 m are $\sim 63 \text{ mg L}^{-1}$.

4.06 Discussion

As there has been little published work on the dissolved fraction of trace metals in the surface microlayer and none relating to freshwaters much of the following discussion relating to oxidation states, speciation and organic complexation is speculative. Undertaking such speciation measurements would have provided a far more robust insight into the processes and environmental conditions affecting trace metals in the surface microlayer.

There is an argument for suggesting that the phytoplankton standing stock may affect the concentrations of dissolved trace metals within the surface microlayer. Though not statistically proven there are points of correlation between the chl α concentrations at 1m and the EF for the dissolved fraction of metals. Of the metals aluminium does not appear related to the chl α at 1m. There is a point of reference occurring as the concentration of chl α decreases from $60 \mu\text{g L}^{-1}$ (late March) to $18 \mu\text{g L}^{-1}$ at 1 and 2 m (early May) with a concurrent increase in EF for manganese (plate), arsenic (plate and screen) and copper and cobalt (plate and screen) and an

increase in the depletion of iron in the surface microlayer. The progression of the chla related to the blue green algae then increases to a maximum in June, $65 \mu\text{g L}^{-1}$, at this point, iron shows enrichment in plate and screen samples, arsenic plate samples become depleted, manganese screen samples exhibit their maximum enrichment and both cobalt and copper have shown a period of enrichment. The work of Shine and Wallace (1996) indicated that copper can migrate to the microlayer with phytoplankton derived SAS and under this theory there is the suggestion that as SAS derived from the blue green algae increases it has resulted in increased EF for the dissolved fractions for manganese, iron, cobalt and copper.

Sampler Devices / Depth

Though inadvisable to directly compare samples taken using different sampling techniques (Carlson, 1982) some information may still be obtained from the result from the comparison. The EF results can indicate that there is a difference in those samples from the depth of the microlayer taken or that each sampler may have a bias towards certain fractions of material, i.e. preferentially collect hydrophobic organic material or readily adsorb aquo-ions. From Wilcoxon test (2) results, Table 4.04, using combined repeat one and two data, aluminium, copper and cobalt results suggest that the chance that the depth of the microlayer makes a difference towards the enrichment of these analytes is less than 66 %. For these metals it is possible to make one or some of three possible conjectures: (i) Statistically there is no difference in the concentration of these metals between SML depths of $\sim 60 \mu\text{m}$ (plate) and $\sim 330 \mu\text{m}$ (screen). (ii) The sampling techniques do not have a bias towards, for instance hydrophobic or hydrophilic organic surfactants that compose the two upper most strata of the surface microlayer (Hardy, 1997) and may contain trace metal complexes. (iii) Conversely if each sampler has a bias towards hydrophobic or hydrophilic organic material then any organic complexation of trace metals there in are at similar relative concentrations.

Manganese, iron and arsenic results, from the Wilcoxon test (2) Table 4.04 indicate that there is a statistical difference between the sampling methods. Manganese and arsenic plate samples are consistently higher than their respective screen samples whilst the opposite is true for iron. For manganese the plate sample is enriched compared to the ULW (Table 4.04). Arsenic screen samples are depleted with respect to the ULW (Table 4.04). Their opposing sampling devices indicate that there is no significant difference between those concentrations and the ULW. For iron it is the plate samples which show significant depletion compared to the ULW. The screen samples also indicate depletion; the chance that this is non random is 76%. The results would indicate that dissolved manganese is concentrated in the upper region of the

microlayer, $< 60 \mu\text{m}$ and/or the speciation of the manganese, for instance Mn(II) aquo-ions or organically complexed manganese, in the microlayer is biased towards the plate sampler. As manganese is not significantly organically complexed (Sunda, 1984) the assumption can be made that it was collected as an inorganic soluble phase. It is therefore this phase which is enriched at $< 60 \mu\text{m}$ and an argument maybe given that the plate sampler may have a preference towards the sampling of inorganic soluble ions.

The microlayer is depleted in dissolved iron with this depletion decreasing with depth, $[\text{Fe}]_{\text{plate}} < [\text{Fe}]_{\text{screen}} < [\text{Fe}]_{\text{ULW}}$, suggesting that dissolved iron is removed at the microlayer. Conversely both microlayer samplers may not sample the form of dissolved iron which is present in the microlayer though this is potentially unlikely. If the dissolved phase of an element is depleted that element must therefore reside within another phase, i.e. particulate. Brugmann et al. (1992) found a dissolved phase ($<0.45\mu\text{m}$) enrichment of iron using a glass roller on a marine microlayer, however, over 75% of their total iron was in the particulate form. This may then suggest that iron within in the Broadwater microlayers 60 and 300 μm , is within a particulate form $> 0.2 \mu\text{m}$.

Arsenic is interesting in that the difference between the plate and screen is non-random (98 %) with plate concentrations higher than their respective screen samples. However, depletion of arsenic, in relation to the ULW, is significant only in screen samples, 96 %, corresponding plate statistic is 46%. Arsenic is also noteworthy in that the range of its EFs was far more constrained, EFs 0.86 to 1.11, than the metals. The results for arsenic may then suggest that samplers may collect different forms of arsenic; that the screen samples are being diluted by the ULW would not be the case as they mostly show a depletion, for the microlayer to be depleted its concentration must be lower than the ULW and therefore any mixing with the ULW would increase the EF. Arsenic may either be organically complexed (Andreae, 1986) or within the matrix of particulate ferric oxides (Burnol and Charlet, 2010) or iron oxy-hydroxides (Belzile et al., 1989), with dissolved iron also showing depletion in the microlayer. The plate maybe shows a bias towards an inorganic soluble phase as argued in the case for manganese. Organically complexed arsenic can be present as phytoplankton excreted mono and dimethylarsonic acids (Andreae, 1978), this can account for up to 50 % of the total arsenic, occurring at the height of the phytoplankton growing season (Sohrin et al., 1997). Arsenic as inorganic As(III) (arsenite) in the lake environment accounts for usually 10 – 20 % of the total arsenic (Andreae and Froelich, 1984; Barringer et al., 2011) with the remaining as oxidised As(V) (arsenite). This reduced form is present on manganese and iron oxides (Peterson and Carpenter, 1983; Scott, 1991). The probability that plate sampled arsenic is due to random

chance is 54 %, yet the sign of the Wicoxon test, W, for test (3) comparing against the ULW, is still in agreement with that calculated for the screen samples. If on occasions there is sufficient arsenic in organic form this may be a limiting factor in plate collection. What cannot be ruled out due to the lower relative depletion of arsenic in plate samples is that it has an atmospheric source (Majestic et al., 2009). Assuming a sporadic atmospheric source or a sporadic appearance of a SML that can retain a constant atmospheric source than arsenic will occasionally be enriched in the shallower microlayer relative to the deeper microlayer. The key factor would then be the loss mechanism, which due to its general depletion can also be assumed to be rapid. The loss mechanism is most probably through the formation of iron and manganese colloidal and particulate material and its subsequent settling from the microlayer.

Paradox of Microlayer Removal

The physical sampling of the microlayer has produced a paradox in the results. Under the assumption that following sampling the microlayer is refreshed both vertically and horizontally one of these sources is depleted relative to the other and causes a dilution of the microlayer at the point of sampling. Generally the repeat samples have a lower enrichment factor than the first sample. When the microlayer is enriched logically any dilution occurring vertically is with the ULW, this then cause the microlayer to be less enriched and hence show a lower EF as the results tend to show, Figures 4.11 – 4.13. However, when the microlayer is depleted than any mixing with the higher concentration ULW should result in an increase in the EF, which does not tend to occur. The decrease in EF when the microlayer is depleted would indicate the horizontal migration of the microlayer and the mixing of depleted microlayer at the sample site decreases the EF. A third theory is that the water which is diluting the microlayer is from a layer directly beneath the microlayer and when the sampled thicknesses of the microlayer are removed this layer of water which reforms the microlayer is also depleted but more so than the microlayer with respect to the ULW. This theory would then suggest that the gradient of change for dissolved metals through the microlayer stretches further into the water column than the screen sampled depth, ~ 330 μm .

Aluminium

Aluminium is not generally thought to be biologically required (Williams, 2002), though in seawater it has been shown that phytoplankton can take it up passively (Quiroz-Vazquez et al., 2008). Aluminium can be complexed by humic type materials, though these materials will readily swap the aluminium for iron if iron is available (Yang and van den Berg, 2009). Within

a freshwater system aluminium can be in 4 potential forms, which may pass through a 0.2 μm filter. Ionic aluminium, which if present will hydrolyse to a particulate aluminium hydroxyl complex, alumina-silicate clays and organically complexed aluminium. There is the potential (though no measurements were made) that fine clay particles may pass through the filter pores. If these are present then their stabilisation in the microlayer could be due to the enhanced organic material. Clays have relatively high surface energies and as such are wettable (Hunter, 1980b) however, this high energy will also cause them to readily adsorb natural organic surfactants (Hunter, 1980a) and hence decrease their surface energy. This is important for those particles that are in a shallower depth of microlayer, closer to the air-water interface. With decreasing depth of the microlayer the sorption of hydrophobic and amphipathic (lipid-like organic molecule with opposing hydrophobic and hydrophilic moieties) organic material on the clays and particulate material becomes less stable. Particles that are organic rich and have low surface energies will have enhanced residence times in the microlayer (Hunter, 1980b).

If the assumption is made that there is some organically complexed aluminium, it has been shown that light at 300 nm will photochemically breakdown these organic complexes in freshwater and release aluminium into the ionic phase (Kopacek et al., 2005). With less than 0.1 % adsorption of light at the microlayer (Plane et al., 1997) UVB (280 – 315 nm) is present with which to initiate photochemical activity. In the ionic phase aluminium will then undergo hydrolysis forming a particulate phase which again can adsorb organic material. Stabilisation of fine aluminium particulates by organic material in the microlayer increases relative concentrations of 0.2 μm filterable material and hence shows enrichment to underlying water.

The main sources or elements to a lake system are riverine input, groundwater flow, overland flow and atmospheric inputs. As mentioned in section 4.02.01, the broadwater is an enclosed system with the main inputs from groundwater flow and atmospheric deposition. During thermal stratification of the Broad (late March onwards) the groundwater source of material to the microlayer is minimised to diffusion only rates. Thermal stratification will also minimise the effect of groundwater flow at the lake edges as only input to the top layers can affect the microlayer. Particulate material in the microlayer has residence times of c.10 minutes (Hunter, 1980b); though laboratory studies have shown increased residence times from 1.5 to 15 hours for particulate material these were subsequently drastically decreased when a wind (3.6 m s^{-1}) was applied to the microcosm (Hardy et al., 1985), the generally low residence times will minimise the affect of the groundwater flow as sampling was not undertaken in wet conditions. The remaining source of new material is therefore from atmospheric deposition.

Aerosol dust is primarily alumina-silicate mineral soil material (Jickells and Spokes, 2001). Using the crustal abundances of elements (Wedepohl, 1995) the concentration in the dissolved fractions were normalised to aluminium. The only element in Broadwater samples to show a similarity in its relationship to aluminium to that of their crustal abundances is iron sampled from within the ULW, Table 4.08. From within the microlayer there is depletion in the ratio of iron to aluminium compared to their crustal abundances. All other elements showed an elevation (2 to 3 orders of magnitude) in their dissolved phase ratio to aluminium compared to their crustal abundances.

Table 4.08. Comparison of dissolved phase mean iron concentration, normalised to aluminium, to the average crustal abundance

	Wedepohl, 1995	ULW	% difference	SML	% difference
Fe	0.54	0.53 ± 0.31	-2	0.3 ± 0.2	-39

The results of the normalisation of iron to aluminium may suggest that in the microlayer the enrichment of aluminium has a baseline value which can be attributed to aluminosilicate material. In addition to the aluminosilicate material there are also aluminium hydroxide (Stumm and Morgan, 1996) and organically complexed aluminium (Kopacek et al., 2005). In the ULW the relative concentration of the inorganic soluble ions and organically complexed aluminium are lower compared to the microlayer. If aluminium is hydrolysed in the microlayer from organically complexed forms (Kopacek et al., 2005) which are photosensitive at UVB wavelengths (Yang and van den Berg, 2009), not attenuated at the microlayer (Plane et al., 1997), this can ultimately produce a colloidal material which will be iron poor in relation to fine aluminosilicate minerals. Whilst in the ULW the ratio of iron to aluminium is tending towards average crustal aluminosilicate values (Wedepohl, 1995) with these clays held in suspension by the neutralisation of their surface charge as they adsorb surface active substances (Hunter, 1980a). The other metals at all depths showed far larger ratios to aluminium than suggested by a purely crustal source. What cannot be delineated is whether their excess is due to anthropogenic material deposited at the microlayer or in situ cycling of elements (sourced initially from ground and point sources) as no flux measurements (point sources, atmosphere – deep waters – sediments) were undertaken. There is a sparsity of measurements for aluminium in the surface microlayer, the only available data set from Narvekar and Singbal (1993), measured in the Eastern Arabian Sea, found the dissolved aluminium to be so close to unity they only measured the particulate phase with which they found an average EF of 2 with a range from 0.9 to 10.8.

Manganese

That the microlayer is a region of enhanced redox activity, due to the combination of increased concentrations of organic material and low UV light attenuation (see Section 4.01), may be shown by the enrichment of manganese. Between pH 6-8, Mn(II) aquo ions account for more than 95 % of the solution species in freshwater (Davison, 1993); as such the dissolved fraction is the major contributor to total Mn. Mn(II) can be formed by organic reduction mediated by humic materials, this occurs in the dark but the rate is increased in the presence of light (Spokes and Liss, 1995; Sunda et al., 1983). Re-oxidation is slow for Mn(II) (Horst and Zabel, 1996; Stone and Morgan, 1984), the primary loss mechanisms being particle scavenging or precipitation in alkaline conditions (Stumm and Morgan, 1996) or bacterial-mediated oxidation (Emerson et al., 1982; Sunda and Huntsman, 1988). The oxidation of Mn(II) to Mn(III/IV) results in an efficient trace metal scavenger, this process has been hypothesised to reduce enrichment factors of iron in a marine microlayer (Brugmann et al., 1992). The oxidation of Mn(II) can then be proposed as a mechanism for removal of iron and arsenic (Peterson and Carpenter, 1983; Scott, 1991). With respect to iron the enrichment of manganese is interesting as the properties of iron and manganese are similar; they are biologically required and redox active but with one major difference: their reduced forms have very different oxidation rates, $\text{Fe(II)} \gg \text{Mn(II)}$. The reduction of MnO_x can also be increased through an electron transfer to the MnO_x from reduced iron (Hem, 1978; Scott, 1991).

Manganese has been measured from within surface microlayers in primarily a variety of marine locations and shows a range of enrichment values. Grotti et al. (2001) measuring the total manganese in Antarctic Ice leads estimated an EF of 4.6. In the Baltic sea the dissolved fraction (< 0.45 μm) of manganese in the microlayer showed an EF of 2.5 (Brugmann et al., 1992), whereas Hunter (1980b) measuring total manganese in the coastal North Sea measured a mean EF of 1.2 (range 0.3 to 2.1). In a freshwater system Antonowicz and Trojanowski (2010) measured seasonal changes in total manganese, with an average EF for plate samples of 2.25 and for screen samples of 1.69. The range of EF for dissolved phase manganese in this study, for the plate is 0.14 to 3.24 and for the screen is 0.12 to 2.35.

Iron

These results are the first known measurements of dissolved iron in a freshwater microlayer. The general depletion of iron in the microlayer observed in this study though contrasting the findings of Brugmann et al. (1992), who found EFs of 1.1 in the brackish Baltic Sea, were within a similar range. Where the authors assessed 20 microlayer seawater pairs and attributed their low, though enriched, enrichment factors to low air temperature and minimal biological activity; hence little formation of organic chelates. The authors did find that in the microlayer > 70 % of the total iron was in the particulate form and attributed this to adsorption and co-precipitation with MnO_x. Within an aquatic environment, dissolved iron undergoes hydrolysis reactions to form colloidal iron oxy-hydroxides but these are still biologically available (Rich and Morel, 1990) and can be retained by an active biological iron recycling mechanisms (Hutchins et al., 1993). The ultimate oxidation rate of iron is dependant on the ligands present assuming a well oxygenated system (Millero, 1985). In freshwater these will primarily be carbonate and oxygen as well as organic (Stumm and Morgan, 1996). Iron-hydrated ions and Fe(II) complexes are water soluble whereas Fe(III) occurs largely in the particulate or colloidal phase (Stumm and Morgan, 1996). The photoreductive dissolution of Fe(III) (oxy)hydroxides decreases rapidly with increasing pH (Sulzberger and Laubscher, 1995; Waite and Morel, 1984) whereas organic material has the potential to increase the rate of Fe(III) photo-reduction (Waite and Morel, 1984) but, depending on the relative stability of Fe(II) and Fe(III) organic complexes, the rate of Fe(II) re-oxidation can be enhanced (Emmenegger et al., 1998) or slowed (Miles and Brezonik, 1981; Rijkenberg et al., 2008; Shaked et al., 2004; Steigenberger et al., 2010). Such organic complexation needs to be sufficiently fast to out-compete hydrolysis and precipitation / adsorption reactions (Jickells and Spokes, 2001). Though no work has been done on the speciation of iron in the microlayer it can be suggested from the results of this study that oxidation of reduced iron is faster than both organic complexation and photoreductive dissolution of Fe(III) (hydr)oxides. This conjecture is based on the general depletion of dissolved iron in the microlayer which is a known region of organic material enrichment relative to the ULW. As enrichment of the dissolved iron is not present than iron may either be in the colloidal or particulate phase (> 0.2 μ m), these can be associated with either biological detrital material (Stumm and Morgan, 1996) and also adsorbed onto manganese oxides (Brugmann et al., 1992).

If the case were that there was some soluble iron formed through a LMCT of iron (hydr)oxides (Faust and Zepp, 1993; Waite and Morel, 1984) or organically complexed Fe(III) (Barbeau, 2006; Barbeau et al., 2003) then the corresponding loss mechanism is rapid in respect

to the formation. Surface hydrolysis (Stumm and Morgan, 1996) and the subsequent flocculation of charged particles could be said to be occurring faster than the sorption of organic hydrophobic material which leads to a neutralisation of the surface charge. Flocculation leads to eventual aggregation and is the mechanism for particulate matter removal from the microlayer. What may then be seen in the ULW is a remineralisation of this iron. The formation of soluble inorganic iron hydroxides as with the manganese may show an affinity for the plate but due to their rapid adsorption on to detrital material their concentrations are lower in the microlayer than in the ULW. Speculatively, the fate of dissolved iron in the SML is due to rapid oxidation and scavenging from the microlayer by either organic detrital material or Mn(III/IV). The inability to compare between iron and manganese agrees with Salomons and Baccini (1986) who suggest that within a lake system the manganese and iron cycles are practically independent.

Three previous sets of work have measured iron in the SML and calculated EFs. The EF have been calculated for: total Fe, EF = 7.3 using a roller to sample an Antarctic ice lead (Grotti et al., 2001); particulate Fe ($> 0.4 \mu\text{m}$ filtered), EF = 0.8 range 0.6 – 1.3 in the Costal North Sea (Hunter, 1980b); and dissolved Fe ($< 0.45 \mu\text{m}$ filtered), EF = 1.1, using a screen to sample in the Baltic Sea (Brugmann et al., 1992). The range for the measurements from this study, EF 0.1 to 1.2 (Plate) and EF 0.2 to 1.5 (screen) are of a similar range to both those of Brugmann et al. (1992) and Hunter (1980b) though the filtered fraction measured is smaller and generally the results suggest that there is depletion (Table 4.05, Wilcoxon test 3).

Arsenic

Arsenic oxy-anions can pass through cell membranes along the same pathway as phosphate (Mehlorn, 1986); As(V) is a phosphate analog (Sanders and Windom, 1980). The broad is phosphate limited (Claire Hughes personal communiqué) so there is therefore a rapid internal cycling of the phosphorous within the system. If the phytoplankton are actively seeking phosphate there is the potential that there is also an increase in the passive uptake of arsenic and subsequent excretion of an organically complexed form (Andreae and Klumpp, 1979). There is therefore the potential for a larger concentration of ‘fresh’ organically bound arsenic. One of the two main sources of organic ligands to a lake system is fresh material derived from phytoplankton; this has a turn over rate of up to two weeks. The other source being refractory organic matter to which 70 – 80% of the total dissolved organic molecules belong and is the result of enzymatic degradation (Stumm and Morgan, 1996). Inorganic arsenic can be as either arsenate or arsenite; arsenite can occur in lake systems through the reductive dissolution of MnO_2 and ferric (hydr)oxides by arsenate, this occurs for instance on the surface of Mn(III,IV)

oxides (Scott, 1991). After formation of the inner sphere complex electrons are transferred from As(III) to the Mn which result in the release of oxidised As(V) and reduced Mn(II) (Scott, 1991). The results indicated that the two elements generally depleted in the microlayer were arsenic and iron (Figure 4.12; Wilcoxon test 3, Table 4.05), so therefore any mechanism where both are removed could be said to be an important process, one such mechanism in the scavenging of arsenic into its matrix during the formation of ferric (hydr)oxides (Burnol and Charlet, 2010). The potential for a proportion of arsenic to be bound to ‘fresh’ organic material also had interesting implications for the sampling device as explained in Section 4.06.01. The small range in arsenic EF, plate 0.86 – 1.11 and screen 0.87 – 1.08 are similar to the range calculated by Cuong et al. (2008) for a coastal microlayer in Singapore, EF 0.9 – 1.1.

Cobalt and Copper

Both cobalt and copper are essential trace nutrients (Bowen, 1966). Organic complexation can also occur for both cobalt (Nolan et al., 1992) and copper (Shine and Wallace, 1996). During the formation of manganese and iron (oxy)-hydroxides both cobalt and copper are known to be incorporated into their matrix (Burnol and Charlet, 2010). Organically complexed copper has been seen to migrate to the microlayer with the presence of SAS (Shine and Wallace, 1996). Whilst in an inorganic form copper within in colloidal and / or particulate material will be under the influence of gravitational settling. Therefore, for these metals, these processes, migration with SAS to the microlayer and gravitational settling from, maybe occurring at similar rates and is why the microlayer is statistically at unity with the underlying waters. However, what could also be postulated is that an atmospheric source for these metals to the microlayer is depositing material at a similar rate to the microlayer as they are lost from it. Both Hunter (1980b) and Shine and Wallace (1996) suggest that the primary source of copper to the microlayer is from the water column. Enrichments for cobalt and copper occur for the screen sampled microlayer during May and June and for the plate sampled microlayer during May (Figure 4.13). During this period the blue green algae is slowly growing and stabilising within the surface waters (1 – 2 m, Figure 4.06) this would suggest that the times of enrichment for cobalt and copper are affected by phytoplankton production in the water column and the subsequent production of phytoplankton derived SAS (Shine and Wallace, 1996).

With respect to published values of calculated EF for cobalt and copper the results from this study are in good agreement, even when considering different fractions (Table 4.09). However this study was conducted in freshwater whilst all other published values are derived from seawater.

Table 4.09. Comparison of cobalt and copper EF to published values.

Reference	sample local	sampler	fraction	EF
Cobalt				
Brugmann et al. (1992)	Baltic Sea	screen	0.45 μm dissolved	1.2
Pattenden et al. (1981)	North Sea coastal waters	Bubble microtome	total (normalised to sodium)	1.3 - 76
This study		plate	0.2 μm dissolved	0.2 – 1.6
		screen	0.2 μm dissolved	0.3 – 1.2
Copper				
Cuong et al. (2008)	Singapore coastal waters	roller	0.45 μm dissolved	0.9 – 1.2
Grotti et al. (2001)	Antarctic ice lead	roller	total	1.6
Brugmann et al. (1992)	Baltic Sea	screen	0.45 μm dissolved	1.5
Hunter (1980b)	North Sea coastal waters	screen	particulate ($> 0.45 \mu\text{m}$)	0.6 (0.2 - 1.1)
This study		plate	0.2 μm dissolved	0.2 – 1.6
		screen	0.2 μm dissolved	0.7 – 1.2

4.07

Conclusions

The above work has measured concentrations of the dissolved fraction (0.2 μm filtered) of aluminium, manganese, iron, cobalt, copper and arsenic in a lacustrine surface microlayer and related these to a corresponding underlying water sample collected at a depth of 0.1 m. The concentrations have been used to develop a relationship based on the ratio of the measured concentrations, termed an enrichment factor. These enrichment factors can be dependant on the microlayer sampling techniques, which remove different thicknesses of microlayer. Table 4.10 shows a summary of the enrichment factor relationships for the six metals / metalloids.

Table 4.10. Summary of the Wilcoxon test relationships between surface microlayer and underlying water for the dissolved trace metals considered.

depth	60 μm Vs 340 μm	60 μm Vs -10 cm	340 μm Vs -10 cm
samples	plate Vs screen	plate Vs ULW	screen Vs ULW
Al	Unity	Enriched	Enriched
Mn	Enriched	Enriched	Unity
Fe	Depleted	Depleted	Depleted
Co	Unity	Unity	Unity
Cu	Unity	Unity	Unity
As	Enriched	Unity	Depleted

Aluminium is enriched compared to the ULW in microlayer thicknesses of 60 and 330 μm . There are two reasons: UVB induced photochemical cycling (Kopacek et al., 2005) from organically complexed aluminium (Yang and van den Berg, 2009) and its subsequent formation into hydrolysed inorganic soluble ions (Stumm and Morgan, 1996) occurring in the SML. Due to little correlation with the biology of the water column there is the supposition that the aluminium is sourced from fine grained alumina-silicate atmospheric dust. The neutralisation of the surface charge of this atmospherically deposited material through the sorption of SAS can lead to an enhancement of its residence time in the SML (Hunter, 1980a).

Manganese is enriched in the shallow microlayer $< 60\mu\text{m}$ in depth. The dissolved phase manganese is probably as a Mn(II) aquo-ion (Davison, 1993). Theoretically there can be increases in the concentration of Mn(II) due to the microlayer itself: Increased photochemical oxidation of organic material subsequently increasing the rate of Mn(III/IV) reduction (Spokes and Liss, 1995; Sunda et al., 1983). There is also the possibility of the reduction on Mn(III/IV) by reduced iron and arsenic (Scott, 1991), both depleted in the microlayer increasing the Mn(II) concentration. Though a 0.2 μm filtration can be used to physically separate manganese

oxidation states (Stone and Morgan, 1984), it is only 90 % efficient and does not preclude the presence of dispersed colloidal Mn(III/IV) material.

Dissolved iron is depleted at all depths in the microlayer and this depletion increases as depth of the microlayer decreases. There appears a strong causal relationship between dissolved iron in the microlayer and the succession of biology in the water column.

Cobalt and copper appear close to unity at all depths in the microlayer and with the ULW, when they show enrichment this is related to the growth of slow growing cyanobacteria.

Arsenic is depleted in the microlayer at thicknesses of around 330 μ m. The paradox of the arsenic being depleted in screen sampled thicknesses of microlayer, yet at unity in a plate sampled thicknesses of the microlayer may be due to a bias within the sample collected. However, a caveat must be suggested in that the use of small number of data, six samples, did not allow quantitative statistical calculation.

For iron and manganese the depletions / enrichments in plate samples are greater than screen samples suggesting that depletion / enrichment increase as depth of the microlayer decreases. Barker and Zeitlin (1972) suggested that EF should increase as the thickness of the microlayer decreases, less dilution with ULW, and results for manganese would suggest that this occurs. The results suggest that for dissolved iron this does not occur so as the microlayer thickness decreases there is an increase in the mechanism converting the dissolved to the particulate fraction.

The results show that there is variability in the dissolved fraction of trace metals in the surface microlayer. This variability can be due to both processes occurring within the water column, and in the microlayer itself. Those within the microlayer are related to the mineralisation of reduced species of metals and their subsequent loss from the microlayer on and in particulate material.

Chapter Five

Water-Particle Interactions in a Photochemically Active System

5.00 **Introduction**

This work is the first of three experimental chapters looking at what can affect changes in the production and redox cycling of hydrogen peroxide and iron in model marine surface microlayers. This chapter is an initial set of trial experiments comparing the formation of photochemically active redox species and the affect particulates have on them. The reason for the addition of particles to a system comes from the work in Chapter 4, comparing the concentrations of 0.2 μm filtered metals in a freshwater microlayer. Those results indicated that there is an enrichment of dissolved manganese; this is expected to be as Mn(II) as a 0.2 μm filtration should remove greater than 90 % of Mn(IV) from the solution, but a depletion of dissolved iron. These elements, similar in their potential for photochemical reduction were controlled by different processes. Mn(II) was hypothesised to be enriched due to the photochemical reduction of MnO_2 minerals and a subsequent long half life of the Mn(II) aquo ion. Iron on the other hand, following photochemical reduction was depleted due to its hydrolysis and subsequent sorption on to colloidal material. This material then under went fast sedimentation from the microlayer and remineralisation in the underlying water, dissolved iron concentrations increased with the thickness of the surface microlayer sampled and on into the underlying water. Though there are differences due to the ionic strengths of freshwater and seawater the processes these metals undergo are similar. This work was at an initial stage of research with the findings used to define a more comprehensive suite of experiments (Chapter Six). There were two initial aims of these experiments: i) Produce a photochemically redox active analogous sea-surface microlayer system containing hydrogen peroxide and reduced iron and manganese. ii) Induce further reduction of iron and manganese into the soluble phase following the addition of an artificial particulate.

This chapter also introduces the experimental method and categorises the light spectrum used during these and subsequent experiments. The experiments used either a natural seawater phytoplankton exudate or humic acid combined into 0.2 μm filtered North Sea seawater to represent a surface microlayer. The systems were irradiated to induce the production of H_2O_2 and Fe(II) (and potentially Mn(II)) and then a particulate phase was added. The organics and seawater itself were the sources of superoxide and hence H_2O_2 and the oxidised iron and manganese for the production of Fe(II) and Mn(II). The experiments were formulated from a series of published works (see below) looking at both the production of Fe(II) from extracted and concentrated natural marine organic (NMO) and the effect that organic material has on the oxidation of Fe(II). This work uses NMO that has not been chemically extracted, though it was size fractionated; instead it was freshly obtained from an iron limited phytoplankton culture.

The primary difference within these experiments is the addition of the artificial particulates to a photochemically active system induced from the NMO. These experiments also employed a quasi-simultaneous Fe(II) – H₂O₂ analysis system using a single valve, flow injection analysis chemiluminescence (FIA-Cl) system with luminol, see Chapter 3.

The experiments were initially based on irradiation experiments of Miller et al. (1995); these were the first seawater incubations (with and without added dissolved organic matter (DOM)) measuring and kinetically modelling, Fe(II) and H₂O₂ production. Though the experiments in this work have a higher temporal resolution (44 s compared to 14 minutes for the Fe(II) and 44 s compared to 3-5 minutes for the H₂O₂). The work was also influenced by Meunier et al. (2005) who modelled Fe(II) and H₂O₂ in marine and freshwater system specifically with added extracted NMO; though they compared different size fractions and used a kinetic model with a parallel set of organic equations to explain the reactions of Fe(II). Stone and Morgan (1984) measured the light induced organic reduction of MnO_x in two stages – consecutive dark and light phases. None of the previous works included an addition of an artificial particulate into their photochemically active seawater systems. The experiments were also developed from iron photo-dissolution experiments which included seawater enhanced with organic material and additions of iron prior to commencing the incubation of the media with artificial particulates. These experiments are Kuma et al. (1992), additions of 1 and 5 μ M Fe(III) in the presence of 50 μ M various organic substances; Voelker et al. (1997) who used low pH seawater with 40 μ M lepidocrocite (γ -FeOOH) and 10 mg L⁻¹ Suwannee River fulvic acid (SRFA) and Rose and Waite, (2006), additions from 50 up to 1000 nM Fe(III) in the presence of SRFA from 0.1 to 5.0 mg L⁻¹. Particles used in the previous experiments were of a single type and experiments concentrated on measuring the change in concentration of reduced iron; whereas the following work used mixed metal particulates and the affect they have on an active photochemical system. The experiments also incorporated the work of Sunda and Huntsman (1994) and Spokes and Liss (1995) who showed that there is a photochemical reduction of MnO_x to Mn(II). To measure the effects of changes brought about by the perturbations, a FIA-Cl system was used to measure H₂O₂ and Fe(II) (Chapter 3) and an ICP-MS (Section 2.04.08) was used to measure soluble Mn(II). The analytes, H₂O₂ and Fe(II) were measurable quasi-simultaneously, every 44 s, and Mn(II) measured on a longer temporal scale, c. 6 minutes.

There are two caveats within these experiments. The first is that the effect particulates had on the luminol chemiluminescence was not assessed prior to the experiments. The second is more integral to the measurements. Organic material (O'Sullivan et al., 1995) and superoxide can affect the luminol chemiluminescence signal (the superoxide radical reacts with luminol

negative ion forming a luminol negative radical, the first step in the formation of alpha-hydroxy-hydroperoxide (α hhp) intermediate (Merenyi et al., 1990; Rose and Waite, 2001)), however, the affect of the organic material is usually incorporated into the calculation of the blank (ie signal attributed to seawater components, see Section 3.02.03) whilst the affect of superoxide is usually not expected to be relevant; this is as the production of superoxide within the flow cell related to the oxidation of Fe(II) at high pH is \sim 100 times greater than in the sample based on sample Fe(II) concentrations between 1 and 1000 nM (Rose and Waite, 2001). The experiments utilise UV radiation and as such there will be changes in the composition of the organic material through time due to photo- (Del Vecchio and Blough, 2002) or hydroxyl induced oxidation (Goldstone et al., 2002; White et al., 2003). Also, there will be changes in the production of superoxide through the photochemical excitation of DOM and the subsequent oxidation of oxygen (Micinski et al., 1993) or Fenton like reactions with iron (Voelker and Sedlak, 1995), copper (Gray, 1969; Moffett and Zika, 1983) and manganese (Hansard et al., 2011), therefore a component of the blank signal can also change over time. The experiments themselves encompassed three stages; a dark, light and particulate stage. The dark stage itself allows for a control to the light stage (identical media though in the dark). One set of experiments used the base media North Sea seawater only, so changes that are different from this system are due to the additions of the organic material.

No explicit work was done on the affects of changes of the organic material to the chemiluminescence, for this analytical set up the assumption that the changes to the organic material would make negligible difference to the blank and that the production of superoxide would also have negligible effect on luminescence, which has been cautioned by Rose and Waite (2001), had to be used throughout. Fe(III) (\sim 200 nM), Cu(I), Mn(II) (>117 nM) and V(IV) have all been shown to strongly affect the luminol based analysis of both H₂O₂ and Fe(II) (O'Sullivan et al., 1995; Seitz and Hercules, 1972; Ussher et al., 2009; Yuan and Shiller, 1999), whilst H₂O₂ itself can affect the chemiluminescence attributed to Fe(II) (O'Sullivan et al., 1995; Yuan and Shiller, 1999). Catalytic reactions of iron by Cu(II) and MnO₂ at the pH of the mixed sample and reagent can reduce Fe(II) and remove it from the sequence of reactions that induce luminol chemiluminescence. With an increased concentration of the luminol reagent, 1.5 mM (O'Sullivan et al. (1995) recommend >500 μ M) the interferences due to Cu(II) and MnO₂ are not strong and the luminol reagent will favour the superoxide formed during oxygen Fe(II) oxidation, due to the fast kinetics of the reactions (O'Sullivan et al., 1995). H₂O₂ will affect the Fe(II) analysis though this will only occur at concentrations > 100 nM (Rose and Waite, 2001) or > 1000 nM (King et al., 1995). Conversely Fe(II) has been shown to have only minimal affect on the luminol chemiluminescence in the presence of H₂O₂ (Klopf and Nieman, 1983)

with Fe(II) affecting the analysis of H₂O₂ when the H₂O₂ concentrations are low ~ 2 nM (Yuan and Shiller, 1999).

5.01 **Experimental Method**

5.01.01 **Seawater, Reagents, Organics and Particulates**

Seawater was collected from a variety of off shore North Sea locations, this had one affect on the experiments in that they all did not have the same base material, however, the assessment of the experimental blank would include the differences in these samples. The salinity of the various North Sea waters was around 34.5 (Bristow, 2009). The seawater on collection had been filtered through a Whatman GF/F filter and frozen (Bristow, 2009). Following defrosting the water was then filtered through a Whatman 0.2 µm track-etched polycarbonate filter. This water was then stored for up to five months in the dark at 4 °C before it was refiltered again through a 0.2 µm filter and again stored in the dark for use within the next four weeks.

1.5 mM luminol (Sigma Aldrich, Luminol 98 %) solutions buffered with 0.08 M K₂CO₃ (Fisher) and aged for 24 hours at 4 °C was adjusted to pH 11.2 with 2 M HCl (Fisher). The luminol reagent for H₂O₂ analysis was spiked to 60 µM with Co(II). The luminol reagent is produced by combining ~ 0.203 g luminol with ~ 8.25 g of K₂CO₃ into a brown polypropylene container and adding 750 mL UPW. The reagent is sonicated for 5 minutes before placing in the fridge. H₂O₂ and Fe(II) standards were produced by dilution of their appropriate stocks. The primary H₂O₂ standard was made by adding 2 mL of H₂O₂ stock (Fisher), 2.63 M, into a weighed volume of UPW, nominally 50 mL, giving a concentration of ~100 mM. The primary standard was stored in the dark at 4 °C for up to 6 days. The ~18 µM Fe(II) (Fe(II) sulphate, Fisher) stock was produced by combining the required weight into 30 mL UPW acidified to less than pH 2 with double quartz distilled (in house) HNO₃. The primary and working standards were produced through a serial dilution of this stock. The Fe(II) stock was renewed every month. The mixed experimental seawater media and UPW, used for the production of H₂O₂ standards, were stored in the dark overnight to allow latent H₂O₂ to decompose and any Fe(II) to oxidise. The limits of detection (LOD) for all the experiments are, for Fe(II), 0.6 ± (σ) 0.5 nM (range 0.004 – 1.9 nM, n = 31) and for H₂O₂, 8 ± (σ) 8 nM (range 0.01 - 34 nM, n =31).

Three organics were used: an aged (>4 months) culture residue from *Thalassiosira pseudonana* grown in F2 medium in a chemostat; a fresh (2-9 days old) culture residue from *Fragilariopsis cylindrus* grown in low iron, Aquil medium and humic acid at concentrations of 0.5, 1.0 and 2.0 mg L⁻¹ (Sigma). The *Fragilariopsis* exudate was obtained as a 0.7 µm filtrate and stored in the dark at 4 °C. The *Thalassiosira* exudate was used as either a 0.2 µm filtered extract (repeat experiments), or as a 2.0 µm filtered extract (light regime comparison experiments Chapter 6). The humic acid stock was either freshly prepared and directly mixed with the seawater, resulting in approximately pH 7.4 or the stock was left for 24 hours before combining with the seawater, 24 hours before incubation, resulting in a slight decrease in pH of approximately 0.2 units to the seawater. Within humic acids there are large concentrations of carboxylates (Averett et al., 1989), on mixing with water these will deprotonate decreasing the pH (Fox and Whitesell, 2004). If this is left over time the carboxylate ions will achieve equilibrium. Small volume additions to seawater will therefore be neutralised by the buffering capacity of the seawater again if sufficient time is allowed. However, this may not occur if there is insufficient time between mixing of the humic acid and subsequently combining this within the seawater.

The particulate additions used in the experiments consisted of either single or combined artificial particulates containing Fe(III) ferrihydrite, a mixed state manganese (III/IV) oxide (MnO_{1.9}) and aluminium hydroxide, Al(OH)₃. The iron and manganese phases are both known to be photochemically active (Spokes and Liss, 1995; Sulzberger and Laubscher, 1995; Sunda et al., 1983; Waite and Morel, 1984). The Fe(III) phase was produced according to Wells et al. (1991). Briefly, ferric chloride, (FeCl₃.6H₂O, Sigma-Aldrich (Puriss ACS) was weighed into a container and a quantity of UPW was added giving a final iron concentration of 0.4 mM. This was left for an hour in which time the iron polymerises forming a colloidal ferrihydrite. This ferrihydrite is the starting material for naturally occurring crystalline iron oxyhydroxides (Crosby et al., 1983). Taking aliquots of this and heating them for 5 minutes by means of a water bath increases their crystalline structure towards goethite (~ 50 °C) and then hematite (~90 °C) (Johnston and Lewis, 1983). The following experiments used ferrihydrite heated to 50 °C, goethite, FeO(OH), (FERR50) as the iron particulate phase; this particulate is less crystalline than the hematite, Fe₂O₃ (FERR90) and more labile to photochemical reduction (Sulzberger and Laubscher, 1995).

A 1.4 µM MnO_{1.9} suspension was prepared according to Sunda et al. (1983) and Spokes and Liss (1995) by stoichiometrically combining manganese chloride (MnCl₂, Sigma), potassium permanganate (KMnO₄, Sigma) and potassium hydroxide (KOH, Fisher) in a 3:2:4

molar ratio, respectively. Briefly, the method consists of combining KMnO_4 and KOH to the required concentration and taking a 20 mL aliquot and adding this by means of a burette to 180 mL MnCl_2 solution whilst vigorously stirring. The pH of the sample is measured over an hour and appropriate small volume additions of KOH and HNO_3 are used to maintain a neutral pH whilst the system is mixing. The manganese particulate phase should be stable for up to two years (van den Berg and Kramer, 1979). Recoveries of the manganese particulate were tested by reducing five 1 mL aliquots by adding them to 9 mL of 1 M oxalic acid (Fisher) filtering them and comparing against these against the stock through analysis by an ICP-MS. The resultant recoveries of the four samples were 115, 91, 95 and 96 %. Using a 0.2 μm filtrate for analysis has the effect of removing greater than 90 % of the Mn(IV) particulate from a solution allowing physical separation to identify oxidation state (Stone and Morgan, 1984).

The aluminium hydroxide is stable in the neutral to approximately pH 8 range. Due to its amphoteric nature (Baes and Mesmer, 1976; Williams and Frausto da Silva, 1996), as the pH decreases and increases the precipitate will dissolve (Furrer and Stumm, 1986).

5.01.02 pH and Temperature

pH and temperature were measured on a Jenway 3150 pH and temperature meter. pH was measured on the NBS scale (Covington et al., 1983), as such the measurements can be an over estimation of the sample medium due to ionic differences from the reference to the test solutions. This uncertainty can be in the order of, or greater than, 0.01 pH units (Dickson, 1984). The Jenway 3150 meter has a resolution of 0.01 units with an accuracy of ± 0.02 units therefore the error on the meter will incorporate the minimum expected differences. With respect to inter-comparing pH measurements with published values the differences in the liquid junction potential for each pH probe can be different (Dickson, 1993) therefore for very accurate pH measurements $> \pm 0.01$ this is inadvisable, though with respect to this work an intercomparison is not required.

5.01.03 Experimental Setup

The FIA-Cl system including the photon multiplier tube (PMT) was powered up; whilst these were warming, ultra pure water (UPW) was ran through the system as a rinse. The reagents and seawater were removed from the fridge. The luminol reagents were altered to pH 11.2 and Co(II) (final concentration 6 μM) was added to the H_2O_2 reagent. Seawater and reagents were then placed in a covered water bath set to the ambient laboratory temperature.

When the reagents were at the ambient air temperature they were removed from the water bath. At this point the experimental seawater was decanted into a wash bottle for use with the standards and into the quartz glass incubation vessel (following UPW and three seawater rinses). The incubation vessel was then placed in a plastic bag and re-immersed in the water bath. The bath was at ambient laboratory temperature plus two or three degrees to compensate for the additional temperature within the light box, dependant on the number of bulbs being used for that experiment.

The test calibrations were then started; these allowed an understanding of how the luminol reagents were working on the day and were used to set the sensitivity of the PMT. The test calibrations also gave an idea of what concentrations were being seen in the experiment to allow preparation of a comprehensive set of standards for the calibration directly following the experiment. The calibration of the signal for H_2O_2 was undertaken in the same way as that for Fe(II), Section 3.03.05. Briefly, the calibration minimises the time between addition and analyses of a reactive species such as Fe(II). Between addition and analyses the transit time is the same for both the experiment and the calibration, and the experimental medium is the same so therefore any reactions taking place are included within the calibration. As the flow rate of the pump tubes is known then the volume of the standard is also known at the point of addition of a small volume ($\sim 10 \mu\text{L}$ for Fe(II) work) aliquot of the working standard. Both the standard and sample are mixed by means of a Teflon coated magnetic flea. There are two unaccounted differences in the calibration these are; the surface to volume ratios, and the surface absorption of the HDPE standard container compared to the quartz glass reaction vessel. Concerning the surface absorption both containers were rinsed three times with the seawater prior to use, this should act to decrease the amount of reaction sites within the system.

With the initial calibration finished, the light box was moved to the laminar flow hood. The bulbs had been switched on for at least 30 minutes prior to moving. The incubation vessel was placed in the light box to which a magnetic flea, pH and temperature probe and the Teflon tubing from the FIA system were added. The system was then stirred; the stirring was to such a degree that a small vortex would be present at the surface inhibiting migration of hydrophobic material to the surface. As the volume decreased through the experiment so also did the stirring rate. Figure 5.01 is a diagram of the experimental setup. Two further Teflon tubes were added, these were to enable a sampling for the analysis of manganese and for the introduction of the particulate phase. Sub-sampling was undertaken by using a 15 mL syringe. Initially two 4 mL sample aliquots were extracted, these were used to wash the syringe, rinse the $0.2 \mu\text{m}$ polycarbonate filter and then rinse a 15 mL centrifuge tube. A further 10 mL of sample was

then extracted; this was passed through the filter and collected. This sample was acidified to less than pH 2 with (quartz double distilled) HNO_3 to enable storage before analysis of $0.2 \mu\text{m}$ filtered manganese (Mn(II)) by the ICP-MS. On completion of the experiment, there was a second calibration, which was used to produce the measured Fe(II) and H_2O_2 results. Finally, with the calibration finished the FIA system was set to run for an hour with 0.1 M HCl acting as a wash.

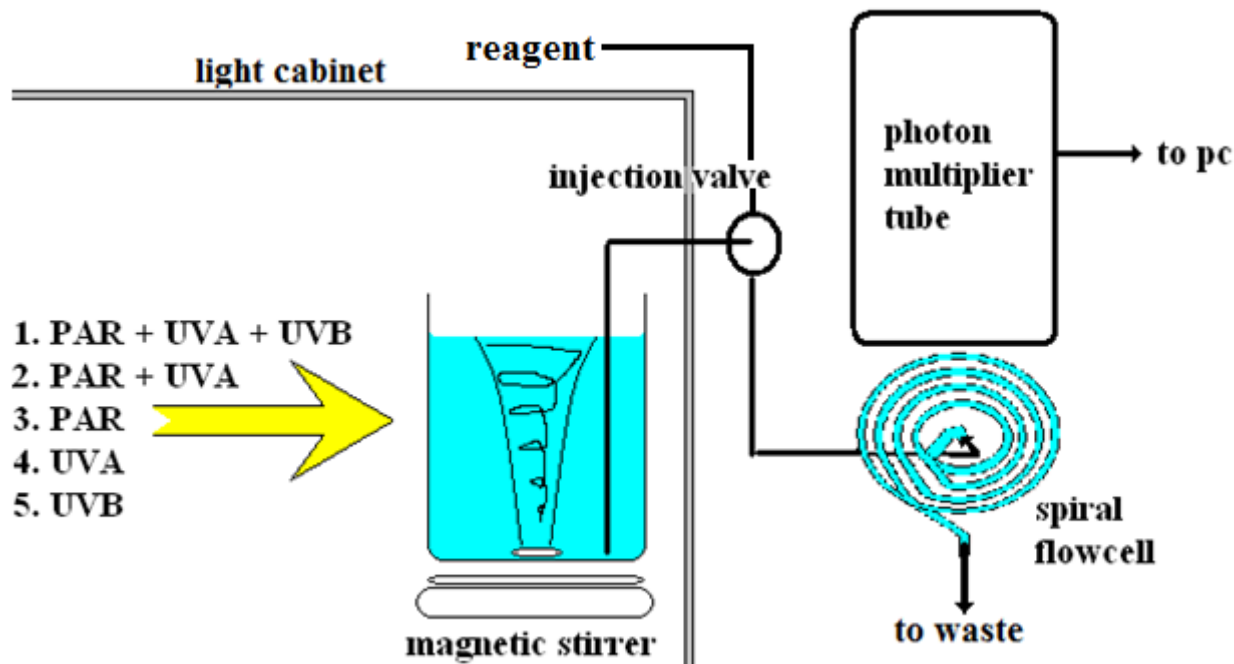


Figure 5.01. Experimental set up.

5.01.04 Light Spectra

The seawater incubations were undertaken in a quartz glass beaker holding 750 mL of the model sea surface microlayer. This was placed inside a light cabinet containing three halogen bulbs; from top to bottom these were; a Philips TLD 18W/840 used as the source of photosynthetically active radiation (PAR, 400 – 700 nm), a Glassguard F20W/BL350 used as the UVA (315 – 400 nm) source and a Reptisun F20T12/REPT used as the UVB (280 – 315 nm) source. The light flux of the bulbs and their combinations was measured using a Macam spectroradiometer, model SR9910, measurements were taken from within the quartz glass beaker with the sensor facing towards the primary UVA source. The PAR and UVB bulbs were within 5cm (above and below) of the UVA bulb. Figure 5.02 shows the breakdown by light regime for each bulb or combination. The percentage contributions have been normalised as a spectral irradiance through a correction based on the length of the irradiating regime. Single

bulb sources are not purely within their specified regimes and there are some overlaps. The UVB bulb has only ~ 5% UVB light with the remaining irradiance as ~ 20 % UVA and ~ 75 % PAR, the proportion of the UVA light in the bulb is in the far UVA, < 360 nm (Figure 5.03). The UVA bulb also contains 1 % UVB and 23 % PAR. The PAR only bulb contains 0.2 % UVB and 1% UVA within its regime. For the initial work a full spectrum incubation was used throughout which involved all bulbs; the spectral irradiance was made up of 3 % UVB (1.4 W m^{-2}), 32 % UVA (15.2 W m^{-2}) and 65 % PAR (30.1 W m^{-2}).

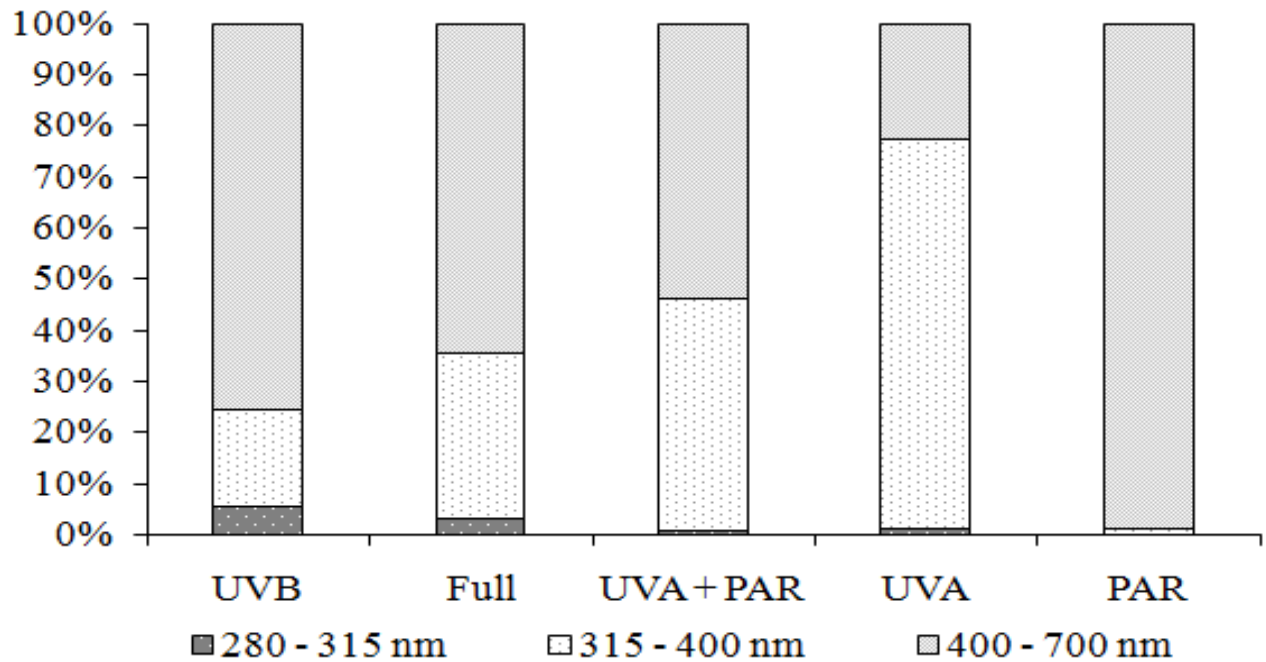


Figure 5.02. Percentage spectral irradiance for each irradiating regime

The light fluxes were compared to the American Society for Testing and Materials, terrestrial reference spectra G173-03 (SSI), which is a composite spectrum for all mainland USA over the space of a year (Figure 5.03). With respect to light in the UVB range (290 – 315 nm) there is approximately twice that received when the UVB bulb is in use. The Full spectrum, UVA+ PAR and UVA irradiating regimes produce good likeness within the UVA range from 315 – 350 nm. From their maximum irradiance in the UVA range at ~ 350 nm the irradiating regimes decrease to 400 nm whilst the composite measurement increases towards the cross over into the visible light range. The PAR irradiation for combinations and the pure PAR bulb are greatly reduced compared to the measured reference spectra.

As well as the measured reference spectra the irradiating regimes were compared to the bench mark calculated values of Zepp and Cline (1977) at 40°N for spring noon (Figure 5.04). The Full light spectra provides ~160 % of UV-R and 0.8 % of PAR when compared to these values. In general the incubating regimes provided less than 1% of natural light in the visible

range but comparatively greater than 100 % of the naturally occurring UV-R for those irradiating regimes containing the UVA source.

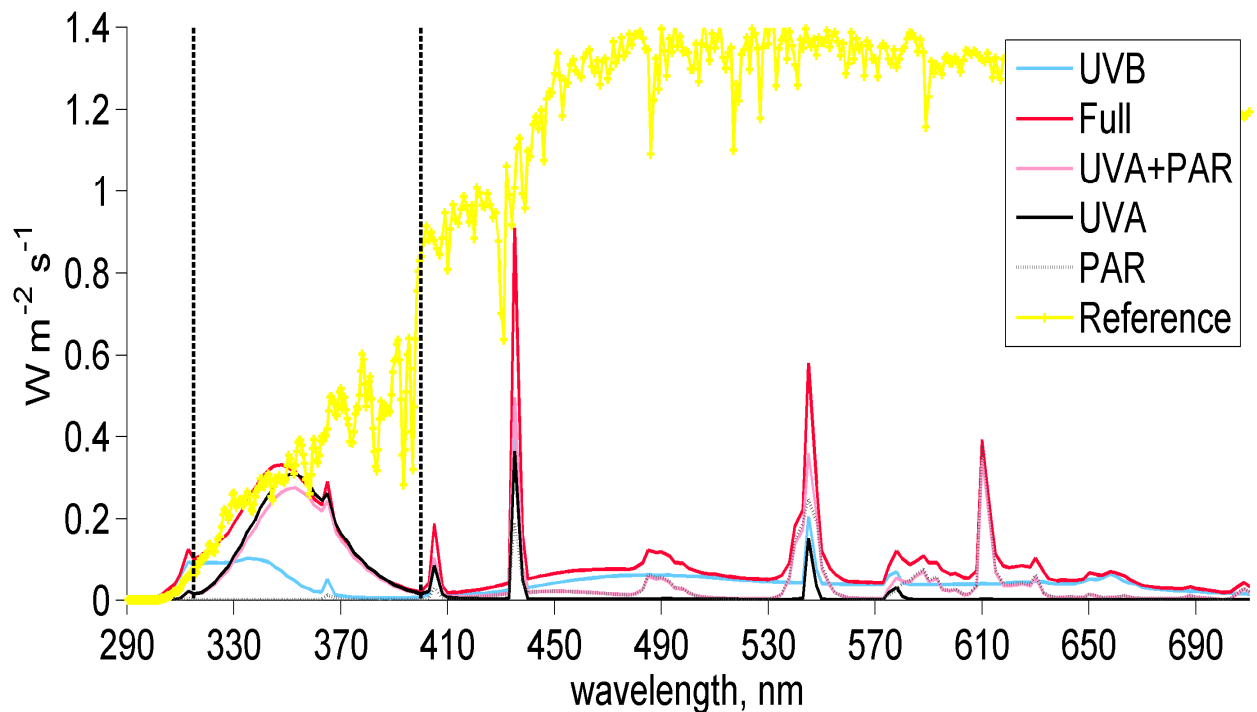


Figure 5.03. Light spectrum fluxes from 290 nm to 710 nm. Vertical dashed lines indicate the starting wavelength for the UVA and PAR wavelengths.

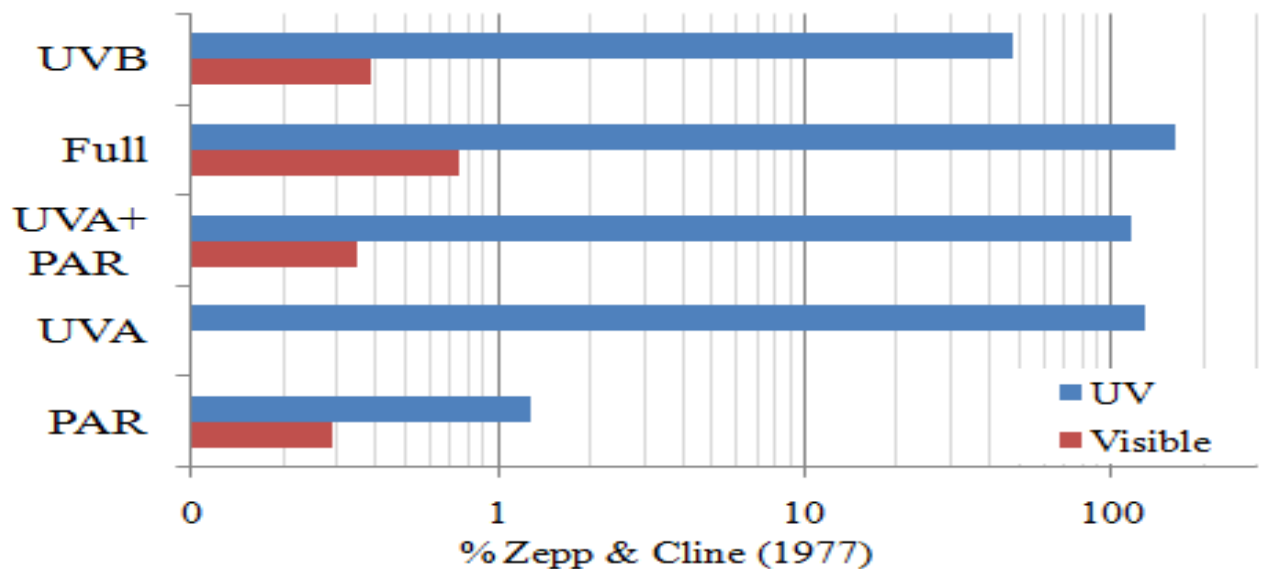


Figure 5.04. Percentage comparison of experiment irradiating regimes (y-axis) for both UV-R (blue) and visible (red) light produced by these regimes to modelled 40°N spring noon values from Zepp and Cline (1977).

5.01.05 Fe(II) Half Life

As the experimental work was carried out in quartz glass an assessment was made of the half life of Fe(II) in a pure water (Figure 5.05). The half life measurement would allow for an understanding of Fe(II) loss within the experimental environment, they were conducted using UPW buffered to pH 7.4 and 8 using 0.1 M NaHCO₃ with small volume additions (< 10 μ L) of Fe(II) held in 2.5 M quartz distilled HCl. The aim was to measure the rate of loss of Fe(II) which would include sorption to and reduction at the surface of the quartz glass and reduction in solution in an oxygenated, particulate free water at the pH of seawater. Figure 5.05 shows the loss of Fe(II) at both pH 7.4 and pH 8, additions were of 226 and 107 nM Fe(II) respectively. The calculated half lives are 824 s ($k = -8.4 \times 10^5 \text{ M}^{-1} \text{ s}^{-1}$, pH 7.4) and 138 s ($k = -5.02 \times 10^6 \text{ M}^{-1} \text{ s}^{-1}$, pH 8), the kinetic rates were calculated as per Millero et al. (1987) and are in good agreement with Millero et al. (1987); Fe(II) half-life at 25 °C and pH 8, 2 mins. What is shown, as expected, is that the half-life of Fe(II) decreases as pH increases and that the FIA-Cl is capable of measuring Fe(II) oxidation from within the experimental environment.

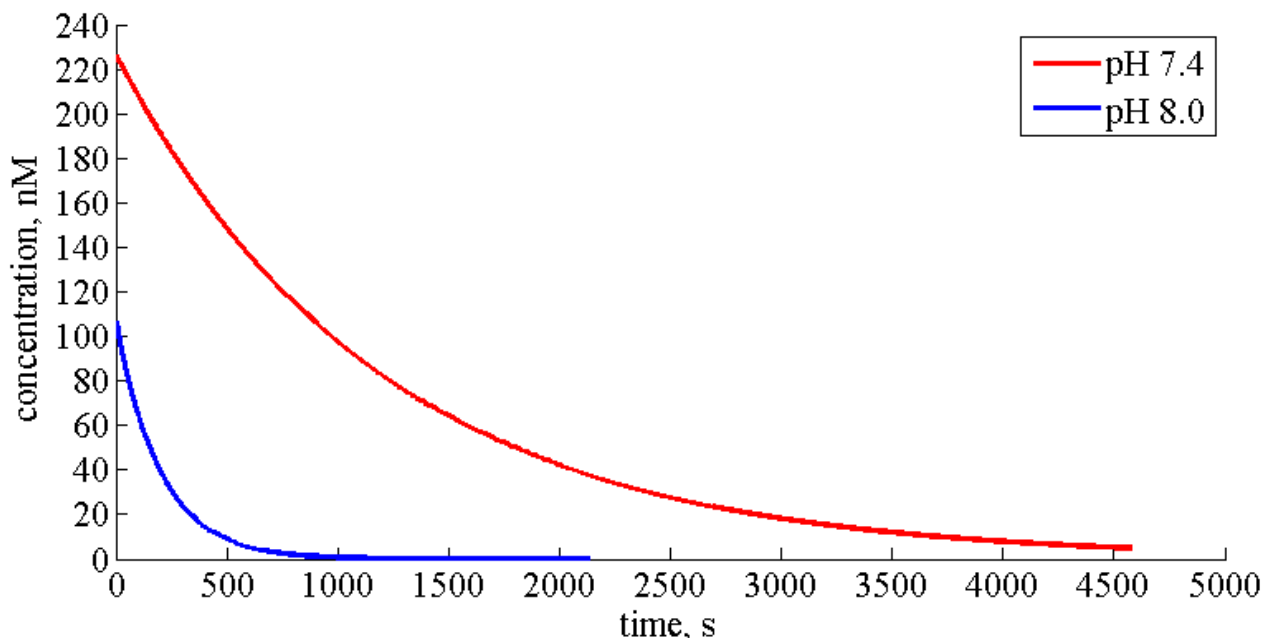


Figure 5.05. Fe(II) oxidation and sorption on to quartz glass at pH 7.4 and 8, (Laboratory lights on). The plot assumes luminol chemiluminescence linearity to Fe(II). King et al. (1995) plumbing was used to enable a continuous mixing of sample and reagent in the flow cell.

5.02 Experiments

The addition of the particulate phase was carried out for two reasons: The first was to assess the effect an addition of particulates has on a sea-surface microlayer system containing photochemically produced H_2O_2 and Fe(II). The second was to measure over a short-term the photochemical production (if any) of reduced iron and manganese from the particulate. Within each experiment there are three phases, the first is the dark phase and lasts for 600 s; this phase of the experiment is only represented by a single point and corresponds to the mean value for the phase or the LOD which ever is higher. The further two phases are the light phase where there is a constant illumination of the sea-surface microlayer analogous medium followed by the third phase, termed the particulate phase, where there is an addition of the particulates to the medium whilst undergoing continued illumination.

The following experiments are in two sets; the first uses phytoplankton exudate, NMO as the initiator source of reactive oxygen species which subsequently act in the redox cycling of iron and manganese. The second set uses humic acid as the initiating source. Experiments were carried out in two repeats. These may not be identical replicates because: i) There may be a change occurring in the organic material through aging in the NMO experiments; ii) experiments were mixed independently so will not be precisely the same and finally, iii) the addition of the particulate phases were not the same on each occasion.

The experimental design for this and the following set of experiments was not rigidly governed with respect to the addition of the particulates but was adaptive based on the results of the preceding experiments. The use of up to three particulates simultaneously was intentional as in an environmental context the deposition of a single element particulate would likely be judged a rare event. Concentrations of specific particulates were to be increased / decreased dependant on the production of reduced iron or manganese from the particulate phase. Using known photo-reducible particulate phases of iron and manganese was required to show that the analytical system and experimental time frame were capable of measuring this photo-reduction should it occur. The inclusion of an aluminium particulate phase was of a purely inquisitive nature and follows from the argument that the majority of atmospheric deposition is as aluminosilicate minerals (Jickells and Spokes, 2001) and therefore the majority of deposition to the sea-surface microlayer would contain aluminium. The changes in the concentration of the NMO was initially planned to cover three incremental increases in the concentration of the *Fragilariopsis cylindrus* NMO but was altered to include a mixed NMO due to limited availability of the *Fragilariopsis cylindrus* NMO. As with the NMO the concentrations of

humic acid used was also set to provide results through which changes could be contrasted based on increasing concentrations of humic acids; what was not initially factored in was the change in pH caused by the use of freshly prepared humic acid stock.

5.02.01 Set 1, NMO Experiments

Table 5.01 shows the particulate additions to the NMO experiments and provides the respective LOD for Fe(II) and H₂O₂. The LOD are calculated as 3 x σ of the zero concentration standard. In table 5.01 the Fe(II) LOD range over 2 orders of magnitude, 0.024 – 1.4 nM, with a mean of 0.6 nM. One reason for this was the organic material within the experimental media. Organic material can suppress the signal attributed to Fe(II) though this is consistent across all Fe(II) concentrations (O'Sullivan et al., 1995; Rose and Waite, 2001) and therefore the sensitivity of the PMT needs to be increased with the subsequent affect of increasing base line noise and decreasing reproducibility. Conversely if the PMT sensitivity is too low then the reproducibility increases as the base line stability increases though the actual sensitivity towards the chemiluminescence signal decreases. The base medium of 0.2 μ m filtered North Sea seawater had additions of three NMO organics; these were:

- 4.4 % v/v 0.2 μ m filtered *Fragilariaopsis cylindrus* (iron limited culture)
- 8.8 % v/v 0.2 μ m filtered *Fragilariaopsis cylindrus* (iron limited culture)
- 8.8 % v/v (combined in equal parts) 0.2 μ m filtered *Fragilariaopsis cylindrus* (iron limited culture) and 0.2 μ m filtered *Thalassiosira pseudonana*.

Table 5.01. Particulates and LOD for NMO experiments

Medium	experiment reference	Metal			total particulate	LOD	
		FERR50	MnO _{1.9}	Al(OH) ₃		Fe(II)	H ₂ O ₂
		nM	nM	nM		mg L ⁻¹	nM
0.2 μ m filtered North Sea seawater	sw-1	1000	80	200	49.5	0.27	12.1
	sw-2	100	80	200	18.8	0.34	15
4.4 % v/v <i>Fragilariaopsis cylindrus</i>	Fc4.4-1	100			4.7	1.4	2.9
	Fc4.4-2	100			4.7	0.34	0.4
8.8 % v/v <i>Fragilariaopsis cylindrus</i>	Fc8.8-1	1000	100		27.9	0.68	14.2
	Fc8.8-2	1000	100		27.9	0.024	3.9
4.4 % v/v <i>Fragilariaopsis</i> & 4.4 % v/v <i>Thalassiosira</i>	mx8.8-1	10000	80		23	0.68	14
	mx8.8-2	10000	80		23	0.75	0.69

During the experiments the pH and temperature were monitored (Figure 5.06). The pH in this set of experiments was generally stable in the light phase ± 0.02 units. The largest changes in pH following addition of the particulates was in the mixed NMO experiments (± 0.04 units following an addition containing 10000 nM FERR50) and in the seawater only experiment, sw-1, (+ 0.04 units following an addition containing Al(OH)_3). The mean starting pH for the experiments was 8.31 ± 0.05 . Initial starting temperatures were 28.9 ± 0.4 °C. *Fragilaropsis* only experiments show a linear temperature increase of ~ 1.5 °C and ~ 0.7 °C for both of the 4.4 % and 8.8% experiments, respectively. The seawater only experiments show linear changes of + 0.5 °C and - 0.5 °C for sw-1 and sw-2 respectively. Based on the temperatures and using the oxygen solubility calculation of Weiss (1970) the initial average oxygen concentration for these experiments was $194.2 \mu\text{M kg}^{-1}$.

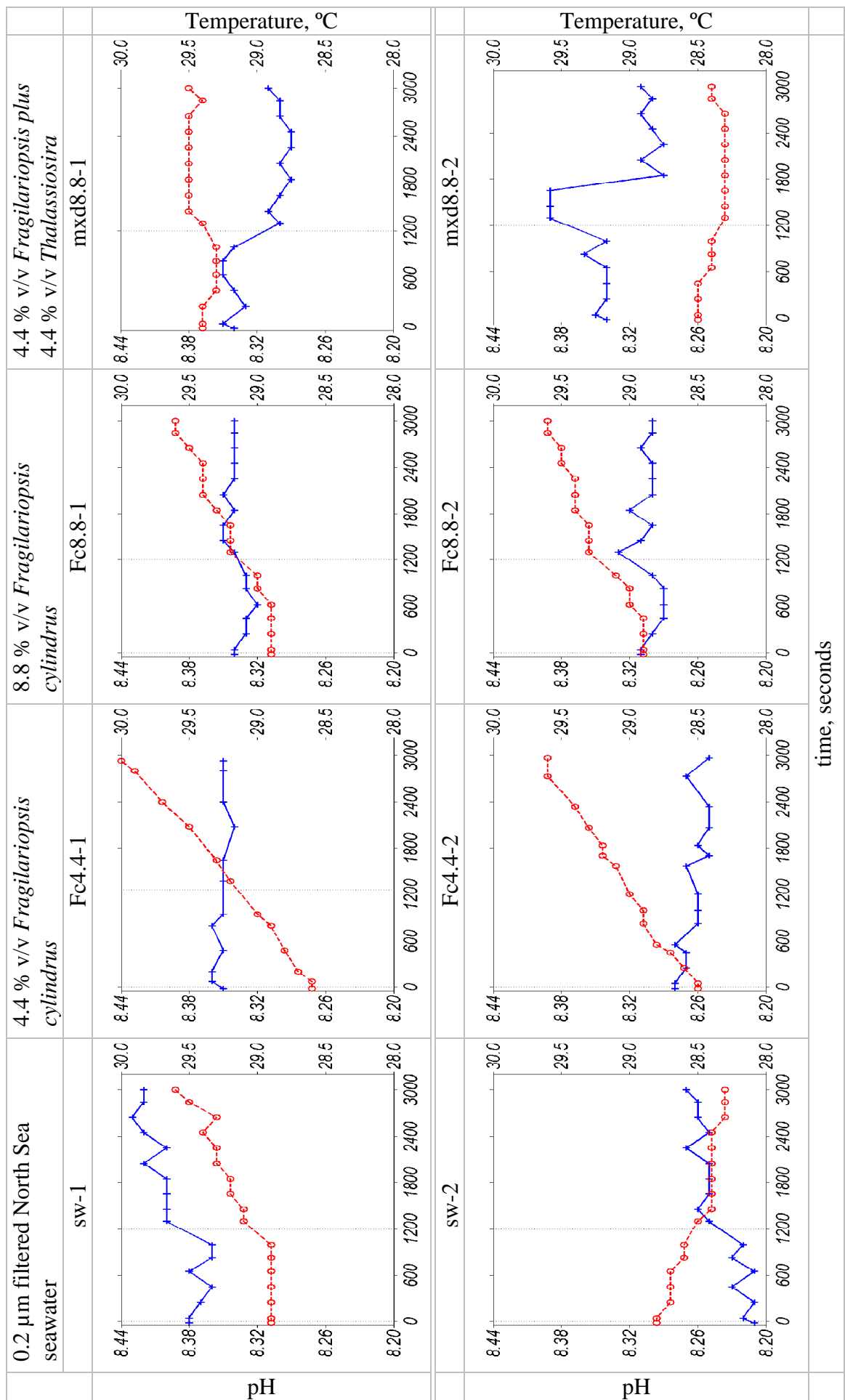


Figure 5.06. pH (blue line with +) and temperature (red line with o) change for NMO experiments. Zero seconds is the point of illumination; the vertical grey line corresponds to the injection of particulates (Table 5.01).

5.02.02 NMO Results – Light Phase

The results for Fe(II), H₂O₂ and Mn(II) in the experiments with NMO are presented in Figures 5.07 to 5.09, respectively. The experiments were expected to have low concentrations of reduced iron as both the base medium and *Thalassiosira* NMO had been aged in the dark (c. 4 months) and the *Fragilaropsis* was grown under iron limited conditions.

Fe(II) Light Phase

In the light phase (Figure 5.07), five systems had measurable amounts of Fe(II); two of these, Fc4.4-2 and Fc8.8-2 NMO experiments show a steady state in place. The mixed organic experiment, mxd8.8-2, shows an increase of ~ 1 nM whereas Fc8.8-1 from the single NMO experiments shows a decrease of ~ 1 nM, though this is primarily due to two sudden losses in concentration occurring at c. 300 and 900 s into the light phase. Experiment, mxd8.8-1, has a sudden increase of ~ 3 nM occurring at 900 s into the light phase with its subsequent loss to beneath the LOD (0.75 nM) over the following c. 170 s. Within the NMO experiment, Fc8.8-2, the signal for both Fe(II) and H₂O₂ suddenly decreases before the addition of the particulates, this was attributed to the PMT and not an artefact of the chemistry due to the magnitude and direction of change and its simultaneous occurrence in both analytes. Except for Fc4.4-1 (Fe(II) LOD 1.4 nM) all other experiments had Fe(II) LOD < 0.75 nM (Table 5.01), the second 4.4 % NMO experiment, Fc4.4-2, with a LOD of 0.34 nM shows that there are large variations in concentration occurring for the Fe(II), which were not seen with the higher LOD. No significant change to the Fe(II) occurred within the light phase of the seawater only experiments. Though sw-1 does show a sudden increase of ~ 1.5 nM at c. 1100 s there are no following points to indicate an oxidation of this Fe(II), suggesting that this sudden increase may not be caused by Fe(II). There is an increase in Fe(II) at the beginning of the light phase in sw-2, the change of concentration is approximately 0.05 nM indicating that only a small potential reducible iron is present in the base medium.

H₂O₂ Light Phase

The light phases (Figure 5.08) of the seawater only experiments show different forms; sw-1 has slowing H₂O₂ production through three stages, sw-2 has a monotonic increase throughout the light phase. The experiments with added NMO generally show a two-stage production in their light phases, with the second production stage slower than the first. H₂O₂ production in the 4.4 % NMO experiments is 4 times higher in Fc4.4-1 than in Fc4.4-2; total

H_2O_2 production (10 nM) in Fc4.4-2 is low relative to all other experiments. Production in the 8.8 % NMO experiments are similar, though the length of time in stage 1 increases from F8.8-1 to Fc8.8-2, approximately 100 nM production over c. 200 and 400 s respectively in stage 1 and approximately 25 nM production in stage 2 for both experiments. In the mixed experiments, the first stage, comparing between mxd8.8-1 and mxd8.8-2, net production decreases from 60 to 40 nM, whilst in their second stages both experiments shows an increase of around 25 nM. H_2O_2 LODs were in the range 0.4 – 15 nM, the seawater only experiments had LODs of 12 and 15 nM whilst those with added NMO had lower LOD, this was expected as organic material has been shown to suppress luminol chemiluminescence (O'Sullivan et al., 1995). Within the NMO experiments the first experiments always had higher LODs ($> \times 4$) than the second experiment (Table 5.01).

Mn(II) Light Phase

Mn(II) light phase results are given in Figure 5.09. Following ICP-MS analysis through the standard addition method there is an uncertainty on the calculation of the concentration due to the fit of the calibration, this uncertainty was applied to all measurements. For all experiments the changes were greater than this error except for the NMO experiment Fc4.4-2. The 0.2 μm filtered manganese \approx total soluble Mn(II) (Stone and Morgan, 1984) concentrations are relatively stable through the light phase. The results do not indicate that there is either a consistent production or loss of Mn(II) in this phase. In Fc8.8-1 and mxd8.8-1 there were small decreases of 5 nM in the light phase, whilst Fc8.8-2 and mxd8.8-2 had slight increases of 7 and 6 nM, respectively. The LOD for manganese analysis from the ICP-MS was 1.3 nM. For the seawater only and 4.4 % NMO experiments, changes were close to or less than the LOD.

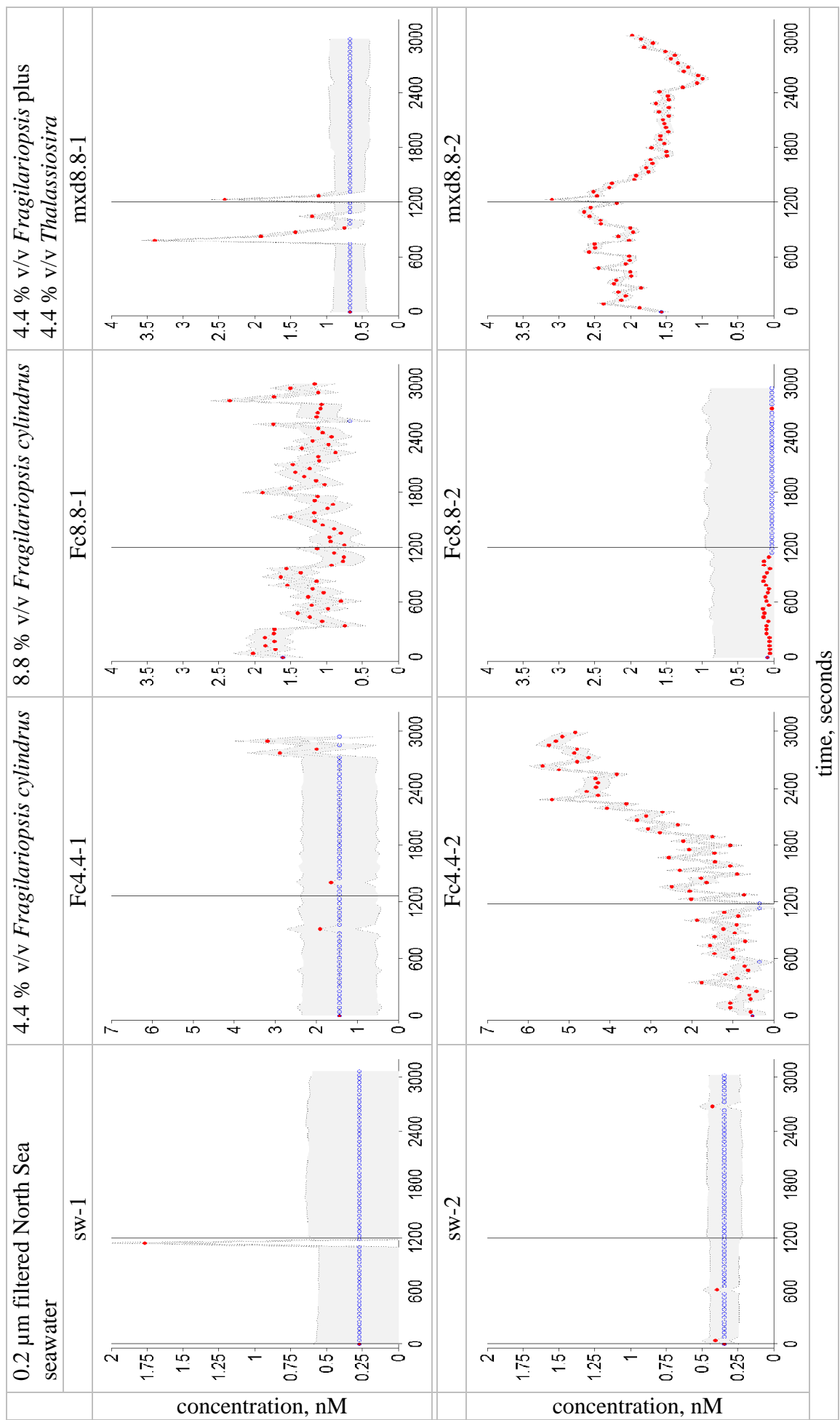


Figure 5.07. Fe(II) traces from NMO experiments. Zero seconds corresponds to the injection of particulates (Table 5.01). Red points are data within the calibration range whereas blue points are those outside of the calibration range ($<\text{LOD}$ or $>\text{concentration highest standard}$). All values have a calculated error this: is represented as a light grey envelope around the data.

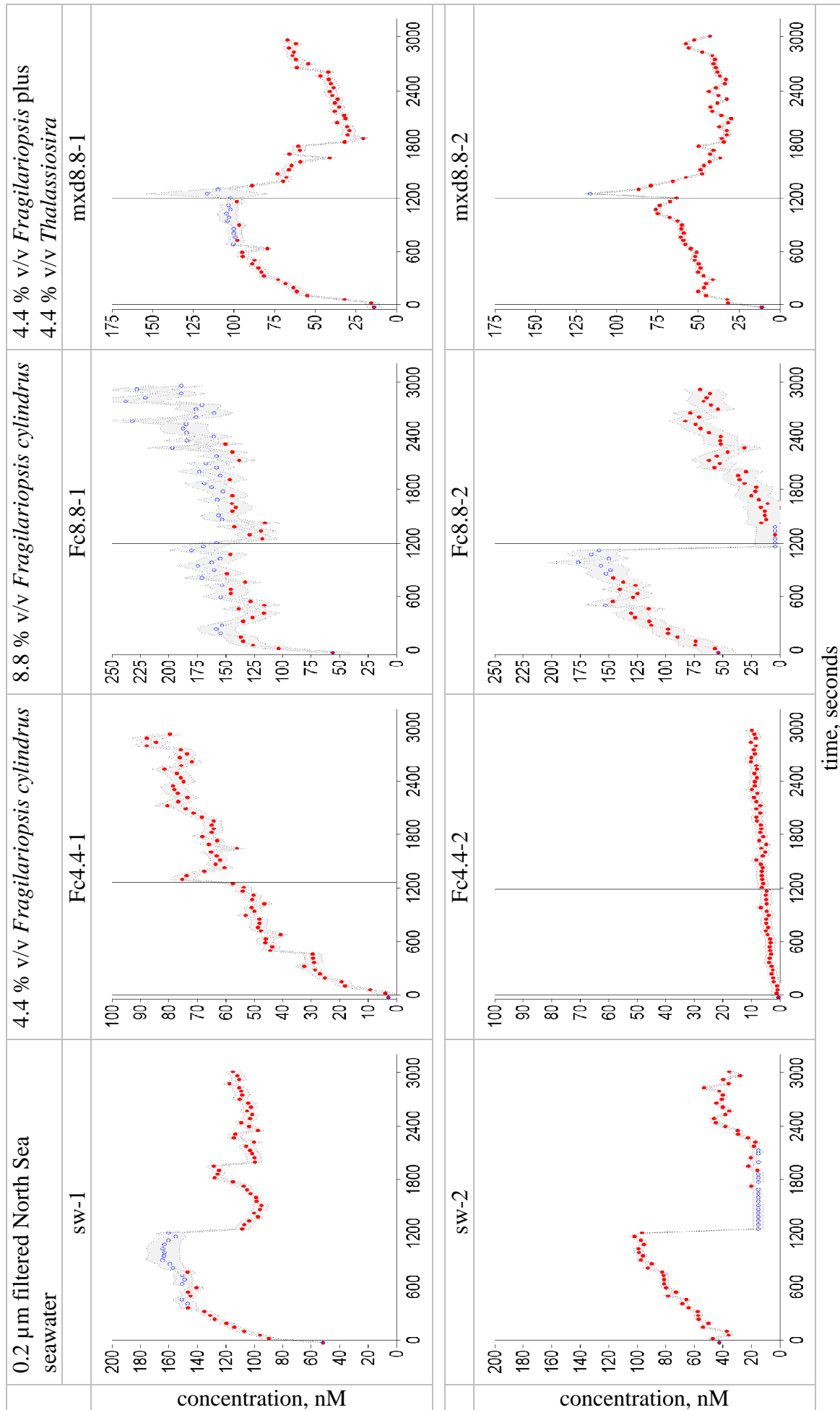


Figure 5.08. H_2O_2 traces from NMO experiments. Zero seconds corresponds to point of illumination; the vertical grey line corresponds to the injection of particulates (Table 5.01). Red points are data within the calibration range whereas blue points are those outside of the calibration range (<LOD or >concentration highest standard). All values have a calculated error this; is represented as a light grey envelope around the data.

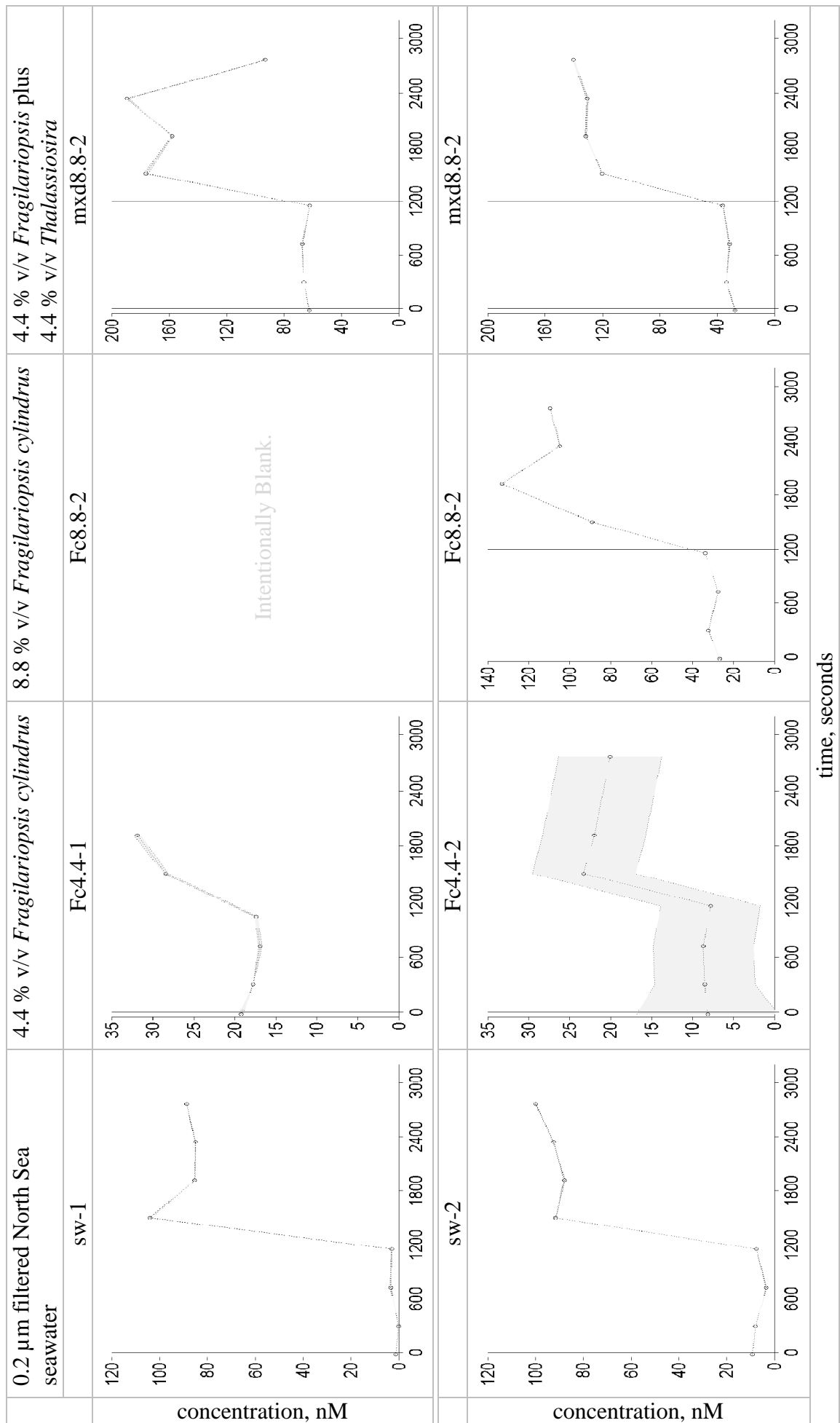


Figure 5.09. Mn(II) traces from NMO experiments. Zero seconds corresponds to the injection of particulates (Table 5.01). All values have a calculated error this is represented as a light grey envelope around the data.

5.02.03 NMO Results – Particulate Phase

The particulate phases are introduced in order of increasing concentrations of FERR50, 100, 1000, 10000 nM and end with the particulate phase which included the aluminium component. This order refers to: 4.4 % v/v *Fragilariopsis cylindrus* (Fc4.4-1 and Fc4.4-2), 8.8 % v/v *Fragilariopsis cylindrus* (Fc8.8-1 and Fc8.8-2), 8.8 % v/v mixed in equal parts *Fragilariopsis* and *Thalassiosira* (mxd8.8-1 and mxd8.8-2), and the seawater only experiments (sw-1 and sw-2). Concentrations were taken up to 10000 nM to see if the elevated concentrations could force the system to show a reduction from the particulate phase to the soluble phase of either Fe(II) or Mn(II).

100 nM FERR50

The 4.4 % v/v *Fragilariopsis cylindrus* experiments had 100 nM FERR50 added to a total of 4.7 mg L⁻¹ particulate phase. The nano-molar concentration addition is inline with that used by Rose and Waite (2006) and Spokes and Liss (1995). The Fe(II) (Figure 5.07) in Fc4.4-2 is the only system to show an increase in its Fe(II) concentration following a particulate addition. The reason for this would be a photochemical ligand to metal charge transfer (LMCT) between sorbed organic material and the FERR50 particulate phase (Waite and Morel, 1984). This indicates that with low H₂O₂ concentrations (< 10 nM) there are measurable values of Fe(II) produced through this photochemical mechanism.

Following particulate injection there is an initial spike in H₂O₂ in Fc4.4-1. Both experiments, Fc4.4-1 and Fc4.4-2, then show a monotonic increase in H₂O₂ at similar rates to that prior to injection. The differences in the total production of H₂O₂, Fc4.4-1 to Fc4.4-2, suggests that the production of Fe(II) is dependant on the photochemistry occurring prior to the addition. Mn(II) shows an increasing production of 11 and 15 nM respectively for Fc4.4-1 and Fc4.4-2. The rapid increase in Mn(II) may suggest that there is either an addition of Mn(II) include within the FERR50 or that within the particulate phase there are reduced metals. Reduced metals, for example Fe(II) when they come into inner sphere contact with oxidised manganese undergo an electron transfer to the manganese leading to its reduction (Scott, 1991; Villinski et al., 2003) with the subsequent oxidation of the donor metal. If this is occurring then this mechanism is slower than the photochemical reduction of iron under low H₂O₂ concentrations indicated by the production of Fe(II) in Fc4.4-2.

1000 nM FERR50

The 8.8 % v/v *Fragilariaopsis cylindrus* had 1000 nM FERR50 and 100 nM MnO_{1.9} to a total particulate concentration of 27.9 mg L⁻¹. The Fe(III) phase is at the maximum concentration used by Rose and Waite (2006) but five times less than that used by Kuma et al. (1992). The manganese concentrations are in line with those of Spokes and Liss (1995) who used 140 nM (with 0.7 nM as radio labelled) and Sunda et al. (1983) who used 10⁻⁸ M concentrations (100 % radio labelled). In Fc8.8-1 there is no apparent direction in the Fe(II) trace due to the large amount of noise in the signal, \pm 0.5 nM. Following injection of particulates there is a decrease in the H₂O₂ concentration prior to it returning to a similar production rate prior to injection. In Fc8.8-2, even with the drop in signal prior to injection, following injection there follows a production of H₂O₂ at a similar rate to that prior to injection. Except for the initial loss of H₂O₂ following addition of the particulates the production rates for H₂O₂ do not change, indicating that over the course of the experiment there is no lasting effect on the photochemical production of H₂O₂.

With 100 nM MnO_{1.9} added there is an initial increase of 35 and then in total 100 nM Mn(II) to the system. Spokes and Liss (1995) and Sunda et al. (1983) following radio labelled isotope work measured photochemical reductions of MnO_{1.9} to Mn(II) in the region of ~20% in 6 hrs, with less than 5 % production occurring in the first hour using natural marine humic acids (Sunda et al., 1983). A 100 % reduction of MnO_{1.9} in the short analytical period, c. 7 minutes therefore seems potentially unlikely. Mn(II) may be present in the FERR50 addition, from the 100 nM FERR50 additions this may be ~13 nM Mn(II) per addition of 100 nM FERR50 though this is unlikely as the specified concentration of Mn within the FeCl₃.6H₂O is \leq 0.1 %. The remaining mechanism for the rapid increase in Mn(II) would be the reductive dissolution of MnO_{1.9} (Scott, 1991; Villinski et al., 2003). With Mn (II) in solution its oxidation will occur, however, its kinetics with oxygen are slow in seawater (Horst and Zabel, 1996; Stone and Morgan, 1984). The extent of this experiment do not allow for a suggestion of oxidation occurring.

10000 nM FERR50

The 8.8 % v/v combined *Fragilariaopsis* and *Thalassiosira* NMO had an addition of 10000 nM Fe (III) and 80 nM MnO_{1.9} to 23 mg L⁻¹. On injection, both mxd8.8-1 and mxd8.8-2 show a sudden increase in Fe(II), 1.7 and 1 nM, respectively. That this increase could be due to residual Fe(II) within the FERR50 cannot be ruled out, the specified Fe(II) content of the

$\text{FeCl}_3 \cdot 6\text{H}_2\text{O}$ is 0.002% which equates to 0.2 nM but the effective change to the concentration of Fe(II) in the FERR50 following processing was unmeasured. In mxd8.8-1 the concentration of Fe(II) then falls to below the LOD, 0.68 nM. In mxd8.8-2 there is a loss of Fe(II) for the following c. 800 s, which is set against the gradual production seen in the light phase. The H_2O_2 also shows a sudden increase in production of ~ 12 and 50 nM for mxd8.8-1 and mxd8.8-2, respectively. Following the sudden increase there is a reduction in H_2O_2 concentration for both experiments over the next c. 800 s. This reduction was also seen in the NMO experiment Fc8.8-1, though not to the same extent. H_2O_2 and Fe(II) follow similar trends in mxd8.8-2 suggesting that there is a link between their net losses. With a decrease in H_2O_2 to around 25 nM in both mixed organic experiments there then follows a net production of H_2O_2 for the remainder of the experiment. With a decrease in H_2O_2 the remaining primary Fe(II) oxidants are oxygen, and superoxide and hydroxide radicals. One or more of these is therefore in excess and acting to oxidise the Fe(II).

FERR50 with 80 nM $\text{MnO}_{1.9}$ and 200 nM Al(OH)_3

Only one set of experiments had aluminium included in the particulate phase addition, these were the 0.2 μm filtered North Sea seawater only systems. The H_2O_2 traces react singularly to the particulate phase with a sudden decrease in concentration in both experiments, sw-1 and sw-2. The only difference between these experiments and those with NMO was the inclusion of the aluminium in the particulate addition. The two seawater experiments had different total concentrations of particulates added, 49.5 and 18.8 mg L^{-1} for sw-1 and sw-2 respectively. Due to the order of magnitude difference in the FERR50 concentrations (sw-1 1000 nM and sw-2 100 nM) the difference in the results cannot be due purely to the concentrations of the particulates. Al(OH)_3 is stable at the experimental pH and not photochemically active. However, there is the possibility, as seen with the manganese particulate phase, that there was a change on combining the aluminium to an acidic FERR50 (pH 5.4), and this resulted in an ionisation of the Al(OH)_3 to Al(OH)_2^+ (Baes and Mesmer, 1976; Williams and Frausto da Silva, 1996). This will then lend itself to the idea that during the hydrolysis of the aluminium, Fe(II) will be scavenged into the aluminium hydroxide matrix (Bertsch et al., 1989). This then removes a production mechanism from within the catalysed dismutation of O_2^\bullet and through the formation of the aluminium particulate phase the increased surface area will increase the rate of catalytic decomposition of H_2O_2 leading to the sudden decrease in H_2O_2 .

5.02.04 Set 2, Humic Acid Experiments

The following set of results compares between different concentrations of humic acid, 0.5 and 2.0 mg L⁻¹, combined into 0.2 µm filtered North Sea seawater. The humic acid experiments are not directly comparable as they have a different pH; 2.0 mg L⁻¹ is at ~ pH 7.4 and 0.5 mg L⁻¹ is at pH 8.1. The difference in the pH from the 2.0 to the 0.5 mg L⁻¹ humic acid experiments was due to the use of a freshly prepared humic acid stock in the 2.0 mg L⁻¹ humic acid experiment, and the length of time that the medium was left to equilibrate. The 0.5 mg L⁻¹ humic acid experiment was given time (18-24 hrs) to buffer itself following the addition. A freshly prepared stock was used to spike seawater to 2.0 mg L⁻¹, the stock was added 2 hours before the experiment, this decreased the pH to 7.4, whereas an aged (24 hours) stock was used to spike the seawater in the 0.5 mg L⁻¹ experiments, 18 – 24 hours before the experiment, leading to a decrease of approximately 0.2 pH units.

The experiment sets, 0.5 and 2.0 mg L⁻¹ humic acid also have a difference in the time of injection of the particulates. The point of injection into the experiment increased from 1200 s to 2220 s (post illumination) for the 2.0 mg L⁻¹ humic acid experiments. The later point of injection was to allow the H₂O₂ and Fe(II) systems to represent the direction of their net production / loss in the light stage or attain a steady-state. The particulates used for the humic acid experiments are given in Table 5.02. The pH (Figure 5.10) was relatively stable over the first c. 1200 s for all experiments, then it increased by ~ 0.15 units for the first two experiments in both sets, whilst in the third experiment of the 0.5 mg L⁻¹ set it increased by around 0.5 units. The changes in pH are around four times greater than in the NMO experiments and all show an increase in the pH suggesting that the photolysis of the humic acid over the course of the experiments may act to increase the pH. Temperature changes (Figure 5.10) during the light stage for the experiments were in the range ± 0.3 °C except for the first 2.0 mg L⁻¹ humic acid experiment, which had a change of - 0.6 °C. Over the particulate phase, temperatures increased by 0.5 °C for the first and third experiments in the 0.5 mg L⁻¹ set whilst the other experiments were relatively stable. The average starting temperature for these experiments was 28 ± 0.7 °C, (n = 5) giving an approximate initial oxygen concentration of 197 µM kg⁻¹.

LODs (Table 5.02) for the 0.5 mg L^{-1} humic acid experiments are around 0.09 and 10 nM for Fe(II) and H_2O_2 , respectively. For the lower pH, higher concentration humic acid experiments the LODs is $\sim 0.28 \text{ nM}$ for the Fe(II) whilst for the H_2O_2 there is a large difference between the two experiments. The first 2.0 mg L^{-1} humic acid experiment has a high LOD as the PMT sensitivity was increased to compensate for the suppression of signal caused by the increased concentration of organics.

Table 5.02. Particulates and LOD for humic acid experiments.

0.2 μm filtered North Sea seawater plus ...	experiment reference	metal		total particulate	LOD	
		FERR50	$\text{MnO}_{1.9}$		Fe(II)	H_2O_2
		nM	nM	mg L^{-1}	nM	nM
0.5 mg L^{-1} Humic acid	HA0.5-1			90	5.2	0.12
	HA0.5-2	100			6.6	0.05
	HA0.5-3	400	300	22.4	0.11	10
2.0 mg L^{-1} Humic acid	HA2.0-1	500	300	24.8	0.3	34
	HA2.0-2	100	300	12	0.26	1.5

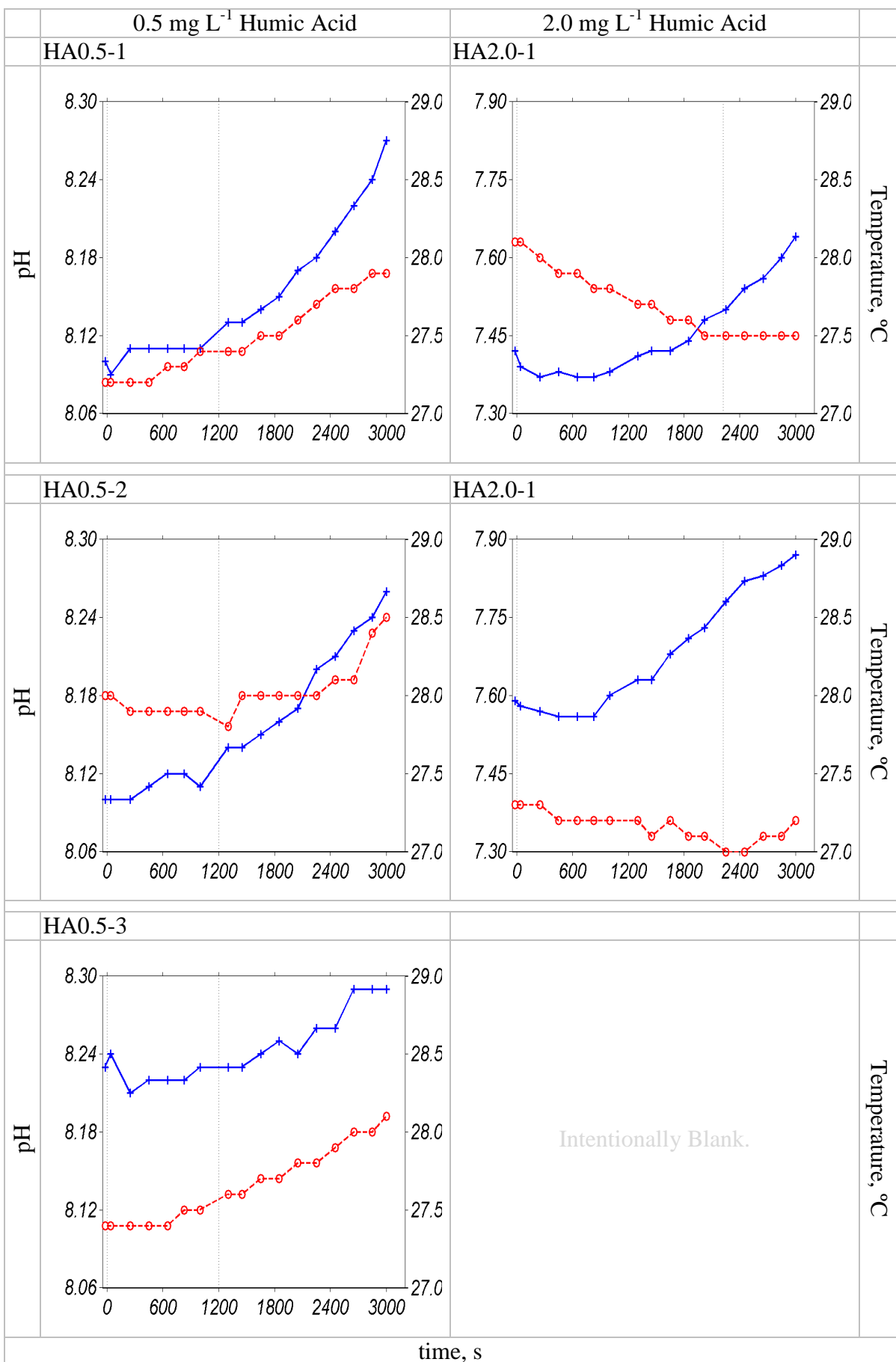


Figure 5.10. pH (blue line with $+$) and temperature (red line with \circ) change for humic acid experiments. Zero seconds corresponds to point of illumination; the vertical grey line corresponds to the injection of particulates (Table 5.02).

5.02.05 Humic Acid Results – Light Phase

Fe(II) Light Phase

Both humic acid systems showed a production of Fe(II) during the light phase, Figure 5.11. That there is Fe(II) production is consistent with the presence of high concentrations of photosensitive carboxylate/iron complexes found in humic substances (Averett et al., 1989), with these able to directly reduce $\text{Fe}(\text{OH})_2^+$ to Fe(II) (Skogerboe and Wilson, 1981). The Fe(II) traces have three stages, an initial stage showing a rapid production, $\sim 1 \text{ nM}$ for all 0.5 mg L^{-1} experiments over the first 300 s. For the 2.0 mg L^{-1} system the initial production of Fe(II) is also over c. 300 s and the concentration increases are approximately 4 and 2 nM for the first and second experiments. The second stage is a quasi steady-state Fe(II) concentration; this is longer in the first experiment than in the second and third 0.5 mg L^{-1} experiments. The ending of the second stage in the 2.0 mg L^{-1} experiments is indicated by a sudden loss of Fe(II) before the system enters a continuous, linear loss of Fe(II).

H_2O_2 Light Phase

As with the previous set of experiments containing NMO (Figure 5.08) the H_2O_2 traces in the humic acid experiments (Figure 5.12) show a two stage production. There is an initial rapid net production (first 300 – 400 s) which then tends to a slower net production. In the longer light phase of the 2.0 mg L^{-1} experiments both experiments show a loss in the concentration of H_2O_2 c. 1200 – 1800 s after illumination, this is more pronounced in the second experiment. The loss in H_2O_2 is seen for the first time, due to the point of particulate injection to this experiments occurring c. 1000 s later. A net loss for H_2O_2 indicates that the H_2O_2 sinks have increased or that the production mechanisms have decreased, or a combination of both.

Changes in concentration over time and concentrations achieved for H_2O_2 in the light phases of each set of NMO repeat experiments showed there were differences and these were probably due to the aging of the NMO. The light phase in the humic acid experiments show a repeatability in their H_2O_2 and Fe(II) traces. With respect to the H_2O_2 , the 0.5 mg L^{-1} humic acid, pH 8.1 experiments, over the first c. 400 s after illumination, all experiments have an increase in concentration of $92 \pm 7 \text{ nM}$ and then until the point of addition of the particulate phase a total increase in concentration of $118 \pm 1 \text{ nM}$. The 2.0 mg L^{-1} humic acid, pH 7.4 experiments, over the first 400 s has an increase in concentration of $121 \pm 5 \text{ nM}$ and up until the point of a net loss in production (transition point) an increase of $155 \pm 5 \text{ nM H}_2\text{O}_2$. Lengthening

the time between illumination and injection of the particulates has allowed the 2.0 mg L⁻¹ humic acid experiment to show a definite trend with respect to the changes in concentration of H₂O₂ and Fe(II). For the 2.0 mg L⁻¹ experiments this is a loss of H₂O₂ within the system, however this case may not be true for either the NMO experiments or the 0.5 mg L⁻¹ humic acid experiments. That these systems have yet to attain either a steady state or show that the system can tend towards a constant production / loss may have an unknown affect on the addition of the particulates as the underlying photochemical system is still in flux. Secondly, if the light phase of the experiment has not achieved a steady state (whether this is as a constant H₂O₂ production and steady-state Fe(II)) then potential model calculations of the system would be inherently flawed.

Mn(II) Light Phase

Mn(II) concentrations are stable throughout the light phase for all the humic acid experiments, with changes of generally \pm 2 nM, Figure 5.13. The one exception is the second experiment in the 0.5 mg L⁻¹ set; this has an increase of 7 nM in the first 5 minutes followed by a loss of 11 nM during the remaining light phase.

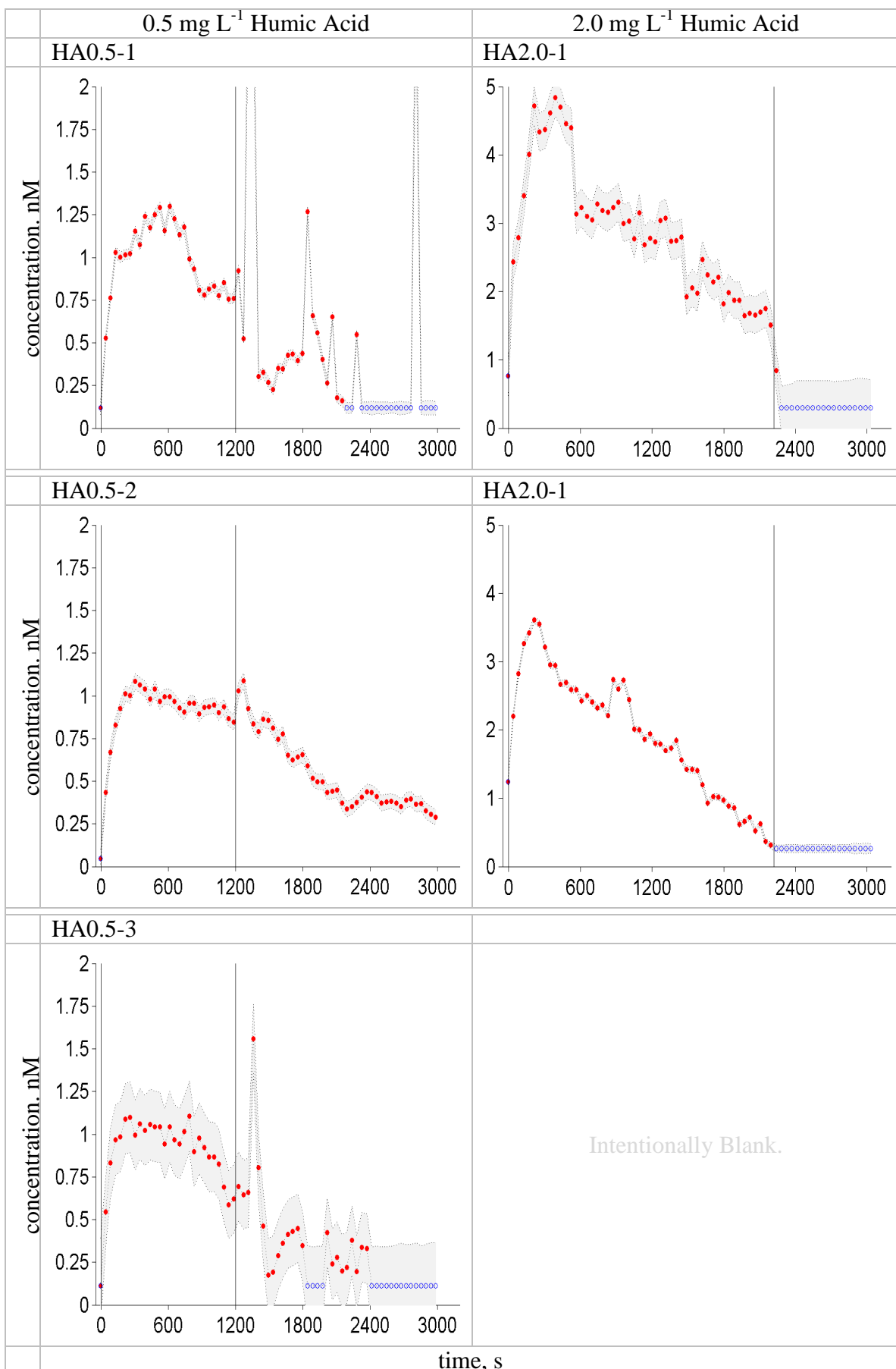


Figure 5.11. Fe(II) traces from humic acid experiments. Zero seconds corresponds to point of illumination; the vertical grey line corresponds to the injection of particulates (Table 5.02). Red points are data within the calibration range whereas blue points are those outside of the calibration range (<LOD or >concentration highest standard). All values have a calculated error; this is represented as a light grey envelope around the data.

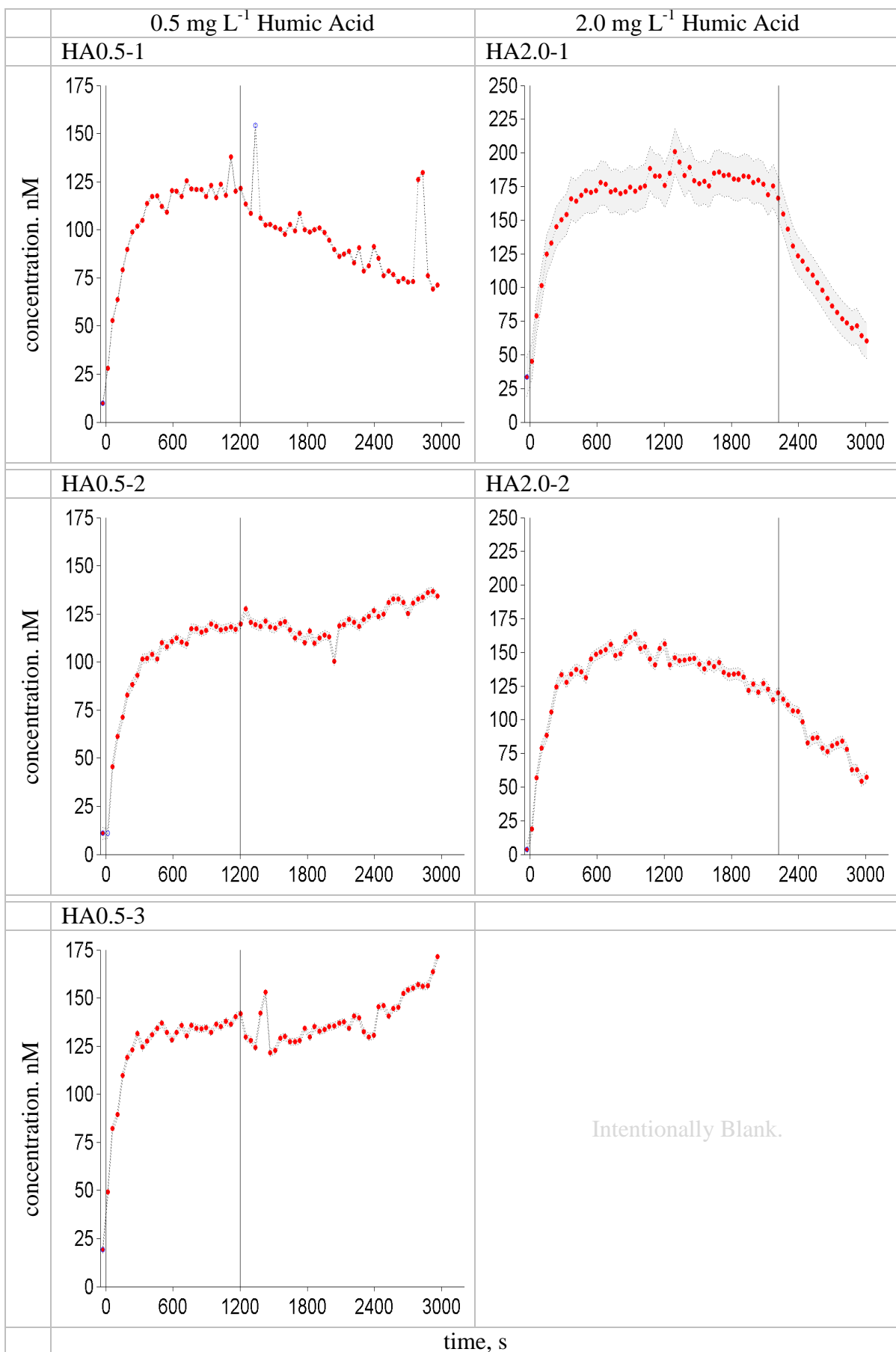


Figure 5.12. H₂O₂ traces from the Humic Acid experiments. Zero seconds corresponds to point of illumination; the vertical grey line corresponds to the injection of particulates (Table 5.02). All values have a calculated error; this is represented as a light grey envelope around the data.

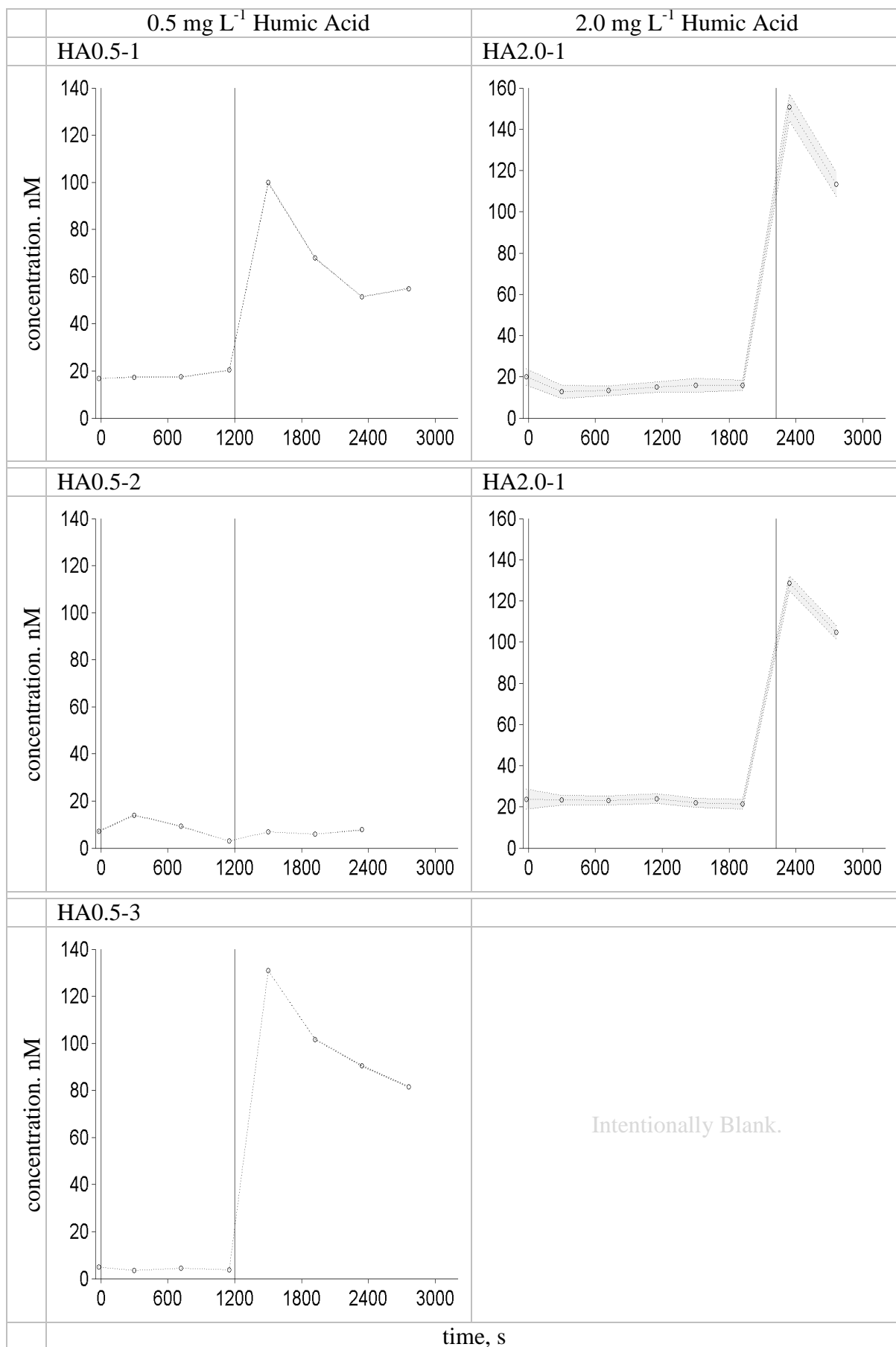


Figure 5.13. Mn(II) traces from humic acid experiments. Zero seconds corresponds to point of illumination; the vertical grey line corresponds to the injection of particulates (Table 5.01). All values have a calculated error; this is represented as a light grey envelope around the data.

5.02.06 Humic Acid Results – Particulate Phase

An initial aim of these experiments was to see, that on addition of an artificial particulate to an analogous photo-chemically active sea-surface microlayer a reduced soluble phase would be produced. From the experiments containing NMO it was noted that changes seen in the Fe(II) and H₂O₂ could also be due to changes in the organic material as it ages when in storage. Humic acid was then used for further experiments as the potential for this to alter during storage was lower and would provide a material that would allow for better reproducibility. Each of the five humic acid experiments also had a different particulate phase added (Table 5.02). In the NMO experiment, Fc4.4-2, there was iron photochemical reduction from the 100 nM addition of FERR50, therefore further FERR50 additions were kept with the range of 100 – 500 nM. Aluminium was not included in the particulate phase due to the effects seen on the H₂O₂ (seawater only experiments Figure 5.08) and its potential for removing Fe(II) from the experiment (Bertsch et al., 1989).

0.5 mg L⁻¹ Humic Acids with 90 nM MnO_{1.9}

On addition of particulates containing MnO_{1.9}, the NMO experiments had shown increases in the Mn (II) concentration (Figure 5.09) equal to and above the concentration of the manganese addition. Only HA0.5-1 (Figure 5.13), had an addition of purely MnO_{1.9}, this was to a concentration of 90 nM and a particulate concentration of 6.2 mg L⁻¹. The Mn (II) increased from the light phase concentration of 20 nM up to 100 nM Mn (II) post injection. Over the 1800 s of the particulate phase the Mn (II) concentration decreased by 50 nM, indicating oxidation of Mn (II). H₂O₂ (Figure 5.12) and Fe(II) (Figure 5.11) systems show a general net decrease in production, however, the Fe(II) is not a continuous loss from the system. The Fe(II) shows a sudden increase followed by a rapid loss which leads first into a single production and loss cycle before the concentration of Fe(II) falls beneath the LOD, 0.12 nM. This suggests that the addition of only MnO_{1.9} causes an uncoupling of the photochemical cycling of Fe(II) and H₂O₂ and this is linked to first the reduction of the MnO_{1.9} particulate phase and than its re-oxidation.

0.5 mg L⁻¹ Humic Acids with 100 nM Fe (III)

The second 0.5 mg L⁻¹ humic acid experiment had an addition of 100 nM Fe (III), total particulate concentration 5.2 mg L⁻¹. Directly after injection both the Fe(II) (Figure 5.11) and H₂O₂ (Figure 5.12) traces show a small increase in their net production above their respective

directions. From the NMO experiments Fc 4.4-1 (Figure 5.07) also with the same concentration of FERR50 added, had a small measurable increase in H₂O₂ though no change was measured in the Fe(II) for this experiment. Within the HA0.5-2 experiment at c. 2800 s there is a net increase in H₂O₂ production. At the same time, the Fe(II) appears to enter a steady-state. For excess H₂O₂ to be produced there is a requirement for the rate of O₂[•] dismutation to increase suggesting the experiment has reverted back to catalysed O₂[•] dismutation, or that a loss mechanism decreases, for example the removal of Fe(II) or other reduced metals by competing reactions. The Mn(II) post injection of particulates increases by 4 nM. For the 4.4 % NMO experiments with the same concentration of Fe(III) there was an increase in Mn(II) of approximately 13 nM. The concentrations of Fe(II) prior to injection of the FERR50 to 100 nM is approximately 0.8 nM in HA0.5-2 (Figure 5.11) and in the 4.4% NMO experiments (Figure 5.07) the Fe(II) is approximately 1 nM. The differences in H₂O₂ concentration are however larger, ~ 120 nM in the 0.5 mg L⁻¹ experiment compared to ~ 50 nM or less in the 4.4 % NMO experiments, the factor of two difference in the concentrations of H₂O₂ may then be the cause of the different increases in concentration of Mn(II) – the higher the H₂O₂ concentration prior to injection of the FERR50 the lower the production of Mn(II) from within the experimental medium.

0.5 mg L⁻¹ Humic Acids with 300 nM MnO_{1.9} and 400 nM Fe(III)

The third 0.5 mg L⁻¹ humic acid, HA0.5-3, experiment had a combined addition of 300 nM MnO_{1.9} and 400 nM FERR50 to a total concentration of 6.6 mg L⁻¹. Fe(II) is initially unchanged from the light phase before a sudden increase in concentration of ~ 1 nM, this is followed by, decreasing in concentration, production and loss cycles, before the Fe(II) concentration falls below the LOD, 0.11 nM. There is a net loss in the H₂O₂ for c. 300 s. Following this loss, the system then transitions into a net production. The changes in the H₂O₂ system may be attributed to both the manganese and FERR50. As HA0.5-1 indicated, the manganese particulate phase can produce a net loss in H₂O₂ and as HA0.5-2 indicated after c. 800 s there is a net production increase with FERR50. The net production increase would indicate the production mechanism, increased catalytic superoxide dismutation, for H₂O₂ is slower then the loss through reductive dissolution of the MnO_x and is more important over longer time scales.

2.0 mg L⁻¹ Humic Acids with 500 nM Fe(III) and 300 nM MnO_{1.9}

For the first 2.0 mg L⁻¹ humic acid experiment on addition of the particulate phase there is a drop in Fe(II) of ~ 1 nM within 88 s. All further measurements were beneath the LOD, 0.3 nM. The H₂O₂ shows a near linear decrease in concentration. Mn(II) concentrations increase from 16 to 151 nM, approximately 50% of the addition of MnO_x; some of this increase, ~ 37 nM is then oxidised in the following 5 minutes.

2.0 mg L⁻¹ Humic Acids with 100 nM Fe(III) and 300 nM MnO_{1.9}

The second 2.0 mg L⁻¹ humic acid experiment has Fe(II) concentrations just prior to addition very close to the LOD, 0.26 nM. Following addition all subsequent changes to the Fe(II) are beneath the LOD. As with the first 2.0 mg L⁻¹ experiment there is a net loss in H₂O₂ at an apparent greater rate than in the light phase, though this is less than the first experiment indicating it is the concentration of Fe(III) as well as the presence of MnO_x which affects the rate of H₂O₂ loss. With the shortened particulate phase the experiments were unable to show whether there would be an increase in Fe(II) production after c. 800 s as seen in the 0.5 mg L⁻¹ experiments.

5.03 Discussion

5.03.01 Light Phase

Fe(II)

The three primary mechanisms for the production of Fe(II) in sunlight waters are: the reduction of Fe(III) by superoxide (Emmenegger et al., 2001; Goldstone and Voelker, 2000; Voelker and Sedlak, 1995) and H₂O₂ (Barb et al., 1951; Weiss, 1935) and a photochemical LMCT. The initial rapid increase in Fe(II) in the humic acid experiments (Figure 5.13) may be due to the photochemical LMCT at the surface of iron (hydr)oxides (Faust and Hoigne, 1989; Faust and Zepp, 1993; Waite and Morel, 1984) or from organically complexed Fe(III) (Barbeau, 2006; Barbeau et al., 2001). Natural marine organic material is important as it determines the overall rate of Fe(II) oxidation (Craig et al., 2008). Organic complexes of iron retain their solubility and prevent hydrolysis (Rose and Waite, 2003a). For Fe(II), its rate of complexation with natural organic material is slower than that for Fe(III) organic complexation and the

complexes are less thermodynamically stable (Rose and Waite, 2003a). The initial stage of rapid Fe(II) production is not seen in the NMO experiments (Figure 5.07) except for a slight increase in mxd8.8-2. Either, the NMO does not possess the organic complex that can rapidly photochemically reduce iron (III) for the initial stage or that the comparative concentrations to the humic acid are low. The assumption that they do not possess this rapid organic-Fe(III) complex may be valid as the NMO are from iron limited or aged (> 4 months) culture residues. This complex may then either be in very low concentrations with respect to the total available iron concentrations of the NMO or available iron is in a semi-refractory state and will not form these organic-complexes when mixed with the organic. If the iron is as an aged hydroxide then the photo-reductive dissolution is on time scales of one hour or more (Wells and Mayer, 1991) so may not play a major role in initial changes seen. Within the initial stage there is a large production of $O_2^{\cdot-}$ as evidenced by the formation of H_2O_2 in both the NMO (Figure 5.08) and humic acid (Figure 5.12) experiments. Superoxide oxidation of Fe(II) is four to five orders of magnitude faster than that by O_2 (Fujii et al., 2010) with the presence of humic substances decreasing Fe(II) oxidation by O_2 (Miles and Brezonik, 1981). Usually the low $O_2^{\cdot-}$ concentrations in the marine environment, pico-molar steady state concentrations (Goldstone and Voelker, 2000; Heller and Croot, 2010b), would not mean that superoxide is a primary oxidant, of Fe(II); however, the inferred rapid production of H_2O_2 may indicate high concentrations of superoxide in the initial phases.

The loss of Fe(II) following initial production in the humic acid experiments (Figure 5.11) implies that either the oxidation of Fe(II) is occurring at a greater rate or that the LMCT has decreased compared to the NMO experiments (Figure 5.07). In the NMO experiments the systems with measurements above the LOD suggest a steady-state is in place. For a steady-state Fe(II) concentration to occur then the rate of reduction of organically and inorganically complexed Fe(III) must be the same as the oxidation of Fe(II) and its complexes and organic stabilisation of Fe(II). Phytoplankton NMO have been shown to increase the half life of Fe(II) in seawater (Kuma et al., 1995; Rijkenberg et al., 2008; Steigenberger et al., 2010). Within the NMO experiments (Figure 5.07) for a steady state either the organically complexed Fe(II) is photochemically stable or there is a rapid cycling between the organically complexed Fe(III) to Fe(II) and back again. Organic Fe(III) complexes, such as those with carboxylate ligands, are more photochemically labile than aquo complexes (Rush et al., 1990; Sedlak and Hoigne, 1993) leading to an increased cycling of Fe(II) and this apparent steady-state. The form of the Fe(II) traces in the humic acid experiments (Figure 5.11) and the changes in concentrations over the three stages, especially those of the 0.5 mg L^{-1} experiments, show how using a known organic material, that is not liable to change through aging in storage such as the NMO, can produce

better reproducibility within the light phase of the experiments. The loss of Fe(II) can also be increased through its oxidation by Cu(II) (Moffett and Zika, 1983).

H_2O_2

H_2O_2 is primarily formed following the dismutation of photochemically produced $O_2^{\cdot-}$ (King et al., 1995; Micinski et al., 1993; Petasne and Zika, 1987; Voelker et al., 1997; Voelker and Sedlak, 1995). The formation is usually catalysed by organic material and dissolved metal ions, but will continue uncatalysed when the superoxide concentration is in excess of these (O'Sullivan et al., 2005), though this is slow above pH 8 (Zafiriou, 1990). The initial light phase H_2O_2 production can therefore be attributed to the catalysed $O_2^{\cdot-}$ dismutation. The initial phase of the humic acid experiments with a high photo-production of reduced iron and presumably other metals such as copper (Witt et al., 2007) can act to enhance the production of $O_2^{\cdot-}$ with the effect of potentially forming a direct replacement for any H_2O_2 lost through its oxidation of reduced metals. The HO^{\cdot} radical produced from the oxidation of Fe(II) and other reduced metals by H_2O_2 will be scavenged by organic material. This organic intermediate formed from this reaction can reduce O_2 to $O_2^{\cdot-}$ with its subsequent reaction with Fe(II) producing H_2O_2 (Voelker and Sulzberger, 1996). However OH^{\cdot} can also oxidise Fe(II) (Barb et al., 1951) and there is also the possibility that with an organic reducing agent present Fe(II) may be regenerated from Fe(III) (Voelker and Sulzberger, 1996). The combination of catalysed superoxide formation and the organic intermediate oxidation of O_2 can lead to the rapid initial phase increase in H_2O_2 if sufficient reduced metals are present through a photo-chemical LMCT of organically complexed Fe(III) (Barbeau, 2006; Barbeau et al., 2001).

The second stage with a slower increase in H_2O_2 would suggest that the catalyst concentrations have decreased and increases in H_2O_2 concentration are due primarily to the uncatalysed dismutation of $O_2^{\cdot-}$. The extended light phase in the 2.0 mg L⁻¹ experiments (Figure 5.12) show that there is an eventual loss of H_2O_2 at ~ pH 7.4. H_2O_2 has a long half life, at its lowest it will be 5 hrs or more in productive tropical seawater (Moore et al., 1993) though rates of photodecomposition increase in irradiation experiments compared to the natural environment (Petasne and Zika, 1987). H_2O_2 photodecomposition in natural seawater runs at ~5 % of the production rate, however, it is dependant on the rate of photoreductants produced with the primary mechanism being the oxidation of Fe(II) by H_2O_2 (Moffett and Zafiriou, 1993). To decrease the concentration of H_2O_2 would require a sink. H_2O_2 at elevated concentrations (> 100 nM (Gonzalez-Davila et al., 2006; Moffett and Zika, 1983)) and temperature (~> 25 °C) outcompetes oxygen for Fe(II) and Cu(I) (Croot and Laan, 2002; Millero and Sotolongo, 1989;

Moffett and Zika, 1987; Voelker and Sulzberger, 1996). It is the pH 7.4 / 2.0 mg L⁻¹ humic acid system which show a definite loss of H₂O₂ from the system (Figure 5.12). These experiments have higher concentrations of Fe(II), 2 to 4 times, compared to the pH 8.1, 0.5 mg L⁻¹ humic acid experiments (Figure 5.11) and therefore the circumstances of the increased concentrations of Fe(II) combined with the lower pH indicates that the H₂O₂ is outcompeting O₂ for the oxidation of Fe(II) and this is known to occur in organic free seawater at < pH 7.5 (Gonzalez-Davila et al., 2006).

Mn(II)

Changes in the light phase concentrations of Mn(II) in either the NMO (Figure 5.09) or humic acid (Figure 5.13) experiments were inconclusive in proving (under experimental constraints) the photochemical production of Mn(II) from within the media. This was not unexpected as previous works (Spokes and Liss, 1995; Sunda et al., 1983) required an addition of artificial MnO_{1.9} particulates that have photochemical reduction rates 5-6 times faster than MnO_x produced through bacterial oxidation of manganese (Sunda and Huntsman, 1994) to show measurable changes, whilst using radioactive tracers, in Mn(II).

5.03.02 Particulate Phase

Fe(III) Additions Only

Three experiments had single additions, to 100 nM, of iron in the form of FERR50, these were; Fc4.4-1 and Fc4.4-2 (Figures 5.07 – 5.09) and HA0.5-2 (Figures 5.11 -5.13). From these 3 experiments the Fe(II) (Figure 5.07) in Fc4.4-2 is the only system to show a continuous increase of Fe(II) following a particulate addition. This experiment is also unique in that the measured concentration of H₂O₂ was low, < 10 nM (LOD 0.4 nM) prior to and post addition. What may have contributed to low photochemical production of H₂O₂ (Figure 5.08) (Fe(II) was in a steady state) was the aging of the fresh organic material (4 days) combined with the low concentration addition (4.4 % v/v). The increase in Fe(II) following addition could be through either photo-reduction of the particulate phase (Waite and Morel, 1984; Wells and Mayer, 1991) or by an organic LMCT on surface complexed Fe(III) (Barbeau, 2006; Barbeau et al., 2001). For a steady state these reduction mechanisms are occurring at a similar rate to the Fe(II) oxidation by O₂. The low concentrations of H₂O₂, ~ 10 nM, in the system ruling this out as the primary oxidant (Gonzalez-Davila et al.(2006) suggest H₂O₂ concentrations > 125 nM, in organic free seawater, are when it will outcompete O₂ for Fe(II) at ~ pH 8.2) of Fe(II) at the

experimental temperature (28.4 °C). The changes in the Mn(II) seen for additions of 100 nM FERR50 suggest that the redox chemistry relating to manganese is not straight forward. The specified concentration of manganese is ≤ 0.1 % of the FERR50 and with initial Mn(II) increases in the particulate phase of + 4 nM, HA0.5-2 (Figure 5.13) or \sim 13 nM, Fc4.4-1 and Fc4.4-2 NMO experiments (Figure 5.09), which are greater than the concentration of manganese, the remaining source of manganese is the base seawater itself. The H₂O₂ concentrations prior to injection of the particulates are different for the three experiments. In Fc4.4-1 and Fc4.4-2 NMO experiments (Figure 5.08) the final concentrations in the light phase are 50 and 5 nM, respectively, whilst in HA0.5-2 the final light phase concentration of H₂O₂ is \sim 110 nM. The production of reduced manganese is therefore apparently independent of the H₂O₂ concentration with respect to the NMO experiments. On addition of the particulates there is some form of perturbation in the experiments and this leads to a reduction mechanism for manganese which was not present within the light phase. One proposed mechanism would be the photo-reduction of Fe(III) at the surface of the FERR50 (Sulzberger and Laubscher, 1995), the Fe(II) is re-oxidised or organically complexed still at the surface of the FERR50, re-oxidation occurs faster at the surface than when Fe(II) is in solution (Hem, 1977; Sulzberger and Laubscher, 1995). Even with faster surface re-oxidation rates of Fe(II), there are still elevated levels of Fe(II); when these reduced ions come into inner-sphere contact with MnO_x it then undergoes a reductive dissolution (Hem, 1978; Scott, 1991) increasing the concentration of Mn(II). That the NMO experiments reduce more manganese than the 0.5 mg L⁻¹ humic acid experiment may be due to a greater formation of Fe(II) organic complexes. That the experiments do not show an increase in Fe(II) unless there are low concentrations of H₂O₂ would indicate that this photo-reduction of surface Fe(III) and reductive dissolution of MnO_x is occurring rapidly (greater than a 44 s analytical cycle) in the presence of higher concentrations of H₂O₂.

Combined Additions

The addition of the 10000 nM FERR50 particulate phase to the combined NMO experiments, mxd8.8-1 and mxd8.8-2, had the effect of decoupling the cycling of Fe(II) (Figure 5.07) and H₂O₂ (Figure 5.08). Following an initial increase (over c. 80 s) in both Fe(II) and H₂O₂ – photochemical LMCT at the surface of iron (hydr)oxides (Faust and Hoigne, 1989; Faust and Zepp, 1993; Waite and Morel, 1984) or from organically complexed Fe(III) (Barbeau, 2006; Barbeau et al., 2001) increasing Fe(II); whilst the continued photo-excitation of organic chromophores subsequently reduces O₂ to O₂^{·-} (Petasne and Zika, 1987) with its catalysed dismutation, in the presence of excess Fe(II), forming H₂O₂ (O'Sullivan et al., 2005). For a loss

of analytes within the system which was actively showing H₂O₂ production and Fe(II) in a steady state during the light phase means that the loss factors become dominant on addition of the particulates. The proposed now dominant mechanism within the experiments which is acting to decrease H₂O₂ is the reverse Fenton reaction (Barb et al., 1951) (Equation 5.01) with Fe(II) being favoured as the reductant over other reduced metals (Moffett and Zika, 1987).



The concentrations of H₂O₂ attained prior to injection of the 10000 nM FERR50 into the combined NMO experiments (Figure 5.08), mxd8.8-1 and mxd8.8-2 are ~ 100 and 70 nM, respectively. These H₂O₂ concentrations are similar to the average seawater concentration, 100 nM (Moffett and Zika, 1983) or experimentally calculated concentration, 125 nM (Gonzalez-Davila et al., 2006) limit on when H₂O₂ becomes the primary oxidant of Fe(II) in warm waters (Millero and Sotolongo, 1989; Moffett and Zika, 1987). These results suggest that with the NMO the H₂O₂ concentration need only be above 25 nM for it to react with the Fe(OH)⁺ ion (Millero and Sotolongo, 1989) or with the NMO Fe(II) ligand. With the reverse Fenton reaction as the dominant H₂O₂ reaction decreasing the Fe(II) and assuming there is no change in the photochemical reduction of iron and organic material, forming O₂^{•-}, then the products of the photochemical reactions are being utilised elsewhere. The half-life of H₂O₂, has also been shown to increase on the filtration of a sample indicating the presence of particulate material can act to shorten its half life (Moore et al., 1993; Petasne and Zika, 1987).

With a decrease in H₂O₂ to around 25 nM (Figure 5.08) in mxd8.8-1 and mxd8.8-2, the remaining primary Fe(II) oxidants are oxygen, and the superoxide and hydroxide radicals. One or more of these is therefore in excess and acting to oxidise the Fe(II) (Figure 5.07). For measurable photoreductive dissolution of Fe(III) from the particulate phase to occur the Fe(II) formed must detach from the interface, if this does not occur the rate of Fe(II) oxidation by O₂ (and potentially also H₂O₂) at the interface is faster than in solution (Hem, 1977; Hem, 1978; Sulzberger and Laubscher, 1995). Assuming there is no reductive dissolution due to the addition of MnO_{1.9}; changes in the 8.8 % NMO experiments with only 1000 nM FERR50 did not show a similar loss of Fe(II) (Figure 5.07) with the same concentration addition of MnO_{1.9} (except a small decrease in H₂O₂ in Fc8.8-2), then it is the addition of 10000 nM FERR50 which causes the loss in both analytes. For Fe(II) this could be due to the increased surface area increasing the potential for surface sorption of Fe(II) and its hydrolysis to Fe(III). The addition of 1000 nM FERR50 (8.8 % NMO experiments) was inconclusive in respect to a change from a steady state in the Fe(II) (Figure 5.08). The addition of FERR50 may then be said to have an affect on the type of Fe(II) complex present. If it is an organic complex that retards the

oxidation of Fe(II) by O₂ and H₂O₂, producing a quasi steady-state Fe(II) (Miller et al., 2009) than the stability of this complex may be decreased with the addition of the particulate phase, i.e. forming a competition between organic complexation and surface hydrolysis of Fe(II) as proposed by Jickells and Spokes (2001). Ruling out changes in H₂O₂ concentration during the 10000 nM FERR50 (Figure 5.08) due to the MnO_{1.9} does not suggest that there is a reaction occurring between the addition of MnO_{1.9} and H₂O₂. The increase in Mn(II), ~ 90 nM, (Figure 5.09) on injection of particulates may be through both organically mediated reductive dissolution (Stone and Morgan, 1984), and Fe(II) reduction of manganese oxides (Equation 5.02) (Grassian, 2005; Hem, 1978). With MnO_{1.9} present in the experiment this will also catalytic increase the rate of H₂O₂ decomposition (Kohler et al., 1975).

H₂O₂ in the 10000 nM FERR50, combined NMO experiment (Figure 5.08) particulate phase after its initial decrease in concentration shows the beginning of a second phase production of H₂O₂; this is also seen in HA0.5-2 and HA0.5-3. For this to occur the loss mechanism seen preceding this production must be minimised and for an increased rate of production there must be the catalytic dismutation of the O₂^{•-} (O'Sullivan et al., 2005). What is of interest in mxd8.8-2 with 10000 nM FERR50 (Figure 5.07 & 5.08) and HA0.5-2 (Figure 5.11 & 5.12), is a simultaneous production of Fe(II) and H₂O₂. If it was the surface sites on the FERR50 where rapid oxidation of Fe(II) occurs and these have now been minimised or that the photochemical production of Fe(II) has entered an ongoing cycling through organic complexation then the continued organic LMCT (Barbeau, 2006; Barbeau et al., 2001) could account for the further production of Fe(II). For excess H₂O₂ to be produced there is a requirement for the superoxide dismutation to increase. LMCT are reducing Fe(III) at the same rate as its oxidation leading to a steady state in that part of the system. The superoxide is in excess of the reduced metals and organic material leading to uncatalysed dismutation (O'Sullivan et al., 2005) forming H₂O₂ as well as catalysed dismutation (King et al., 1995; Micinski et al., 1993; Petasne and Zika, 1987; Voelker et al., 1997; Voelker and Sedlak, 1995) and a net increase in production. The net production increase would indicate that as a production mechanism, increased catalytic superoxide dismutation, for H₂O₂ is potentially slower than its loss through the catalytic reduction by MnO_{1.9} (Kohler et al., 1975), though it may be important on longer time scales. However, reductive dissolution may become more important with continuous inputs of MnO_x. What the 2.0 mg L⁻¹, pH 7.4 experiments suggest is that the concentration of FERR50 does play a role in the rate of loss of H₂O₂ (Figure 5.12) and this is related to the concentration of Fe(III). There were lower concentrations of FERR50, 100 nM compared to 500 nM, from HA2.0-1 to HA2.0-2, but the MnO_{1.9} concentrations were kept

the same. With lower concentrations of FERR50 the rate of loss of H₂O₂ on the particulate phase decreased.

MnO_x Addition Only

MnO₂ is a strong catalyst in the decomposition of H₂O₂ (Kohler et al., 1975). That it is capable of reductive dissolution is seen in HA0.5-1 (Figure 5.12) with an addition of 90 nM MnO_{1.9} only. The H₂O₂ following addition of the particulate decreases from ~120 to 75 nM (Figure 5.12), whilst the increase in Mn(II) (90 nM) occurs within the first 5 minutes following addition of the particulate (Figure 5.13). The change in the Fe(II) (Figure 5.11) in the particulate phase for this experiment has decreasing concentration production and loss cycles. The first cycle increases by > 2nM Fe(II) following addition of the particulates. If H₂O₂ is reacting with both Fe(II) and MnO_{1.9} then as it decreases to below ~ 100 nM, there is a short net production of Fe(II) (~ 1 nM), with the subsequent loss due to other oxidants, e.g. O₂. The initial increase in the particulate phase of Mn(II) (Figure 5.13) for this experiment also suggests that reactions within the particulate phase which may reduce the MnO_{1.9} when it is mixed with the FERR50 were minimal; within the particulate phase there are reduced metals (FERR50 at pH 5.4) which when in inner sphere contact result in electrons being transferred to the MnO_{1.9} leading to its reduction (Hem, 1978; Scott, 1991). This is one hypothesis as why there was large increases of Mn(II) in the NMO experiments. If the Mn(II) is being oxidised by H₂O₂ than Fe(II) will be hydrolysed and lost through sorption onto the particulate post formation of MnO₂ (Brugmann et al., 1992). This outer-sphere bound Fe(III) undergoing photochemical reduction (Faust and Hoigne, 1989; Faust and Zepp, 1993; Waite and Morel, 1984) or LMCT which may account for the decreasing cyclic behaviour of Fe(II) in HA0.5-1 and HA0.5-3 (Figure 5.11) with MnO_{1.9} in their particulate additions.

Al(OH)₃ Additions

The aluminium hydroxide was produced as Al(OH)₃ though on its mixing with the FERR50, at pH 5.4, underwent ionisation to Al(OH)₂⁺ (Stumm and Morgan, 1996; Williams and Frausto da Silva, 1996). A positively charged aluminium hydroxide when added to water cause the coagulation of dissolved organic carbon (DOC) (presence indicated through the production of H₂O₂) leading to a sudden loss mechanism for both Fe(II) and H₂O₂ in the seawater only systems (Urban et al., 1990).

5.03.03 Organic Material

NMO

The sequential experiments (Figures 5.07 and 5.08) with increasing concentrations of NMO, 0.2 μ m filtrate from *Fragilariaopsis cylindrus* exudates, suggest that the organic material is being degraded over time, probably through bacterial reworking whilst in storage, and this affected the production of H_2O_2 during each experiment, Fc4.4-1, Fc4.4-2, Fc8.8-1 and Fc8.8-2 (Figure 5.08). Final H_2O_2 concentration achieved in the 4.4 % experiment drops from ~60 (NMO 2 days old) to ~ 5 nM (NMO 4 days old) H_2O_2 , Fc4.4-1 and Fc4.4-2 respectively. Though the final concentrations of H_2O_2 attained in the 8.8 % NMO experiments are similar ~ 150 nM, Fc8.8-1 (NMO 5 days old) has a rapid increase up to ~ 125 nM in the first 80 s and then gradually increases to ~150 nM, whereas Fc8.8-2 (NMO 6 days old) has a two stage, gradual slowing of production up to 150 nM. This is interesting, as bacterial reworking of phytoplankton exudates forms CDOM (Rochelle-Newall and Fisher, 2002) the initiating chromophore for photochemical superoxide production (Petasne and Zika, 1987). On mixing the long term aged (4 months) NMO, from *Thalassiosira pseudonana*, with the fresh NMO (now 8 and 9 days old), the maximum H_2O_2 concentrations decrease, mxd8.8-1 ~ 100 nM, mxd8.8-2 ~ 70 nM. The initial stage net production also decreases from 60 to 40 nM for mxd8.8-1 to mxd8.8-2 with large differences after c. 200 s. With storage time scales of greater than 60 days less than 5 % of the original phytoplankton produced material will remain and > 60 % of this will be a semi-refractory low molecular weight (LMW) material (Hama et al., 2004). With an expected stable, aged organic, the changes in the 8.8 % mixed experiments would suggest that this is due to the aging of the 'fresh' *Fragilariaopsis* and not the *Thalassiosira*. Fe(II) quasi steady-states were generally seen in the NMO experiments (Figure 5.07 light phase) and this may be due to formation of a slow photochemically reactive organic Fe(II) (Miller et al., 2009; Rose and Waite, 2003a). Meunier et al. (2005) found that it was the LMW fraction that allowed Fe(II) to achieve a steady-state and high molecular weight (HMW) had greater net H_2O_2 production rates. From their modelling work they also found that terrestrially derived organic material, such as humic materials, had higher photochemical reactivity towards Fe(II) than NMO.

Humic Acid

Humic materials have similar characteristics as CDOM and contain large concentrations of carboxylate ions able to form metal complexes (Averett et al., 1989). The carboxylate complexes can act in two ways in the photochemical LMCT of Fe(III) to Fe(II). They can directly complex Fe(III) with the subsequent photo-reduction to Fe(II) and an organic radical (Voelker et al., 1997); with oxygen present the organic radical formed will reduce O_2 to $O_2^{\cdot-}$. The second way is the formation of surface Fe(III) carboxylate complexes on Fe(III) (oxy)hydroxides and their subsequent LMCT (Faust and Hoigne, 1989; Faust and Zeppl, 1993; Waite and Morel, 1984), however the rate of oxidation of Fe(II) on the surface is faster than in solution (Hem, 1977). That the humic acid experiments (Figure 5.11) show an initial rapid production not seen in the NMO (Figure 5.07) experiments would suggest that these carboxylate complexes act rapidly when photo-excited. The subsequent losses would suggest that the formation of organic Fe(II) complexes keeping the Fe(II) in a quasi-steady state (Miller et al., 2009; Rose and Waite, 2003a) is minimal with humic acid (Figure 5.11) compared to the NMO experiments (Figure 5.07). Contrasting humic acid experiments contained different concentrations, 0.5 and 2.0 mg L⁻¹, and were at different pHs, 8.1 and 7.4, and therefore do not allow for a direct comparison. Changes seen in the concentration of Fe(II) (Figure 5.11) may be due to either factor. However, the similarities in their forms suggest that the reactions that the photochemically labile fractions undergo are essentially the same. The H₂O₂ (Figure 5.12) also shows similar light phase forms; a comparison can be suggested as the concentrations attained are higher with higher concentrations of organics as also seen in the NMO experiments.

5.04 Conclusions

There were two initial aims of these experiments: i) Produce a photochemically redox active analogous sea-surface microlayer system containing hydrogen peroxide and reduced iron and manganese. ii) Test if the system following addition of an artificial particulate acts to reduce some or all of the particulate phase to a soluble phase. With respect to the first aim the experimental set-up was successful in quasi-simultaneously measuring the production through photochemical initiation of Fe(II) and H₂O₂, though none was seen for Mn(II). Though a reduction of a particulate phase was seen for MnO_{1.9}, the results for FERR50 were inconclusive. With respect to the MnO_{1.9} particulate phase the rapid reduction seen was not attributed to photochemistry but instead it was due to the reactivity / state of the system on addition of the particulates.

The experiments introduced three factors for consideration in the photochemistry of analogous sea-surface microlayers: an organic component, a light phase and a particulate phase. Of the three, the two most closely linked were the organic component and the light phase. The combination of these factors showed different production stages in H_2O_2 and Fe(II) on initiating the incubation and differences in form from NMO to the humic acid experiments; these were due to age and concentration. H_2O_2 and Fe(II) became coupled within the light phase, showing similar trends during the humic acid experiments and the 8.8 % combined NMO experiments; rapid initial production and then the subsequent oxidation of Fe(II) due to the high concentration of H_2O_2 . The systems were also coupled as under the experimental conditions, temperatures $> 22^\circ\text{C}$, H_2O_2 is the primary and favoured oxidant of Fe(II) in all except one experiment. It was therefore decided, that further research was to be undertaken on those reactions within the light phase and due to better reproducibility of those experiments containing humic acids, these were to be central to these experiments.

With respect to the particulate phase the variations in the additions were too great for a real consensus of the results, though they do appear dependent on the H_2O_2 in the light phase – tentative conclusion from one experiment. With the longer light phase the experiments tend towards a steady-state / net production / net loss of the analytes in the system; to add particulates to a system that is not in a steady state would also make interpretation of those results more difficult. Due to the small time scales of the experiments it was difficult to assess what could be long term trends on addition of the particulates, though some conclusions could be made.

There is production of Fe(II) from FERR50 if the H_2O_2 concentration is low, $\sim 10 \text{ nM}$, experiment Fc4.4-2.

H_2O_2 at concentrations above 25 nM is the apparent primary oxidant of Fe(II) in warm waters ($> 25^\circ\text{C}$) containing organic material especially when their photochemical productions are decoupled by the addition of particulates.

LMCT at the surface of particulates producing Fe(II) are a large sink for H_2O_2 acting to decouple the solution phase photo and redox cycles of Fe(II) and H_2O_2 .

Decoupled systems will realign when the particulate addition sink for the analytes is removed.

Fe(II) sorbed to and oxidised to Fe(III) at the surface of particulates will undergo photochemical reduction when the systems are realigned

Short lived, c. 2 mins, increases of Fe(II) occur with small concentration additions of FERR50 ($< 400 \text{ nM}$) to active systems.

The presence of $\text{MnO}_{1.9}$ will decrease H_2O_2 concentrations faster than uncatalysed superoxide dismutation production rates.

The oxidation of Mn(II) and the subsequent presence of manganese particulates combined with its reductive dissolution can promote cycles of production and loss of Fe(II).

Single additions of $\text{MnO}_{1.9}$ only have short term (< 800 s) affects on H_2O_2 if there was a corresponding addition of FERR50.

The hydrogen peroxide is affected by reduced manganese and at lower pH with increased organics it will be actively sourced as an oxidant.

Environmental Implications

From within the experiments, more importance should be placed on those with NMO. These are representative of materials which may be found in an organically enriched sea surface microlayer. These NMO also show the production of H_2O_2 is dependant on the age of the organic material, though no work was undertaken on very fresh (< 1 hour) NMO material. The addition of particulates to a photochemically active, analogous marine surface microlayer will cause a decrease in the H_2O_2 concentration. In warm waters with H_2O_2 acting as the primary oxidant this may increase the half-life of reduced Fe(II). NMOs appear to retain Fe(II) in a photochemically stable complex where as humic substances show a rapid photochemical reduction of iron, with little stability of the organic complexes subsequently formed, therefore differences in half lives of Fe(II) from freshwater to coastal to open ocean microlayers may be expected. The presence of both types of organics (NMO and humics) could contribute to a long-term presence of reduced iron during the daytime; humic materials producing high concentrations and NMO retaining this concentration in a steady state. If the NMO is not available for the formation of Fe(II) organic complexes, due to UV degradation than the Fe(II) concentrations would decrease rapidly. Referring to the previous work on the measurements of dissolved species in a freshwater microlayer, the surface microlayer itself may have low concentrations of these organics leading to low concentrations of Fe(II) relative to underlying water. Reduction of MnO_x is rapid when introduced to an active photochemical system and could be a causal effect for elevated concentrations of Mn(II) in freshwater surface microlayers.

Chapter Six:

Effect of Irradiating Regime on Reactive Oxygen Species and Iron in Model Marine Microlayer Systems

6.00 Introduction

Cycling of reactive oxygen species (ROS) and iron in seawater can be dependant on the light regime of the irradiating radiation (Cooper et al., 1988; Gerringa et al., 2004; Laglera and van den Berg, 2007; Rijkenberg et al., 2005; Song et al., 2005). UV-radiation (UV-R) has previously been shown to increase the production of the superoxide radical ($O_2^{\cdot-}$) (Petasne and Zika, 1987) in seawater through the excitation of organic chromophores (Moffett and Zika, 1983) with the subsequent dismutation of the $O_2^{\cdot-}$ to hydrogen peroxide, H_2O_2 (Bielski, 1978). Oxidised iron, Fe(III), has also been shown to be photo-reduced when either organically complexed (Barbeau, 2006; Barbeau et al., 2001), with > 99.9 % Fe(III) organically complexed in seawater (Gledhill and van den Berg, 1994; Rue and Bruland, 1995; Wu and Luther, 1995), or via a ligand to metal charge transfer (LMCT) occurring at the surface of iron (hydr)oxides (Faust and Hoigne, 1989; Faust and Zepp, 1993; Waite and Morel, 1984). In cold arctic waters, low in chromophoric dissolved organic matter (CDOM), with dissolved iron estimated to be around 0.9 ± 0.1 nM, ~ 30 % of Fe(II) production is due to UVB radiation, 35 % due to UVA and the remainder due to PAR (Laglera and van den Berg, 2007). Though photoreactions with dissolved inorganic Fe(III) is not significant in waters above pH 6.5 (King et al., 1993), when it does occur the photo-reductive dissolution is on hour time scales (Wells and Mayer, 1991). With the organic complexes of ferric iron retaining iron in a soluble form, these show a greater potential for photo-reduction with irradiation predominantly in the visible / near UV-R range (Sima and Makanova, 1997). However, the type of organic complex can also dictate its photo-reactivity with those from some estuarine waters showing little reactivity towards UV-R production of Fe(II) (Rijkenberg et al., 2006). The presence of organic material can also affect the rate of Fe(II) oxidation, through either inhibition (Miles and Brezonik, 1981; Rijkenberg et al., 2008; Shaked et al., 2004; Steigenberger et al., 2010) or enhancement (Santana-Casiano et al., 2000).

The disproportionation of $O_2^{\cdot-}$ can be catalysed by redox reactive substances, including inorganic (Rush and Bielski, 1985) and organically complexed (Bull et al., 1983) iron; inorganic (Zafiriou et al., 1998) and organically complexed (Voelker et al., 2000) copper, other metals such as manganese (Hansard et al., 2011) and natural organic material (Goldstone and Voelker, 2000). Uncatalysed disproportionation will occur (O'Sullivan et al., 2005), though its rate in seawater at pH 8, will be slow (Zafiriou, 1990). If $O_2^{\cdot-}$ should attain a sufficiently high steady-state concentration in seawater then it will have a direct affect on the reduction and oxidation of metals and set up redox cycles, such as with iron (Miller et al., 1995; Voelker and Sedlak, 1995). The disproportionation of $O_2^{\cdot-}$ forms H_2O_2 . H_2O_2 in sunlit seawater can attain 10^{-7} M or higher

concentrations (Moffett and Zika, 1983; Moore et al., 1993) where as $\text{O}_2^{\cdot-}$ will attain concentrations of 10^{-10} M (Goldstone and Voelker, 2000; Heller and Croot, 2010b). The half life of H_2O_2 is also far greater than $\text{O}_2^{\cdot-}$, minimum of 5 hrs in productive tropical seawater (Moore et al., 1993) compared to a maximum for $\text{O}_2^{\cdot-}$ in Antarctic waters of c. 194 s and from purely uncatalysed dismutation of $\text{O}_2^{\cdot-}$ in coastal waters, the half-life can range from 5 – 20 minutes (Petasne and Zika, 1987). H_2O_2 will act as the primary oxidant in competition with di-oxygen at temperatures of ~ 20 °C or more and at concentrations exceeding > 50 to 125 nM (Croot and Laan, 2002; Gonzalez-Davila et al., 2006; Millero and Sotolongo, 1989; Moffett and Zika, 1987; Santana-Casiano et al., 2006; Voelker and Sulzberger, 1996). However, unlike $\text{O}_2^{\cdot-}$, H_2O_2 in seawater has not yet been shown to produce a redox cycle, though H_2O_2 reduction of Fe(III) would occur in seawater if the pH is reduced to approximately pH 7 (Moffett and Zika, 1987).

The following series of experiments compares the photochemistry of the ROS, H_2O_2 , and iron between different irradiating regimes, UVB (280 – 315 nm), UVA (315 – 400 nm) and photosynthetically active radiation (PAR, 400 – 700 nm) in model seawater microlayers. These results were than modelled with the aim of producing kinetic constants related to the production and cycling of, H_2O_2 and reduced iron, Fe(II). This work assesses the effect irradiating wavelength has on the production and loss rates of H_2O_2 and Fe(II) over a c. 3000 s incubation, in which time the primary analytes, H_2O_2 and Fe(II) can achieve either a steady-state or net loss / production. The comparisons using irradiating regime required to some degree a consistency in the magnitude and form of the cycles of H_2O_2 and Fe(II), therefore the organic material used in the analogous microlayer systems were chosen for their storage stability over time. The experimental systems include humic acid at 1.0 and 2.0 mg L⁻¹ and a 2.0 µm filtered, aged (> 5 months) natural marine organic (NMO) obtained from a culture of *Thalassiosira pseudonana* added to 11% v/v to the base media, 0.2 µm filtered North Sea seawater. Set 1 of these experiments considers only the light phase of those experiments conducted in Chapter 5 using 0.2 µm filtered NMO. The results from the experiments can be examined in two respects. The first is an assessment of the affect the irradiating regime has on the sea-surface microlayer (SML) and the second is a comparison of how the photo-reactivity of H_2O_2 and Fe(II) changes with depth due to preferential absorption of UV-R with depth (Figure 6.01).

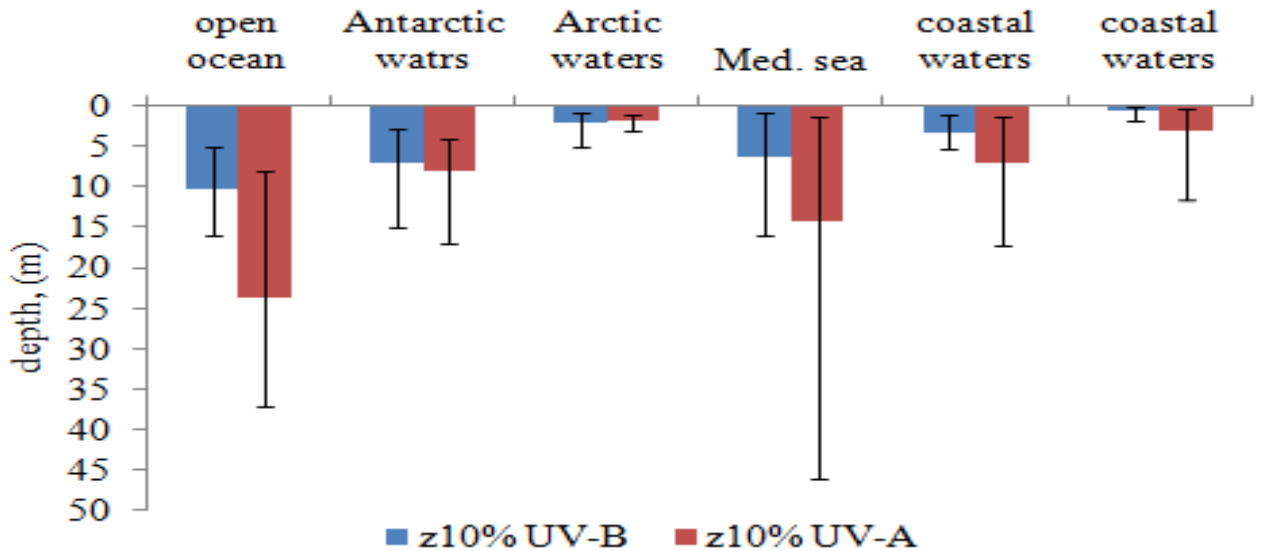


Figure 6.01. Comparison of seawater 10 % irradiance depths for UVB and UVA from Tedetti and Sempre (2006). Values are average depths with error bars indicating the range of the authors collated data.

6.01 Materials and Methods

The materials used, experimental method and the description of irradiating lamps were presented previously in Chapter 5. Table 6.01 shows the irradiance produced during each set of experiments. What must be noted as a possible experimental artefact is that the Full and UVA + PAR spectrums both utilise multiple bulbs. There is therefore the possibility that results seen may be due more to the total energy received rather than only the irradiating regime. However, this argument can still be used in an interpretation of the data as a depth dependent study from Full spectrum to UVA+PAR to PAR as wavelengths removed are those which are preferentially absorbed as depth increases from the surface microlayer.

Table 6.01. Irradiance values for light regime experiments, with comparisons to certain published experiments.

band width	280 – 315 nm	315 – 400 nm	400 – 700 nm	total
energy received				
experiment	W m^{-2}	W m^{-2}	W m^{-2}	W m^{-2}
UVB	1.1	3.8	15.5	20.4
Full	1.4	15.2	30.1	46.7
UVA+PAR	0.2	11.7	14	25.9
UVA	0.2	13.4	3.9	17.5
PAR	0.02	0.1	11.6	11.7
Steigenberger et al.(2010)	0.3	17.6	3.8	21.7
Meunier et al. (2005), solar simulator				1.0 kW m^{-2}

A numerical model describing the concentrations of H_2O_2 , O_2^\cdot , OH^\cdot , $\text{Fe}(\text{II})$ and $\text{Fe}(\text{III})$ was developed in MATLAB using a stiff ordinary differential equation solver (ODE 15s). A Stiff solver is required when the range in the time dependant changes of the model parameters are large and small changes in one may have large effects on the stability of other parameters, thus affecting the overall stability of the attempted solution. This for example can be due to the differences in the model concentrations of say OH^\cdot and $\text{Fe}(\text{III})$, concentration differences are over six orders of magnitude, but small changes in the concentration of the OH^\cdot will have large effects on the time dependant concentration of the $\text{Fe}(\text{III})$.

The resultant time dependant changes in model H_2O_2 and $\text{Fe}(\text{II})$ were then fitted to the experimental observations for the changes in concentrations of H_2O_2 and $\text{Fe}(\text{II})$ from each experiment. The corresponding model reactions are shown in Table 6.02 with a visual representation of the model in Figure 6.02. The model initially utilised ideas from Miller et al. (1995) and Steigenberger et al. (2010), and it also included a suite of similar reactions to Rose and Waite (2002), Meunier et al. (2005) and Santana-Casiano et al. (2006). The model differs from Miller et al. (1995) in four ways: it includes the hydroxyl radical oxidation of $\text{Fe}(\text{II})$; all $\text{Fe}(\text{III})$ is involved in photo-reduction rather than a specific $\text{Fe}(\text{III})\text{-L}$; it also includes O_2^\cdot photo-production and a sink term for O_2^\cdot . The hydroxyl radical oxidation of $\text{Fe}(\text{II})$ and the general O_2^\cdot sink term are also included above that of the Steigenberger et al. (2010) model. Meunier et al. (2005) and Rose and Waite (2002) models both differentiate between inorganic and organically complexed iron with Meunier et al. (2005) implicitly giving an O_2^\cdot sink term and Rose and Waite (2002) measuring an estimated copper concentration as one of the O_2^\cdot sinks, though both systems include $\text{Fe}(\text{II})$ oxidation by the hydroxyl radical.

Table 6.02. Model equations involved in the cycle of reactive oxygen species and redox cycling of iron.

				reference
R1	$Fe(III) + \eta v \rightarrow Fe(II) + products$	k_{RED}	s^{-1}	fitting parameter 1
R2	$O_2 + CDOM + \eta v \rightarrow O_2^{\bullet-} + products$	k_{CDOM}	$M s^{-1}$	fitting parameter 2
R3 ^(a)	$O_2 + Fe(II) \rightarrow O_2^{\bullet-} + Fe(III)$	k_{O2}	$M^{-1} s^{-1}$	calculated as per (i)
R4	$O_2^{\bullet-} + 2H^+ + Fe(II) \rightarrow H_2O_2 + Fe(III)$	1.0×10^7	$M^{-1} s^{-1}$	(ii)
R5 ^(b)	$H_2O_2 + Fe(II) \rightarrow OH^{\bullet} + OH^- + Fe(III)$	k_{H2O2}	$M^{-1} s^{-1}$	calculated as per (iii)
R6	$OH^{\bullet} + Fe(II) \rightarrow OH^- + Fe(III)$	5.0×10^8	$M^{-1} s^{-1}$	(iv)
R7	$O_2^{\bullet-} + Fe(III) \rightarrow O_2 + Fe(II)$	k_{RO}	$M^{-1} s^{-1}$	fitting parameter 3
R8	$3OH^{\bullet} + Fe(III) \rightarrow Fe(OH)_{3(s)}$	2.5×10^4	$M^{-1} s^{-1}$	(v)
R9 ^(c)	$2O_2^{\bullet-} + 2H^+ \rightarrow H_2O_2 + O_2$	k_{SOD}	$M^{-1} s^{-1}$	calculated as per (vi)
R10	$O_2^{\bullet-} + sinks \rightarrow products + O_2$	k_{SOS}	$M^{-1} s^{-1}$	fitting parameter 4

(i) Millero *et al.* (1987)^(a); (ii) Rush and Bielski (1985); (iii) taken from Miller *et al.* (1995)^(b) as per Millero and Sotolongo (1989); (iv) taken from Rose and Waite (2002) (v) taken from Rose and Waite (2002); (vi) Zafiriou (1990)^(c).

(a) kinetic rate is pH and O_2 dependant, the calculation of k_{O2} (Millero *et al.*, 1987) is as follows,

$$\log(k_{O2}) = 21.56 - 1545/T, \text{ where } T \text{ is temperature corrected to } ^\circ\text{K}$$

$$\log(k_{O2}) = \log(k_{O2}) - 3.29 \times I^{0.5} + 1.52 \times I, \text{ where the ionic strength is calculated as } I = 19.9201 \times S / (1.0 \times 10^3 - 1.00488 \times S), \text{ where } S \text{ is salinity in practical salinity units.}$$

$$\log(k_{O2}) = -1 \times \log(k_{O2}) + 1.87 \times pH, (M^{-1} s^{-1})$$

$k_{O2} = k_{O2} \times [O_2]$, O_2 concentration calculated through temperature and salinity dependant.

(b) kinetic rate is pH dependant, the calculation of k_{H2O2} (Millero and Sotolongo, 1989) is as follows,

$$\log(k_{H2O2}) = -3.04 + 1.0 \times pH$$

$$k_{H2O2} = kb$$

(c) kinetic rate is pH dependant, the calculation of k_{SOD} (Zafiriou, 1990) is as follows ,

$$\log(k_{SOD}) = 12.7 - 1.0 \times pH$$

$$k_{SOD} = kc$$

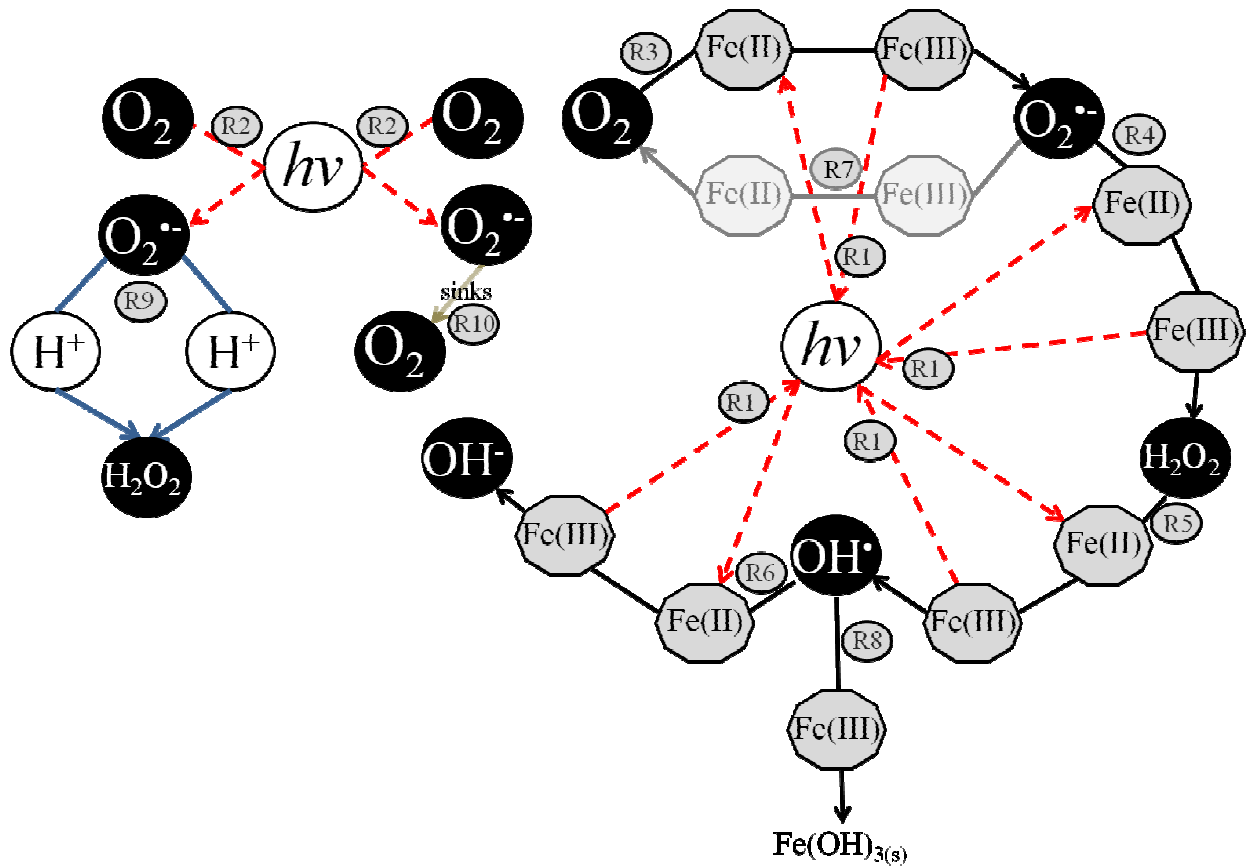


Figure 6.02. Model of combined cycles of reactive oxygen species and iron through photo-reduction and redox reactions. Red arrows indicate the light induced reduction of iron. R numbers refer to the corresponding reaction in Table 6.02

The model was fitted simultaneously to the H_2O_2 and $\text{Fe}(\text{II})$ experimental observations based on the sum of their sum of squares error (SSE) from the data to the model output. To ensure that there was no bias due to an order of magnitude difference or greater in the concentrations of H_2O_2 and $\text{Fe}(\text{II})$ observations were normalised; this was done via their maximum values, with these values subsequently used to normalise the model output. The residuals for each stage and the total combined residual calculated from the actual concentrations are shown in Table A6.01 and A6.02 in the appendix. Model fitting was initially undertaken manually then completed using the Nelder-Mead algorithm (Nelder and Mead, 1965). To ensure that the results of the Nelder-Mead algorithm were not within a local minimum the results were repeated whilst varying the initial guesses of the fitting parameters. The final model fits are not necessarily those which provided the lowest value for the sum of the residual sum of squares for both H_2O_2 and $\text{Fe}(\text{II})$ fits. The reason for this was that even with the normalisation the noise in the H_2O_2 data still affected the sum of the residual values, so that the subsequent fit to the $\text{Fe}(\text{II})$ was poor; on these occasions finessing of the fit reverted to manual control.

Models were not fitted to the whole data set but instead to set stages of the experiment. The transition point between stages was chosen by noting the difference in the gradient of the H_2O_2 data when it was placed on a log scale. The H_2O_2 was used to dictate the transition point due to its formation being dependant on the production and cycling of the photochemically produced $\text{O}_2^{\cdot-}$ and under the experimental environmental conditions could be the primary oxidant of Fe(II) (Croot and Laan, 2002; Gonzalez-Davila et al., 2006; Millero and Sotolongo, 1989; Moffett and Zika, 1987; Santana-Casiano et al., 2006; Voelker and Sulzberger, 1996) and therefore one of its controlling influences. The reasoning for the use of different stages is based on two theories that are directly dependent of the fitting parameters and a series of model and fitting trials. Complex models, such as those of Meunier et al. (2005) and Rose and Waite (2002) allowed for the fitting of all organic reactions, > 7 parameters, to achieve appropriate fits to the data. Whereas simple models such as Miller et al. (1995) and Steigenberger et al. (2010) only used 2 or 3 fitting parameters, these, when applied to the experimental data, were unable to constrain the model to the experimental results. Fitting trials using extensive MATLAB toolbox applications, GlobalSearch and MultiSearch with different fitting algorithms did not provide a good simultaneous fit to both analytes, though the fit to H_2O_2 was superior to the Fe(II) fit, again due to the noise in the signal. Closer inspection of the work by Meunier et al. (2005) shows that their H_2O_2 fit is not so good in their seawater experiments, whilst Steigenberger et al. (2010) model their H_2O_2 data as a curve through two data points! Due to the large array of experiments to undertake a fitting to the resultant model erred towards a simple model with four fitting parameters. The third stage of the experiments termed the constant stage, could be judged to be the most environmentally applicable as the experimental system has undergone in essence a warming up period.

The fitting parameters are: (i) the photochemical reduction of Fe(III) and Fe(III) species since their concentrations were not measured they are not explicitly prescribed in the model; (ii) reduction of oxygen to $\text{O}_2^{\cdot-}$ through photo-reduction of organic material (concentration and type unknown); (iii) $\text{O}_2^{\cdot-}$ reduction of Fe(III) (species and concentration unknown) and (iv) a sink term for $\text{O}_2^{\cdot-}$ – unknown concentrations of other metal ions. Copper (Zafiriou et al., 1998) and manganese (Hansard et al., 2011) are known to react with $\text{O}_2^{\cdot-}$ and an oxidative process can occur through organic material (Goldstone and Voelker, 2000). The theories for why the system should be split into stages is due to the choice of the fitting parameters; three of these parameters are directly related to the cycling of $\text{O}_2^{\cdot-}$, which itself is the primary source of H_2O_2 . (i) H_2O_2 production is from both catalysed and uncatalysed dismutation of $\text{O}_2^{\cdot-}$. Therefore the rate of H_2O_2 production is dependant on both trace metals and organic material; as the concentrations of these catalysts change so to does the type and therefore rate of $\text{O}_2^{\cdot-}$ dismutation, suggesting

the potential for two sets of kinetic values. (ii) Production of $O_2^{\bullet-}$ and the potential for retaining reduced iron in a steady-state are dependant on the organic material present. Due to UV radiation affecting the type of organic material through photo-bleaching (Goldstone et al., 2002; Micinski et al., 1993; Miller et al., 1995; Rijkenberg et al., 2005; Rose and Waite, 2003b) this will change through the course of the experiment.

Initial Fe(III) concentrations for each experiment which were used in the model were assumed to be equal to the total iron concentration of the medium prior to commencing the experiment. The analysis of the samples for total iron (Table 6.03) was undertaken on an ICP-MS using 1:40 dilutions and standard additions. The corresponding recovery of the National Research Council of Canada, certified reference material, CASS-5, specified concentration, 25.8 ± 2.0 nM, was 106% and was measured at 28 ± 4 nM ($n = 3$), 15 % RSD. The blank was measured at 14.8 ± 0.09 nM with a corresponding limit of detection ($3 \times \sigma$ of 3 ultra pure waters) of 0.3 nM.

Table 6.03. Total iron concentrations of experimental media

medium	nM
0.2 μ m filtered North Sea seawater	134
4.4 % v/v <i>Fragilaropsis cylindrus</i>	134
8.8 % v/v <i>Fragilaropsis cylindrus</i>	134
4.4 % v/v <i>Fragilaropsis plus</i> 4.4 % v/v <i>Thalassiosira</i>	254
11 % 2.0 μ m filtered <i>Thalassiosira pseudonana</i>	679
1.0 mg L ⁻¹ humic acid	287
2.0 mg L ⁻¹ humic acid	301

6.03 Experimental Results

Four sets of experimental results are presented in the following section. The first set is the light phase results from the experiments incubated under a Full spectrum regime described in the previous chapter. The further three sets compare different irradiating regimes on the photochemical initiated production of H_2O_2 and Fe(II) in model marine surface microlayers. To represent the sea-surface microlayer the three experiments have additions of organic material as follows; an aged (> 5 months) 2.0 μ m filtered NMO taken from *Thalassiosira* and humic acid added to a concentration of 1 and 2 mg L⁻¹.

6.03.01 Set 1: 0.2 μm Filtered NMO, Full Spectrum Experiments

The pH, temperature and LOD for these experiments were discussed in Chapter 5, Section 5.02.01.

Stage times

To enable modelling of the results each experiment had to be split into respective stages. Experimental NMO light stage times for the repeat experiments (Figure 6.03) show the extent to which the reactivity of the initiating chromophore for superoxide production changes whilst the NMO is within storage. Within the NMO experiments the second 4.4 % NMO experiment is singular in that there was low H_2O_2 concentrations $< 6 \text{ nM}$, and as such there could have been a choice of fitting the model as a single intermediate stage; if this was done then there is consistency between each NMO replicate. Of the eight experiments in Figure 6.03, only the first seawater experiment showed an initial, rapid production an increase of $\sim 40 \text{ nM}$ within the first analytical cycle of 44 s. If only a single model was fitted to the second 4.4 % NMO experiment then both sets of *Fragilaropsis* NMO experiments show an increase in the length of the intermediate stage from repeat one to two. The transition point between stages in the mixed NMO experiments occurs at a similar time for both experiments. The experiments of Miller et al. (1995) and Meunier et al. (2005) do not have an initial rapid H_2O_2 production; however, their experiments were conducted using concentrated, size fractionated DOM: HMW $< 0.2 \mu\text{m}$ (Miller et al., 1995) and LMW $< 1 \text{ kDa}$ and HMW $< 0.45 \mu\text{m}$ (Meunier et al., 2005). The intermediate stage is that governed by the curve in the log plot of the H_2O_2 data before the systems shift to one of three states; (i) steady-state, (ii) net production, (iii) net loss. Experiments with no initial rapid production are therefore the two stages of a log plot. That these NMO experiments using 0.2 μm filtered NMO do not show a rapid initial H_2O_2 production is consistent with the findings of the near constant production using HMW (< 0.2 or $< 0.45 \mu\text{m}$ filtered) organic material (Meunier et al., 2005; Miller et al., 1995).

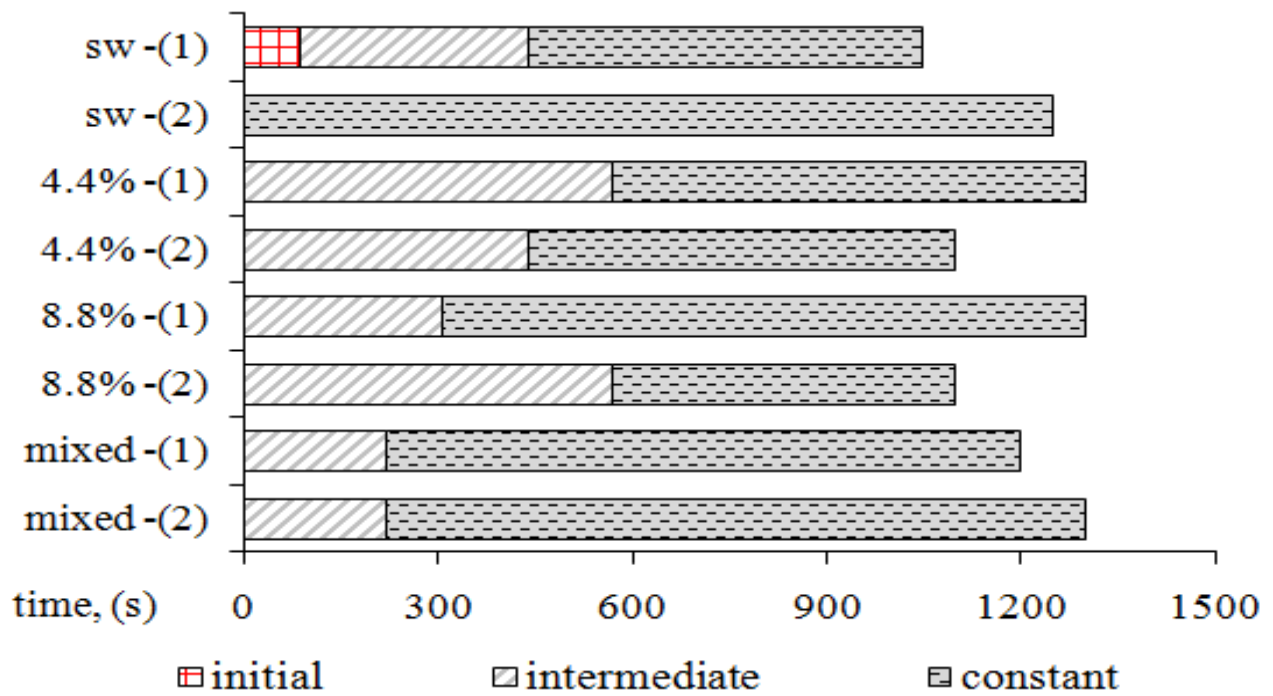


Figure 6.03. Stage timings for the NMO experiments undertaken with Full spectrum incubation.

H_2O_2 apparent rates

H_2O_2 apparent production rates for the NMO experiments are shown in Table 6.04. For those experiments containing NMO, the apparent production rates, for both stages, decrease from the first to the second repeat with the second 8.8 % NMO experiment showing a loss of H_2O_2 . Photochemical H_2O_2 apparent production rates have been determined in the Atlantic and Antarctic waters; they range from 0.2 to 11 nM h^{-1} , (Gerringa et al., 2004; Yocis et al., 2000; Yuan and Shiller, 2001). Higher production rates are expected with an increase in temperature. With a difference of ~ 25 $^{\circ}C$ between incubating temperatures and Antarctic seawater, and using as per Yocis et al. (2000) an estimated correction of $+0.2$ nM h^{-1} $^{\circ}C^{-1}$ provides an additional 5 nM h^{-1} though this still does not account for the production rates in the experiment. Generally the apparent production rates in the intermediate stage are 3 – 21 times greater than in the constant production stage. The differences from the intermediate to the constant production stage may be due to the change from catalysed (Bull et al., 1983; Goldstone and Voelker, 2000; Hansard et al., 2011; Rush and Bielski, 1985; Voelker et al., 2000; Zafiriou et al., 1998) to uncatalysed (O'Sullivan et al., 2005) $O_2^{\cdot-}$ dismutation, or that both are occurring, but the rate of catalysed dismutation has decreased. When the apparent production rates for the constant stage are compared to Moore et al. (1993), with H_2O_2 production rates of between 24 – 134 nM h^{-1} , from a study in the Caribbean, influenced by high DOM inputs, they are in good agreement. That only the constant stage can achieve reasonable apparent rates would suggest that the

experiments can be compared to environmental contexts, but the systems require an initiation period to achieve these apparent rates.

Table 6.04. NMO experiments H_2O_2 apparent stage rates. NC – none calculated. * low H_2O_2 production in the experiment. *Fc* – *Fragilariaopsis cylindrus*.

experiment	H_2O_2 apparent stage rates (nM h^{-1})		
	initial	intermediate	constant
sw – (1)	3118	579	97
sw – (2)	NC	NC	159
4.4% <i>Fc</i> – (1)	NC	283	63
4.4% <i>Fc</i> – (2)*	NC	31*	5*
8.8% <i>Fc</i> – (1)	NC	1402	-2
8.8% <i>Fc</i> – (2)	NC	676	32
8.8% mixed – (1)	NC	975	131
8.8% mixed – (2)	NC	795	46

Results with Model Fits

Figure 6.04 shows the results from the NMO Full spectrum experiments combined with the fitted model data. Represented in Figure 6.04 are the data that are within the calibration range (< LOD or > concentration highest standard) in red and those outside of this range in blue. The data are surrounded by a grey envelope which is calculated for each point based on the error from the calibration calculation. There are three model parameters shown: the corresponding H_2O_2 and Fe(II) models are thick black lines and the model $\text{O}_2^{\cdot-}$ output is a thin black line.

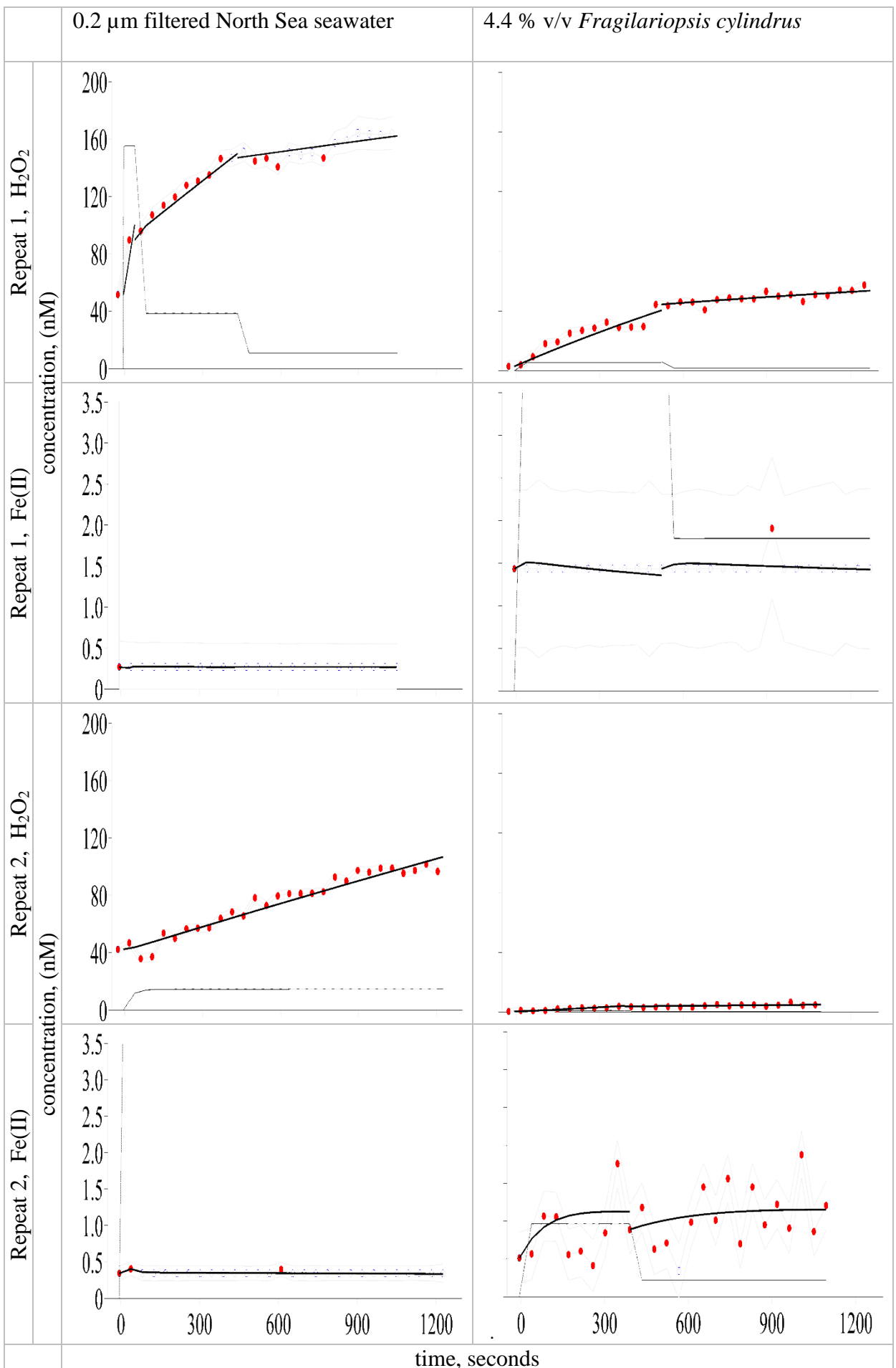


Figure 6.04.a. NMO, Full spectrum incubation experiments with model fits. See text for explanation of parameters

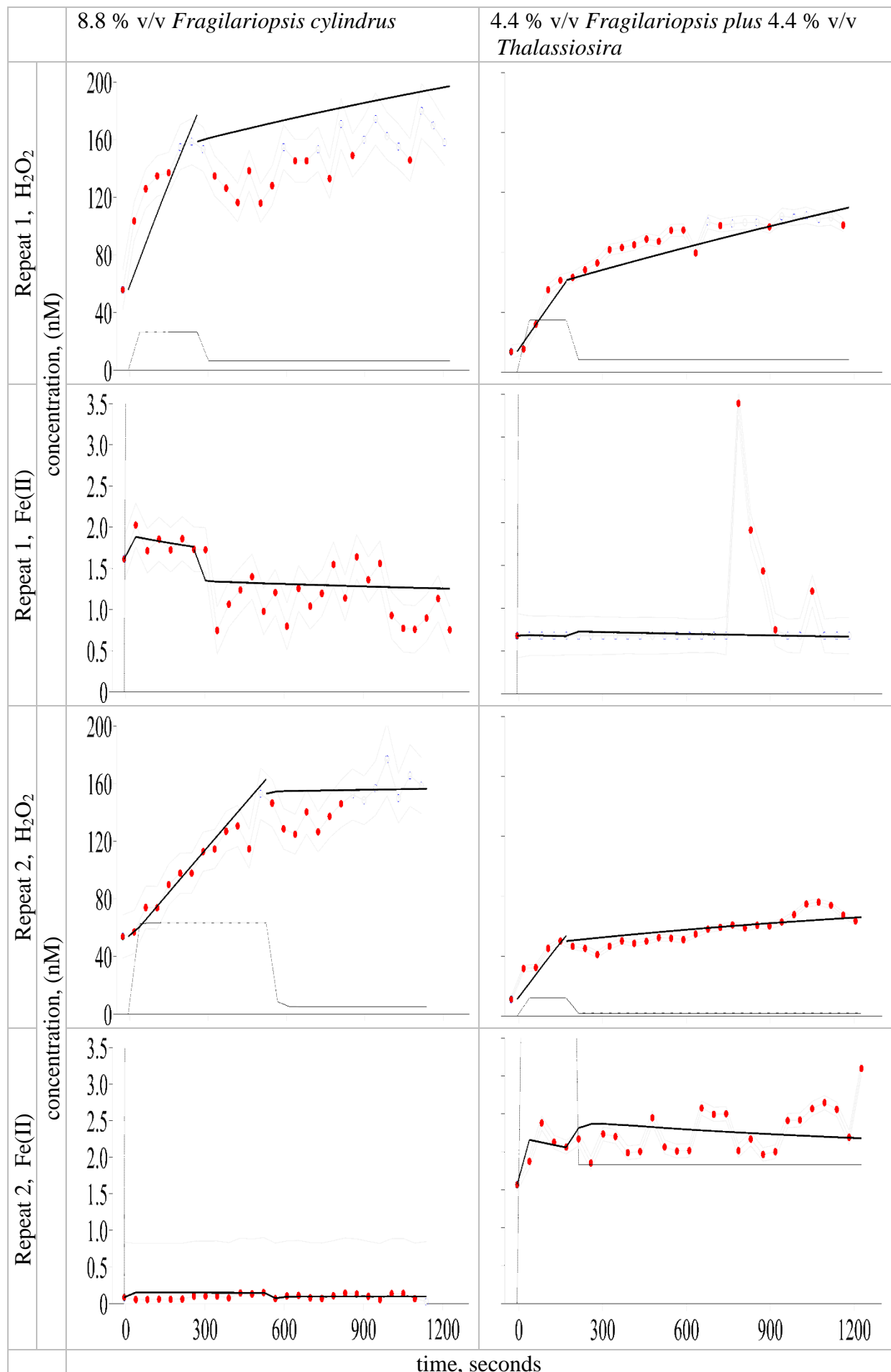


Figure 6.04.b. NMO, Full spectrum incubation experiments with model fits. See text for explanation of parameters

H_2O_2

The experiments with added NMO show a two-stage production in their light stages, with the second production stage slower than the first, as indicated by the apparent production rates (Table 6.04). H_2O_2 overall production in the 4.4 % NMO experiments is 4 times higher in repeat 1 than repeat 2; total H_2O_2 production (10 nM) in the second 4.4 % NMO experiment is low relative to all other experiments. Total production in the 8.8 % NMO experiments are similar, though the length of time in stage 1 increases from repeat 1 to 2, with a concurrent decrease in the apparent production rates, approximately 100 nM H_2O_2 produced over c. 300 and 600 s, respectively. In the mixed NMO experiments, the first stage, comparing between repeats 1 and 2, net production decreases from 60 to 40 nM, whilst in their second stages both experiments show an increase of around 25 nM. H_2O_2 LODs were in the range 0.4 – 15 nM. The seawater only experiments had LODs of 12 and 15 nM whilst those with added NMO had lower LOD.

H_2O_2 is primarily formed following the dismutation of photochemically produced $O_2^{\cdot-}$ (King et al., 1995; Micinski et al., 1993; Petasne and Zika, 1987; Voelker et al., 1997; Voelker and Sedlak, 1995). The formation is usually catalysed by organic material and dissolved metal ions, but will continue uncatalysed when the $O_2^{\cdot-}$ concentration is in excess of these (O'Sullivan et al., 2005), though this is slow above pH 8 (Zafiriou, 1990). That there is minimal change from a steady-state concentration of Fe(II) or indeed any production (seawater only experiments) would indicate that the initial / intermediate stage H_2O_2 production could be attributed to the catalytic affect of species other than Fe(II). These can include; organic material (Goldstone and Voelker, 2000) and / or other reduced metals such as copper (Voelker et al., 2000; Zafiriou et al., 1998) and manganese (Hansard et al., 2011). The combination of the catalysed superoxide formation and the organic intermediate reduction of O_2 leading to, in the intermediate stage, relatively high apparent rates of H_2O_2 production (Table 6.04).

$Fe(II)$

Four experiments show consistent measurements of Fe(II), repeats 2 of the 4.4% and 8.8% NMO experiments, these show a steady-state in place. Repeat 2 in the mixed experiment shows an increase of ~ 1nM where as repeat 1 in the 8.8 % NMO experiment shows a decrease of ~ 1 nM, though this decreases is through two sudden losses in concentration occurring at c. 300 s and 900 s into the experiment. No significant change to the Fe(II) occurred within the seawater only experiments. That there was no change was anticipated and was probably due to

the reactivity of iron (oxy)hydroxides especially to $O_2^{\cdot-}$ decreasing with aging (Fujii et al., 2006). The mechanisms for the production of Fe(II) in sunlight waters are: The reduction of Fe(III) by superoxide (Emmenegger et al., 2001; Goldstone and Voelker, 2000; Voelker and Sedlak, 1995) and H_2O_2 (Barb et al., 1951; Weiss, 1935), or a photochemical ligand to metal charge transfer (LMCT) of iron (hydr)oxides (Faust and Hoigne, 1989; Faust and Zepp, 1993; Waite and Morel, 1984) or from organically complexed Fe(III) (Barbeau, 2006; Barbeau et al., 2001). Natural marine organic material is important as it determines the overall rate of Fe(II) oxidation (Craig et al., 2008). Organic complexes of iron retain their solubility and prevent hydrolysis (Rose and Waite, 2003a). For Fe(II), its rate of complexation with natural organic material is slower than that for Fe(III) organic complexation and the complexes are less thermodynamically stable (Rose and Waite, 2003a). None of the NMO experiments explicitly show a consistent loss of Fe(II) but instead those systems with measurements above the LOD suggest a steady-state concentration is in place. For a steady-state Fe(II) concentration to occur the rate of reduction of organically and inorganically complexed Fe(III) must be the same as the oxidation rate of Fe(II) and its complexes and organic stabilisation of Fe(II). Phytoplankton exudate NMO have been shown to increase the half life of Fe(II) in seawater (Kuma et al., 1995; Rijkenberg et al., 2008; Steigenberger et al., 2010). Within the NMO experiments for a steady-state, either the organically complexed Fe(II) is photochemically stable or there is a rapid cycling between the organically complexed Fe(III) to Fe(II) and back again. Organic Fe(III) complexes, such as those with carboxylate ligands, are more photochemically labile than aquo complexes (Rush et al., 1990; Sedlak and Hoigne, 1993) leading to an increased cycling of Fe(II) and a potential mechanism for the apparent steady-states.

6.03.02 Set 2: 11 % v/v 2.0 μm Filtered *Thalassiosira pseudonana*, Light Regime Comparison Experiments

pH & Temperature

Changes in pH and temperature for the light regime comparison experiments containing 11% v/v *Thalassiosira* NMO are shown in Figure 6.05. The pHs for these experiments were generally similar; average initial pH 8.14, range pH 8.13 – 8.16. The starting temperatures were relatively poorly constrained for this set of experiments, range 22.8 to 28.7 °C. This equates to initial O₂ concentrations, assuming equilibrium with the atmosphere, ranging between 194.8 to 214.9 $\mu\text{M kg}^{-1}$, using the solubility data of Weiss (1970). pH tends to decrease over the first 300 – 900 s following illumination. After this time, the Full spectrum experiment shows a gradual increase in pH for the remainder of the experiment; the UVA experiment shows a gradual decrease in pH whilst the pH in the remaining experiments is relatively constant. Temperatures within the UVB (24.4°C), UVA+PAR (25.3°C) and PAR (24.3°C) remain relatively stable for the first 1500 s and then decrease by ~ 0.4 °C for the latter half of those experiments. The stability of the temperature over the first 1500s in these experiments would suggest that the change in the measured pH is not caused by changes in temperature. The Full spectrum experiment with an initial temperature of 28.7 °C decreases linearly over the course of the experiment by 2.3°C, this change equates to an increase in oxygen due to the temperature change of ~ 12.7 $\mu\text{M kg}^{-1}$. The UVA only experiment has a near linear increase in temperature from 22.8 to 23.9 °C, the change in temperature equates to a decrease in oxygen concentration due to temperature of ~ 6.2 $\mu\text{M kg}^{-1}$.

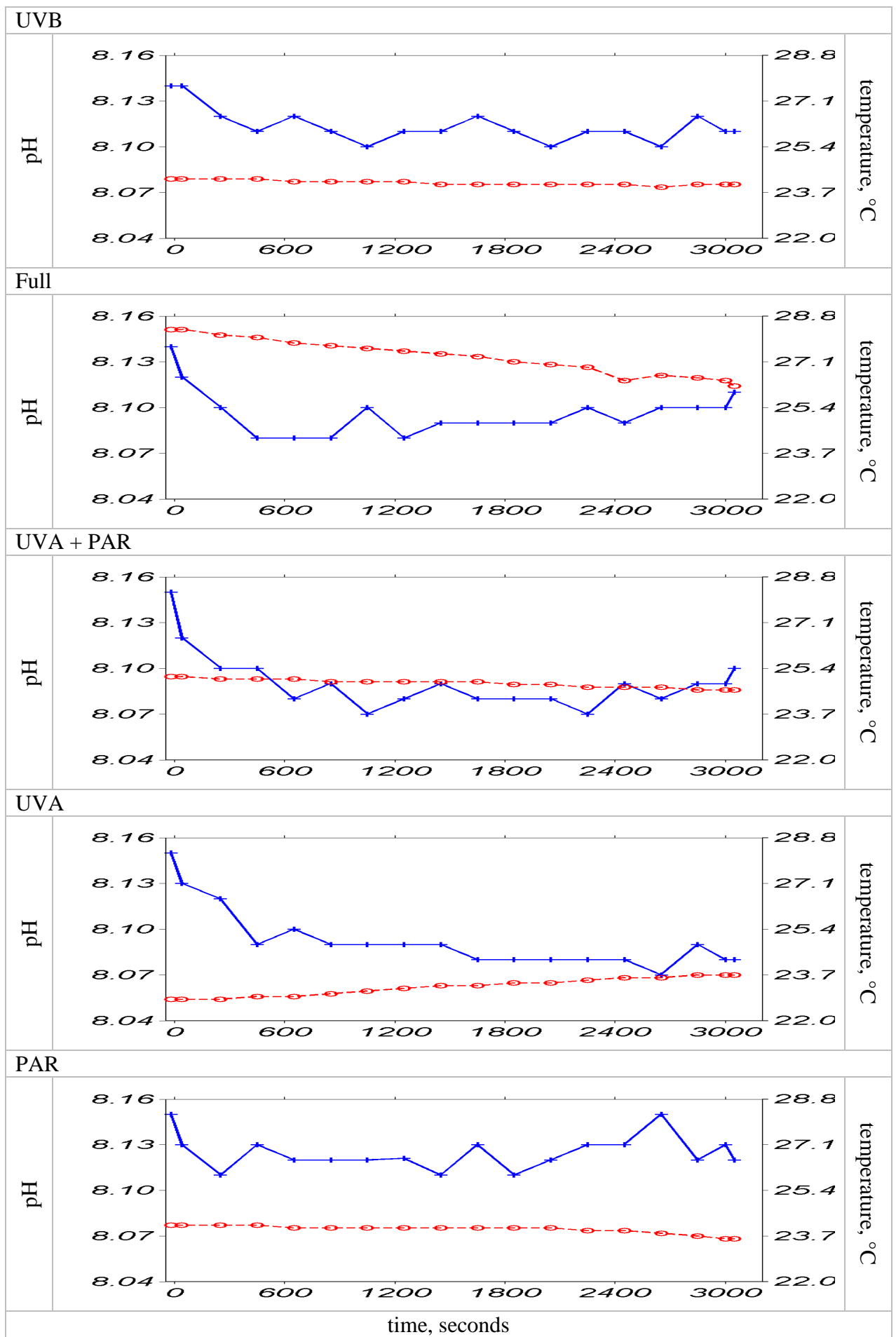


Figure 6.05. pH (blue line with +) and temperature (red line with o) change for the 11 % v/v 2.0 μ m Filtered *Thalassiosira pseudonana* experiments

Stage Times

For the comparison *Thalassiosira* NMO experiments the stage times are shown in Figure 6.06. The initial stage from these experiments has a rapid H₂O₂ production, which was not seen with additions of only HMW NMO material (<0.2 µm filtered). Within the *Thalassiosira* NMO experiments those containing UVB also had a concurrent rapid, initial Fe(II) production. This would indicate that the initial Fe(II) rapid production is due to UVB when using 2.0 µm filtered NMO. The length of time, based on the H₂O₂, in the initial stage appears influenced by the total UVA light received; the more UVA light the shorter the initial stage with no production seen at all within the PAR experiment. The experiments of Miller et al. (1995) and Meunier et al. (2005) do not have an initial rapid H₂O₂ production and this may be due to the use of HMW < 0.2 µm (Miller et al., 1995) and LMW < 1 kDa and HMW < 0.45 µm (Meunier et al., 2005) material, whereas a 2.0 µm filtered NMO was used throughout the NMO light regime comparison experiments. This would again suggest, as with the Fe(II) that the initial rapid stage of H₂O₂ production in the NMO experiments is due to a > 0.2 µm fraction in the aged NMO. The intermediate stage is that governed by the curve in the log plot of the H₂O₂ data before the systems shift to one of three states; (i) steady-state, (ii) net production, (iii) net loss. Due to the UVB only system entering a net loss in H₂O₂ for the final c. 800 s of the experiment, the intermediate stage result is not directly comparable as it encompasses the point of inflection in the log plot and the time of net H₂O₂ production prior to loss in the system. The other experiments containing either a large proportion of UVA or PAR only, all show a continuous net production of H₂O₂ in the final stage; this suggests that to ensure a continued net production there must be specific wavelength set effecting the H₂O₂ production. As the UVB system contains a large proportion of PAR (UVB_(PAR) > PAR_(PAR)) and only far UVA (< 360 nm), this continued net production would have to be due to the UVA radiation > 360 nm. UVB is also the major environmental wavelength that decomposes organic material to LMW constituents (Kieber et al., 1990; Mopper et al., 1991).

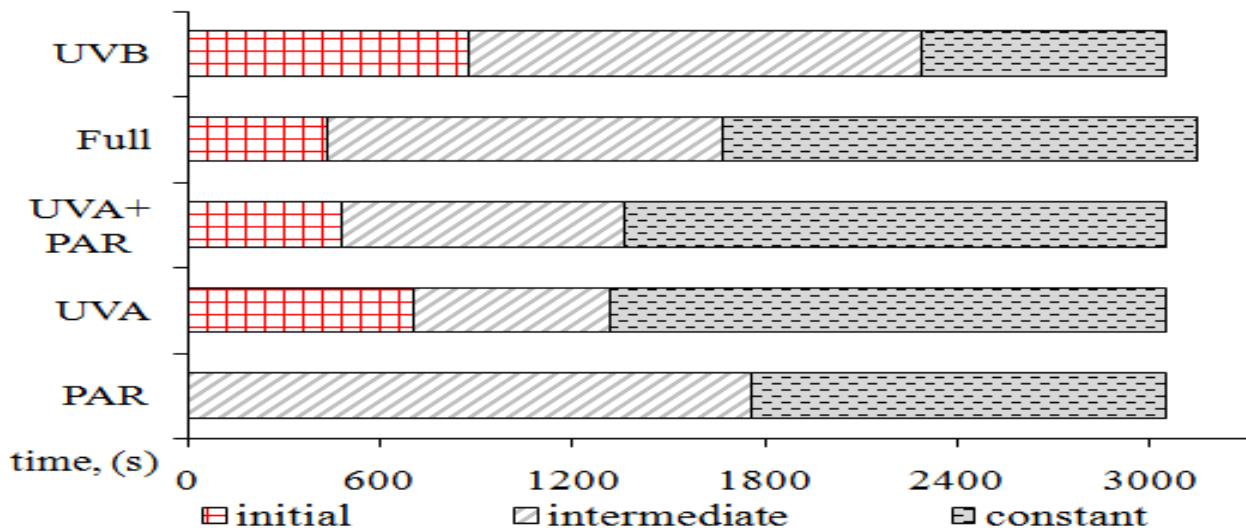


Figure 6.06. 11 % v/v 2.0 μm filtered *Thalassiosira pseudonana* NMO stage times

H_2O_2 Apparent Rates

H_2O_2 apparent production rates for the *Thalassiosira* experiments are shown in Table 6.05. Those NMO systems containing a majority of UVA in their irradiating spectra show how the apparent production rate of H_2O_2 decreases, for all stages, as the amount of the total light and UVA received decreases. The calculated apparent results for all stages are comparable to the calculated rates of Moore et al. (1993) with apparent production rates between 24 – 134 nM h^{-1} . The Full spectrum apparent production rates in the intermediate stage are an order of magnitude less than in the mixed NMO Full spectrum experiment (Table 6.04), whereas the constant stage is of a similar rate to the second repeat mixed NMO experiment. This comparison is difficult to assess further as the 0.2 μm filtered fraction only contained a v/v 4.4 % whereas the 2.0 μm filtered fraction was added to 11 % v/v.

Table 6.05. 11 % v/v 2.0 μm Filtered *Thalassiosira pseudonana* NMO experiments: LODs and H_2O_2 apparent stage rates. NC – none calculated.

experiment	LOD		H_2O_2 apparent stage rates (nM h^{-1})		
	H_2O_2	Fe(II)	initial	intermediate	constant
	nM	nM			
UVB	1.3	0.31	107	49	-8
Full	4.8	0.44	193	76	46
UVA + PAR	1.2	0.14	128	58	26
UVA	0.01	0.91	118	11	24
PAR	2.5	0.64	NC	0	22

Limits of Detection

Table 6.05 also provided the LOD for each analyte for the light regime comparison NMO experiments with 11 % *Thalassiosira*. LOD were calculated based on $3 \times \sigma$ of the sea-surface microlayer analogous material only - blank. The blank signal is made up of all potential reactants of luminol from within the experimental media that induce chemiluminescence, except the analytes. The H_2O_2 LODs are all below 5 nM, this is an order of magnitude greater than those of Yuan and Shiller (1999) however, this LOD was low enough not to impact on the modelling of the changes seen within the experiments. The Fe(II) LODs are all below 1 nM and again are generally sufficient to see initial changes within the experiments. Calibration of the Fe(II) data was similar to that of Meunier et al. (2005) who also produced a calibration curve within identical experimental media directly after their experimental runs; their Fe(II) LOD was 0.2 nM.

Results with Model Fits

H_2O_2 and Fe(II) results with their model fits are shown in Figure 6.07. O_2^\bullet and hence H_2O_2 production is seemingly influenced by both UVA and UVB and these may affect different organic initiating sources. The reasoning for invoking different initiating sources is based on the total H_2O_2 concentrations attained from those experiments without UVB, UVA+PAR and UVA only. These experiments have approximately 4 times more UVA and 5 times less UVB in their irradiating regimes than the UVB experiment and attain similar H_2O_2 concentrations. The UVB experiment also shows after c. 2400s of illumination a net loss in H_2O_2 whilst those containing substantially more UVA do not show a net loss. However, bleaching of the organic material (Goldstone et al., 2002) by UVB cannot be ruled out, though the Full spectrum experiment, which also contains UVB, does not show a net loss in H_2O_2 . The stage at which there is net loss in H_2O_2 during the UVB experiment occurs prior to a point of net loss in the Fe(II) data; a lag that has been seen in previous experimental work (Rose and Waite, 2003b).

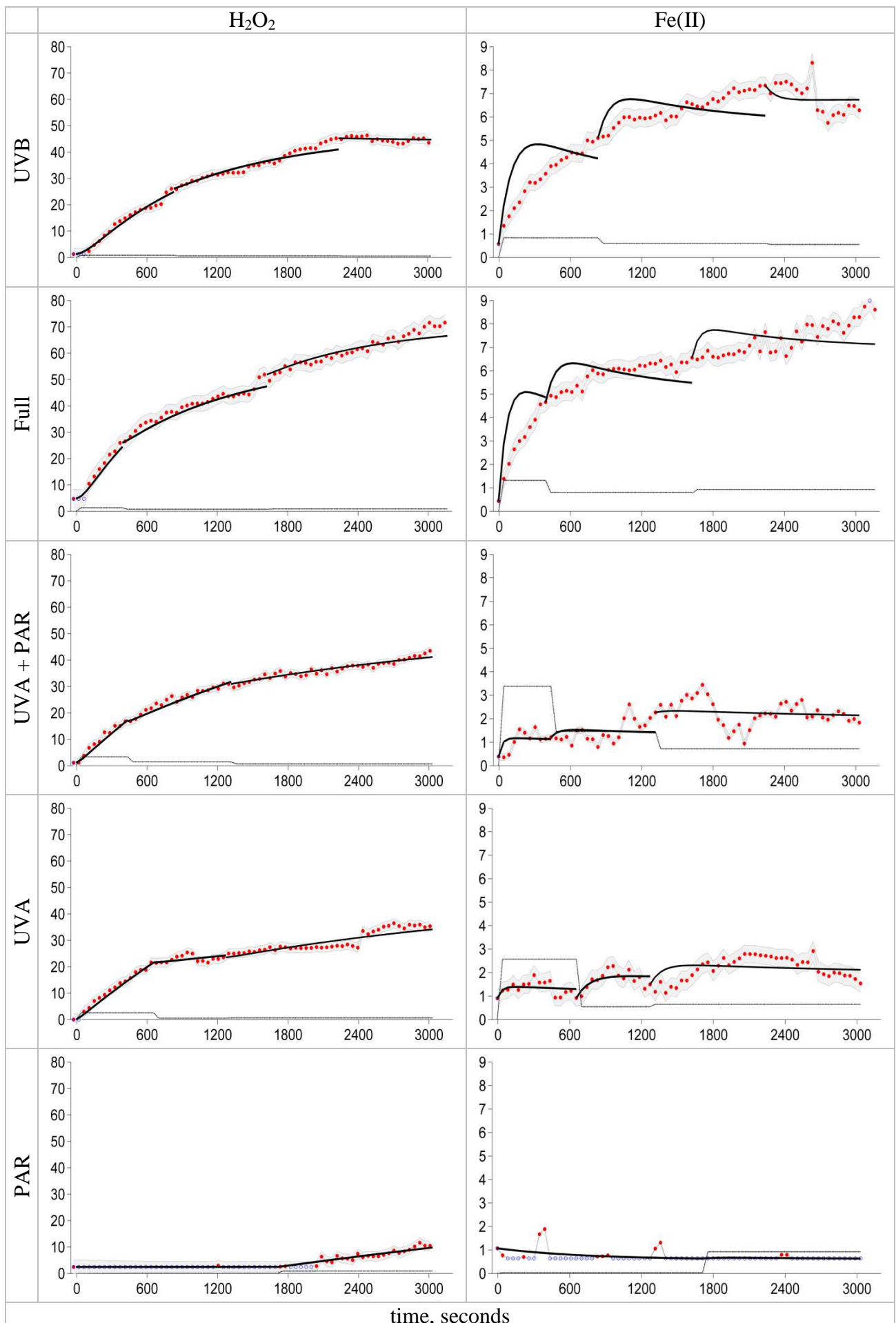
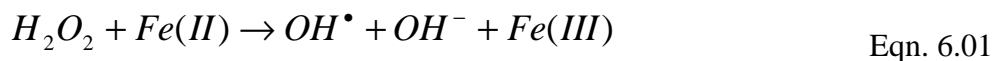


Figure 6.07. 11 % v/v 2.0 μm filtered *Thalassiosira pseudonana* NMO experimental results (concentration in nanomolar) with model fits. See text for explanation of colours and lines.

What also cannot be ruled out is that as H₂O₂ net production decreases in the UVB experiment there is a possible strong sink mechanism for H₂O₂, which is required due to its long half-life, > 5 hrs (Moore et al., 1993). A potential sink for H₂O₂ which will also decrease the concentration of Fe(II) would be model reaction 5, (Equation 6.01 below). A second potential sink would be increased photodecomposition of organic material due to the UVB. Conversely the experiments containing UVB eventually show a constant production of Fe(II) and this would agree with Laglera and van den Berg (2007) who show an increase in the half-life of Fe(II) as the irradiating wavelength decreases. The previous chapters work also suggested that reactions on particulate surfaces could decrease the concentration of H₂O₂.



Within the modelling of the data, the kinetics for this reaction, Equation 6.01 (Millero and Sotolongo, 1989), were kept constant, but this may not be the case as there may be catalytic processes occurring. Further sinks for H₂O₂ may be a similar reductive reaction as equation 6.01 but with reduced copper. Subsequent oxidation of Fe(II) may also occur through the reductive dissolution of oxidised copper (Moffett and Zika, 1983) and manganese (Grassian, 2005; Hem, 1978).

The 11% NMO results based on Fe(II) can be categorised into three groups. The first group contains UVB in its irradiating spectrum and show a rapid initial production which then moves into a constant net production – UVB and Full spectrum experiments. The second group are those experiments with their UV-R in the predominantly UVA range, these show oscillating production and loss cycles. Maximum concentrations occur approximately half-way through these UVA experiments. Except for the Full spectrum experiment the remaining experiments containing UVA tend towards a net loss of Fe(II), though this is curtailed by the termination of the experiments. There are four measurable peaks (pairs of data) above the Fe(II) LOD, 0.64 nM in the PAR experiment suggesting there is some Fe(II) production but it is not significant when compared to irradiating regimes containing UVA and UVB. The result for the PAR only experiment would also suggest that the changes seen in the UVB experiment are due primarily to the UVB and not to the 15.5 W m⁻² PAR within its irradiating spectrum. The PAR within the irradiating regimes, UVB, Full and PAR experiments, is less than 1 % of that in the natural environment, based on the calculations of Zepp and Cline (1977). Thus the experiments cannot rule out the photo-production of Fe(II) from light within the visible light regime; with ~ 35 % of Fe(II) photo-production in Arctic waters attributed to PAR (Laglera and van den Berg, 2007).

As explained earlier, model fitting was carried out on H₂O₂ stage times and was simultaneously constrained by both H₂O₂ and Fe(II) observations. As these functions of the fit are based around the H₂O₂ stage times and the relative changes in H₂O₂ concentration are larger than those in Fe(II) concentration, the fits are generally better for H₂O₂. The resulting Fe(II) fits suggests that for the developed model there are either insufficient fitting parameters to achieve a good fit for both constraints and / or that the model is incomplete with respect to the cycling of Fe(II). H₂O₂ model fits are generally good, though they cannot achieve the general curvature of the data, they do tend to stay within the error envelopes of the data. Fe(II) model fits for those systems containing UVB are poor. The model was initially developed from a series of models that assume the continued oxidation of Fe(II) and its loss from the system. This loss of Fe(II) the model can show but it cannot be forced (as it stands) to show a continued net production, nor a relatively (in terms of the model) slow initial Fe(II) production. The model also has difficulty in representing the oscillatory production / loss behaviour of Fe(II) in the irradiating regimes controlled by UVA. However it takes a reasonable mid point following the initial production in each stage.

6.03.03 Set 3: 1.0 mg L⁻¹ Humic Acid at ~ pH 8.3, Light Regime Comparison Experiments

pH & Temperature

The initial temperature and pH of the 1.0 mg L⁻¹ humic acid experiments were generally similar between experiments. The starting pH for the experiments ranged between pH 8.27- 8.3 whilst initial temperatures were within ± 1 °C of 25.4 °C. Changes in pH and temperature for each experiment are shown in Figure 6.08. pH generally decreases over the first 900 – 1200 s of illumination for all except the Full spectrum experiment. Following this decrease experiments generally show a constant pH after this time. The initial decrease in pH for these experiments last 300 - 600 s longer then those in the NMO (Figure 6.05) experiments. The decreasing order for the change in pH over the first third of the experiment of the 1.0 mg L⁻¹ humic acid experiments, is Full > UVA+PAR > UVA, with changes to the UVB and PAR experiments similar. This is the same order as initial pH changes during the NMO experiments, suggesting there is a potential reaction which can decrease pH and is based on the total UVA received. Temperatures were generally stable throughout the light stage of the experiments, except for the UVB only experiment which decreased by ~ 1 °C over the full term, 3000 s and the Full spectrum experiment which increased by ~ 0.4 °C over the last 2400 s. The average initial starting temperature, 25.4 °C, allows for an approximate calculation for the concentration of O₂, 205.6 µM kg⁻¹, based on the methodology of Weiss (1970).

LOD for both H₂O₂ and Fe(II) in the 1.0 mg L⁻¹ humic acid experiments (Table 6.06) are higher by around a factor of 2 when compared to those from the NMO experiments (Table 6.05) at a similar pH.

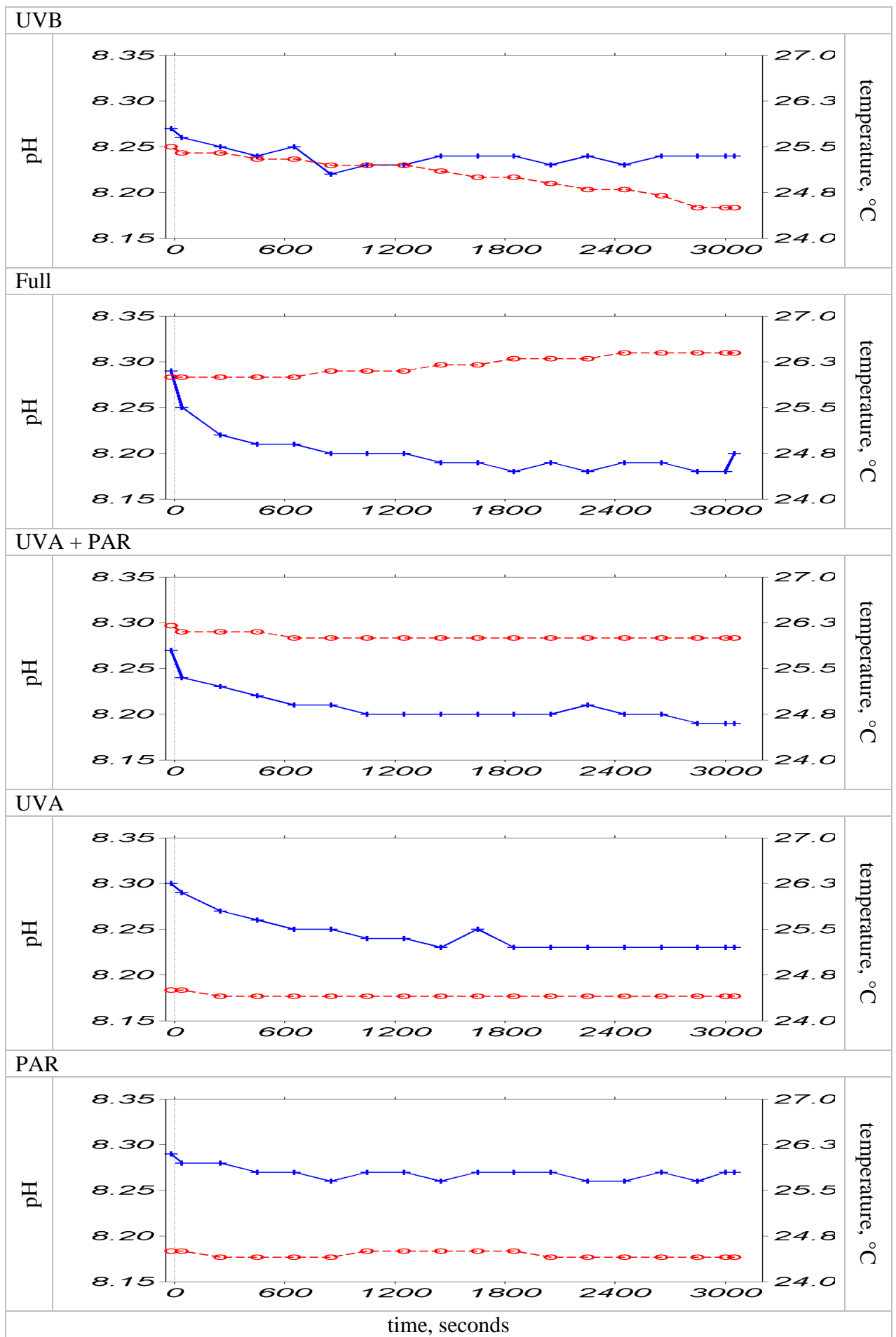


Figure 6.08. pH (blue line with +) and temperature (red line with o) change for the 1.0 mg L⁻¹ humic acid experiments.

Stage Times

Stage timings for the 1.0 mg L^{-1} humic acid experiments are shown in Figure 6.09. The initial stage is different to the rapid production seen in the $2.0 \mu\text{m}$ filtered NMO experiments; rather it appears that there is a lag in the system before production of H_2O_2 increases above the experimental LOD, $\sim 6 \text{ nM}$. The H_2O_2 experimental data from (Meunier et al., 2005) show an increase in the rate of production of H_2O_2 after c. 5 minutes, the initial stage in the 1.0 mg L^{-1} humic acid experiments lasts c. 300s. Unlike the NMO experiments (Figure 6.07) the fastest production of H_2O_2 occur in the intermediate stage for the 1.0 mg L^{-1} experiments. Except for the UVA+PAR experiment the change from intermediate to constant stage occurs at a similar point, c. 900 s into the experiment.

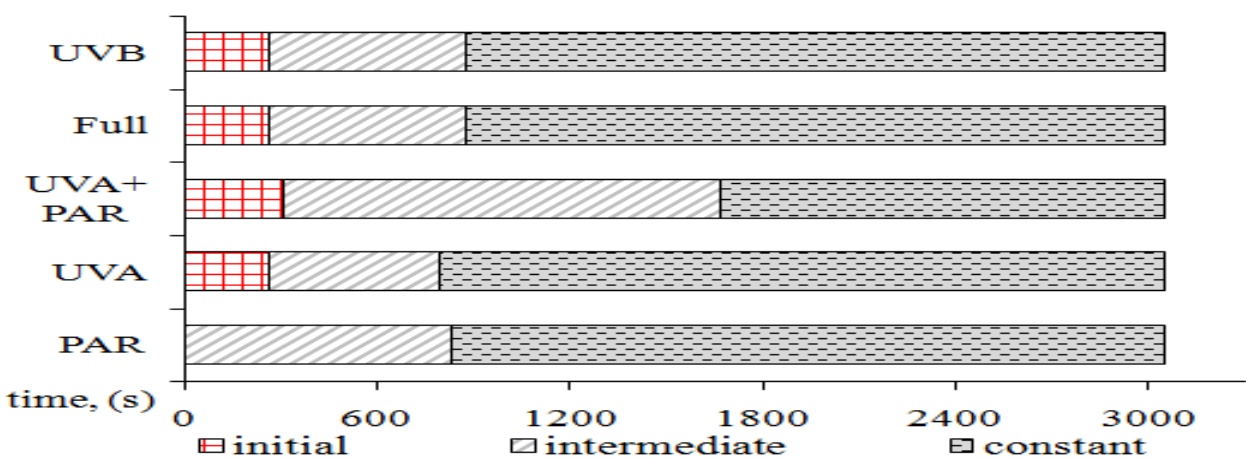


Figure 6.09. 1.0 mg L^{-1} humic acid stage times

H_2O_2 Apparent Rates

The apparent production of H_2O_2 from the 1.0 mg L^{-1} humic acid experiments is dependant on the light regime. H_2O_2 concentrations achieved by the end of the experiment decrease based on the irradiating regime, the order for the decrease in total concentration achieved is Full \approx UVA+PAR $>$ UVA $>$ UVB $>>$ PAR. This result suggests that the irradiating regime affecting the production of H_2O_2 is the UVA range, and it is this which produces the greatest concentration of H_2O_2 . The experiments indicate that as depth from the microlayer increases H_2O_2 production should decrease based on humic acids as the initiating chromophores. The calculation of apparent rates (Table 6.06) is not perfect, as the transition point between stages may coincide with a spike or dip and this will affect the calculation. However, they do give an idea if the experiments are showing similarities to an environmental context. The

apparent rates in the initial stage of these experiments are examples of apparent rates that are skewed by a sudden change; this is as at the end of this stage in the Full and UVA only experiments, where there are increases in H_2O_2 . The 1.0 mg L⁻¹ humic acid experiments have approximately two times higher H_2O_2 apparent production rates compared to the 11% 2.0 μm filtered NMO experiments. The intermediate rates in the 1.0 mg L⁻¹ humic acid experiments are of a similar range, 127 – 199 nM h⁻¹, to the initial stage in the 2.0 μm filtered NMO experiments, 107 – 193 nM h⁻¹, and relate mainly to those irradiating regime containing a large proportion of UV-R.

Table 6.06. 1.0 mg L⁻¹ humic acid experiments: LODs and H_2O_2 apparent stage rates. NC – none calculated.

experiment	LOD		H_2O_2 apparent stage rates (nM h ⁻¹)		
			initial	intermediate	constant
	H_2O_2 nM	Fe(II) nM			
UVB	8.1	1.0	0	127	49
Full	5.6	1.7	80	166	97
UVA + PAR	6.7	1.7	0	199	57
UVA	3.4	0.67	107	164	69
PAR	7.2	0.68	NC	0	1
cold water, Yocis et al. (2000)			range	0.2 – 11 nM h ⁻¹	
warm water, Moore et al. (1993)			range	42 – 134 nM h ⁻¹	

Intermediate stage apparent production rates are consistently high in all except the PAR experiment which correspondingly has an order of magnitude less UV-R. The constant stage of the experiments all show a net production in H_2O_2 within the range of apparent rates measured in warm tropical seawater affected by dissolved terrestrial (riverine input) organic material (Moore et al., 1993). The constant stage H_2O_2 apparent production rates for 1.0 mg L⁻¹ humic acid in seawater are directly related to the UVA radiation received, Figure 6.10.

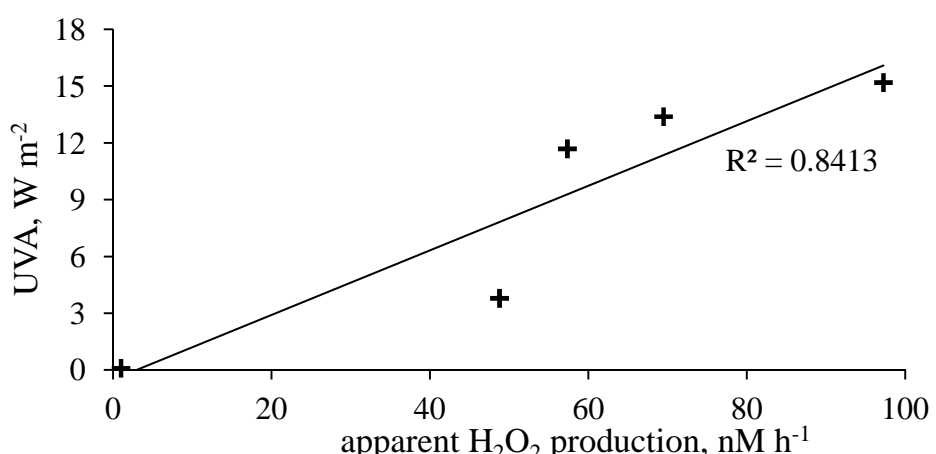


Figure 6.10. Relationship between constant stage apparent H_2O_2 production rates and irradiation received in the UVA (315 – 400 nm) range.

Results with Model Fits

The Fe(II) in the 1.0 mg L⁻¹ humic acid experiments show distinct differences related to the irradiating regime (Figure 6.11). The Full and UVA+PAR experiments show a dampening oscillatory form before their Fe(II) concentrations fall to below their LODs, 1.7 nM. In the Full spectrum experiment there is a dual frequency oscillation with amplitudes of around 10 and 3 nM; whilst the UVA+PAR experiment shows a single oscillation of around 2nM, frequency c. 600s. Fe(II) has been shown to have an oscillatory behaviour with additions of dissolved organic material (DOM) (Rose and Waite, 2003b; Song et al., 2005). The Fe(II) behaviour in the 1.0 mg L⁻¹ experiments could then be attributed to changes in the DOM within the system and as this is photo-oxidised, Fe(III) is being reduced through a LMCT, the subsequent Fe(II) is then oxidised or organically complexed. Fe(III) which is subsequently organically complexed then goes through the cycle again with the subsequent photo-oxidation of the corresponding DOM fraction releasing Fe(II) into the cycle. Changes in Fe(II) species cannot be differentiated with the experimental set up though, inorganic complexes, Fe(CO₃), Fe(CO)₃(OH)⁻ and FeCl⁺ would form at amounts equal to or greater than the Fe²⁺ aquo- ion (King, 1998), with Fe(II) organic complexes greatly in excess of the inorganic complexes (Nolting et al., 1998; Volker and Wolf-Gladrow, 1999) and therefore potentially contributing more to the overall redox chemistry than inorganic complexes (Emmenegger et al., 1998). That the oscillatory behaviour of Fe(II) decreases from Full > UVA+PAR > PAR would suggest that this may also occur with depth in the surface ocean and that steady-state Fe(II) in shallower waters influenced by terrestrial organic material is in fact highly variable.

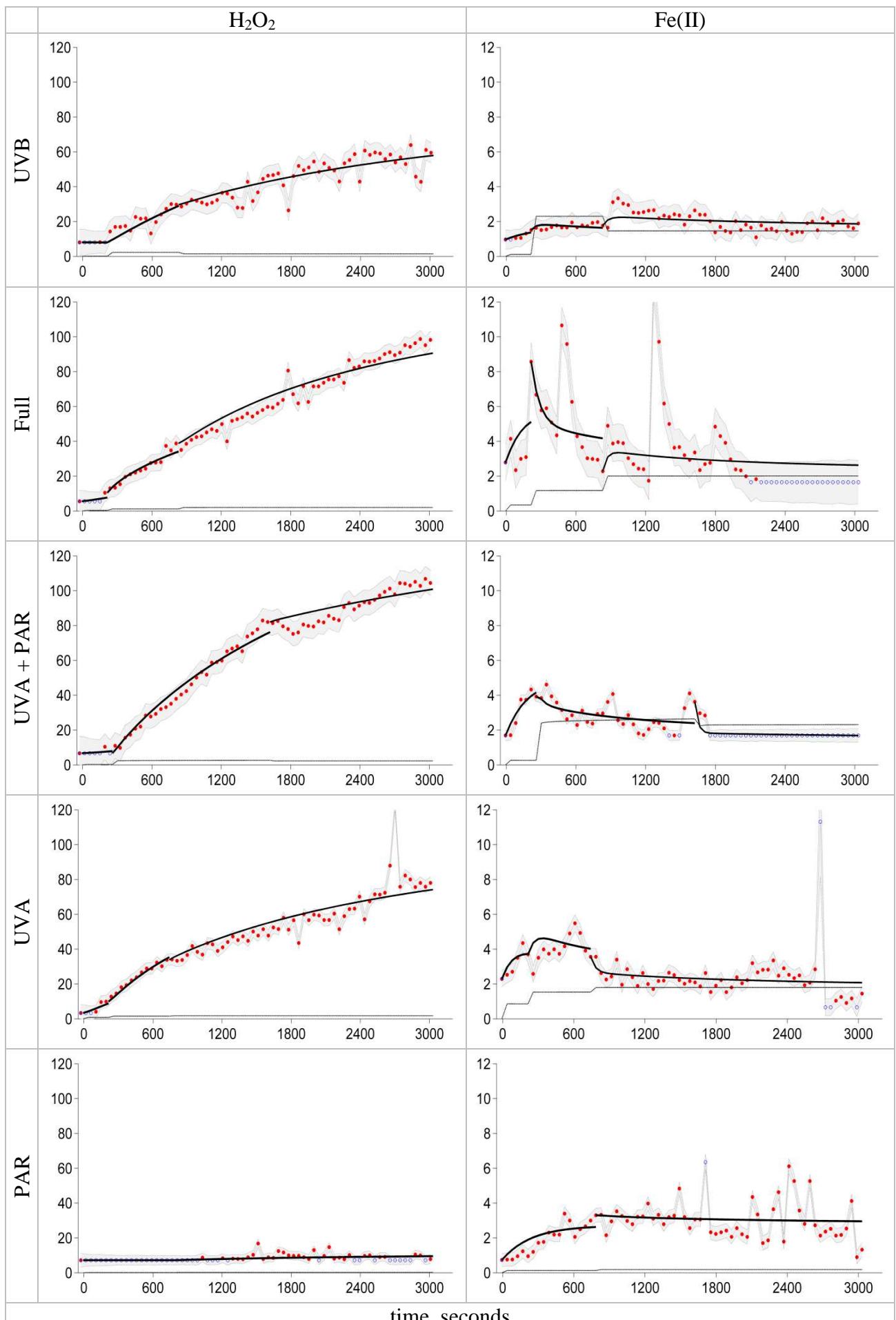


Figure 6.11. 1.0 mg L^{-1} humic acid experimental results (concentration in nanomolar) with model fits. See text for explanation of colours and lines.

Over the first c. 260 s of those experiments containing near UVA (>360 nm) in their irradiating regimes, the increases in Fe(II) are faster than in the UVB and PAR only experiments. The UVB and PAR experiments show similar forms; gradual increase in Fe(II) before attaining a transition from a production to a loss at c. 900 s. The loss stage then tends towards a steady-state Fe(II) concentration \sim 2.5 nM. The UVA experiment attains a maximum Fe(II) concentration, 5.8 nM, within c. 600 s; the following loss leads on to a steady-state concentration of \sim 2 nM. A steady-state also occurs after c. 900s in both the UVB and PAR experiments. The contrasting forms of the experiments would indicate that both PAR and UVA radiation can affect Fe(II) cycling. UVA produces an oscillatory behaviour whilst PAR produces a gradual increase which then declines to a steady-state. This would agree with Sima and Makanova (1997) that it is near UV-R and visible light which affects the cycling of organic ferric iron complexes. However, there is an apparently synergistic effect occurring in the Full spectrum experiment with 1.0 mg L⁻¹ humic acid between UVA and UVB light causing intense cycling of Fe(II).

Assuming there is little O₂^{•-} production under PAR due to minimal H₂O₂ formation (achieved modelled O₂^{•-} $<$ 0.5 nM); though it may be the case that in fact there are low concentrations of catalysts for O₂^{•-} dismutation. What can be supposed is that the concentrations of Fe(II) seen would then be only due to a photochemical organic LMCT and not a reduction of Fe(III) by either O₂^{•-} or H₂O₂. That there are similarities between the PAR and UVB experimental Fe(II) traces even with the differences in H₂O₂ production, maximum achieved H₂O₂ concentrations 10 and 60 nM respectively (Figure 6.11), then suggest that the H₂O₂ concentration achieved in the UVB experiment is insufficient to greatly affect the redox cycling of Fe(II). That the oscillatory Fe(II) behaviour occurs concurrently with more rapid H₂O₂ production, as in the Full, UVA+PAR and UVA experiments, which attain higher concentrations, maximum concentrations, 90, 100 and 80 nM respectively, may then suggest that under those experimental conditions involving the UVA influenced production of H₂O₂, there is a coupling of the H₂O₂ and Fe(II) cycles.

Model fits on the H₂O₂ data (Figure 6.11) are reasonable, though the model has trouble being constrained to the constant increase in the Full spectrum experiment, as the Fe(II) generally shows a decrease in concentration. Due to the oscillating behaviour of Fe(II) in those experiments containing UVA, model fits are generally poor. However, they do represent a mid point for the Fe(II) observations but not the variation, as is the case for the PAR experiment. In the PAR experiment the slow initial increase in Fe(II) could not be modelled. This inability in the model is a systematic fault as it was also unable to adapted to the NMO experiments under

the influence of UVB radiation (Figure 6.04) which also show an initial linear increasing production of Fe(II).

6.03.04 Set 4: 2.0 mg L⁻¹ Humic Acid at ~ pH 7.5, Light Regime Comparison Experiments

pH & Temperature

The starting pH for the 2.0 mg L⁻¹ humic acid light regime comparison experiments was similar for all but the UVA+PAR experiment; most experiments range between pH 7.56- 7.59 whilst the UVA+PAR experiments starts at pH 7.32. Initial temperatures were within ± 0.8 °C of 26.6 °C. The O₂ starting concentrations from the range of initial temperatures was between 198.9 – 204.2 $\mu\text{M kg}^{-1}$ based on the methodology of Weiss (1970). Changes in pH and temperature for each experiment are shown in Figure 6.12. pH is relatively stable over the first c. 900 s of the light phase of the experiments; which was not seen in the previous experiments at a higher pH. After c. 900s the pH then increases for all experiments by between 0.1 and 0.2 pH units. Temperatures were generally stable throughout the experiments for all except the UVA only experiment which decreased by ~ 1 °C over the full term, 3000 s.

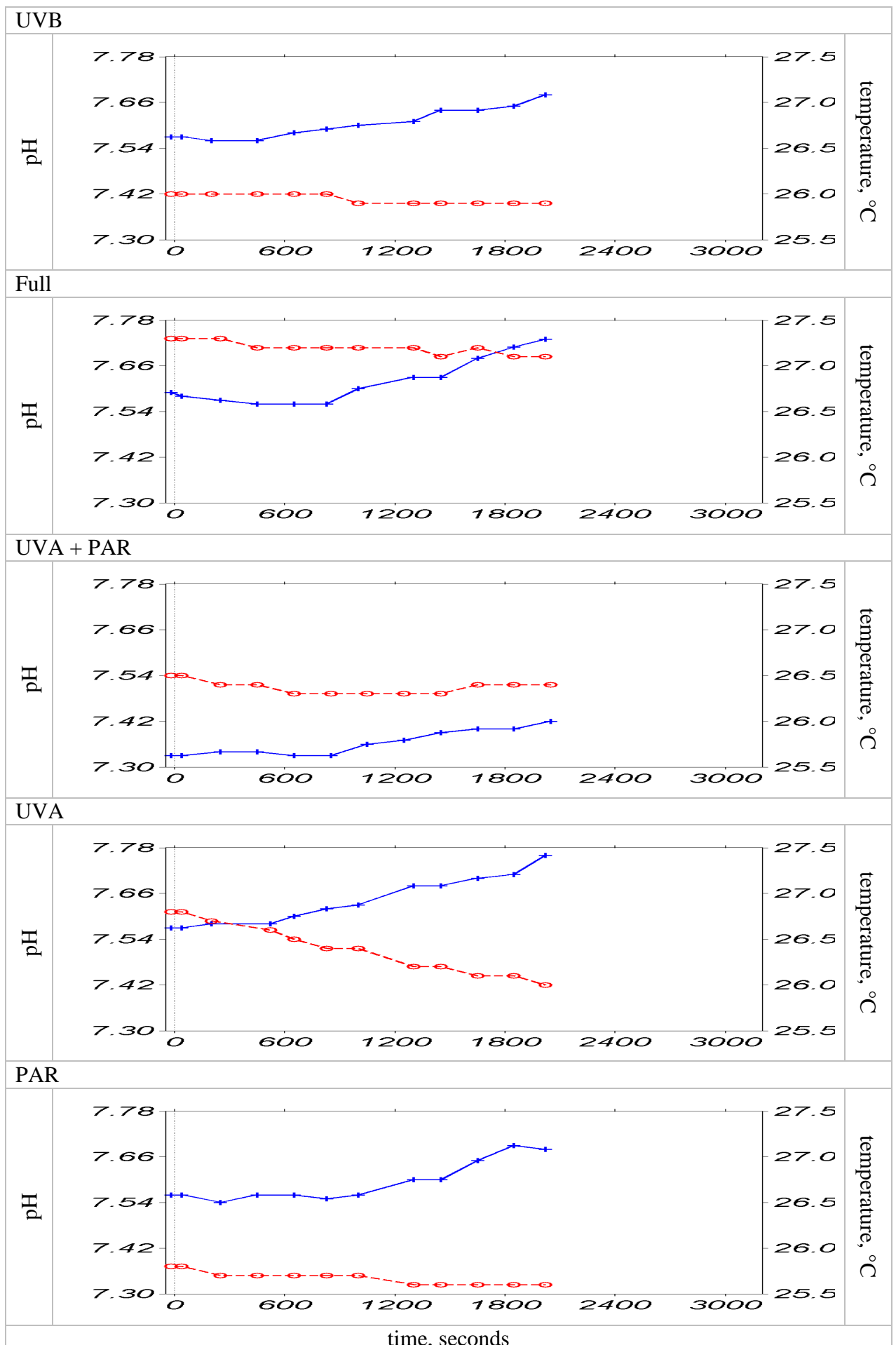


Figure 6.12. pH (blue line with +) and temperature (red line with o) change for the 2.0 mg L⁻¹ humic acid experiments.

Stage Times

Stage times used to govern the model fits for the 2.0 mg L^{-1} humic acid experiments are shown in Figure 6.13. The 2.0 mg L^{-1} humic acid experiments have three stages based on the form of the H_2O_2 results; these correspond to an initial rapid production, an intermediate stage and in the case of these experiments the third stage represents a loss of H_2O_2 from the system. Only two previous experiments indicated rapid H_2O_2 production, these were NMO Full spectrum experiments (Figure 6.04) - seawater only, repeat one, and the 8.8 % 0.2 μm filtered NMO, repeat one. With respect to the 1.0 mg L^{-1} humic acid experiments, though there is a doubling of the humic acid concentration, the second factor within the experiments was the lower pH medium and this may have had an affect on the production of H_2O_2 . As the rate of disproportionation of HO_2 , the conjugate base of $\text{O}_2^{\bullet-}$, decreases with decreasing pH (Millero, 1987) the rapid increase must instead be related to the catalysed dismutation of $\text{O}_2^{\bullet-}$. The decreased pH can act to increase the half life of Fe(II) in seawater from 2 minutes (pH 8.1) to c. 22 minutes (pH 7.5) (Millero et al., 1987). The lower pH may also alter the dissociation of organic material (Millero et al., 2009). Intermediate phases show a decreasing length of time from Full > UVB > PAR > UVA+PAR > UVA.

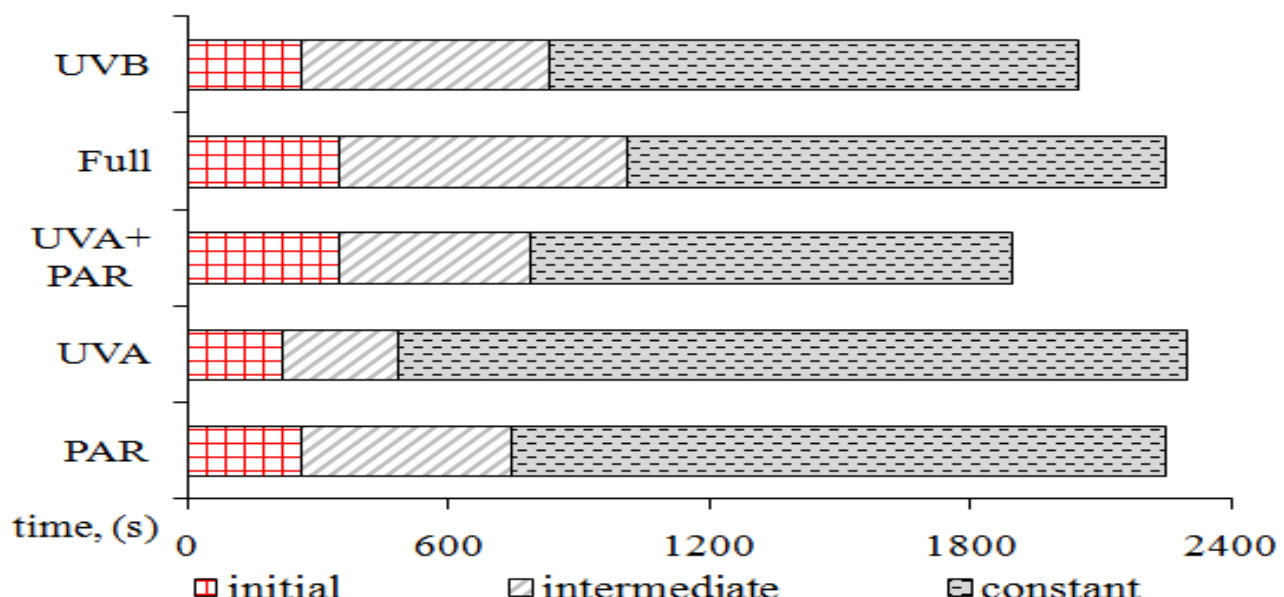


Figure 6.13. 2.0 mg L^{-1} humic acid stage times

H₂O₂ Apparent Rates

The apparent production rates for the ~ pH 7.5, 2.0 mg L⁻¹ humic acid experiments are given on in Table 6.07. The initial production rates are between ~1000 nM h⁻¹ (UVA+PAR) and ~2500 nM h⁻¹ (UVB). These high initial apparent rates can be attributed to the organic catalysed dismutation of O₂[•] from within humic substances. This can be primarily through the redox structures, quinone-hydroquinone, (Goldstone and Voelker, 2000), which with a lower pH 7.5, compared to pH 8.3, become more reactive. What is also interesting is the change in order for the reactivity of the organic material to the irradiating regime in the intermediate stage; in the 1.0 mg L⁻¹ experiments, the apparent rates decreased from UVA+PAR > Full \approx UVA > UVB >> PAR where as in the 2.0 mg L⁻¹ experiment the apparent rates decreased from UVB > Full > UVA = PAR > UVA+PAR. In the 1.0 mg L⁻¹ experiments the UVA irradiation induced the fastest production of H₂O₂ whereas in the 2.0 mg L⁻¹ experiments it was the UVB. With UVB light being primarily responsible for the photodecomposition of humic acid based organic materials (Kieber et al., 1990; Mopper et al., 1991) it may be that this photodecomposition will increase with the lower pH.

Table 6.07. 2.0 mg L⁻¹ humic acid experiments: LODs and H₂O₂ apparent stage rates.

experiment	LOD		H ₂ O ₂ apparent stage rates (nM h ⁻¹)		
	H ₂ O ₂	Fe(II)	initial	intermediate	constant
	nM	nM			
UVB	0.8	0.54	2521	443	-294
Full	1.5	0.26	1512	165	-142
UVA+PAR	18	0.41	1027	129	-40
UVA	18	0.39	1552	148	-54
PAR	25	0.39	1552	148	-54
cold water, Yocis et al. (2000)		range	0.2 – 11 nM h ⁻¹		
warm water, Moore et al. (1993)		range	42 – 134 nM h ⁻¹		

Fe(II) LODs from within the 2.0 mg L⁻¹ experiments range between 0.26 – 0.54 nM and are comparable to those from within the 2.0 μ m filtered NMO experiments (Table 6.05). The H₂O₂ LODs cover an order of magnitude, those for the UVA+PAR, UVA and PAR experiments are around 20 nM. These are high relative to all other experiments and are due to an increase in the sensitivity of the PMT and the affect it has on the stability of the measurement of chemiluminescence.

Results with Model Fits

H_2O_2 experiment results (Figure 6.14) indicate that UVB radiation has a large effect on the production of H_2O_2 . Over the first two stages this irradiating regime promotes the fastest apparent production and has the fastest rate of loss in the constant stage (Table 6.07). What is interesting is the antagonistic affect in the Full regime experiment on the production of H_2O_2 which also includes the UVB bulb. With ~ 100 nM less H_2O_2 produced and a 50 % slower apparent rate of loss, the initial pHs for the UVB and Full spectrum experiments are 7.56 and 7.59 respectively and they both increase by 0.1 and 0.2 pH units respectively, suggesting that the difference is not due to the pH. Therefore there is an effect of near UVA (>360 nm) radiation acting to retard the affect of UVB photo-bleaching of humic organic material (Kieber et al., 1990; Mopper et al., 1991). With respect to the UVA there is also a synergistic affect with PAR as the UVA+PAR experiment does not show a pronounced loss but instead a steady-state in the system. This is contrary to the calculation of apparent H_2O_2 rates (Table 6.07); the difference can be explained by the transition point between stages coinciding with a spike or dip. The lower pH in these experiments has promoted the reactivity of humic acids towards PAR. There is a 2-stage production of H_2O_2 under the influence of PAR, not seen in either the 1.0 mg L^{-1} humic acid, pH 8.3 experiments (Figure 6.07) or the $2.0\text{ }\mu\text{m}$ filtered NMO, pH 8.1 experiments (Figure 6.11).

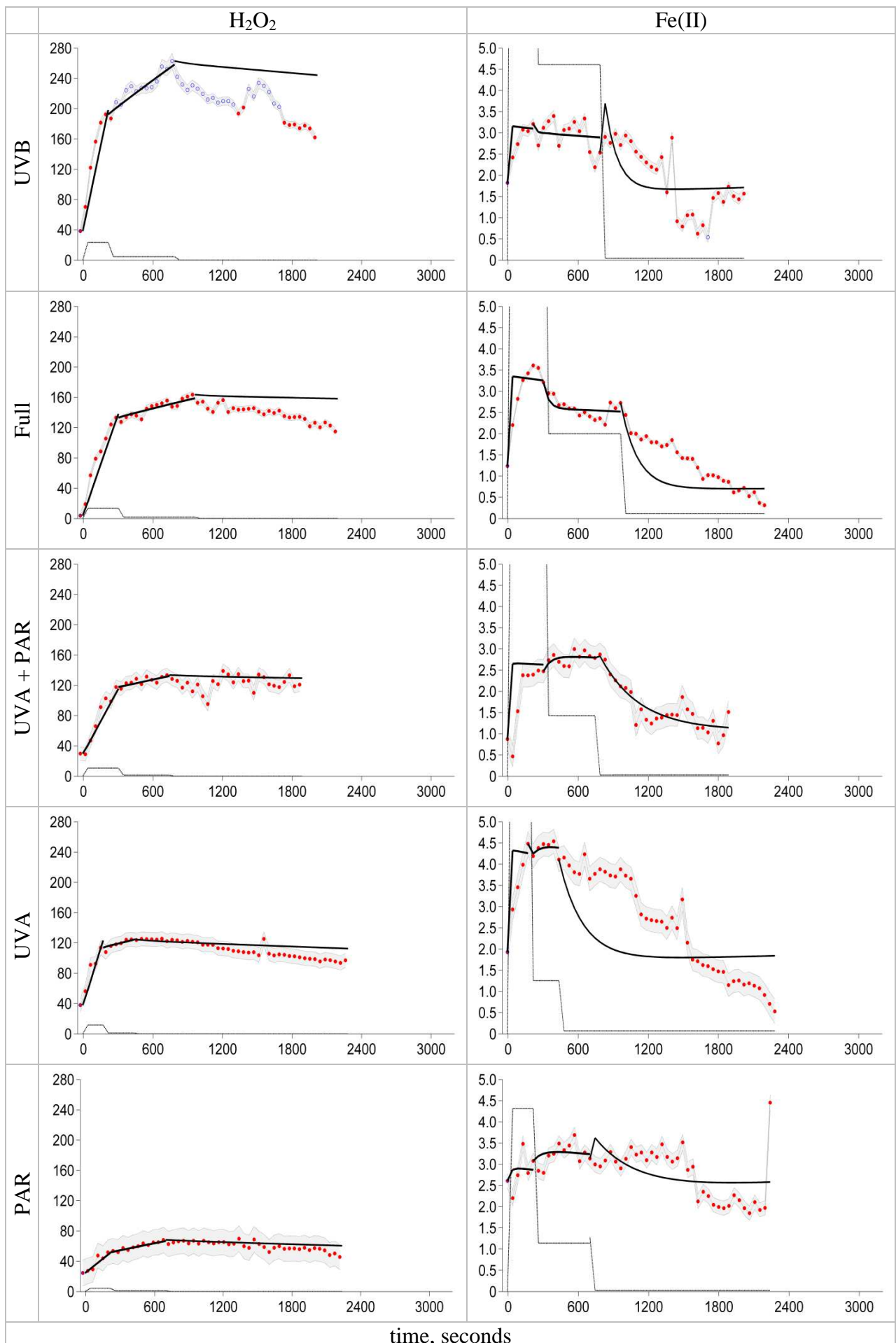
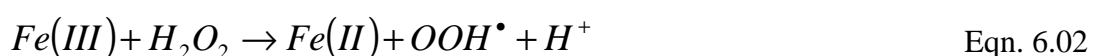


Figure 6.14. 2.0 mg L^{-1} humic acid experimental results (concentration in nanomolar) with model fits. See text for explanation of colours and lines.

All experiments show an initial rapid increase in Fe(II) concurrently with the rapid increase in H₂O₂ (Figure 6.14). For the UVB incubation this increase is in the region of 1.5 nM whereas with the incubations with predominantly UVA radiation this is > 2 nM; the PAR experiment has an initial increase of ~ 1.5 nM. Within the UVA+PAR and PAR only experiments there is a phenomena directly after illumination where the Fe(II) concentration decreases. Following the initial increase, there is a short-term stabilisation of Fe(II), which lasts the longest in the PAR experiment, c. 1200 s and c. 900s in the UVA+PAR and UVB experiments indicating that it is probably light in the visible range acting to retain Fe(II) within the experiments, potentially through the cycling of ferric-organic complexes (Sima and Makanova, 1997) as also seen with the 1.0 mg L⁻¹ humic acid experiments. This was not seen in the 2.0 µm filtered NMO experiments indicating that the organic molecule involved in the cycling of the ferric-organic complexes is either not present or it is at low concentrations in those experiments.

The model fits for the initial and intermediate stages for Fe(II) concentrations were relatively good. The model could not be forced to show a slower initial rapid production as with previous experiments, but the end of the initial stage was reasonably approximated by the model. With respect to the intermediate phase, this was either a fair representation of a mid point, or followed the loss of Fe(II) reasonably well as in the Full spectrum experiment. For the UVA and Full spectrum experiment, Fe(II) shows a linear loss from the system in the constant phase. For these experiments the model was unable to accurately mimic this rate of loss, instead it tended to produce an exponential decline. Either Fe(II) is being oxidised at a slower rate than predicted by the model or there is a production mechanism in place. The H₂O₂ observations show a loss from the experiments in the constant stage for all except the UVA+PAR experiment; this experiment has a corresponding Fe(II) model fit which is a good representation of the observations. The loss of H₂O₂ during short-term (< 2 h) photo-irradiation experiments has been seen in freshwater at pH 6 (Southworth and Voelker, 2003). For a decreased rate of Fe(II) loss coupled with a decrease in the H₂O₂ concentrations requires a sink for H₂O₂ which can regenerate Fe(II) into the system which is not included within the model. The proposed mechanism for this is the catalytic reduction by H₂O₂ of Fe(III), Equation 6.02, generalised from Barb et al. (1951).



The initiation for this reaction is a hydroxyl ion induced decomposition of H₂O₂ - equation 6.03 (Barb et al., 1951). For all experiments pH is seen to increase from c. 900s onwards into the experiment. Equation 6.02 will only occur when the ratio of H₂O₂ to Fe(II)

increases and as shown the 2.0 mg L⁻¹ experiments have produced the highest relative H₂O₂ concentrations. This result suggests that at the experimental pH there is sufficient H₂O₂ for there to be to H₂O₂ decomposition by the hydroxyl ion. The presence of reduced copper will initially react with H₂O₂. However, when this has been preferentially reduced only then will equation 6.02 occur and may explain why there is a > 900 s lag with the experiments.



6.04 Model Discussions

Model fitting to the observations of H₂O₂ and Fe(II) was through four fitting parameters; two of these are directly related to the irradiating regime, k_{CDOM} (M s⁻¹) (Equation 6.04) and k_{RED} (s⁻¹) (Equation 6.05).



The further two fitting parameters are related to sink terms for O₂^{•-}, the first being directly related to the cycling of iron through the reduction of Fe(III), k_{RO} (M⁻¹ s⁻¹) (Equation 6.06). The second of these incorporates all other sinks for O₂^{•-}; these are related to the cycling of other trace metal species and organic material, k_{SOS} (M⁻¹ s⁻¹) (Equation 6.07). However, this sink, which includes reactions with copper does not include the H₂O₂ production mechanism through the reaction of reduced metals and organic material and O₂^{•-}.



Estimates from model fits for k_{CDOM} ranges from 1.2 x 10⁻¹¹ M s⁻¹ (Weber et al., 2005) to 9.5 x 10⁻¹⁰ M s⁻¹ (Meunier et al., 2005), with a range based on a series of fits from 9.2 x 10⁻¹² to 1.43 x 10⁻¹⁰ M s⁻¹ (Steigenberger et al., 2010).

The first experimentally based calculation for seawater of k_{RED} was, 6.3 x 10⁻⁴ s⁻¹ by Miller et al. (1995). From modelling work by Weber et al. (2005) the value was calculated as 1.53 x 10⁻⁵ s⁻¹. In Arctic waters the apparent production of Fe(II) has been measured between 9.1 x 10⁻² and 5.3 x 10⁻³ s⁻¹ and decreases as irradiating wavelength decreases (Laglera and van den Berg, 2007).

For inorganic and organically complexed Fe(III), k_{RO} has been calculated as 1.5 x 10⁸ M⁻¹ s⁻¹ and 1.2 x 10⁸ M⁻¹ s⁻¹ respectively (Rose and Waite, 2002) and through model fittings has

been estimated at $<10^4 \text{ M}^{-1} \text{ s}^{-1}$ (Meunier et al., 2005) or $8.56 \times 10^6 \text{ M}^{-1} \text{ s}^{-1}$ (Steigenberger et al., 2010). The results from Rose and Waite (2002) suggest that there is little difference between the rate of $\text{O}_2^{\bullet-}$ reduction of organically and inorganically complexed Fe(III). However the large range > 4 orders of magnitude may be explained by the organic material used - SRFA (Rose and Waite, 2002) and $\sim 0.4 \mu\text{m}$ filtered non specific NMO, HMW organic material (Meunier et al., 2005) or specifically *Phaeodactylum tricornutum* exudate (Steigenberger et al., 2010).

The model estimation for k_{SOS} is treated as a second order rate reaction; this is different to most other authors. Steigenberger et al. (2010) did not use a sink for $\text{O}_2^{\bullet-}$, whereas Meunier et al. (2005) used a first order rate constant, 1.16 s^{-1} , which was estimated from Voelker et al. (2000) and Goldstone and Voelker (2000). Rose and Waite (2002) did invoke a second order reaction though this was only with inorganic copper, Cu(I), 2.0×10^9 and Cu(II), $6.6 \times 10^8 \text{ M}^{-1} \text{ s}^{-1}$, with a copper concentration of 0.45 nM. The reaction with Cu(II) has been measured up to $1.1 \times 10^{10} \text{ M}^{-1} \text{ s}^{-1}$ (Zafiriou et al., 1998). With respect to Mn(II) its reduction by $\text{O}_2^{\bullet-}$ in seawater has been estimated to be of the order of 6×10^6 to $1 \times 10^7 \text{ M}^{-1} \text{ s}^{-1}$ (Hansard et al., 2011). With only organic material, superoxide dismutation has been calculated in the tropical open ocean and ranges between, 1.0×10^4 to $3.5 \times 10^5 \text{ M}^{-1} \text{ s}^{-1}$ (Heller and Croot, 2010a). The primary organic constituents in $0.2 \mu\text{m}$ filtered seawater which have been suggested to induce this dismutation are, quinones, glutathione and/or siderophores (Heller and Croot, 2010a). Coastal humic substances have higher first order rates of dismutation of superoxide (Goldstone and Voelker, 2000) compared to open ocean waters (Heller and Croot, 2010a).

6.04.01 NMO Full Spectrum Experiments Kinetics

k_{CDOM}

From within the seawater only and $0.2 \mu\text{m}$ filtered NMO experiments k_{CDOM} ranged from 3.3×10^{-10} to $2.9 \times 10^{-7} \text{ M s}^{-1}$ (Figure 6.15). The ranges in the k_{CDOM} values are generally higher than the calculated published values of Weber et al. (2005), Meunier et al. (2005) and Steigenberger et al. (2010). Only the constant stage in the second seawater experiment and the second 4.4 % and 8.8 % fresh NMO experiments had k_{CDOM} of a comparable magnitude to the published values. The rate of photochemical $\text{O}_2^{\bullet-}$ production decreased for all NMO experiments from intermediate to constant stage in the experiments; the rate also decreased from the first to the second repeat experiments relative to both stages. During the intermediate stage the rate of production tended to increase with increasing concentration of NMO from 4.4 to 8.8 %, and again to an equivalent concentration but with 50 % of the NMO as

aged (> 4 months), this trend in the production rate is also true for the second 4.4% experiment with low, < 10 nM, production of H_2O_2 . In the constant stage the first repeat experiments all increase in the same order as in the intermediate stage; however, for the second 8.8 % experiment the rate of k_{CDOM} is an exception as it decreases from experiment 1 to 2.

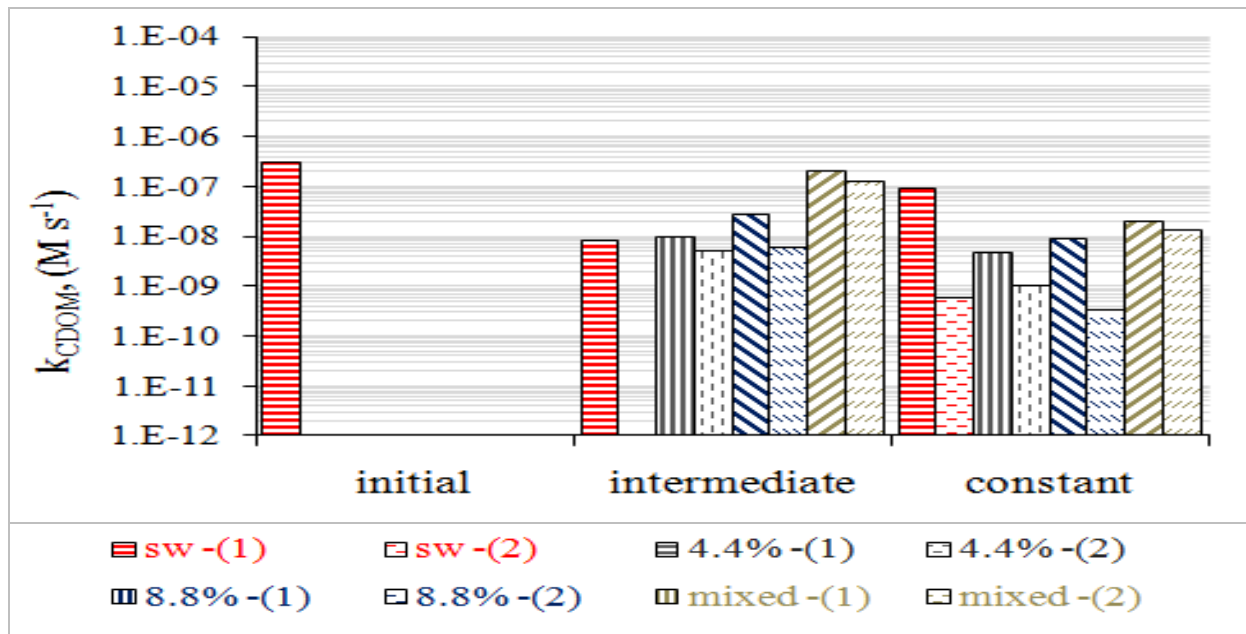


Figure 6.15. k_{CDOM} rate constants for the $0.2 \mu\text{m}$ filtered NMO Full spectrum experiments.

CDOM is produced through the bacterial reworking of phytoplankton exudates (Rochelle-Newall and Fisher, 2002) and the experimental results suggest that as the fresh NMO ages under storage the sensitivity of the organic material towards photochemical oxidation decreases. However, the sensitivity increased when using the mixed NMO, suggesting that a lengthened storage time increases the bacterial reworking of the NMO towards a more photo-reducible material. The initial bacterial reworking of phytoplankton exudates may not have initially formed the requisite CDOM. The *Fragilariopsis cylindrus*, grown in a low iron, Aquil medium, was grown as an axenic culture and as such the required bacteria should not have been present.

Comparing, the first and second experiments, the smallest relative differences occur within the mixed experiments; assuming a relatively stable photochemically reactive organic material in the aged NMO (*Thalassiosira pseudonana*) than the difference maybe due to the use of the fresh NMO (*Fragilariopsis cylindrus*). As a measure of the photo-induced reactivity of the organic material towards the reduction of oxygen, the results would suggest that this reaction rate decreases with the aging of the organic material, i.e. from repeat one to two. The reaction rate also decreases with the continued irradiation of the sample indicating either the affect of the UV photo-bleaching (Micinski et al., 1993; Miller et al., 1995; Rijkenberg et al., 2005; Rose and

Waite, 2003b) or the change from HMW to LMW organic material (Hama et al., 2004) on the reactivity of the organic material. The reaction rate for the second seawater experiment is within the same order of magnitude, 10^{-10} M s⁻¹, as the second 8.8 % fresh NMO experiment. This again indicates that bacterial reduction of organic material to form HMW organics, suitable for photochemical reactivity, may occur on time scales longer than a week, as suggested by Hama et al. (2004).

k_{RED}

With respect to the model fits for Fe(II) they were not as well constrained. However, in terms of the calculation of the sum of squares of the error, residuals, from the observations they are generally four to five orders of magnitude lower (Appendix, Table A6.01) than the H₂O₂ fits. In the experiments containing NMO, those with organic material (aged and fresh) to 8.8 % indicate that k_{RED} in the repeat experiments is higher (Figure 6.16). The second 4.4 % experiment with low H₂O₂ production had a lower k_{RED} than in the first experiment; this comparison would suggest that the production of H₂O₂ is related to the production of Fe(II). Low H₂O₂ production subsequently requires lower photo-reduction of Fe(III) to sustain the lower H₂O₂ and Fe(II) steady-states in the experiments (Figure 6.04). Two experiments did however show a slight trend away from a Fe(II) steady-state; these were the second 4.4 % and first 8.8 % NMO experiments, showing a slight production and loss respectively.

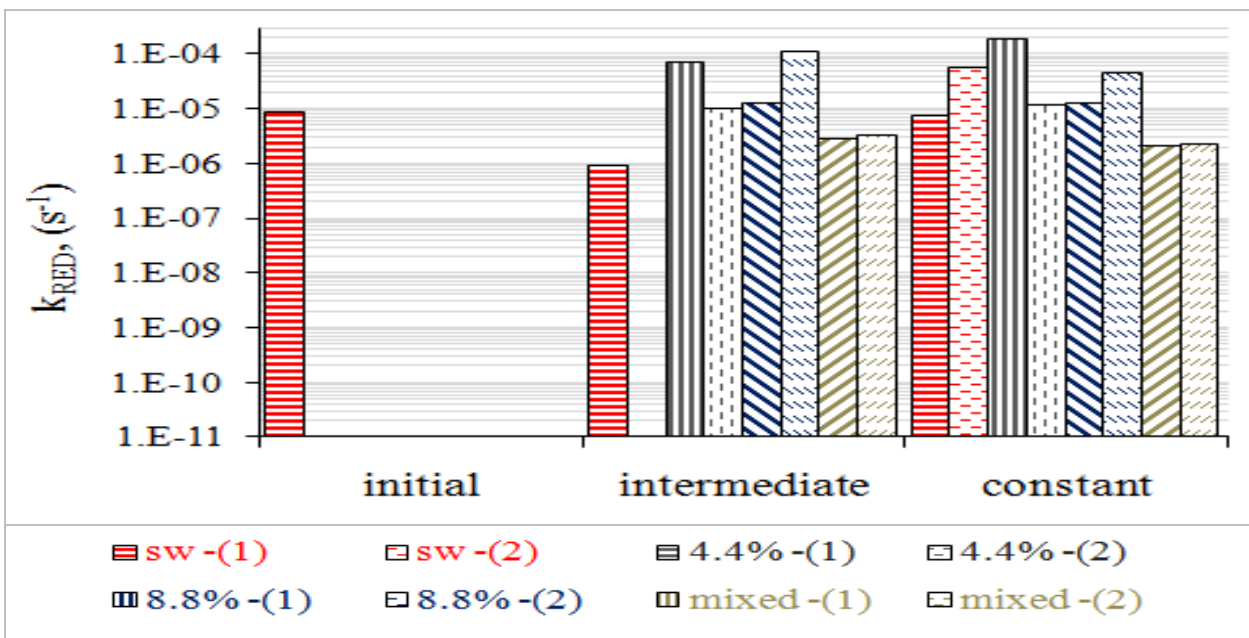


Figure 6.16. k_{RED} rate constants for the 0.2 μ m filtered NMO Full spectrum experiments.

For a Fe(II) steady-state to be in place requires that either the organic complexation of Fe(II) is faster than its oxidation – organic material can either inhibit (Miles and Brezonik, 1981; Rijkenberg et al., 2008; Shaked et al., 2004; Steigenberger et al., 2010) or enhance (Santana-Casiano et al., 2000) this rate of oxidation – or that the photo-chemical cycling between organic Fe(III) to Fe(II) is rapid in terms of the analytical timings. Organic complexes of ferric iron retain iron in a soluble form, with these organic complexes showing a greater potential for photo-reduction (Sima and Makanova, 1997). With the 0.2 μm filtered NMO tending to show near Fe(II) steady-states and the rate of k_{RED} in the first experiments indicating a lower reactivity than in the second experiments, it may be that with fresher organic material it is complexes with Fe(II) retaining the Fe(II) in the steady-state whereas as the fresh organic material ages there are less complexes with Fe(II) but to compensate the photo-reactivity of the Fe(III) complexes increase.

The question arises that with low H_2O_2 and the required decrease in k_{RED} to require the requisite Fe(II) steady-state, is it the reduced rate of oxidation of organically complexed Fe(II) (Miles and Brezonik, 1981; Rijkenberg et al., 2008; Shaked et al., 2004; Steigenberger et al., 2010) by the lower H_2O_2 concentration or an increased photo-reduction of Fe(III) organic complexes? That it is organically complexed and not inorganic iron species which are considered is because the rate of inorganic photo-reduction of Fe(III) is relatively slow (Sulzberger and Laubscher, 1995; Wells and Mayer, 1991). For the constant stage of the experiments the second seawater only experiment has the highest rate of photo-chemical reduction of Fe(III), for all except the first 4.4 % NMO experiment. This high photo-reduction may be indicative of the findings of Rose and Waite (2002) that there is little difference between the photo-reduction rate of organically and inorganic Fe(III), especially if the assumption is made that through storage there are lower concentrations of residual organically complexed Fe(III) retained in the system. The intermediate and constant stages in all the NMO experiments and the constant stage in the seawater only experiments have calculated k_{RED} values in line with those of Miller et al. (1995) $6.3 \times 10^{-4} \text{ s}^{-1}$, and Weber et al. (2005) $1.53 \times 10^{-5} \text{ s}^{-1}$.

k_{RO}

Under the assumption that available Fe(III) is limited in the redox cycling with O_2^\bullet due to aging of the seawater and the *Thalassiosira pseudonana*; aging acts to reduce the reactivity of iron (oxy)hydroxides (Fujii et al., 2006). Also, because there are low iron concentrations within the *Fragilariaopsis cylindrus* organic material, k_{RO} would become important when Fe(II) is in a steady-state, and subsequent redox cycling would be initiated from newly organically

complexed Fe(III) occurring within the experiment. k_{RO} is a mechanism for $O_2^{\cdot-}$ to be directly involved in the redox cycling of trace metals (Barb et al., 1951), and ultimately decreases the $O_2^{\cdot-}$ available for the dismutation to H_2O_2 . For the fresh NMO experiments (4.4 and 8.8 %) in the intermediate phase (Figure 6.17) k_{RO} decreases from the first to the second experiment with an order of magnitude difference in the 8.8 % NMO repeat experiments. The second 4.4 % NMO experiment with low H_2O_2 is the only experiment using fresh NMO which has an increase in k_{RO} in the constant phase. k_{RO} for the seawater only experiments showing both a three stage increase in H_2O_2 or a constant production have similar values for k_{RO} , 7.1×10^3 to $8.6 \times 10^3 \text{ M}^{-1} \text{ s}^{-1}$, though these are less than those containing NMO, except for the second 8.8 % NMO experiment constant stage and are in line with the estimations of Steigenberger et al. (2010) $8.56 \times 10^6 \text{ M}^{-1} \text{ s}^{-1}$, and Meunier et al. (2005) $<10^4 \text{ M}^{-1} \text{ s}^{-1}$.

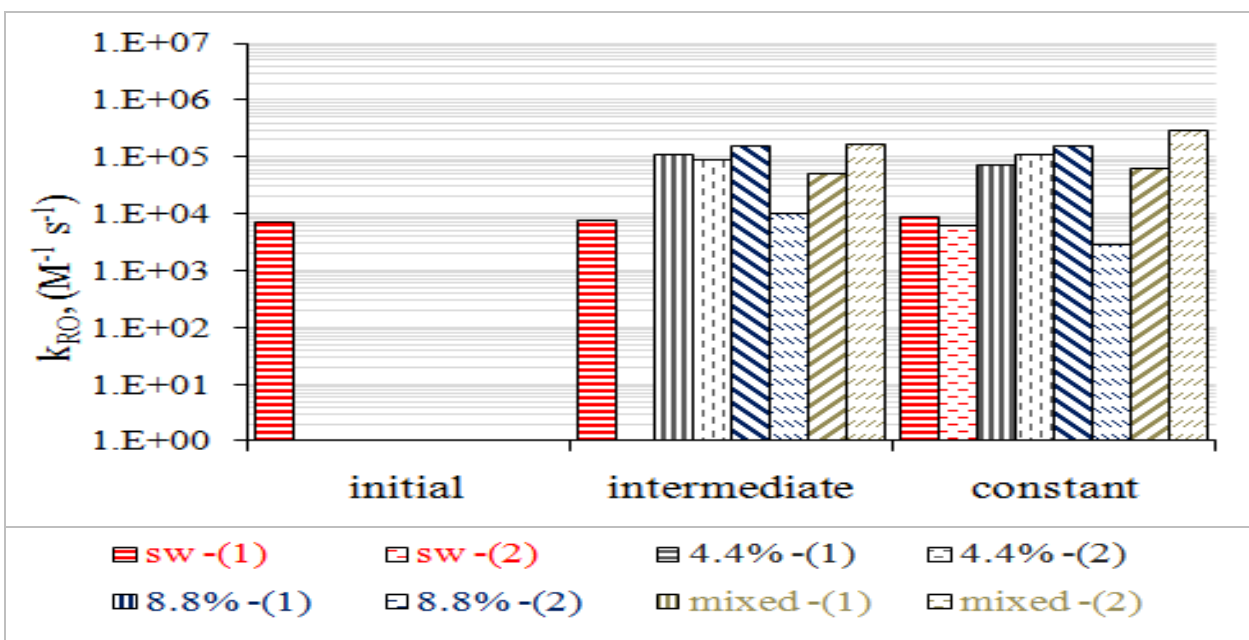


Figure 6.17. k_{RO} rate constants for the $0.2 \mu\text{m}$ filtered NMO Full spectrum experiments.

k_{SOS}

All other sinks for $O_2^{\cdot-}$ were utilised within the model under the k_{SOS} second order rate constant; however, there is a caveat within their use as they do not induce the catalysed dismutation of $O_2^{\cdot-}$ to H_2O_2 . The calculated range of second order reaction values for k_{SOS} is, 1.7×10^7 to $1.0 \times 10^{10} \text{ M}^{-1} \text{ s}^{-1}$ (Figure 6.18). These calculated values are inline with those for $O_2^{\cdot-}$ reactions with inorganic copper species, Cu(I), 2.0×10^9 and Cu(II), $6.6 \times 10^8 \text{ M}^{-1} \text{ s}^{-1}$ (Rose and Waite, 2002) and $1.1 \times 10^{10} \text{ M}^{-1} \text{ s}^{-1}$ (Zafiriou et al., 1998). For the fresh NMO experiments it appears that k_{SOS} decreases with increasing storage time, potentially indicating that the

photochemical reactivity of the organic material to a LMCT on Cu(II) to Cu(I) (Moffett and Zika, 1983) decreases. As expected this rate constant had to be increased within the model when the observed concentrations of H₂O₂ were low, as in the second 4.4 % NMO experiment, though it was in a similar order of magnitude as the mixed NMO experiment.

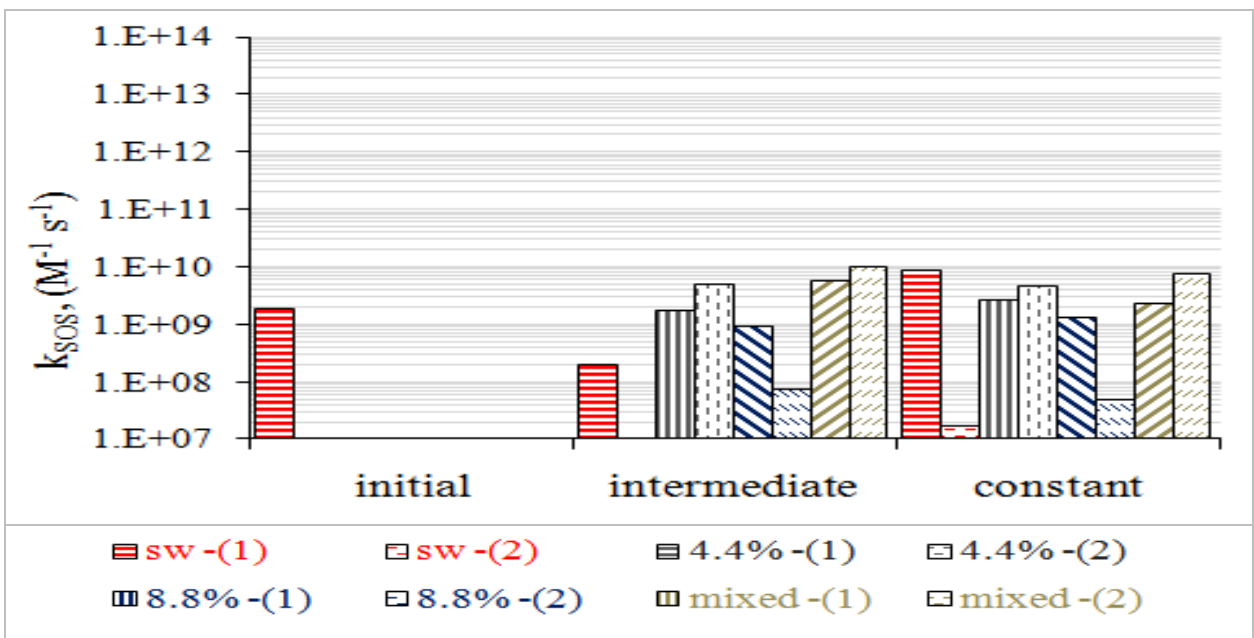


Figure 6.18. k_{SOS} rate constants for the 0.2 μm filtered NMO Full spectrum experiments.

6.04.02 Light Regime Comparisons – k_{CDOM}

11 % v/v 2.0 μm Filtered *Thalassiosira pseudonana*

The values for k_{CDOM} in the 2.0 μm filtered *Thalassiosira pseudonana* combined to 11%, NMO experiments shows a distinct trend related to both irradiance and wavelength (Figure 6.19). As irradiance decreases from Full spectrum, to UVA+PAR to single light regimes (Table 6.01) the rate of k_{CDOM} decreases within the intermediate and constant stages. However, in the initial stage the UVA source has a higher production rate than the UVB source indicating that it is the UVA during the initial stage affecting the increased production rate. The UVB experiment during the constant stage was the only NMO experiment to indicate an apparent loss of H₂O₂, -8 nM h⁻¹ (Table 6.05); this was with a corresponding production of superoxide at 1.1 x 10⁻⁸ M s⁻¹.

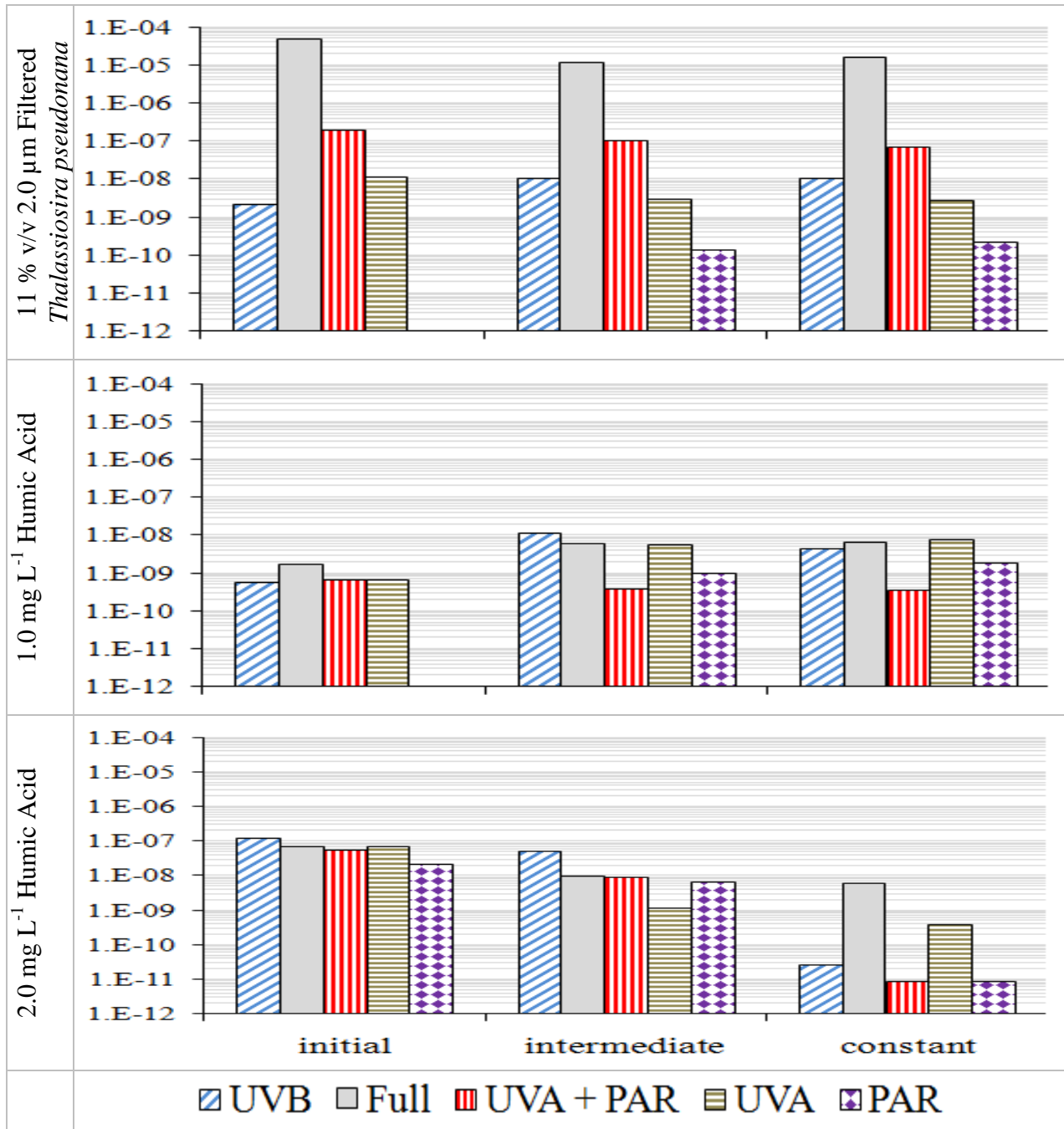


Figure 6.19. k_{CDOM} ($M s^{-1}$) light regime comparisons.

The measured PAR contained approximately 1.5 % of UV-R ($0.1 W m^{-2}$) and 0.3 % of PAR ($11.6 W m^{-2}$), compared to Zepp and Cline (1977), and was sufficient to enable an observed production of H_2O_2 in the constant stage of the experiment. The preferred reactant for catalysed dismutation of O_2^\bullet is Fe(II) (Fujii et al., 2010). The Fe(II) concentration in the experiment with 2.0 μm filtered NMO and PAR was observed to be low, $< LOD$ of 0.64 nM. Under these light conditions and assuming that H_2O_2 production is due to uncatalysed, slow, dismutation of O_2^\bullet , low Fe(II) concentrations, than the apparent production rate for H_2O_2 , over the constant stage of this experiment, $22 nM h^{-1}$ (Table 6.05), may then be indicative of uncatalysed dismutation. That this rate was similar within also the UVA+PAR and UVA

experiment constant stages of $\text{O}_2^{\cdot-}$ again suggest that this rate can be dependant on experimental conditions. Interestingly this rate is inline with Yocis et al (2000) (with temperature correction) for their measured apparent H_2O_2 production rates in Antarctic waters low in trace metals and organic material. Comparing the $0.2\text{ }\mu\text{m}$ filtered (mixed) NMO Full spectrum experiment (Figure 6.15) and the Full regime experiment (Figure 6.19) utilising $2.0\text{ }\mu\text{m}$ filtered NMO the rate of $\text{O}_2^{\cdot-}$ production increases by 2 orders of magnitude.

1.0 mg L^{-1} Humic Acid

Trends in the 1.0 and 2.0 mg L^{-1} humic acid experiments are not as apparent as that in the NMO experiment (Figure 6.19). In the initial phase of the 1.0 mg L^{-1} experiment k_{CDOM} values are similar for the UVB ($5.5 \times 10^{-10}\text{ M s}^{-1}$), UVA+PAR ($6.4 \times 10^{-10}\text{ M s}^{-1}$) and UVA ($6.4 \times 10^{-10}\text{ M s}^{-1}$) experiments, and the total energy received was also similar, 20.4 , 25.9 and 17.5 W m^{-2} , respectively. The Full spectrum incubation, total energy received 46.7 W m^{-2} , shows the fastest initial rate of $\text{O}_2^{\cdot-}$ production. As the majority of irradiance for the Full spectrum experiment is in the UVA and PAR ranges it would be the combination of these that affects the rate in the initial stage with the light in the UVA range ($315 - 400\text{ nm}$) as the primary energy source. The UVB does contain some UVA, 3.8 W m^{-2} , in the far UVA range $< 360\text{ nm}$.

The PAR experiment (1.0 mg L^{-1}) does not show significant changes in H_2O_2 above the LOD, 7.2 nM . The rate of k_{CDOM} in the intermediate and constant stages for the PAR only experiment is in range of the other experiments. For a system under the influence of PAR radiation this suggests that this is a minimum production rate required to sustain a photochemically produced steady-state H_2O_2 concentration, $k_{\text{CDOM}} 1 \times 10^{-9}\text{ M s}^{-1}$. This is one to two orders of magnitude lower than the models of Weber et al. (2005), Meunier et al. (2005) and Steigenberger et al. (2010).

The 1.0 mg L^{-1} initial stages apparent production rates should have been 0 nM h^{-1} for H_2O_2 ; transition region between stages has the initial stage increasing at the end which distorts the calculation of the apparent production rate stage calculations. The intermediate and constant stages do show apparent H_2O_2 production rates (Table 6.06). k_{CDOM} for the initial stages, except for the Full spectrum experiment, were less than $1 \times 10^{-9}\text{ M s}^{-1}$. The experiments of note are the Full spectrum and UVA+PAR experiments. The UVA+PAR experiment has the lowest values of k_{CDOM} in the intermediate and constant stages, approximately an order of magnitude lower than the other experiments, and has the longest time spent in the intermediate stage, c. 1200 s . This is approximately twice as long as the UVB, FULL and UVA experiments. The UVA+PAR

experiment with k_{CDOM} set to less than $1 \times 10^{-9} \text{ M s}^{-1}$ was the experiment with the highest observed H_2O_2 concentrations in the 1.0 mg L^{-1} humic acid experiments. For the Full spectrum experiment, k_{CDOM} , is relatively low, when compared to the differences in the NMO experiment. What may be occurring is that UVB, UVA and PAR affect different sections of the organic material and antagonistic effects in those experiments with combined irradiating regimes are reducing the rate of $\text{O}_2^{\cdot-}$ production in the intermediate and constant stages of those experiments. Or that the different regimes promote different sinks for $\text{O}_2^{\cdot-}$ and this in turn affects the production of H_2O_2 . This antagonistic affect does not occur for UVB and PAR; this is as there is a high proportion of PAR within the UVB irradiating regime (Table 6.01). In general the effect of irradiating regime is not as straightforward as the experiment using NMO and appears affected by antagonistic effects of irradiating regime on the humic acid.

2.0 mg L^{-1} Humic Acid

Initial phase photo-production of $\text{O}_2^{\cdot-}$ in the 2.0 mg L^{-1} experiments tends to decrease as UVB decreases (Figure 6.19). This trend is not straight forward, as the UVA experiment has a higher production rate than both the Full and UVA+PAR experiments; this was also seen in the intermediate and constant stages of the 1.0 mg L^{-1} humic acid experiments. The difference from the 1.0 mg L^{-1} humic acid experiment may be attributed to the lower pH, and the effect this has on the reactivity of the humic acids and may be promoting those organic constituents reactive to UVB. The trend is similar within the intermediate phase, however, following its initial rapid production rate, k_{CDOM} in the UVA experiments is lower than in both the UVA+PAR and PAR experiments. The model was unable to fit well to the H_2O_2 and Fe(II) observations in the constant production phase of the 2.0 mg L^{-1} humic acid experiments. The exception to this was the UVA+PAR and to some degree the PAR experiment. Both of these experiments have a steady-state H_2O_2 concentration in their constant stage which the model was able to represent (within the scatter of the observation or calculated error of the observations). The other three experiments show a definite loss of H_2O_2 which the model was unable to represent. The values of k_{CDOM} for these experiments are given as the maximum estimated value before the model, during this stage, predicts further increases in the rate of H_2O_2 production.

6.04.03 Light Regime Comparisons – k_{RED}

*11 % v/v 2.0 μ m Filtered *Thalassiosira pseudonana**

The Fe(II) observations of the 2.0 μ m filtered *Thalassiosira pseudonana* combined to 11%, NMO experiments can be split into three groups: Those influenced by UVB, those by UVA and finally the PAR experiment. With respect to the model fits those for the UVA+PAR, UVA and PAR experiments are a fair representations of the Fe(II) observations. The UVB and Full spectrum experiments have similar initial stage k_{RED} values (Figure 6.20). The low k_{RED} value for the UVA+PAR experiment in the initial phase may be a value which could indicate for that stage the fitting parameters were at a local minimum and not the global minimum; this, in part, could be due to the poor fits to the Fe(II) observations.

The initial, intermediate and constant stages indicate similar photo-chemical reduction rates, k_{RED} , in the UVB and Full regime experiments, ranging from 7×10^{-5} to $1.2 \times 10^{-4} \text{ s}^{-1}$. As both UVB and UVA decrease so too does k_{RED} , indicating it is these wavebands that are influential on k_{RED} . Compared to the production of $O_2^{\cdot-}$, which shows a distinct affect with the total energy received, with UVA being the primary initiating source, Fe(II) photo-production appears related more to UV-R, with UVB the most influential in the rate of reduction. This suggest there should be higher concentrations of Fe(II) in the surface microlayer and near surface seawater due to the presence of UVB. Comparing the UVB and Full spectrum experiments, the model results suggests an antagonistic effect between UVB and UVA, as the Full spectrum experiment in the intermediate and constant stages indicates lower rates of reduction than the purely UVB experiment. As there is little change in k_{RED} across the three stages this suggests that there is little UV-R bleaching of NMO affecting this rate.

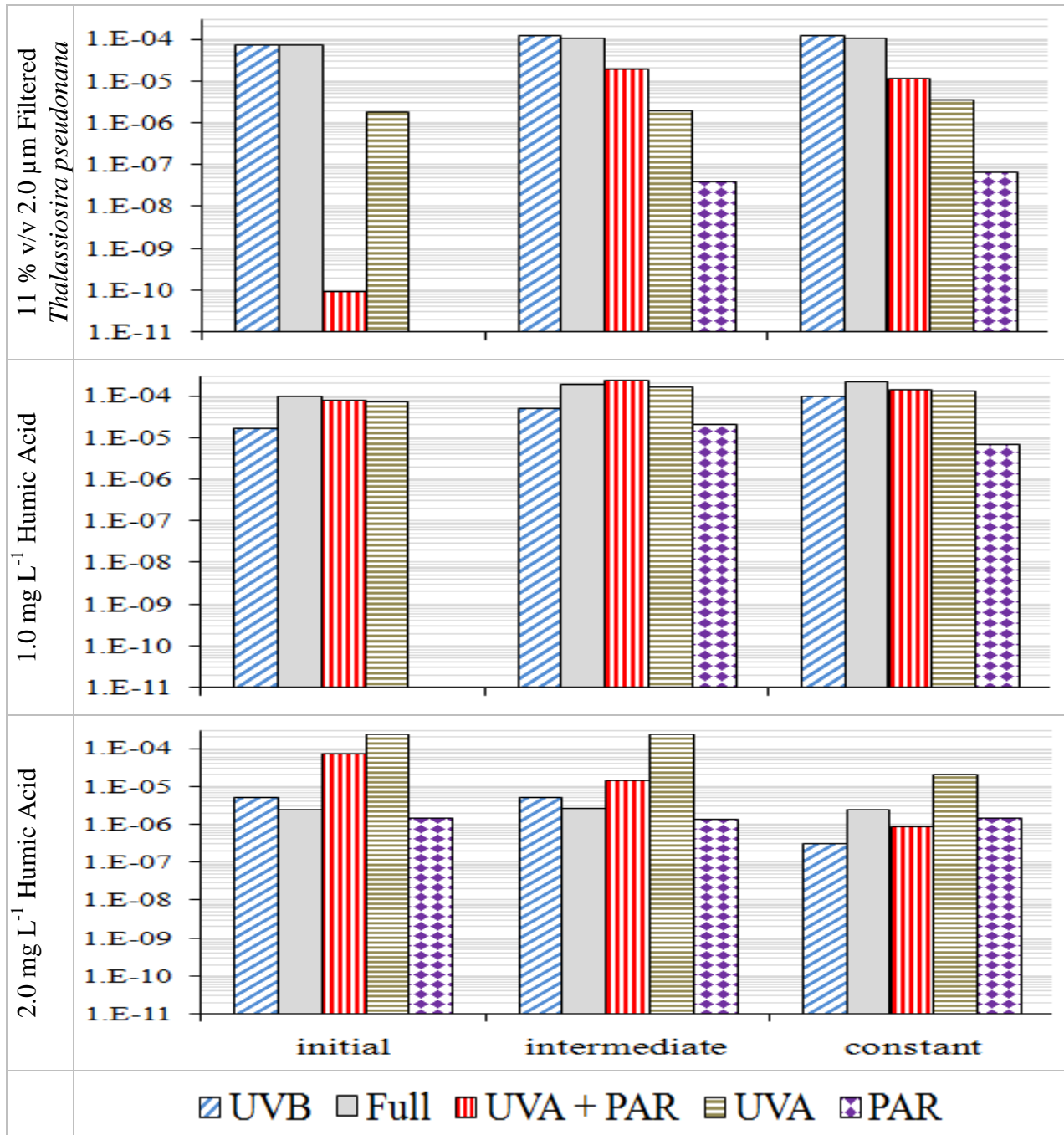


Figure 6.20. k_{RED} (s^{-1}) light regime comparisons.

1.0 mg L^{-1} Humic Acid

Unlike the NMO experiments, it appears that it is the UVA radiation which controls the photo-reduction of Fe(III); with higher k_{RED} values in those 1.0 mg L^{-1} experiments containing UVA (Figure 6.20). In all stages of the 1.0 mg L^{-1} humic acid experiments, those experiments containing significant UVA photo-reduce Fe(III) faster than those with UVB or PAR only. Those systems containing a large quantity of UVA in their irradiating regimes, Full spectrum, UVA+PAR and UVA experiments also show an oscillating Fe(II) trace. The model was unable

to represent these oscillations, though reasonable midpoint values were achieved. Oscillations in Fe(II) have been shown in laboratory experiments through repeated inputs of organic material (Song et al., 2005). If as proposed for the k_{CDOM} humic acid experiments, that in fact there are different organics reacting with different wavelengths, these organics may not be involved in k_{RED} as the rate does not show a significant change between stages. The humic acid appears less reactive to UVB compared to the NMO. That there is some bleaching of the organic material (Micinski et al., 1993; Miller et al., 1995; Rijkenberg et al., 2005; Rose and Waite, 2003b) is to be expected and it may be this, that when caused by both UVB and UVA, results in the oscillatory Fe(II) behaviour. The intermediate stages of these experiments indicate that the UVA+PAR radiation has the strongest affect on k_{RED} . This agrees with Laglera and van den Berg (2007) who estimated that 70% of the apparent production of Fe(II) was due to UVA and PAR wavelengths, and also with Sima and Makanova (1997), who suggest that the organic complexes of ferric iron show the greater potential for photo-reduction with irradiation predominantly in the visible / near UV-R range.

2.0 mg L⁻¹ Humic Acid

The initial stage k_{RED} values would indicate an enhancement of the antagonistic effect occurring in the 1.0 mg L⁻¹ humic acid experiments (Figure 6.20). With respect to the Fe(II) observations in the 2.0 mg L⁻¹ experiments, they show a marked difference in form compared to the 1.0 mg L⁻¹ humic acid experiments and NMO experiments without UVB. UVA irradiation of humic acids at a lower pH relative to the 1.0 mg L⁻¹ humic acid experiments induces the highest rate of reduction, which decreases as other light regimes are introduced, followed by PAR and then UVB, with the antagonistic effect of UVB greater than that for PAR. As the rate of reduction in the initial stage is greater in the UVB than in the Full spectrum and PAR experiments then potentially the changes induced to the organic material and probably the organically complexed Fe(III) undergoing photo-reduction are again in different complexes.

6.04.04 Light Regime Comparisons – k_{RO}

k_{RO} as a second order rate constant for all the experiments (Figure 6.21) are generally between the ranges of Meunier et al. (2005), $<10^4$ M⁻¹ s⁻¹ and Steigenberger et al. (2010) 8.56×10^6 M⁻¹ s⁻¹. Unlike k_{CDOM} and k_{RED} the reaction rates of the loss terms for O₂^{•-} are not directly related to the irradiating regime. However, assuming that Fe(III) becomes organically complexed following its initial photochemical reduction and subsequent oxidation (noting that > 99.9 % Fe(III) organically complexed in seawater (Gledhill and van den Berg, 1994; Rue and

Bruland, 1995; Wu and Luther, 1995)), and as these complexes may alter under different irradiating regimes, then there is the potential for the O_2^\cdot rate of reduction to also alter in line with the changing complexes.

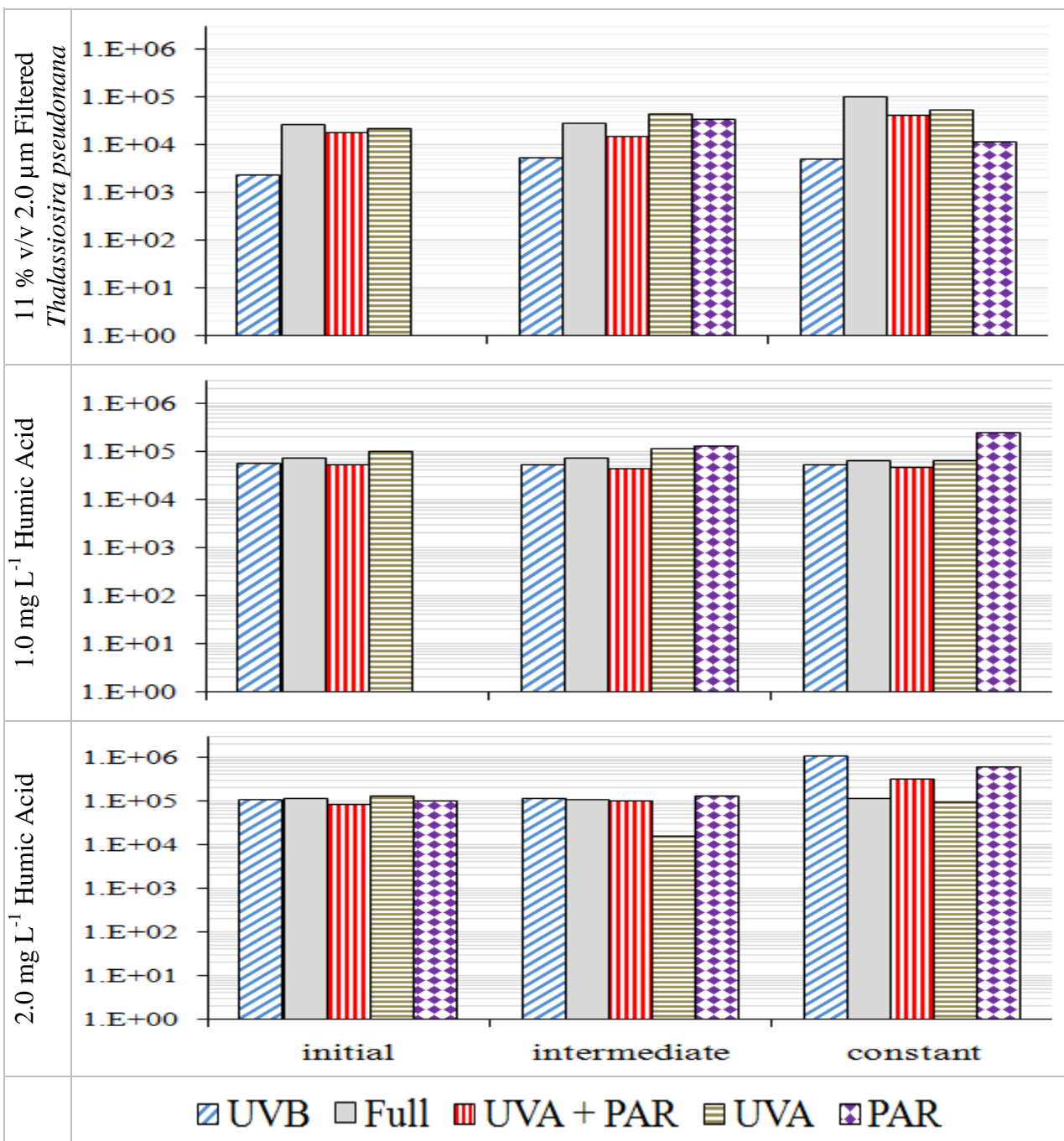


Figure 6.21. k_{RO} ($\text{M}^{-1} \text{s}^{-1}$) light regime comparisons.

11 % v/v 2.0 μm Filtered *Thalassiosira pseudonana*

With low production rates of O_2^\cdot for the UVB NMO experiment there is a corresponding low rate for k_{RO} , (Figure 6.21). This experiment has high concentration Fe(II) observations, and

high values for k_{RO} suggesting that it is k_{RED} and not the redox reaction with $O_2^{\cdot-}$ which is producing the Fe(II) for the NMO. The UVB experimental result is in contrast to the other experiments with UV-R, with its order of magnitude lower reaction rate, k_{RO} . The Full spectrum experiment, which shows a continued increase in Fe(II) throughout the experiment requires an increased k_{RO} (relative to the other experiments in the same media) in the constant stage for the model to represent this. This suggests that for this experiment and the UVA and UVA+PAR with oscillatory Fe(II) traces k_{RO} becomes more important and what may be occurring is that the $O_2^{\cdot-}$ and iron are entering redox cycles. The PAR experiment shows an interesting comparison between stages. Intermediate stage, steady-state H_2O_2 and gradual loss of Fe(II) with a higher rate of k_{RO} , compared to the constant stage with H_2O_2 production but steady-state Fe(II) and a lower k_{RO} . So to attain a steady-state Fe(II), k_{RO} must decrease and for the PAR experiment a steady-state Fe(II) then leads to the $O_2^{\cdot-}$ being utilised elsewhere, as indicated by the production of H_2O_2 .

1.0 mg L⁻¹ Humic Acid

k_{RO} is relatively consistent across the three stages of the 1.0 mg L⁻¹ humic acid experiments, ranging between 4.2×10^4 to $2.4 \times 10^5 \text{ M}^{-1} \text{ s}^{-1}$, with the higher values related to the PAR experiment (Figure 6.21). The PAR experiment had a low k_{RED} value to allow a modelling of the observed Fe(II) production and steady-state for this experiment. To compensate for this low k_{RED} value and knowing that model behaviour requires an increase in Fe(II) to produce an increase in H_2O_2 , for the PAR experiment k_{RO} was required to be increased in the model. This suggests that the Fe(III) reacting with $O_2^{\cdot-}$ may not be available or is of limited reactivity for photo-chemical reduction under PAR. k_{RO} is generally constant for the remaining experiments containing UV-R and they show initial increases in Fe(II) followed by either a pronounced redox cycle or a steady-state. These experiments tend towards an eventual loss of Fe(II) suggesting that an oxidation mechanism is occurring at a faster rate and this initiates within the intermediate phase of the experiments.

2.0 mg L⁻¹ Humic Acid

Excluding four exceptions across the three stages, for all the experiments the rate of k_{RO} in the 2.0 mg L⁻¹ experiments at pH ~ 7.5 was in the range, 8.3×10^4 to $1.3 \times 10^5 \text{ M}^{-1} \text{ s}^{-1}$ (Figure 6.21). The exceptions are a low value, $1.5 \times 10^4 \text{ M}^{-1} \text{ s}^{-1}$ in the intermediate phase of the UVA experiment, with a low corresponding stage k_{CDOM} value and higher values in the constant stage for the UVB, UVA+PAR and PAR experiments, all of which have appreciably better model fits

(Figure 6.14). That the range in values for the experiments are similar to the 1.0 mg L⁻¹ humic acid experiments at pH 8.1 would indicate that pH has little effect on this rate. As mentioned in relation to the NMO, to attain a steady-state Fe(II) k_{RO} must decrease, the 2.0 mg L⁻¹ constant stage has high values of $k_{RO} > 1 \times 10^5 \text{ M}^{-1} \text{ s}^{-1}$ and it is during this stage of these experiments that there is a constant loss of Fe(II) from within the experiments (Figure 6.14).

6.04.05 Light Regime Comparisons – k_{SOS}

11 % v/v 2.0 μm Filtered *Thalassiosira pseudonana*

Within the constraints of the model, and unlike k_{RO} , k_{SOS} appears directly related to k_{CDOM} for the NMO experiments (Figure 6.22). Table 6.08 shows the normalised ratios of k_{SOS} to k_{CDOM} for each experiment and stage; excluding the intermediate stage in the PAR experiment with no apparent production of H₂O₂ and therefore an increased rate value for k_{SOS} , all other experiments average a ratio of 1.1 within the range 0.3 to 1.7. To some degree this may either indicate that the major sinks for O₂^{•-} are related to its production mechanism and / or are influenced by the irradiating regime. As the production mechanism is related to the organic material then its photo-oxidation either increases the relative sinks by either promoting the reduction of trace metals or itself becoming a major sink within the system.

Table 6.08. Ratio of $k_{SOS} : k_{CDOM}$ for the NMO experiments, normalised to the Full spectrum constant stage. NC – none calculated.

	initial	intermediate	Constant
UVB	1.1	1.7	1.7
Full	0.7	1.2	1.0
UVA+PAR	0.3	0.6	1.3
UVA	0.4	1.7	1.4
PAR	NC	27.3	0.9

k_{SOS} values for Full and UVA+PAR experiments are $> 1 \times 10^{10} \text{ M}^{-1} \text{ s}^{-1}$ (Figure 6.22), which is the value proposed as the rate of reaction for O₂^{•-} and inorganic copper species (Zafiriou et al., 1998). With the reaction with Fe(III) and Fe(II) modelled there are therefore other potentially strong sinks remaining. These sinks may be other redox sensitive trace metals or a fraction of the organic material that is greater in size than CDOM. The estimated reaction rate of O₂^{•-} with CDOM is 1.0×10^4 to $3.5 \times 10^5 \text{ M}^{-1} \text{ s}^{-1}$ (Heller and Croot, 2010a).

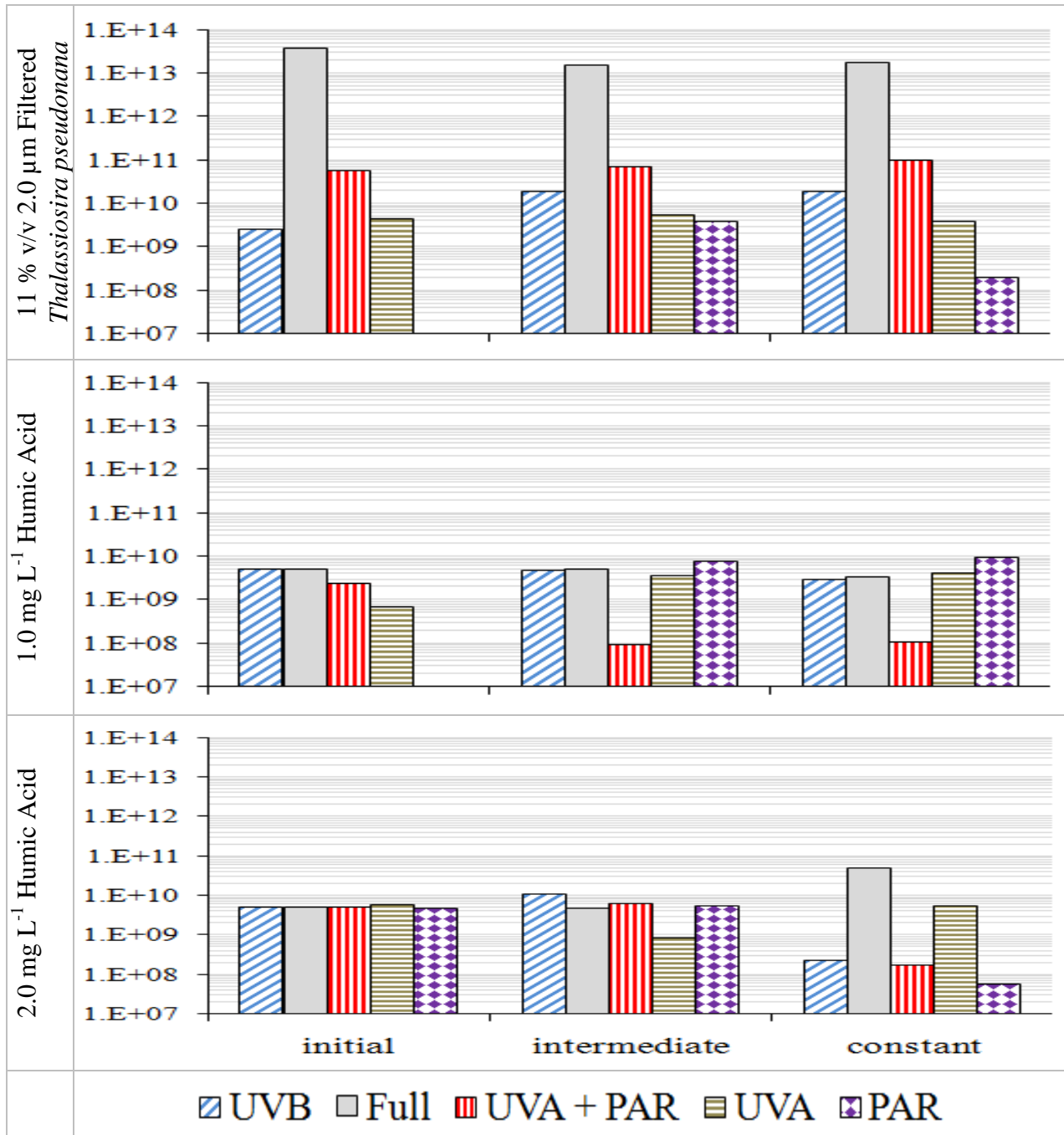


Figure 6.22. k_{SOS} ($M^{-1} s^{-1}$) light regime comparisons.

1.0 mg L⁻¹ Humic Acid

For the 1.0 mg L⁻¹ humic acid experiments k_{SOS} is less than $1 \times 10^{10} M^{-1} s^{-1}$ (Figure 6.22). Within the initial phase k_{SOS} decrease in line with reductions in irradiation from far to near UV-R as would be expected with a decrease in the production of Cu(I) from a LMCT of organic Cu(II) complexes (Moffett and Zika, 1983). This change with the irradiating regime would suggest that from within the humic acid the sink is photochemically produced and is in range of that for reactions of copper with O_2^{*} .

2.0 mg L⁻¹ Humic Acid

The 2.0 mg L⁻¹ humic acids for the initial and intermediate phases are generally $< 1 \times 10^{10} \text{ M}^{-1} \text{ s}^{-1}$ (Figure 6.22). Unlike the 1.0 mg L⁻¹ experiments there does not appear to be a relationship in the initial phase with light regime and/or UV-R. Within the constant phase the model fits that are slightly better to the Fe(II) observations are from the UVB, UVA+PAR and PAR experiments; these have correspondingly lower values for k_{SOS} by one to two orders of magnitude compared to the Full spectrum and UVA experiments.

6.04.06 Discussion

Two different organic materials were used to initiate the production of O₂^{•-}. Those from the NMO would be more representative of marine organic material and to some degree autochthonous organic material in a freshwater environment rather than the soil derived humic acids. However, due to the storage, > 60 days, less than 5 % of the original phytoplankton exudate remains so if compared to a marine environment it may be more similar to material seen in upwelling regions or during the winter overturning in the surface mixed layer. For this reason discussions will concentrate on the NMO experiments when discussing differences within the SML and those with depth through the water column. However, the comparison of humic acids at \sim pH 7.5 and pH 8.1, even though the experiments were undertaken with different concentrations, may be enlightening. Within the comparison of pH between experiments it should be noted that the humic acids in the lower pH environment would show a lower potential to flocculate and ultimately be removed from the system due to their inherent acidity, so these experiments may not be as directly comparable to a marine environmental context.

As indicated earlier it would appear that UVB has the greatest effect on the reduction of Fe(III) to Fe(II), k_{RED} (Figure 6.17). The 10 % light level for UVB ranges from approximately 1 m (near coastal waters) to 10 m (open ocean) (Figure 6.01). The available UVB for the UVB and Full spectrum experiments was 1.1 and 1.4 W m⁻² respectively, referring back to the comparison of the irradiating regimes and the measured spectrum over mainland USA (Chapter 5, Figure 5.03) the irradiation is very similar. This would suggest that within the sea-surface microlayer the production mechanism for Fe(II) would be directly related to the available UVB irradiation and there should theoretically be an enhancement of Fe(II) within the surface microlayer. This result agrees with Rijkenberg et al. (2005) though, as with Laglera and van den Berg (2007), their experiments were conducted in cold waters, < 4 °C. Whereas the experiments presented here were conducted at > 25 °C where the primary oxidation mechanism for Fe(II)

shifts from O_2 to H_2O_2 (Croot and Laan, 2002; Gonzalez-Davila et al., 2006; Millero and Sotolongo, 1989; Moffett and Zika, 1987). The marked difference between the observations of Fe(II) under UVB and UVA, i.e. approximately 4 times higher steady-state concentrations, in the NMO experiments also suggests the potential for higher Fe(II) concentrations in the SML.

Both k_{CDOM} and k_{RED} were calculated (NMO experiments) to have decreasing rates as the wavelength of UV-R increased (Figure 6.19 and 6.21) from far to near-visible light.

Intriguingly, k_{SOS} also shows the same trend as k_{CDOM} . Relating the decrease in UV-R to depth, due to preferential absorbance of lower wavelength UV-R as depth increases, would suggest that the ultimate effect of the redox cycling of O_2^\cdot may not be as strong with depth due to its effective removal mechanism, as indicated by k_{SOS} , showing a near constant ratio to k_{CDOM} (Table 6.08). What the observations do show is UVA and PAR induced redox cycling of Fe(II) and this was found in both the NMO and the 1.0 mg L^{-1} humic acid experiments. Whether this was due to O_2^\cdot , H_2O_2 (reduction reaction of Fe(III) by H_2O_2 not used in the model though the results in the 2.0 mg L^{-1} humic acid experiments suggests that this may be occurring) or with organic material as suggested by Skogerboe and Wilson (1981) could not be determined with the model.

The effect of pH appeared to be more strongly related to the photo-reactivity of the organic material (Millero et al., 2009) rather than increase in the half life of reduced iron (Millero et al., 1987). Humic acids contain a large proportion of carboxylate metal ligands (Averett et al., 1989) and as the pH decreases the will achieve a higher equilibrium concentration (Fox and Whitesell, 2004). The increased reactivity of k_{CDOM} (Figure 6.19), seen for the lower pH experiments and being attributed to humic acids, are still lower than those for NMO and also appear more strongly influenced by UVB. NMO appears more strongly influenced by UVA.

6.05 Conclusions

The above work is one of the first attempts at directly relating the effect of the irradiating regime on kinetic rate constants for certain proposed reactions of ROS and iron. The estimation of the rate constants is based on observations of Fe(II) and H_2O_2 in seawater incubation experiments. These results can be related to both reactions occurring within the surface microlayer and how the rates can change with depth through the water column.

Results have shown a range of Fe(II) observations including a continued increase in production, oscillatory behaviour and a steady loss of Fe(II) but not as usually measured the exponential decay of Fe(II). The experiments indicate that as depth from the microlayer increases, hence UVA decreases, H₂O₂ production should decrease based on both humic acids and aged NMO (2.0 μ m filtered) as the initiating chromophores.

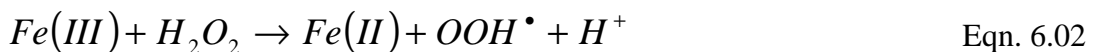
Rapid H₂O₂ production will occur with NMO material > 0.2 μ m under the influence of UV-R. UVA light influences this rapid production, this agrees with the results from O'Sullivan (2005); the lower the available UVA the slower the rate of this rapid production but the longer time over which it will occur. Only UVB will induce rapid Fe(II) production when using 2.0 μ m filtered NMO. H₂O₂ apparent production from aged 2.0 μ m filtered NMO will decrease by an order of magnitude compared to 0.2 μ m filtered fresh NMO. O₂^{•-} and hence H₂O₂ production appears influenced by UVA and UVB, and these regimes may be affecting different organic initiating sources.

UVA will induce periodic oscillations in Fe(II) when irradiating aged NMO and humic acid in seawater at its natural pH. This oscillatory behaviour will decrease as depth in the water column increases. The steady-state Fe(II) in shallow waters influenced by terrestrial organic material may in fact be highly variable. UVB influencing NMO produces a constant production of Fe(II); this agrees with Laglera and van den Berg (2007) who show an increase in the half-life of Fe(II) as the irradiating wavelength decreases.

There is a synergistic affect between UVA and UVB light occurring with humic acid at seawater pH causing intense oscillatory behaviour in Fe(II). The results suggest it is a combination of organic material and H₂O₂ that controls this oscillatory behaviour. Short period Fe(II) oscillations end when H₂O₂ increases above ~70 nM, when irradiating humic acid at natural seawater pH, whereas longer period Fe(II) oscillations occur with H₂O₂ concentrations < 40 nM with NMO. For NMO a net loss in H₂O₂ can occur. When it does it will precede a net loss in Fe(II) and this lag has also been seen in previous experimental work (Rose and Waite, 2003b). When the pH is reduced this lag does not appear.

With a decrease in pH the influence of UVB increases with respect to the production of H₂O₂ from humic acid initiating chromophores. UVB light is primarily responsible for the photodecomposition of humic acid based organic materials (Kieber et al., 1990; Mopper et al., 1991). With increased H₂O₂ production under UVB the photochemical decomposition of the humic substances can induce a loss of H₂O₂. At a lower pH an antagonistic affect was seen in

the combined UVB and UVA irradiation on the production of H₂O₂ from humic acid initiating chromophores. Within the microlayer the potential of this antagonistic affect, related to UVB, will be limited as there is also a synergistic affect between UVA and PAR which will act to retain a steady-state H₂O₂ in surface waters. The decreased pH of the 2.0 mg L⁻¹ humic acid experiments may have acted to promote the reactivity of humic acids towards PAR. PAR at lower pH will retain Fe(II) within a steady-state with humic acids, potentially through the cycling of ferric-organic complexes (Sima and Makanova, 1997). The ferric-organic complexes with respect to the NMO are at low concentration or not present. The decreased pH results in either Fe(II) being oxidised at a slower rate than predicted by the model or there is a production mechanism in place. For a decreased rate of Fe(II) loss coupled with a decrease in the H₂O₂ concentration requires a sink for H₂O₂ which can regenerate Fe(II) into the system. The proposed mechanism for this is the catalytic reduction by H₂O₂ of Fe(III), this is simplified in Equation 6.02, generalised from Barb et al. (1951).



H₂O₂ at warm temperatures has been estimated to be the primary oxidant of Fe(II), when H₂O₂ is in excess of ~ 125 nM (Santana-Casiano et al., 2006). The results from the experimental work suggest that with the addition of organic material the minimum H₂O₂ required to become the primary Fe(II) oxidant is in the range 25 to 70 nM.

k_{CDOM} , as a measure of the photo-induced reactivity of organic material towards the reduction of oxygen, will decrease with the aging of fresh NMO material. The rate of photochemical O₂[•] production also decreases as the length of the irradiation increases when using NMO, indicating either the affect of UV photo-bleaching (Micinski et al., 1993; Miller et al., 1995; Rijkenberg et al., 2005; Rose and Waite, 2003b) or a change from a HMW to lower reactivity LMW organic material (Hama et al., 2004; Meunier et al., 2005). k_{CDOM} for NMO shows a distinct trend related to both irradiance and wavelength. As total irradiance and UVA decreases the rate of k_{CDOM} decreases. The reactivity of the NMO increases by 2 orders of magnitude from the 0.2 μm filtered NMO to the 2.0 μm filtered NMO.

Antagonistic affects occur when irradiating humic acid between UVB and UVA and UVA and PAR, these result in reduced rates of O₂[•] production. This may in fact be the affect of promoting different sinks for O₂[•], which in turn may be reactive to specific irradiating regimes. As pH decreases the rate of k_{CDOM} shows lower reactivity to UVA light and UVB becomes the controlling irradiation when incubating humic acids in seawater.

As both UVB and UVA decrease so to does k_{RED} indicating it is these wavebands that are influential in controlling the reduction of organically complexed Fe(III). $O_2^{\cdot-}$ production showed a distinct correlation with the total energy received, with UVA being the primary initiating source. Fe(II) photo-production on the other hand appears related more to UVB, and increasing UVB will result in higher concentrations of Fe(II) in the surface microlayer, though there appears to be an antagonistic affect between UVB and UVA on k_{RED} . However, there appears to be little affect on the long term reactivity of the non specific Fe(III) from UV-R. When compared to NMO the humic acids show a preferential affect from UVA on k_{RED} .

For NMO the low values for k_{RO} suggest that it is k_{RED} and not the redox reaction with $O_2^{\cdot-}$ which is the major production mechanism for Fe(II). As k_{RO} increases under the influence of UVA irradiation there is subsequently an oscillatory behaviour in Fe(II) which suggests that as k_{RO} increases $O_2^{\cdot-}$ and iron enter a redox cycle. Changes in pH have little affect on k_{RO} for humic acids. For Fe(II) to be present in a steady-state, as when influenced by PAR only, then k_{RO} must be low; increasing k_{RO} has the overall affect of decreasing Fe(II) concentrations under the experimental conditions this is due to the rapid rate of reaction between Fe(II) and H_2O_2 .

k_{SOS} appears directly related to k_{CDOM} for the NMO experiments. As the production mechanism is related to the organic material then its photo-oxidation either increases the relative sinks by promoting the reduction of trace metals or itself becomes a major sink within the system. With humic acids the rate of k_{SOS} is similar to the measured reactions with copper (1998).

The experiments took a broad approach with respect to the composition of the experimental media analogous to the sea-surface microlayer. To enable a modelling of this broad range of experimental results, and in contrast to published works, ROS were judged to be of more importance than Fe(II). With respect to the range of experimental results the model could be said to represent the chemistry of ROS and Fe(II) reasonably well. This is especially true as the model was required to produce both a production and loss of ROS and Fe(II) whilst being constrained by two sets of observations. The model was kept to a simple ROS and Fe(II) model with a minimal set of fitting parameters. Though the model may not have been able to represent the Fe(II) observations as well, it did highlight areas of knowledge which are lacking with respect to ROS, for example the catalysed dismutation of $O_2^{\cdot-}$ forming H_2O_2 . What was also noted was that as the model fits deteriorate then the relationship of the rate constants becomes more subjective. The resulting Fe(II) fits suggests that for the developed model there

are either insufficient fitting parameters to achieve a good fit for both constraints and / or that the model is incomplete with respect to the cycling of Fe(II).

Chapter Seven

Ozone Initiated Cycling of Hydrogen Peroxide and Reduced Iron, in a Batch Reactor Containing Seawater

7.00 Introduction

Ozone concentration in the tropical Atlantic marine boundary layer is approximately 32 ppbv (Lee et al., 2009). Concentrations of ozone above the Atlantic have increased over the last 30 years (Lelieveld et al., 2004). The increase in O_3 has been between 0.05 and 0.68 ppbv per year, but is dependant on latitude (Lelieveld et al., 2004). The primary cause for O_3 rise is attributed to the increasing emissions of anthropogenic NO_x (Lelieveld et al., 2004), because of this, O_3 concentrations in the marine boundary layer are expected to rise further in the coming centaury. In seawater O_3 decomposition is primarily initiated by iodide (Garland et al., 1980; Thompson and Zafiriou, 1983) and natural organic material (NOM) (Hoigne et al., 1985; Staehelin and Hoigne, 1985; von Gunten, 2003) at the surface microlayer; it can also be potentially decomposed by the hydroxide ion, though this has not been proven in seawater (Sehested et al., 1984; Staehelin and Hoigne, 1982; Weiss, 1935). Except for iodide initiated decomposition all other reactions can result in the formation of reactive oxygen species (ROS). One of the four possible reactions between ozone and NOM is through a 2-electron transfer (von Gunten, 2003); iron that is organically complexed may potentially undergo a ligand to metal charge transfer (LMCT) through the 2-electron reaction resulting in a release to the soluble phase of reduced iron. With the formation of ROS there is also the potential for redox cycles to be initiated, which will affect the cycling of redox reactive metals, for instance that between superoxide, $O_2^{\cdot-}$, and iron (Barb et al., 1951; Voelker et al., 1997; Voelker and Sulzberger, 1996).

Ozone itself is not assumed to directly affect metals in seawater due to its high reactivity with other components of the seawater: Reaction rate with iodide is $\sim 1 \times 10^9 M^{-1} s^{-1}$ (Garland et al., 1980; Liu et al., 2001), Atlantic surface seawater concentration $\sim 100 nM$ (Campos et al., 1996; Campos et al., 1999) and with bromide $2.5 \times 10^2 M^{-1} s^{-1}$ (Clifford and Donaldson, 2007; Haag et al., 1982; Liu et al., 2001) average seawater concentration $0.86 mM$ (Millero, 2006). O_3 will also react with chloride, though it has a slow rate of reaction, $0.003 M^{-1} s^{-1}$ (maximum), (Haag and Hoigne, 1983b; Hoigne et al., 1985), however the high concentration of chloride ion in seawater can act as a near permanent sink for ozone (Grgric et al., 1994). Reactions initiated by the products of ozone decomposition are termed advanced oxidation processes (AOP) (Hoigne and Bader, 1975; Hoigne and Bader, 1976), the primary advanced oxidant is the hydroxide radical (OH^{\cdot}), increasing the O_3 decomposition rate.

As well as the inorganic constituents of seawater, NOM will also decompose O_3 (Hoigne and Bader, 1983a; Hoigne and Bader, 1983b). von Gunten (2003) suggests that reactions

occurring directly between NOM and O₃ are generally attributed to double bonds, activated aromatic systems, amines and sulphides. Reactions of NOM with OH[•] can lead to the formation of O₂^{•-}, which reacts with O₃, propagating its decomposition (von Gunten, 2003). What has been found is that even using a batch reactor containing seawater (small volumes, 100s mL, with constant O₃ throughput) there is a near infinite capacity for the reduction of O₃ (Garland et al., 1980).

The four experiments presented in this work are the first such experiments to measure quasi-simultaneously production of H₂O₂ and Fe(II) in seawater with added organic material due to the presence of atmospheric O₃. The estimated experimental atmospheric concentrations range between 30 and 90 ppbv. The results may not be truly representative of a marine environment due to the use of an enclosed batch reactor. With an enclosed system the primary O₃ reactants, especially iodide, will become limited. However, under certain environmental conditions, if there is insufficient surface mixing, or with waters low in NOM and iodide, than at the microlayer there will be a change to the rate of ozone oxidation through the formation of non-reactive species (McKay et al., 1992) and propagation reactions occurring. The first of the four experiments contained only 0.2 µm filtered North Sea seawater with a corrected headspace O₃ concentration of 30 ppbv, this was used as the baseline comparison. The NOM was then increased through the addition of 1.0 mg L⁻¹ humic acid (Sigma) with increased head space O₃ concentrations (corrected for reactions with glass) of 45, 68 and 90 ppbv. For clarity the concentration of O₃ from the production source will be used throughout to name the four experiments and not the corrected values which were used during model calculations.

7.01 Materials and Methods

The analytical method for the experiments is the same as for the previous experiments described in Chapters 5 and 6. For the ozone experiment the quartz glass beaker was placed in a larger (5 L) borosilicate glass beaker (covered in black plastic), a blacked out watch glass-plate was used as a lid on the 5 L beaker. The Ozone source (see below), a 2B Technologies Ozone Calibration Source tubing and FIA-Cl tubing (Chapter 5) were placed though the beaker spout which was then sealed. All experiments were conducted in the dark so as to prevent any photochemical production of O₂^{•-} and Fe(II). The ozone source was directed over the quartz beaker with an initial headspace of ~ 300 mL; by the end of the experiment this had increased to ~ 800 mL. There was a large glass surface area in the reaction vessel; the underside of the watch glass-plate, the inside of the 5 L beaker and inside and outside of the quartz glass beaker. Due to the reactivity of O₃ with glass, the concentration of O₃ with in the experimental medium

would not be that produced by the ozone source. Tests showed an approximately 50 % loss of O₃ due to reactions with the glass – headspace O₃ during testing was measured using a 2B Technologies, Model 205, Ozone Monitor. An approximately 50 % loss of O₃ has also been seen previously in a 2 L glass cell (Martino et al., 2009). The background (laminar flow hood) ozone concentration was measured at approximately 27 ± 10 ppbv (n = 21, 3 measurements a day over 7 days). The experimental concentrations applied from the O₃ source to the model sea-surface microlayer material were, 60, 90, 135 and 180 ppbv.

The ozone was produced using 2B Technologies, model 306, Ozone Calibration Source (OCZ). The OCZ can produce ozone in the range 30 – 1000 ppbv with a precision of 2.0 ppbv / 1% O₃ concentration (which ever is highest), at a constant flow rate of 2.5 L min⁻¹. The ozone is produced through the UV (λ 185 nm) photolysis of O₂ in the ambient air. The air used during photolysis is initially scrubbed prior to photolysis and then the re-circulated into a scrubbed clean air stream to the required concentration.

Total iron concentrations for each experiment were used within the model to represent the total Fe(III) concentration prior to commencing the experiment. The analysis of the experimental media for total iron (Table 7.01) was undertaken on an ICP-MS using 1:40 dilutions and standard additions. The corresponding recovery of the National Research Council of Canada, certified reference material, CASS-5, specified concentration, 25.8 ± 2.0 nM, was 106% and was measured at 28.0 ± 4.0 nM (n = 3), 15 % RSD. The blank was measured at 14.8 ± 0.09 nM with a corresponding limit of detection (3 x σ of 3 ultra pure waters) of 0.3 nM.

Table 7.01. Total iron concentrations of experimental media

medium	nM
0.2 μ m filtered North Sea seawater	134
1.0 mg L ⁻¹ humic acid	287

7.02 Numerical Model

A numerical model (Table 7.02) was produced comprising of 28 reactions, set within 16 single order differential equations. The reaction scheme for reactions of O₃ in water was based on Westerhoff et al. (1997) and adapted to that as suggested by Lovato et al. (2009) for reactions of ozone in basic solutions with the exception of the reaction of Fe(II) and O₃. The results of the model were fitted simultaneously to the H₂O₂ and Fe(II) observations, based on the sum of their sum of squares errors (SSE), from the model output to the data. To ensure that there was no

bias, due to an order of magnitude difference or greater in the concentrations of H₂O₂ and Fe(II), they were normalised; this was via their maximum values, with these values subsequently used to normalise the model output. Model fitting was initially undertaken manually then completed using the Nelder-Mead algorithm (Nelder and Mead, 1965). To ensure that the results of the Nelder-Mead algorithm were not within a local minimum the fitting was cycled between fitting each analyte singly and then both combined. Results were then checked by applying the results from the other experiments and re-analysing these as the initial parameters. The final model fits are not necessarily those which provided the lowest values for the residual of the sum of the SSE for both H₂O₂ and Fe(II) fits, as on occasions a preferential fit to one of the analytes was detrimental to the other. Good model fits were on occasion discarded if on further analyses of the model output, looking at all experimental variables, one or more indicated that they were unstable, i.e. negative values or very large unsustainable concentrations.

The Henry's Law constant for the solubility of ozone for ionic media was calculated as per Kosak-Channing and Helz (1983), Equation 7.01.

$$\ln K_h = -2297 T^{-1} + 2.659 I - 688.0 IT^{-1} + 12.19 \quad \text{Eqn. 7.01}$$

Where T is the temperature in °K and I is the molar ionic strength. The molar ionic strength was calculated through the salinity by the equation of Millero (1985), Equation 7.02.

$$19.9201S / (1.0 \times 10^3 - 1.00488S) \quad \text{Eqn. 7.02}$$

Where S is the salinity in practical salinity units, in the case of the North Sea seawater, the salinity was 34.5, mean value of seawater sampled by Bristow (2009). The transfer of O₃ to the seawater in the experiment was not corrected for a depositional velocity which can change due to O₃ reactions within the seawater. Deposition velocity of ozone can also increase with stirring (Hsu et al., 2002; McKay et al., 1992) and also with an increase in both organic material (McKay et al., 1992) and iodide as stated earlier. The system was instead assumed to be at equilibrium with the concentration within the headspace of the reactor, corrected with the 50 % reduction of O₃ due to reactions with the glass.

Table 7.02. Model equations

	Equation	rate		reference
R1	$3O_3 + I^- \rightarrow IO_3^- + 3O_2$	1.2×10^9	$M^{-1} s^{-1}$	Liu et al. (2001)
R2	$O_3 + Br^- \rightarrow O_2 + OBr^-$	1.6×10^2	$M^{-1} s^{-1}$	Grguric et al. (1994)
R3	$O_3 + OBr^- \rightarrow 2O_2 + Br^-$	3.3×10^2	$M^{-1} s^{-1}$	
R4	$2O_3 + OBr^- \rightarrow 2O_2 + BrO_3^-$	1.0×10^2	$M^{-1} s^{-1}$	
R5	$O_3 + Cl^- \rightarrow O_2 + OCl^-$	3.0×10^{-3}	$M^{-1} s^{-1}$	
R6	$O_3 + OCl^- \rightarrow 2O_2 + Cl^-$	1.1×10^2	$M^{-1} s^{-1}$	
R7	$2O_3 + OCl^- \rightarrow 2O_2 + ClO_3^-$	3.0×10^1	$M^{-1} s^{-1}$	
R8	$O_3 + OH^- \rightarrow HO_2^- + O_2$	7.0×10^1	$M^{-1} s^{-1}$	Staehelin and Hoigne (1982)
R9	$O_3 + HO_2^- \rightarrow HO_2^\cdot + O_3^\cdot-$	2.2×10^6	$M^{-1} s^{-1}$	
R10	$O_3 + O_2^\cdot- \rightarrow O_3^\cdot- + O_2$	1.6×10^9	$M^{-1} s^{-1}$	Sehested et al. (1984)
R11	$O_3^\cdot- + H_2O \rightarrow OH^\cdot + O_2 + OH^-$	2.5×10^1	s^{-1}	Glaze and Kang (1989)
R12	$OH^\cdot + O_3 \rightarrow HO_2^\cdot + O_2$	3.0×10^9	$M^{-1} s^{-1}$	Tomiyasu et al. (1985)
R13	$OH^\cdot + O_3^\cdot- \rightarrow O_3 + OH^-$	2.5×10^9	$M^{-1} s^{-1}$	Tomiyasu et al. (1985)
R14	$OH^\cdot + HO_2^- \rightarrow HO_2^\cdot + OH^-$	7.5×10^9	$M^{-1} s^{-1}$	Christensen et al. (1982)
R15	$OH^\cdot + H_2O_2 \rightarrow HO_2^\cdot + H_2O$	2.7×10^7	$M^{-1} s^{-1}$	Christensen et al. (1982)
R16	$OH^\cdot + \text{sinks} \rightarrow \text{products}$	k_{OHS}	s^{-1}	fitting parameter
R17	$NOM + O_3 \rightarrow O_2^\cdot- + \text{products}$	k_{NOM}	s^{-1}	fitting parameter
R18	$2O_2^\cdot \xrightarrow{2H^+} H_2O_2 + O_2$	k_{SOD}	$M^{-1} s^{-1}$	calculated as per (i)
R19	$2O_2^\cdot + Z \xrightarrow{2H^+} H_2O_2 + O_2 + \text{products}$	k_{PSDO}	s^{-1}	fitting parameter
R20	$HO_2^\cdot \Leftrightarrow O_2^\cdot- + H^+$	pKa 4.8		
R21	$O_3 + Fe(III) \rightarrow Fe(II) + \text{products}$	k_{RED}	$M^{-1} s^{-1}$	fitting parameter
R22	$O_2^\cdot- + Fe(III) \rightarrow O_2 + Fe(II)$	k_{RO}	$M^{-1} s^{-1}$	fitting parameter
R23	$3OH^\cdot + Fe(III) \rightarrow Fe(OH)_{3(s)}$	2.5×10^4	$M^{-1} s^{-1}$	as per (iv)
R24	$O_3 + Fe(II) \xrightarrow{H_2O} OH^\cdot + OH^- + O_2 + Fe(III)$	5.7×10^5	$M^{-1} s^{-1}$	Logager et al. (1992)
R25	$O_2 + Fe(II) \rightarrow O_2^\cdot- + Fe(III)$	k_{O2}	s^{-1}	calculated as per (ii)
R26	$O_2^\cdot- + Fe(II) \xrightarrow{2H^+} H_2O_2 + Fe(III)$	1.0×10^7	$M^{-1} s^{-1}$	Rush and Bielski (1985)
R27	$H_2O_2 + Fe(II) \rightarrow OH^\cdot + HO^- + Fe(III)$	k_{H2O2}	$M^{-1} s^{-1}$	calculated as per (iii)
R28	$OH^\cdot + Fe(II) \rightarrow OH^- + Fe(III)$	5.0×10^8	$M^{-1} s^{-1}$	Rose and Waite (2002)

(i) k_{SOD} calculated as per Zafiriou (1990)^(a); (ii) k_{O2} calculated as per Millero et al. (1987)^(b); (iii) k_{H2O2} taken from Miller et al. (1995)^(c) as per Millero and Sotolongo (1989); (iv) Rose and Waite (2002)

(a) kinetic rate is pH dependant, the calculation of k_{SOD} (Zafiriou, 1990) is as follows ,

$$\log(ka) = 12.7 - 1.0 \times pH$$

$$k_{SOD} = ka$$

(b) kinetic rate is pH and O_2 dependant, the calculation of k_{O_2} (Millero *et al.*, 1987) is as follows,

$$\log(kb1) = 21.56 - 1545/T, \text{ where } T \text{ is temperature corrected to } ^\circ\text{K}$$

$$\log(kb2) = \log(kb1) - 3.29 \times I^{0.5} + 1.52 \times I, \text{ where the ionic strength is calculated as}$$

$$I = 19.9201 \times S / (1.0 \times 10^3 - 1.00488 \times S), \text{ where } S \text{ is salinity in practical salinity units.}$$

$$\log(kb3) = -1 \times \log(kb2) + 1.87 \times \text{pH}, (M^{-1} s^{-1})$$

$$k_{O_2} = kb3 \times [O_2], (s^{-1}), O_2 \text{ concentration calculated through temperature and salinity.}$$

(c) kinetic rate is pH dependant, the calculation of $k_{H_2O_2}$ (Millero and Sotolongo, 1989) is as follows,

$$\log(kc) = -3.04 + 1.0 \times \text{pH}$$

$$k_{H_2O_2} = kc$$

Below is a list of the composition of the experimental media wherein the reaction rates of ozone and AOP reactions were measured.

Reaction 1: Γ rate measured in pure water at pH 6.7, temperature 25 °C, ionic strength 0.1 M (various buffers) (Liu *et al.*, 2001).

Reactions 2 to 7: Br^- and Cl^- rates measured at pH 8.0 in NaBr and NaCl solutions, respectively, with equivalent bromide and chloride seawater concentrations (Grguric *et al.*, 1994)

Reactions 8 and 9: Rates measured in pure water at pH 10, ionic strength 0.15 M (Staehelin and Hoigne, 1982).

Reaction 10: Rate measured in pure water between pH 10 to 13, temperature 20 °C (Sehested *et al.*, 1984).

Reaction 11: Rate measured in pure water at pH 7.6 to 7.8, temperature 23 ± 2 °C, with bicarbonate concentrations ranging from 0 - 6.0 mM (Glaze and Kang, 1989).

Reactions 12 and 13: Rates measured in pure water at ~ pH 10, with sodium carbonate buffer between 0 and 3.0 mM (Tomiyasu *et al.*, 1985).

Reactions 14 and 15: Rates measured in pure water in the pH range 6.8 to 13.8, temperature range 14 to 160 °C (Christensen *et al.*, 1982).

7.03 Experimental Results with Model Fits

During the experiments the pH and temperature were monitored (Figure 7.01). Initial pH values for the four experiments ranged from pH 8.19 down to pH 8.12. pH was generally stable through the course of the experiments with changes of less than 0.02 pH units – this stability was not seen in the change of irradiation experiments (Chapter 6). The starting experimental temperatures range between 24.7 to 26.3 °C. The changes in temperature through the course of the experiments were less than 0.5 °C. The experiments with 90 and 180 ppbv O_3 had temperatures linearly decreasing whilst the 60 ppbv O_3 experiment had a linear increase in temperature; the temperature in the 135 ppbv experiment was stable throughout the experiment. Based on the calculation for oxygen solubility, Weiss (1970), and assuming equilibrium with the

atmosphere, the oxygen concentration for the experiments was between 208.0 and $202.6 \mu\text{M kg}^{-1}$.

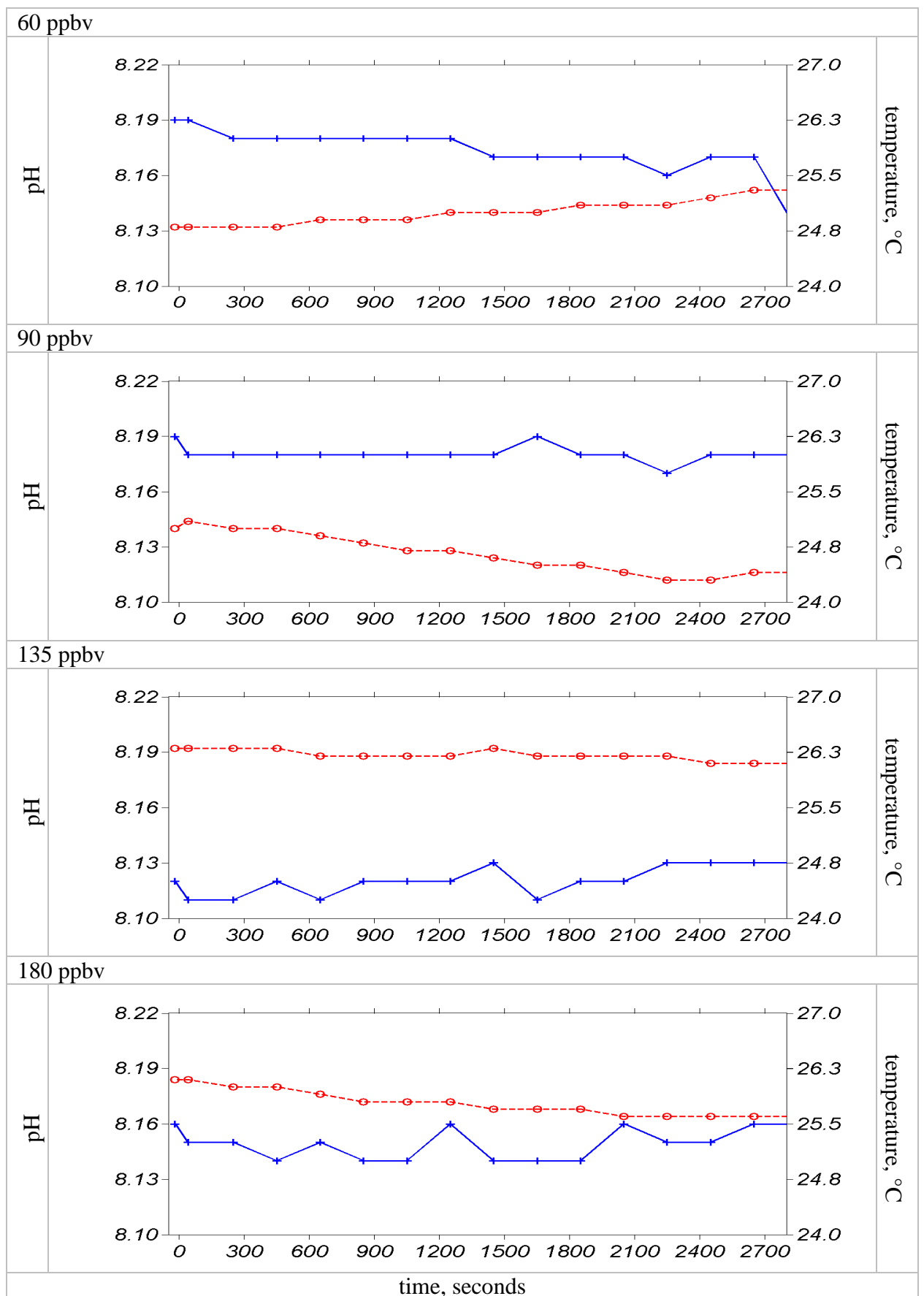


Figure 7.01. pH (blue line with $+$) and temperature (red line with o) change for experiments.

The experimental results with model fits are shown in Figure 7.02 for H₂O₂ and Fe(II) and for Fe(II) only, using an expanded axis in Figure 7.03. Within the Figures the H₂O₂ observations are indicated by diamonds and the Fe(II) by circles. The observations are surrounded by a grey envelope which is an error estimate for each point based on the fit of the non-linear calibration. The red line is the H₂O₂ model output and the blue line is the Fe(II) model output. The black dashed line is the model output for O₂[•]. Zero seconds corresponds to the introduction of O₃ into the headspace. All observations which were below the limit of detection (LOD), Table 7.03, were treated as being equal to the LOD.

Table 7.03. Limits of detection for H₂O₂ and Fe(II) analyses for experiments.

medium and O ₃ input concentration	Limit of Detection, nM	
	H ₂ O ₂	Fe(II)
seawater with 60 ppbv	1.5	1.1
seawater and 1.0 mg L ⁻¹ with 90 ppbv	2	1.9
seawater and 1.0 mg L ⁻¹ with 135 ppbv	1.1	1.3
seawater and 1.0 mg L ⁻¹ with 180 ppbv	7.5	0.04

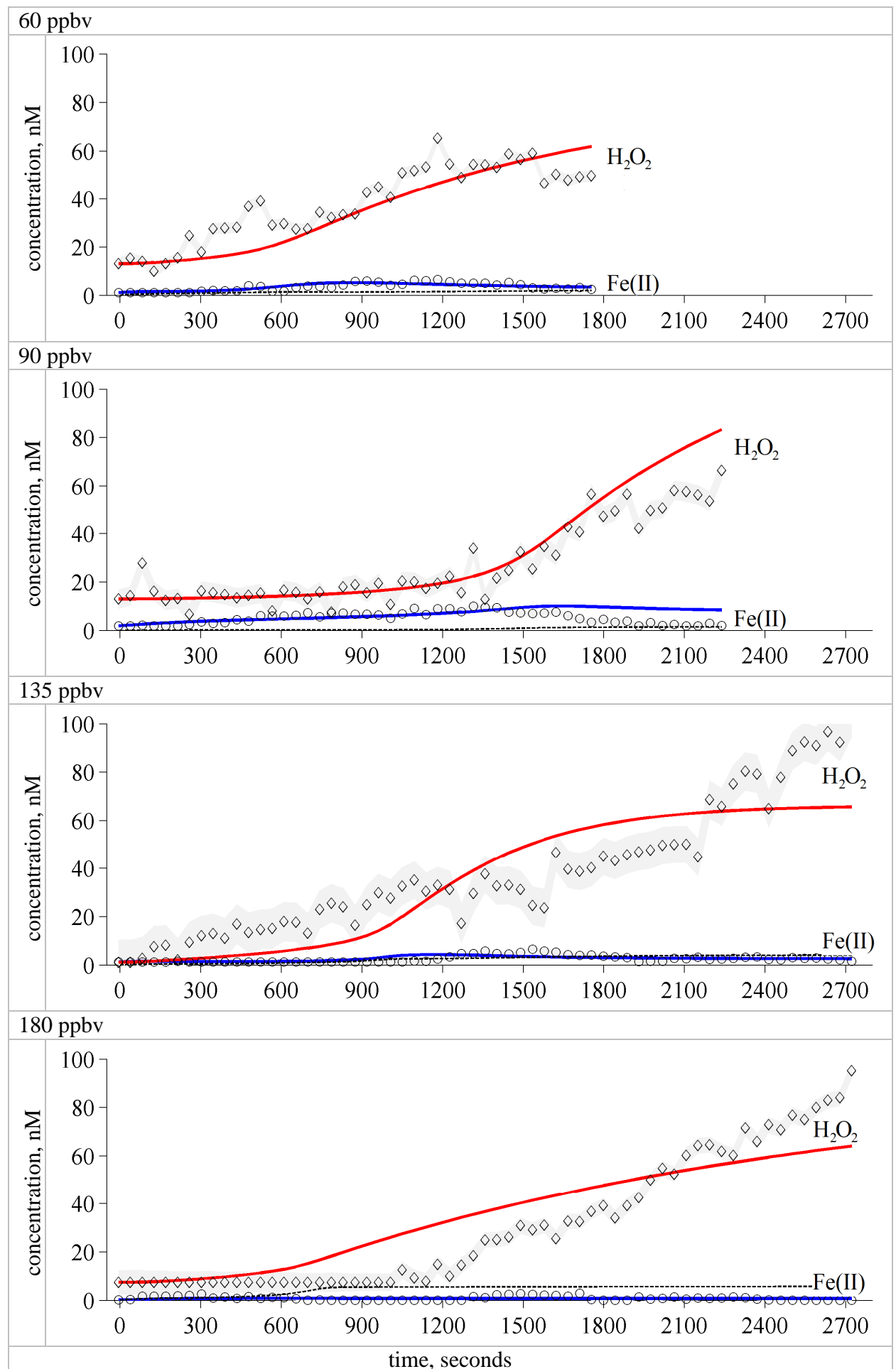


Figure 7.02. H_2O_2 and Fe(II) observations with model fits. See text for explanation of Figure.

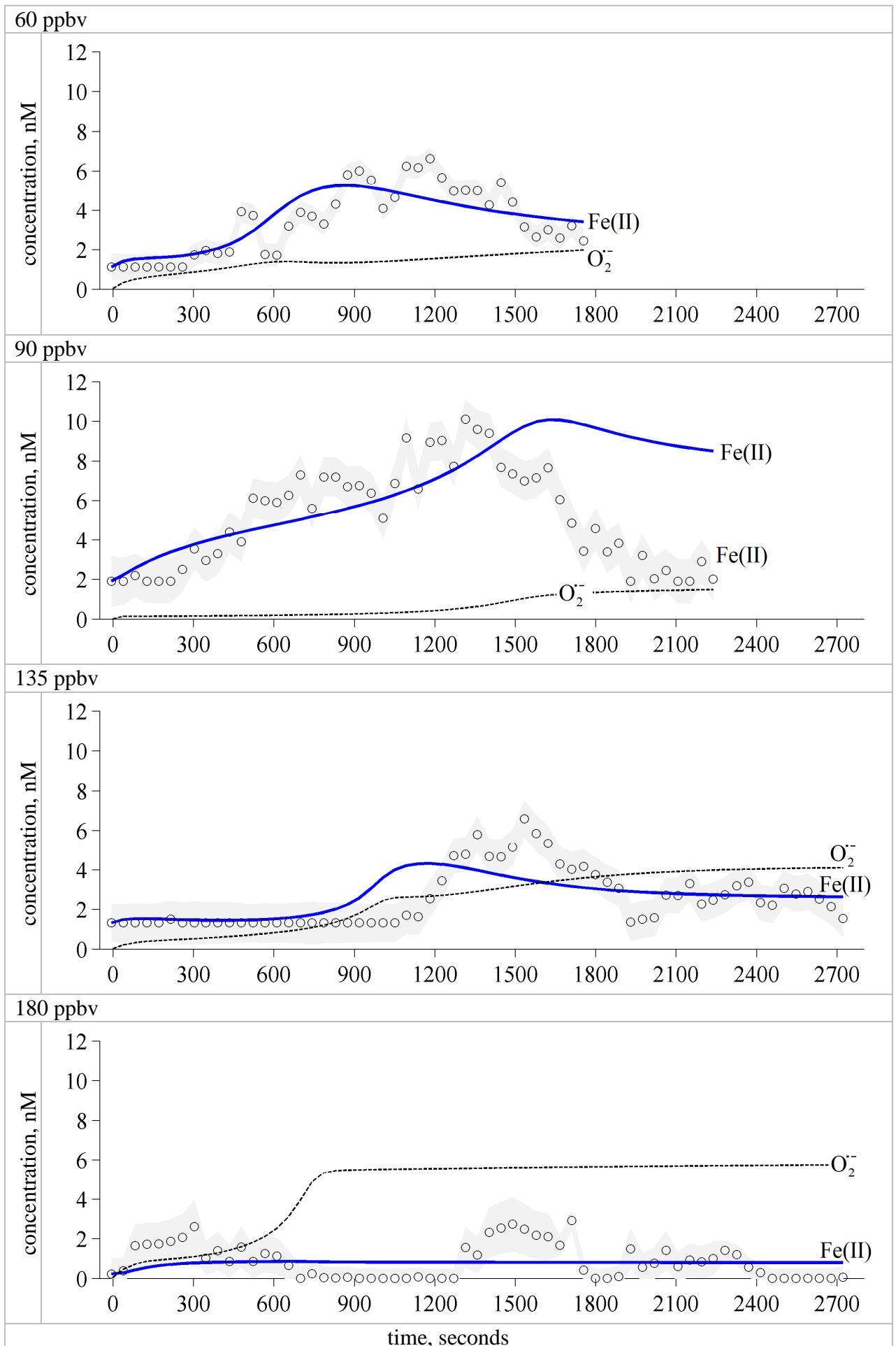


Figure 7.03. Fe(II) observations with model fit. See text for explanation of Figure.

The H_2O_2 observations indicate a two stage production in those experiments, which contain humic acid, 90, 135 and 180 ppbv experiments (Figure 7.02). This two stage production is contrasted against the seawater only which shows an approximate linear increase, 15 up to 60 nM, in the first 1200 s before the H_2O_2 observation indicate a steady-state for the remaining 600 s. The H_2O_2 apparent production rate (APR) for the seawater only experiment over the first 1200s is 105 nM h^{-1} (Table 7.04). This APR is comparable to that seen for the photochemical production of H_2O_2 in organic rich seawater in the tropical Atlantic, 24 – 134 nM h^{-1} (Moore et al., 1993). The change of the H_2O_2 APR in the 90 and 180 ppbv experiments occurs at c. 1400 s and 1000 s, respectively. There is a change in slope in the 135 ppbv experiment, though this occurs later at c. 2150 s. The H_2O_2 APR before (APR 1) and after (APR 2) the change in slope are given in Table 7.04.

Table 7.04. H_2O_2 apparent production rates

O_3 headspace ppbv	APR 1 nM h^{-1}	APR 2
60	105	-15
90	13	169
135	75	330
180	0	185

Fe(II) in the 60 ppbv experiment shows a straightforward production and loss cycle commencing 300 s into the experiment (Figure 7.03). Maximum Fe(II) obtained is ~ 6 nM occurring at c. 1150 s. The 90 ppbv experiment also shows a single production and loss cycle commencing c. 300 s into the experiment; maximum Fe(II) obtained is ~ 10 nM and this occurs c. 1400 s into the experiment. The 135 ppbv experiment has a c. 1000 s lag before Fe(II) production commences, the maximum Fe(II) produced is similar to that in the 60 ppbv experiment, ~ 6 nM. Following the Fe(II) production of ~ 6 nM in the 135 ppbv experiment, Fe(II) is gradually lost from the system; the last 600 s of the experiment show the concentration both gradually decreasing whilst fluctuating around ~ 3 nM. There is relatively low production of Fe(II) in the 180 ppbv experiment, that which does occur is over three cycles. The first cycle occurs at the initial input of O_3 to the experiment, and shows a production and loss cycle over 700 s attaining a concentration of 3 nM. The second and third cycles commence at 1200 and 1900 s, and attain 3 and 2 nM Fe(II), respectively.

That Fe(II) shows decreasing production with increasing O_3 may be due to potentially three mechanisms; i) The increased concentrations of O_3 in the aqueous phase is available to rapidly oxidise the Fe(II). This may be occurring at a faster rate than that stated in the model,

$5.7 \times 10^5 \text{ M}^{-1} \text{ s}^{-1}$, which was measured at pH 2 (Logager et al., 1992). This rate may indeed be pH dependant as seen with that for O_2 (Millero et al., 1987) and H_2O_2 (Millero and Sotolongo, 1989). ii) The model results with the increased concentrations of organic material indicate an increase, near doubling concentration of $\text{O}_2^{\cdot-}$. This higher concentration of superoxide acting to oxidise the Fe(II); this theory may also be combined with, iii) a higher production of OH^{\cdot} which is also acting to oxidise Fe(II).

It is interesting that the change in H_2O_2 APR occurs at significant points in the Fe(II) observations. With respect to the seawater only experiment (60 ppbv O_3) when the H_2O_2 observations indicate a steady-state $\sim 55 \text{ nM}$, the Fe(II) observations are showing a loss of Fe(II) from the experiment. The first 1.0 mg L^{-1} humic acid experiment (90 ppbv) shows a loss of Fe(II) from the system commencing around 1400 s. It is at this point in the experiment that the H_2O_2 observations show an increase in the APR from 51 up to 169 nM h^{-1} . Increasing the atmospheric O_3 concentration to 135 ppbv had two affects: i) APR increases from 13 to 75 and 169 to 330 nM h^{-1} for APR 1 and APR 2, respectively; ii) production of Fe(II) does not commence until c. 1000 s into the experiment; experiments with 60 and 90 ppbv O_3 show Fe(II) production occurring after c. 300 s. The change in APR in the 135 ppbv experiment occurs after a production and loss of Fe(II), with the Fe(II) indicating a steady-state / net loss from the experiment. The change in the H_2O_2 APR in the 180 ppbv experiment (Figure 7.02) occurs in line with the start of the second Fe(II) production cycle (Figure 7.03).

Model Fits

With respect to the H_2O_2 model fits, the best fits were for the experiments with lower concentrations of O_3 , 60 and 90 ppbv (Figure 7.02). The same is also the case for the Fe(II) model fits (Figure 7.03). The 135 ppbv model shows a similar Fe(II) form, though it occurs c. 300 s before the observations. The corresponding H_2O_2 fit is poor and the model is unable to represent the two consecutive H_2O_2 APR. The point of APR change in the model is apparently governed by the concentration of iodide. The rate constant used in the model was $1.2 \times 10^9 \text{ M}^{-1} \text{ s}^{-1}$ (Liu et al., 2001), Garland et al. (1980) estimated a value of $2.0 \times 10^9 \text{ M}^{-1} \text{ s}^{-1}$. These rates may in fact be too high or alternately with the higher concentrations of O_3 there is some other mechanism at work. The 180 ppbv model fits were unable to represent the oscillatory behaviour in the Fe(II) cycle (Figure 7.03), instead only a steady-state was established following an initial production of Fe(II). In the 180 ppbv experiment, the change in the model H_2O_2 APR occurs 600 s prior to the observations, with the second stage of H_2O_2 production lower than the observations.

To obtain the numerical model fits, 5 fitting parameters were used to alter the form of the model. Fitting parameter rate constants are given in Table 7.05 and compared in Figure 7.04.

Table 7.05. Calculated rate constants for fitting parameters

experiment	k_{NOM}	k_{PSDO}	k_{OHS}	k_{RED}	k_{RO}
	s^{-1}	s^{-1}	s^{-1}	$M^{-1} s^{-1}$	$M^{-1} s^{-1}$
60 ppbv	5.0	4.8×10^{-5}	8.1×10^{-3}	5.3×10^{-2}	12
90 ppbv	19	9.2×10^{-4}	5.0×10^{-2}	3.3×10^{-2}	2.8×10^5
135 ppbv	6.8	5.0×10^{-4}	4.8×10^{-2}	2.5×10^{-2}	7.6
180 ppbv	11	3.7×10^{-5}	1.6×10^1	5.2×10^{-4}	3.1×10^4

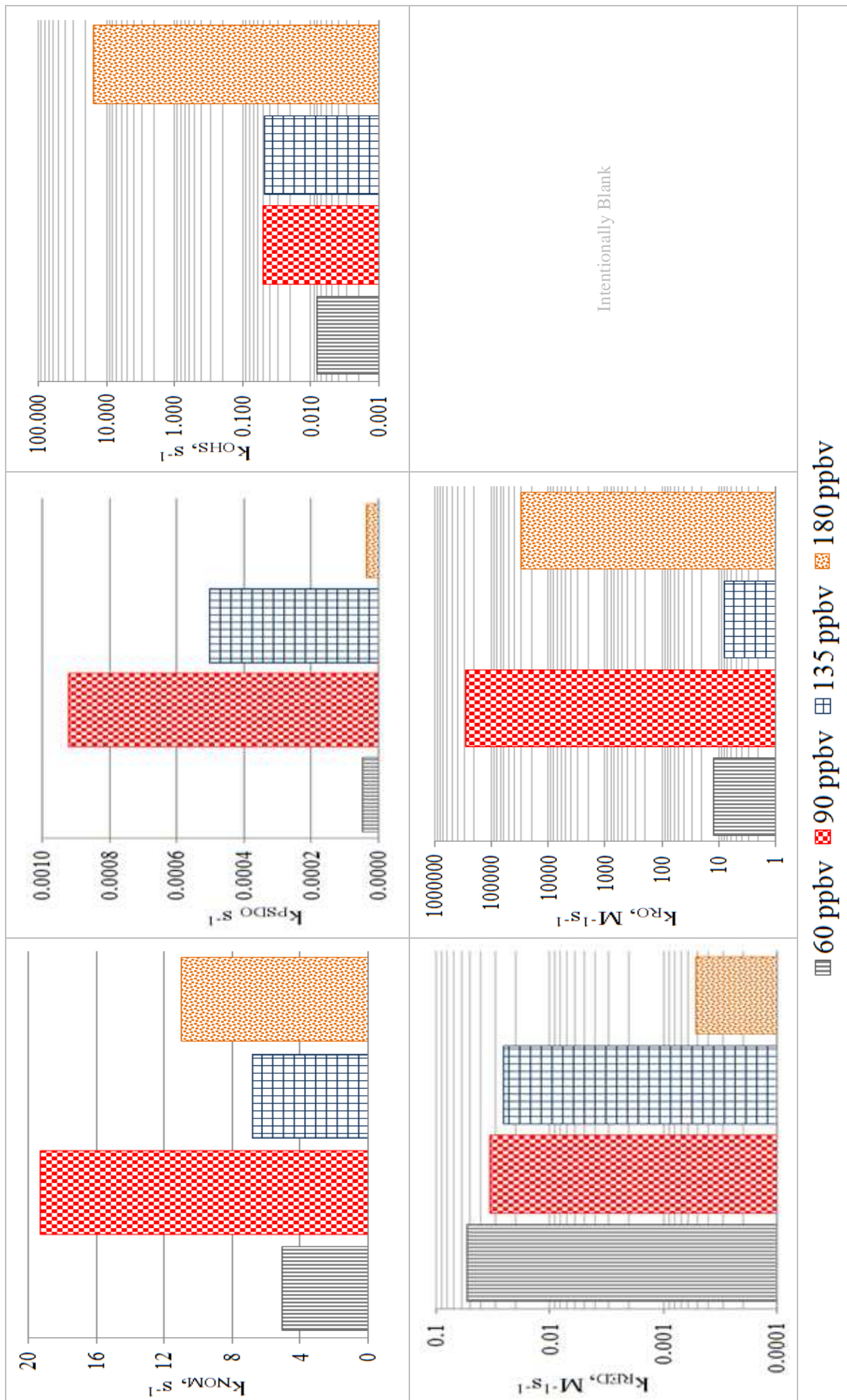


Figure 7.04. Comparison of fitting parameter rate constants

The results of the experiments have shown that atmospheric O₃ under the correct circumstances, and within environmental constraints, can induce a net production of H₂O₂ and Fe(II). O₃ decay in natural waters is characterised by a fast initial decrease followed by a second phase where O₃ decreases with first order kinetics (von Gunten, 2003). Part of the reason for this is its reactivity with the organic material (Garland et al., 1980; Hoigne and Bader, 1983a; Hoigne and Bader, 1983b; Joy et al., 1980; von Gunten, 2003) and iodide (Garland et al., 1980) present. With respect to dissolved organic carbon (DOC), its decomposition increases with increasing atmospheric O₃ but at the same time the rate of O₃ decomposition also increases (Joy et al., 1980). Joy et al. (1980) discuss DOC, however, the same process could also occur with all fractions of NOM. This increase in O₃ decomposition relative to the rate of NOM decomposition may be the reason why the forms of the H₂O₂ observations change as the O₃ concentration increases. Table 7.06 gives a conceptual idea based on the form of the H₂O₂ and Fe(II) observations as to the predicted changes in the rates of NOM decomposition and O₃ decomposition.

Table 7.06. NOM and O₃ linear and stepwise conceptual decomposition relative rates.

experiment	NOM decomposition	O ₃ decomposition
60 ppbv	slow	slow
90 ppbv	medium	similar rate to 60 ppbv
135 ppbv	fast	faster
180 ppbv	very fast	similar rate to 135 ppbv

The conceptual idea when applied to the surface microlayer has O₃ decomposition increasing stepwise whilst NOM decomposition increases linearly. Whilst there is slow O₃ decomposition, relative to the rate of NOM decomposition, Fe(II) will increase relatively quickly from initiation of the O₃ source, (60, 90 and 180 ppbv experiments, Figure 7.03). With increased O₃ decomposition at higher O₃ input rates there is less or low Fe(II) production. This is seen as no Fe(II) production over the first c. 1200 s of the 135 ppbv experiment, and also as the O₃ increases again (180 ppbv) there is some initial Fe(II) production but the concentration produced has decreased.

Model

Iodide concentrations were explicitly stated within the model (reaction 1, Table 7.02); however, the concentrations were not measured. The explicit values were initially calculated as a model fitting parameter, in a range of 40 to 200 nM, before being implemented as explicit values. Iodide Atlantic and Pacific surface seawater concentrations are approximately 100 and 200 nM, respectively (Campos et al., 1996; Campos et al., 1999). Based on an iodide half-life of 70 days (Campos et al., 1996) and using an initial assumed concentration of ~ 100 nM combined with the length of time the water had been removed from frozen storage, c. 90 days, the residual iodide in the seawater only experiment, with 60 ppbv O₃, was estimated to be around 40 nM. The sensitivity analysis for the iodide for the three experiments undertaken with model marine microlayer experiments (1.0 mg L⁻¹ humic acid) indicated an iodide concentration of ~ 170 nM. The reaction between iodide and O₃ does not produce free radicals which either accelerate O₃ decomposition or take part in AOP (Bichsel and von Gunten, 1999).

Reactions with bromide and chloride have been utilised in the model, reactions 2 to 7 (Table 7.02), as a known sink mechanism for O₃, but do not affect further model reactions. With respect to the usual discussions involving O₃ deposition to the sea surface seawater reactions within OH[·], Br[·] and Cl[·] are not usually given due to their low relative reactivity or concentration with respect to I[·] and NOM. The formation of chloride and bromide radicals can occur through both direct ozone reactions with bromide (Haag et al., 1982; Liu et al., 2001) and chloride (Haag and Hoigne, 1983b) and through AOP reactions with bromide (Haag and Hoigne, 1983a; von Gunten and Hoigne, 1994) and chloride (Grebel et al., 2010; Grguric et al., 1994). The potential bromide and chloride radicals which are formed following reactions with O₃ are not considered in this study though the AOP reactions of bromide and chloride in and with pure water are well documented (Grebel et al., 2010). With respect to the formation of bromide and chloride radicals which may be formed, reactions involved with OH[·] are used to encompass any potential reactions that the Br[·] and Cl[·] may undertake.

As the experimental system is a batch reactor, there are finite concentrations of initial O₃ reactants. The finite concentration of most importance are the iodide and NOM, as when these are exhausted then the reaction between O₃ and OH[·], which leads to propagation reactions (reactions 8 to 16, Table 7.02) become important. Propagation reactions if they occur in seawater can lead to the formation of O₂^{·-} and H₂O₂. Involved in the propagation reactions for O₃ decomposition is the AOP reaction between OH[·] and O₃. The hydroxide radical is a non-

specific reactant and as such to mitigate its effect a sink term was applied as a fitting parameter (reaction 16, Table 7.01).

With respect to the main emphasis of the model as a system being constrained by observations of H_2O_2 and Fe(II) an important reaction was the production of O_2^\cdot through the oxidation of NOM (reaction 17, k_{NOM} Table 7.02). This reaction encompasses a range of reactions. The first mechanism included is the direct reaction of O_3 with NOM; this has been shown to occur through four reactions, one of which leads directly to the production of O_2^\cdot (von Gunten, 2003). The second mechanism to be included is due to the reaction between the hydroxide radical (formed during O_3 decomposition) and NOM, this leads to the formation of carbon centred NOM radicals which subsequently reduce O_2 to O_2^\cdot (von Gunten, 2003), in a similar way to that initiated by the photochemical excitation of CDOM (Blough and Del Vecchio, 2002; Goldstone and Voelker, 2000). Though the reaction rate for NOM with OH^\cdot has been measured at $2.5 \times 10^4 \text{ (mg L}^{-1}\text{)}^{-1} \text{ s}^{-1}$ (von Gunten, 2003), the further reactions have not been measured. This reaction rate was also not applied within the model as the concentration of NOM in the base seawater was unknown.

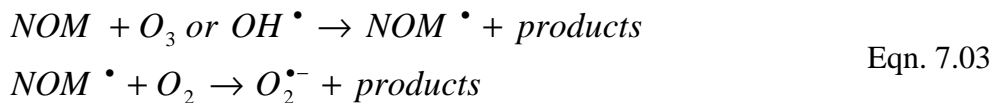
Included within the model is a fitting parameter (reaction 19, k_{PSDO} Table 7.02) which covers the formation of H_2O_2 due to the catalysed dismutation of O_2^\cdot by NOM (Goldstone and Voelker, 2000), Cu(I) (Zafiriou et al., 1998) and organically complexed copper (Goldstone and Voelker, 2000) and Mn(II) (Hansard et al., 2011) and which also may occur with other redox sensitive metals. This parameter as with the uncatalysed dismutation requires 2 O_2^\cdot molecules for every H_2O_2 .

There has been no previous evidence of Fe^{3+} reduction by O_3 , though Fe(III) can be oxidised by O_3 under alkaline conditions to Fe(IV) (Perfiliev et al., 2007). No work has been undertaken on the potential for organically complexed Fe(III) reduction due to a LMCT during the two electron oxidation of NOM by O_3 (von Gunten, 2003). Under this hypothesis a fitting parameter was applied (reaction 21, k_{RED} Table 7.02). k_{RED} is first order with respect to the O_3 and Fe(III), with the Fe(III) concentration taken as the measured total iron, Table 7.02. It must be noted that the total iron concentration will not be representative of the actual concentration of the species of Fe(III) available, though under an environmental consideration greater than 99 % of Fe(III) is complexed by organic ligands (Gledhill and van den Berg, 1994; Rue and Bruland, 1995; Wu and Luther, 1995).

Fe^{2+} can be oxidised by O_3 forming FeO^{2+} and O_2 , at pH 0 -2 (Logager et al., 1992). FeO^{2+} is unlikely to be present at the pH of seawater, it would instead be FeOH^{2+} (Millero et al., 1995). The understanding of the reaction sequence in basic solutions for the oxidation of Fe(II) is not known, therefore the rate of this reaction (reaction 24, Table 7.02) was taken as the total rate as calculated by Logager et al. (1992) for Fe^{2+} oxidation to Fe^{3+} under the assumption that Fe(II) is in excess of dissolved O_3 .

k_{NOM}

Production of $\text{O}_2^{\cdot-}$ has been shown in the marine environment through the photochemical excitation of organic material, forming organic radicals which subsequently reduce oxygen (Goldstone and Voelker, 2000; Zafiriou, 1990). A similar process can occur with both O_3 and OH^{\cdot} radicalising organic material (von Gunten, 2003). k_{NOM} (s^{-1}) encompasses all potential mechanism for $\text{O}_2^{\cdot-}$ production from the production of NOM radials, Equation sequence 7.03.



k_{NOM} is first order with respect to O_3 , whereas $\text{O}_2^{\cdot-}$ production is due to organic radical reduction of oxygen; organic material concentration unknown and O_2 assumed to be at equilibrium with the atmosphere. Across the four experiments k_{NOM} ranges between 5 and 19 s^{-1} . The seawater only experiment, 60 ppbv had the lowest value for k_{NOM} 5 s^{-1} , this is estimated from within aged 0.2 μm filtered seawater. The production rate decreases as the concentration of O_3 in the headspace increases with those experiments containing humic acid.

If the rate of NOM decomposition increases with increasing concentration of O_3 this may explain why k_{PSDO} decreases in those experiments with an additional 1.0 mg L^{-1} humic acid (Figure 7.04). k_{PSDO} would decrease if the rate at which NOM is converted to a non-reactive organic (McKay et al., 1992) increases, so removing a proportion of the potential $\text{O}_2^{\cdot-}$ dismutation catalysts. As the potential for k_{PSDO} decreases it highlights a failing within the model, and is why the model is less able to represent the observations of H_2O_2 in the 135 and 180 ppbv experiments. The primary reactants with O_3 in seawater are iodide (Garland et al., 1980), constant in all three humic acid experiments and NOM (Hoigne et al., 1985; Staehelin and Hoigne, 1985; von Gunten, 2003). The model had no term for the reaction of NOM and O_3 leading to a removal of both from the system; the main reason in modelling terms was that the concentration of NOM was not prescribed, k_{NOM} was used as the $\text{O}_2^{\cdot-}$ production term. What a variable and finite O_3 sink term would do is increase the length of time before the model output represents the point of change in H_2O_2 APRs. The sink term was assessed, though this was as

an iodide sensitivity analysis. However, due to the requirement of prescribing the iodide concentration in the models with a similar medium, the iodide concentrations were kept consistent. A calculation of an O_3 sink term in relation to NOM would have large affects on the calculation of k_{NOM} and at this was not sufficiently constrained.

k_{PSDO}

The catalysed dismutation of $O_2^{\cdot-}$ to form H_2O_2 was assessed through k_{PSDO} . The 60 and 180 ppbv experiments indicate low catalytic dismutation relative to the other experiments. The actual relative change in k_{PSDO} between the experiments is low, one order of magnitude. The three experiments with additional humic acid have k_{PSDO} decreasing from $9.2 \times 10^{-4} \text{ s}^{-1}$ (90 ppbv) to $3.7 \times 10^{-5} \text{ s}^{-1}$ (180 ppbv). That the 60 and 180 ppbv experiments have a similar k_{PSDO} , even with different medium, suggests that there are two different types of chemistry occurring. The first, in the aged filtered seawater, may be due to low concentrations of the catalysts. Whereas, in the high concentration O_3 experiment (180 ppbv), even with the additional organic material acting as a potential catalyst, there is a more rapid organic material oxidation leading to a non-reactive species (McKay et al., 1992), therefore its catalytic effect is minimised due to the higher O_3 concentration.

Within the 180 ppbv experiment the actual production of $O_2^{\cdot-}$, not involved in O_3 decomposition, may also be insufficient to undergo catalytic dismutation, though the rate of $O_2^{\cdot-}$ catalytic dismutation is greater than uncatalysed dismutation (O'Sullivan et al., 2005; Zafiriou, 1990). The form of the H_2O_2 observations suggests that the catalytic dismutation is occurring later in the experiment as the H_2O_2 APR increases in the higher concentration O_3 experiments (90, 135 and 180 ppbv). $O_2^{\cdot-}$ non-catalytic dismutation will occur when the concentration of $O_2^{\cdot-}$ is in excess of the potential catalysts (Zafiriou, 1990). However, there still remains the possibility that O_3 propagation reactions which lead to an increase in $O_2^{\cdot-}$, are now occurring, and this leads to the increased H_2O_2 for APR 2 (Table 7.04).

The same theory as that applied to k_{PSDO} can also be applied to k_{RED} as it is a LMCT in the organically complexed Fe(III) that induces the release of Fe(II). With the increase in NOM decomposition in conjunction with the increase in O_3 there was subsequently less Fe(II) production; maximum Fe(II) concentrations achieved were 10, 6 and 3 nM for the 90, 135 and 180 ppbv experiments, respectively.

The H_2O_2 observations (Figure 7.02) are in contrast to the results of Staehelin and Hoigne (1982) who suggest that H_2O_2 does not accumulate in ozonized solutions above pH 7. Their theory for this is the strong reaction between O_3 and the H_2O_2 conjugate base, the peroxy radical HO_2^- , $2.2 \times 10^6 \text{ M}^{-1} \text{ s}^{-1}$ (Staehelin and Hoigne, 1982). However, the results do agree with Heikes (1984) who showed H_2O_2 production, up to pH 6.8, and attributed this to O_3 aqueous phase reactions and also to reactions with hydrocarbons. In the model the equilibrium constant for H_2O_2 , pK_a 11.62 was not used, as such the only HO_2^- in the model was through the reaction of O_3 and OH^- , $7.0 \times 10^1 \text{ M}^{-1} \text{ s}^{-1}$ (Staehelin and Hoigne, 1982). The reason that the equilibrium constant was not applied within the model was due to the very high reaction rate between OH^- and HO_2^- , $7.5 \times 10^9 \text{ M}^{-1} \text{ s}^{-1}$ (Christensen et al., 1982), which has a large detrimental affect on the production of H_2O_2 . Staehelin and Hoigne (1982) assessed ozone decomposition in ‘pure water’, whereas in terms of the model the accumulation of H_2O_2 was within seawater. H_2O_2 accumulation was attributed to the production and subsequent dismutation of O_2^\cdot through; i) ozone oxidation of organic material – the formation of organic radicals leading to the reduction of oxygen to O_2^\cdot ; and ii) the presence of reduced metals, if they are in a sufficiently high concentration, for example in the redox cycles with Cu(I) (Zafiriou et al., 1998), Fe(II) (Rush and Bielski, 1985) and Mn(II) (Hansard et al., 2011). The change in APR for H_2O_2 formation and subsequent net loss of Fe(II) can also be due to the increase in the concentration of hydroxide ions as the threshold limit (NOM decomposition rate) of dissolved humic acid moieties controlling O_3 reactions (Buffle et al., 2006) has been surpassed.

From the results of the modelling it is still not possible to say what mechanism is involved in the change in the APR in the experiments. There are three potential mechanisms: i) A change in NOM from O_3 reactive to O_3 non-reactive due to O_3 decomposition – as such there should probably be a recalculation of the rate constants. ii) The O_3 chemistry has shifted from initiation to propagation reactions leading to the formation of ROS, especially O_2^\cdot . This then allows for a higher APR of H_2O_2 , especially in the later half of the higher concentration O_3 experiments – as such the model is unable to be constrained by these reactions. iii) The catalytic dismutation of O_2^\cdot has increased and the concentration of these catalysts are now in excess due to O_3 decomposition. H_2O_2 in the initial stages of the experiments shows little if any production. With highly reactive O_3 species available during this stage of the batch reactor system it may be suggested that within an environmental context that O_3 does not induce the production of H_2O_2 though it can potentially reduce the available iron. The batch reactor model system may occur if there was minimal mixing at the surface microlayer (McKay et al., 1992). However, should there be production of H_2O_2 then this occurs under a specific ratio of O_3 decomposition to NOM decomposition, O_3 concentrations of ~ 30 and ~ 68 ppbv for these

experiments. Only when O₃ concentrations achieve greater than ~ 68 ppbv will the production of reduced iron become limited.

k_{RED}

k_{RED} is a conceptual construct based on the unproven potential for a LMCT within organically complexed Fe(III) as the molecule is reduced by O₃, or even OH[•] leading to the production of Fe(II). This reaction is a first order reaction in respect to both Fe(III) and O₃, the rates are similar, 5.3, 3.3 and 2.5 x 10⁻² M⁻¹ s⁻¹ for the lower concentration O₃ experiments, 60, 90, 135 ppbv, respectively. These three experiments also have reasonable Fe(II) model fits. The 180 ppbv model fit is poor in comparison due to the observations showing an oscillatory Fe(II) behaviour. The model could only produce a steady-state, as such *k_{RED}* for this experiment was estimated to be 5.2 x 10⁻⁴ M⁻¹ s⁻¹, two orders of magnitude lower.

The rate of *k_{RED}*, ~ 3.6 x 10⁻² M⁻¹ s⁻¹ (mean value for 60, 90 and 135 ppbv experiments) is two to three orders of magnitude higher than the equivalent photochemical reductive processes, as estimated by Miller et al. (1995) and Weber et al. (2005), respectively. It is also three to four orders of magnitude higher than that estimated by modelling the results from the photochemistry experiments, using 0.2 µm filtered seawater only, Section 6.04.01; it is two orders of magnitude higher than the mean of the 1.0 mg L⁻¹ humic acid photochemistry experiments, 1.1 x 10⁻⁴ s⁻¹, Section 6.04.03. However, *k_{RED}* is comparable to photochemical reduction rates measured in low organic, Arctic waters, 9.1 x 10⁻² to 5.3 x 10⁻³ s⁻¹ (Laglera and van den Berg, 2007).

k_{RO}

k_{RO} is the linking term between the cycles of O₂^{•-}, H₂O₂ and Fe(II). The affect of this rate constant is that as it increases it not only increases Fe(II), but also leads to an increase in H₂O₂, up to a certain threshold. The reason for this is the high rate of Fe(II) catalysed H₂O₂ production, 1.0 x 10⁷ M⁻¹ s⁻¹ (Rush and Bielski, 1985). To some degree, *k_{PSDO}* and *k_{RO}* should show similar forms in their estimations when comparing between experiments; this is under the assumption that an amount of *k_{PSDO}* is due to metal induced catalytic dismutation (Hansard et al., 2011; Voelker et al., 2000; Zafiriou et al., 1998). Both rates show a large increase with the addition of organic material, from the 60 to 90 ppbv experiment, however, the relative change in *k_{RO}* with respect to the 135 ppbv experiment does not follow the pattern of the *k_{PSDO}* rates, though this may be an artefact of the poor relative H₂O₂ fit.

The H_2O_2 observations can be split into two groups, those that indicate H_2O_2 production commencing within the first c. 300 s, (60 and 135 ppbv experiments) and those that do not have H_2O_2 production until after c. 1000s (90 and 180 ppbv). k_{RO} can also be grouped according to the observed grouping; low values of k_{RO} for the 60 and 135 ppbv experiments, 12 and $7.6 \text{ M}^{-1} \text{ s}^{-1}$, respectively, and high values for the 90 and 180 ppbv experiments, 3.8×10^5 and $3.1 \times 10^4 \text{ M}^{-1} \text{ s}^{-1}$, respectively.

Estimations of k_{RO} within photochemical experiments has a large range, this is due to the organic material used. Estimated rates of k_{RO} for organically complexed Fe(III) are; $1.2 \times 10^8 \text{ M}^{-1} \text{ s}^{-1}$ (Rose and Waite, 2002) and for non-specific Fe(III), $< 10^4 \text{ M}^{-1} \text{ s}^{-1}$ (Meunier et al., 2005) and $8.6 \times 10^6 \text{ M}^{-1} \text{ s}^{-1}$ (Steigenberger et al., 2010). Rose and Waite (2002) suggest that there is little difference between the rate of $\text{O}_2^{\cdot-}$ reduction of organically and inorganically complexed Fe(III). Previous experimental work involving the same medium as the 60 ppbv experiment calculated k_{RO} due to photochemical reactions within the system to be $\sim 7.0 \times 10^3 \text{ M}^{-1} \text{ s}^{-1}$ (Section 6.04.01) and with a 1.0 mg L^{-1} addition $\sim 8.1 \times 10^4 \text{ M}^{-1} \text{ s}^{-1}$ (Section 6.04.04). The resulting estimated k_{RO} for the 60 ppbv experiment $12 \text{ M}^{-1} \text{ s}^{-1}$, is two orders of magnitude lower than k_{RO} with photochemically produced $\text{O}_2^{\cdot-}$ and organic material affected through photochemistry. Except for the 135 ppbv experiment the resultant estimates for k_{RO} , 2.8×10^5 and $3.1 \times 10^4 \text{ M}^{-1} \text{ s}^{-1}$, 90 and 180 ppbv, respectively, are of a similar rate when humic acid was included to a concentration of 1.0 mg L^{-1} .

k_{OHS}

The indiscriminate reactivity of OH^{\cdot} required that a sink term be utilised. The sink term was to prevent this radical controlling the model output, because of its high rate of reactivity, as evidenced in reactions 12 to 15 and 28 (Table 7.02) – $\geq 5.0 \times 10^8 \text{ M}^{-1} \text{ s}^{-1}$. From the 60 ppbv experiment to the 90 and 135 ppbv experiments k_{OHS} increases by an order of magnitude. This is attributed to the increased organic material; for the 90 and 135 ppbv experiments k_{OHS} was similar, 5.0×10^{-2} and $4.8 \times 10^{-2} \text{ s}^{-1}$, respectively. In respect to the model k_{OHS} was then increased by three orders of magnitude to allow the model solution to better represent the 180 ppbv observations.

The results of this chapter show that there is the potential for O_3 which impinges on the surface microlayer to induce the production of reduced iron and ROS, H_2O_2 and by analogy O_2^\cdot . The experimental media low in iodide and finite organic material may be representative of a sea surface microlayer that is undergoing stagnation due to low wind driven mixing. This may then extending the potential for regions where O_3 may induce H_2O_2 and Fe(II) production.

That k_{RED} and k_{RO} are shown to be of similar rates to that seen within an environmental (k_{RED}) and laboratory controlled (k_{RO}) photochemistry context is interesting. During times of decreased photochemistry there exists the potential for the reduction of iron by both direct O_3 reactions and through the formation of O_2^\cdot during night time and polar winters. Production rates were calculated in aged filtered seawater and with additions of humic acid; using fresh marine organic material may increase both the H_2O_2 and Fe(II) production rates.

With sufficiently high atmospheric O_3 , e.g. double the present concentration above the sea surface microlayer, the reactions of O_3 at the microlayer may lead to enhanced steady-state concentrations of reduced iron.

Experiments show that relatively small changes in O_3 concentration, ~ 15 ppbv, may alter the production of H_2O_2 and Fe(II) at the surface microlayer. Seasonal O_3 concentrations in the tropical North Atlantic can range between 23.1 to 40.1 ppbv (Lee et al., 2009).

Modelling of the lower concentration O_3 experiments (60 and 90 ppbv) was good considering the required minimisation to two sets of observations. Due to the potential reaction rates of O_3 chemistry and NOM changing as O_3 concentrations increase the model shows an increasing inability to model the observations when higher concentrations of O_3 were used. With respect to an environmental context, high O_3 concentrations are approximately two to three times that measured above the tropical Atlantic, concentration 32.1 ppbv (Lee et al., 2009).

Chapter Eight:

Conclusions

Due to the physical nature of the surface microlayer and the imposed constraint of trace metal analysis, precise measurements of low concentration analytes, the scientific understanding of the surface microlayer is limited with respect to processes trace metals undergo therein. This study aimed to increase both knowledge of and especially the perturbations to redox cycles of metals within the surface microlayer of aquatic systems. Direct measurements of the microlayer show temporal and spatial variability of its main component, a gelatinous dissolved organic material (Wurl and Holmes, 2008). With a complex matrix the analyses of trace metals is even more difficult.

The work has successfully combined the use of fieldwork and laboratory studies to elucidate controlling mechanisms. These mechanisms are related to the dissolved (0.2 μ m filtered) fraction of, aluminium, manganese, copper, cobalt and arsenic and specifically relate to reactive oxygen species, especially hydrogen peroxide and dissolved / reduced iron. Though field and experimental work were undertaken in fresh and marine waters, respectively, the result from each can still aid in the understanding of the other.

As the first such measurement of the seasonal progression of dissolved metals in an aquatic microlayer the fieldwork (Chapter 4) was successful. Freshwater systems are unique in their local and environment, where as marine waters are homogenous and pervasive. However, the systems follow similar cycles of primary production and physical processes such as overturning. An important message from the results of the seasonal variability in the microlayer is that a single or even integrated measurement may not be sufficient to categorically state there is enrichment of a specific analyte. For all elements the results showed that over a seasonally averaged cycle, elements tended towards unity with the underlying water. The time series of calculated enrichment factors showed relatively large, yet well constrained variations in enrichment with the enrichments factors in good agreement with published values from the marine environment, Hunter (1980b) and Cuong et al. (2008). The dissolved fraction of these metals can also show depletion occurring within the microlayer. What this study did show is that the use of enrichment factors may be a gross oversimplification of a system in essence a comparison of a mean concentration to an arbitrary depth.

From using the available literature it was suggested that the reduction of Mn(III / IV) by reduced iron and arsenic (Scott, 1991) leading to the production of Mn(II) was an important mechanism acting to deplete dissolved iron and arsenic and enrich dissolved manganese in the microlayer (Chapter 4). This theory, especially relating to iron and manganese was shown through the addition of a $\text{MnO}_{1.9}$ particulate phase to a photochemically active system leading to

a reduction of the particulate phase and a decrease in the available reduced iron (Chapter 5). The rate of Mn(II) production was rapid and highlights the importance of using a photochemically active system, rather than a system at equilibrium as used by Spokes and Liss (1995) and Sunda and Huntsman (1988), to initiate the reduction from a particulate phase. The catalysed oxidation of iron by MnO_{1.9} was also seen to increase the decomposition of hydrogen peroxide (Chapter 5). This rate of decomposition was seen to be faster than the uncatalysed dismutation of superoxide, estimated to provide an apparent production of hydrogen peroxide, under the experimental constraints of 22 nM h⁻¹ (Chapters 5 and 6); based on the results of incubations under PAR and with low reduced iron concentrations.

The experiments also showed that an ionised aluminium particulate phase will have a large affect on hydrogen peroxide and iron in the surface microlayer. During the hydrolysis of the aluminium, reduced iron will be scavenged into the aluminium hydroxide matrix (Bertsch et al., 1989). This then removes a production mechanism from within the catalysed dismutation of superoxide and through the formation of the stable aluminium particulate phase the increased surface area increases the rate of catalytic decomposition of hydrogen peroxide leading to decreasing concentrations, as seen in Chapter 5.

Organic material is the primary constituent of the microlayer and to all respects this was proven to be of the most importance in both the field and laboratory work. With respect to the fieldwork, all analytes except aluminium were shown to have specific points of either significant enrichment or depletion in the microlayer. These points occurred due to changes in (succession) and / or due to times of phytoplankton growth or loss within the UEA Broad; changes in iron and manganese could be attributed to succession, an insight not yet published but inferred to in the literature (Kuznetsova et al., 2005). A caveat in the experimental work is that no work was carried out in organic free media to acts as controls to both the model microlayer systems and the base seawater. In the laboratory work organic material is used as the initiating material for superoxide production both due to photochemistry and through its reduction by ozone and hydroxide radicals. Organic material can also catalyse the dismutation of superoxide to hydrogen peroxide. It is also the source of organically complexed oxidised iron, which will lead to the production of reduced iron due to a ligand to metal charge transfer (LMCT), occurring due to both photo and ozone induced reduction. Iron (II) can also be organically complexed potentially inhibiting its oxidation.

The experimental work used a range of organic material. There were two types of natural marine organic (NMO); 0.2 µm filtered culture residue from *Fragilariaopsis cylindrus*

grown in low iron media and 2.0 μm filtered culture residue from *Thalassiosira pseudonana*. Humic acid was also used at 1.0 and 2.0 mg L⁻¹. The NMO are more representative of autochthonous material and these were judged to be of more importance with respect to an environmental context. The results of the light regime comparison experiments show a strong relationship between the 2.0 μm filtered *Thalassiosira pseudonana* NMO and irradiating regime.

There is one failing within the work and this is to explicitly prove that dissolved iron is enriched in the microlayer compared to its underlying water. The result from the time series for the mean seasonal enrichment of iron in a freshwater microlayer is in contrast to results of laboratory experiments. Though there are certain times of dissolved iron enrichment in the microlayer, generally the results indicated a depletion of dissolved iron. Laboratory experiments utilised two separate sources, light and ozone, to initiate the redox cycling of iron with the ROS, hydrogen peroxide and superoxide. With UVB light and a NMO there are high steady-state concentrations of Fe(II) relative to other irradiating regimes. NMO complexes of Fe(III) indicated a preference to UVB induced reduction where as those that initiate superoxide production appear to favour UVA (Chapter 5). Ozone at atmospheric concentrations ranging between ~ 30 to ~ 70 ppbv was shown to initiate production of reduced iron and potentially extend its half-life within the microlayer. However, hydrogen peroxide production due to the presence of ozone would only occur in either low organic water or when available organics had attained a non-reactive status (Buxton et al., 1988).

Laboratory experiments utilised a simple adaptation to a well trialled analytical method, flow injection analysis (FIA) measuring the chemiluminescence of luminol. The adaptation was a re-configuration of the load / inject valve to enable an analysis of two analytes, for this work they were hydrogen peroxide and reduced iron. The system has shown good sensitivity for hydrogen peroxide 19 ± 20 nM and for iron (II) 0.7 ± 0.7 nM. The rate of measurement of the analytes was relatively high at one analysis every 22 seconds, allowing for a high temporal measurement of the changes in the analytes as they underwent experimental perturbations. The simple adaptation proved successful in the measurement of the analytes and allowed for a more robust constraining during the modelling of the results. However even this rate of analysis may have been insufficient to capture the proposed redox changes occurring at the surface of the particulate additions (Chapter 5). Considering all results from the laboratory experiments, what would have improved both that and the modelling work would have been more time spent on achieving lower limits of detection for Fe(II). This would have provided remarkable insight into the eventual steady state concentrations achieved.

Modelling of the laboratory observations was only conducted on two of the three sets of experiments. Modelling exercises were undertaken on the results of the light regime change experiments and on those with changes to the atmospheric ozone, the model was constrained by both hydrogen peroxide and iron (II). From the light regime changes to the ozone experiment the basic ROS and Fe(II) model was enhanced. The primary changes were the addition of the catalysed dismutation of superoxide to form hydrogen peroxide, a reaction between hydroxide radical and hydrogen peroxide and a sink term for the hydroxide radical. Results from low pH, humic acid experiments suggest that at ~ pH 7.5 or lower, the reduction of Fe(III) by hydrogen peroxide should be considered and would therefore be more important to freshwater systems. Though the model behaved well with respect to the modelling of the light regime changes it was still insufficient to predict the changes seen to the Fe(II). As the model was simply constrained to a minimal series of fitting parameters this may in fact be incorrect and instead a suite of reduced iron organic fitting parameters should have been used as per Meunier et al (2005).

The results in Chapter 6 suggest that UVA and UVB will act on different organic groups / molecules in the NMO. Different organic structures appear to control the production of superoxide and hydrogen peroxide, and affect reduced iron through its production by a LMCT and through sustaining elevated concentrations of reduced iron through complexation. The light regime comparison results are not straight forward to interpret due to the three stages of production – initial stage a warming up period and potentially the estimated kinetic reaction rates are unlikely to occur in an environmental context. The final stage of the light regime comparison experiments were those which would be most representative of an environmental context, during this stage the apparent production of hydrogen peroxide were in a similar range to that which has been seen in organic rich tropical waters (Moore et al., 1993).

With respect to the 2.0 μm filtered NMO, the production of superoxide is directly related to both the total energy received and wavelength, as both the total energy received and wavelengths increase from 315 nm, superoxide production decreases. This then suggests that as depth from the microlayer decreases superoxide production also decreases. However, this decreased rate of production is balanced by an increase in the length of time this rate occurs for.

A synergistic affect within the microlayer will occur between UVB and UVA to produce an oscillatory behaviour in reduced iron. For these warm water experiments the results suggest this is due a combination of both the organic material and the concentration of hydrogen peroxide. The periodicity of these oscillations increases as the concentration of hydrogen peroxide decreases. Though both UV-R wavelengths are likely to induce a LMCT in organic

material, resulting in the formation of reduced iron at the microlayer, UVB will be the most important. UVB by itself was the only wavelength to induce a rapid production of reduced iron.

Ozone was shown in Chapter 7 to initiate production of hydrogen peroxide and reduced iron as it impinges on the surface microlayer. The presence of organic material will act to inhibit this production whilst conversely it will advance the production of reduced iron. Ozone due to its reactivity is not likely to directly affect any water deeper than the microlayer. However, the resulting products of ozone decomposition can potentially be drawn into deeper waters. The Southern Ocean for example with increased UVB and gradually increasing, though presently low O_3 , and lower atmospheric particulate loading may be a region of increasing concentrations of iron in the microlayer. Due to the low temperature, the oxidation kinetics of iron would be controlled by O_2 . These oxidation rates decrease with organic complexing of Fe(II), if suitable organics are present, and could therefore lead to a higher steady-state concentration of Fe(II) in the SML.

Reduced iron in both sets of modelled work was related to the concentration and changes in hydrogen peroxide. Both the experiments irradiating marine microlayers, especially with UV-R and when there were low active-organics in the atmospheric ozone experiments, show a near continuous production of hydrogen peroxide, a major oxidant for reduced iron. However, the addition of a particulate phase, especially containing manganese and aluminium, can act to reduce the concentration of hydrogen peroxide, keeping the potential photochemical production in check. This result has interesting connotations, as experiments that look at the production of reduced iron from the particulate phase may also need to measure the changes in the primary oxidants of iron. This is due to reactions on the surface of the particulate phase acting to remove a primary oxidant and hence increase the apparent production rate of reduced iron due to its longer half-life.

The light regime experiments indicated that hydrogen peroxide and iron (II) are controlled by different irradiating regimes, UVB and UVA, respectively. The ozone experiments showed a production of iron (II) even with no equivalent hydrogen peroxide production. These results may suggest that those organic molecules which complex Fe(III) are more readily able to undertake a LMCT than undertake the reduction of di-oxygen and hence form superoxide. As these molecules are found in both NMO and humic materials one can suggest that the majority of reduced iron in the near surface waters is formed by a LMCT rather than from within a redox cycle. However, there is the potential for redox cycles to be initiated especially if the Fe(III) organic complex is newly formed. The NMO material was one which

had been stored at low temperature for many months and would be representative of newly upwelled waters or when there is a break down of the seasonal stratification and deep winter mixing occurs.

Take Home

Dissolved metals in the microlayer are within a system that is kept in balance and controlled through the influence of light on the formation of ROS and the addition of particulate material. Ozone itself would only influence ROS under certain conditions, low organic and iodide circumstances. With respect to reduced iron, it has been shown to have a distinct diel cycle in surface waters (Weber et al., 2005), therefore the affect of ozone can be assumed to be minimal when UV-R and PAR are present. What it does not preclude is the effect of ozone over night and during polar winters acting to retain a higher than predicted steady state concentration of Fe(II).

Future Work

The work undertaken in this thesis can be developed further. With respect to the measurements from within the microlayer this can be advanced through three potential mechanisms. The first would be for a longer time series to be setup. The second would be to measure concentrations of wet and dry atmospheric deposition, deep water and possibly groundwater inputs to the system to better constrain the budgets and fluxes. Finally measurements of organic and inorganic species, and the different size fractions would better allow for an understanding of the processes occurring in the microlayer.

The simple adaptation to the FIA-Cl method worked very well. To further enhance these style laboratory studies would require specific measurements at a similar temporal scale. Those of most use initially would be oxygen and superoxide. The system could then be further enhanced through the measurements of copper and manganese. There is a new luminol derivative which shows the potential for real time measurement of copper (II), however, this requires photo-excitation (Luo et al., 2009). A derivative of coumarin – umbelliferone, could also be used for the real time chemiluminescence measurement of manganese (II) (Watanabe et al., 2008). Development work on both of these chemiluminescence methods could potentially allow for a high temporal analytical resolution during their use and be combined into a FIA system. It would also be interesting to compare elements such as arsenic and iron with additions of manganese. Laboratory work on very fresh culture residue of different size fractions could

also enlighten the processes seen in the microlayer and aquatic systems. Under this auspice the work could then be applied directly to phytoplankton cultures whilst undergoing short term stress, due to say the influence of UVB, or temperature change, or from the light to the dark (or vice-versa) or alterations to the atmospheric chemistry. However, all changes to the experimental work must require a careful consideration to the production of chemiluminescence by luminol.

The use of a computer model to represent the observations worked to an extent. Though better iron models have been developed it is the interaction between the metals and the organics which is the unknown. The problem with this side of the work is that by including extra fitting parameters their validity decreases as fitting parameters would eventually be controlling fitting parameters. The only solution is to design a full set of experiments modelled at each stage and then the model is advanced through the knowledge. This still leaves the potential unknown of changes in the organic through the course of a single experiment and that the model will then become a very specific system and have less application to an environmental context.

Appendices

Chapter One: Appendix

Table A1.01, part a. Published work on the measured concentrations and calculated enrichment factors for specific fractions of trace metals in the SML

reference	sampling site	collection method	analyte	SML conc., nM	SML depth, μm	ULW conc., nM	ULW depth, m	fraction	EF
Antonowicz and Trojanowski (2010)	Eutrophic lake in northern Poland	plate	Mn	1533 (364–5883)	80 – 115	841 (211–4751)	0.2	Total, after microwave assisted, HNO_3 digestion	2.25
			Cd	7.8 (0.2 – 21.2)		3.9 (0.1 – 10.3)		Total, after microwave assisted, HNO_3 digestion	2.61
		screen	Pb	13.4 (4.7–25.9)		8.5 (4.0 – 19.9)			1.57
			Mn	1332 (268–5661)	250 - 300				1.69
			Cd	6.1 (0.1 – 16.5)					1.95
	Estuarine lake, Lake Gardno, northern Poland	plate	Pb	12.7 (4.0 – 40.9)				Total, after microwave assisted, HNO_3 digestion	1.62
			Cu	657 (529 – 895)	90 -120	181 (96 – 228)	0.15		5.5 (0.06 – 23)
			Zn	483 (402 – 583)		202 (194 - 42 (41 – 42)			2.0 (0.3 – 10)
			Pb	193 (152 – 225)					4.5 (0.5 – 20)
			Cu	273 (179 – 330)	200 -320				2.4 (0.1 – 19)
Trojanowski and Antonowicz (2011)*	Estuarine lake, Lake Gardno, northern Poland	screen	Zn	414 (373 – 466)				Total, after microwave assisted, HNO_3 digestion	1.7 (0.1 – 8.5)
			Pb	133 (111 – 168)					3.2 (0.5 – 14)
	Singapore	roller	Cr	0.65 – 2.72		1		total	1.4 – 3.4
			Ni	0.07 – 0.22				dissolved	1.0 – 1.1
			Cu	0.46 – 2.10				total	0.9 – 2.2
			Zn	0.31 – 0.50				dissolved	0.9 – 1.2
			As	1.25 – 5.72				total	1.7 – 5.0
Cuong et al. (2008)			Cr	0.27 – 0.72				dissolved	0.9 – 1.2
			Ni	5.42 – 15.37				total	1.3 – 3.0
			Cu	1.79 – 3.31				dissolved	0.8 – 1.8
			Zn	1.34 – 1.19				total	0.9 – 1.1
			As	0.02 – 0.08				total	0.7 – 2.6
			Cd	0.02 – 0.05				dissolved	0.6 – 1.9
			Pb	0.11 – 0.51				total	1.9 – 3.4
				0.02 – 0.12				dissolved	1.1 – 1.2

Table A1.01, part b. Published work on the measured concentrations and calculated enrichment factors for specific fractions of trace metals in the SML

reference	sampling site	collection method	analyte	SML conc., nM	SML depth, μm	ULW conc., nM	ULW depth, m	fraction	EF
Grott et al. (2001)	Antarctic ice lead	roller	Mn	1.46 \pm 0.38		0.32 \pm 0.02		total	4.6
			Fe	133 \pm 24		18.3 \pm 2.4			7.3
			Cu	0.94 \pm 0.15		0.59 \pm 0.08			1.6
Mignon and Nicolas (1998)	NW Mediterranean	screen	Cd	43 (35 – X)	440	0.8 (0.5 – 1.2)	10	Total, pH 2 extractable	55
			Pb	13 (6 – 31)		0.7 (0.5 – 0.8)			100
Hardy and Cleary (1992)	North Sea, German Bight	•drum •screen •plate	Ni	4 (3 -5)	•34 \pm 18, •30 – 55, •200 - 400	4 (2 – 7)		Total, APDC and DDDC extractable	0.9 – 1.7
			Cu	34 (22 – 73)		10 (5 – 19)			4.7 – 8.8
			Zn	213 (160 -314)					1.9 – 4.7
			Cd	4 (0.2 – 1.6)		3 (0 – 14)			1.7 – 2.7
			Pb	7 (4 -10)		10 (5 – 19)			3.2 – 6.1
Brugmann et al. (1992)	Baltic Sea	screen	Mn	0.7	250 – 450	0.4	0.2	0.45 μm dissolved	2.5
			Fe	89		54			1.1
			Co	0.03		0.07			1.2
			Ni	11		9			1.1
			Cu	13		8			1.5
			Zn	39		17			2.0
			Pb	0.5		0.2			2.2
			Cd	0.3		0.2			1.5

Table A1.01, part c. Published work on the measured concentrations and calculated enrichment factors for specific fractions of trace metals in the SML

reference	sampling site	collection method	analyte	SML conc., nM	SML depth, μm	ULW conc., nM	ULW depth, m	fraction	EF
Hardy et al. (1990)	Estuarine and Coastal waters, Chesapeake Bay	roller	Cr	18 (2 – 70)	50	8	0.2	0.45 μm dissolved (one ULW comparison)	1.1
			Ni	30 (24 – 38)		32			1.2
			Cu	28 (17 – 46)		29			1.6
			Zn	306 (186 – 492)		251			1.47
			Cd	0.5 (0.4 – 0.8)		4			1.47
			Pb	3 (1 – 5)		1			4.67
Narvekar and Singbal (1993)	Eastern Arabian Sea	Screen	Al	187 (62 – 657)	212		1	Total	2 (0.9 -10.8)
Pattenden et al. (1981)	Coastal, North Sea	bubble microtome	Co		0.1 – 1.0		Total (normalised to sodium)	< 1.3 – 76 <5 - < 50 210 - 410	
			Zn						
			Pb						
Cross et al. (1987)	Coastal waters, Los Angeles	roller	Mn	31 – 159	50		Total, after HNO_3 digestion		
			Fe	4 – 88					
			Ni	5 – 54					
			Cu	10 – 286					
			Zn	36 – 1908					
			Cd	0.5 – 28					
			Pb	0.5 – 6					

Table A1.01, part d. Published work on the measured concentrations and calculated enrichment factors for specific fractions of trace metals in the SML

reference	sampling site	collection method	analyte	SML conc., nM	SML depth, μm	ULW conc., nM	ULW depth, m	fraction	EF
Hardy et al. (1987)	Coastal waters, Puget Sound	roller and plate	Cu	4328 (16 – 5 \times 10 ⁶)	30 – 60			Total	
			Cd	5 (0.9 – 24)					
			Pb	300 (3 – 3164)					
Hunter (1980b)	Coastal Waters, North Sea	screen	Mn	161 (78 – 370)	300 ± 66	200 (54 – 483)	0.2	Total	1.2 (0.3 - 2.1)
			Fe	7.4 (2.8 - 15) μM		8.9 (3.3-18) μM			1.2 (0.8 - 1.7)
			Ni	83 (6 – 614)		29 (6 - 127)			1.1 (0.1 - 2.8)
			Cu	28 (7 – 84)		11 (4 – 25)			0.6 (0.2 - 1.1)
			Zn	82 (30 – 202)		54 (24 – 132)			0.8 (0.3 - 1.7)
			Cd	3 (0.5 – 8)		4 (0.5 – 20)			1.1 (0.1 - 2.4)
			Pb	18 (7 – 52)		10 (3 – 19)			0.6 (0.2 - 1.4)

Chapter Four: Appendix

A4.01 Method of Calculation for the Correction Factor for First Three Sampling Missions of 2008

During the sampling of the UEA Broad the analytical protocol on the ICP-MS was undergoing refinement. The final analytical set up as given in Chapter 2, section 2.04.09 included the analysis of samples retrieved on the 27th March 2008 and 9th May 2008. These samples had previously been analysed as a 1:10 dilution using a standard calibration with and without CCT gas. During these previous analyses samples from the 8th of January, 18th of February and 13th of March had also been analysed, however the recovery for the certified reference material during these analyses was not as accurate. A successful attempt was made on producing a linear regression between these samples, from the final configuration and the previous attempts. Figure A4.01 shows the linear regression comparison of these data.

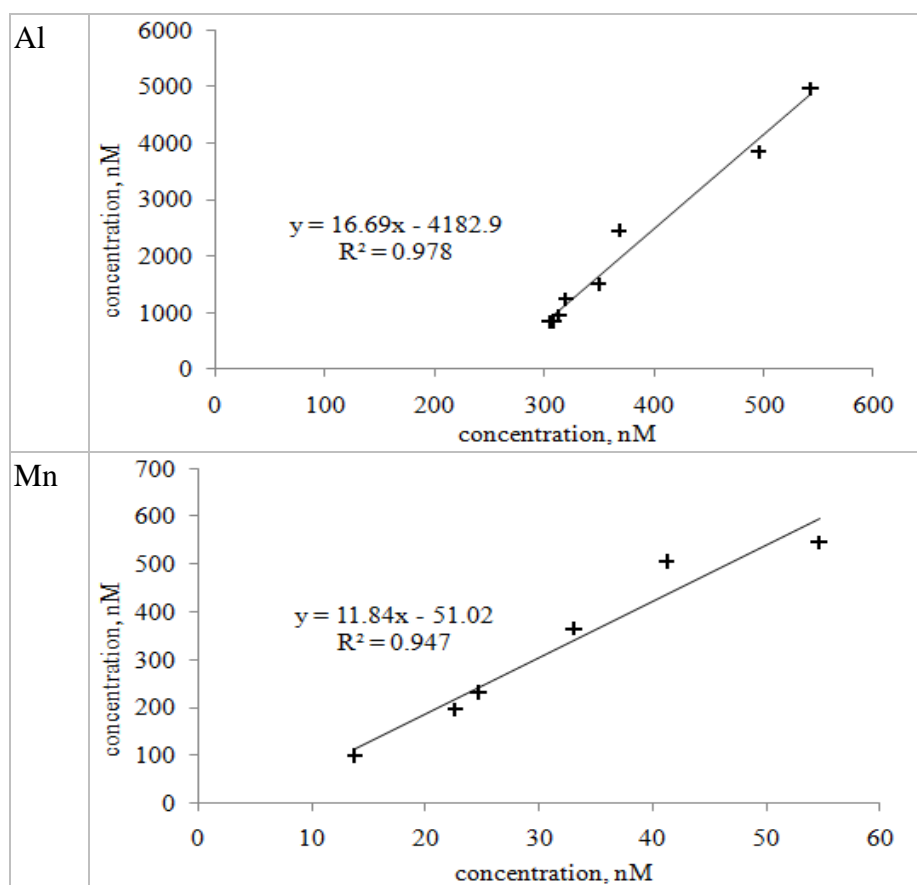


Figure A4.01. Linear regression comparisons for aluminium and manganese

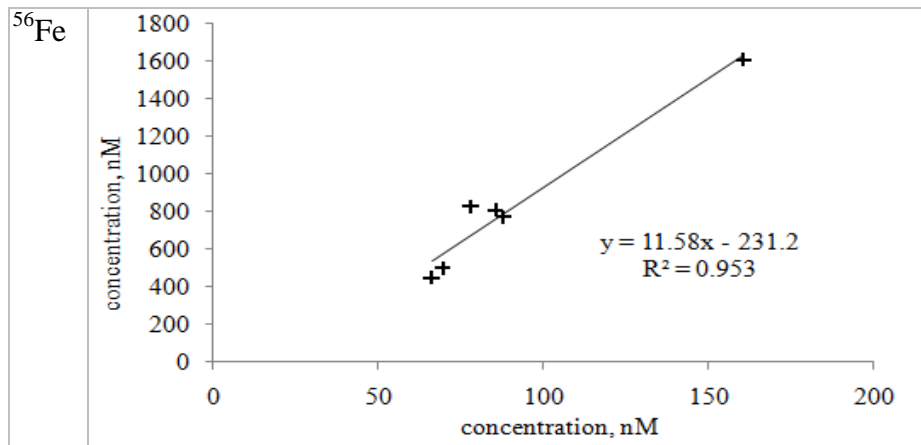


Figure A4.02. Linear regression comparison for iron

A Fisher, one tailed, F test was also applied to the data to check the statistical significance of the regression; it was also used to calculate the error on the linear regression, Table A4.01.

Table A4.01. Fisher test statistics for comparison of samples analysed using two ICP-MS configurations.

	F	probability	degrees of freedom (n - 2)	r ²	Y estimated error	error equivalent ordinate axis concentration, nM
Aluminium	268	< 0.01, F = 21.2	6	0.98	249	14.9
Manganese	71	< 0.01, F = 21.2	4	0.95	48	4.1
⁵⁶ Iron	82	< 0.01, F = 21.2	4	0.95	100	8.7

Using the standard regression form, $y = bx + a$, a correction was then applied to the data from the 8th of January, 18th of February and 13th of March, Tables A4.02 to A 4.04. The error for these values was calculated through the propagation of errors technique,

$$\text{error} = \sqrt{x_{equ.}^2 + x_{msrd.}^2}$$
, where $x_{equ.}$ is the error equivalent ordinate axis concentration and $x_{msrd.}$ is the error for the measured sample.

Table A4.02. Original measurement and corrected concentrations for aluminium

$y = 16.69x - 4182.9$	original measured	error	corrected	error
	concentration nM	nM	nM	nM
8 th January 2008, Julian Day 8				
Bulk	183	39	262	42
Plate (1)	4144	34	499	37
Plate (2)	1663	37	350	40
Screen (1)	X	X	X	X
Screen (2)	1028	38	312	41
18 th February 2008, Julian Day 49				
Bulk	508	39	281	42
Plate (1)	1699	37	352	40
Plate (2)	3148	35	439	38
Screen (1)	200	39	263	42
Screen (2)	705	38	293	41
13 th March 2008, Julian Day 73				
Bulk	533	39	283	42
Plate (1)	X	X	X	X
Plate (2)	X	X	X	X
Screen (1)	1476	37	339	40
Screen (2)	908	38	305	41

Table A4.03. Original measurement and corrected concentrations for manganese

$y = 11.84x - 51.02$	original measured	error	corrected	error
	concentration nM	nM	nM	nM
8 th January 2008				
Bulk	6170	10	526	10
Plate (1)	7458	9	634	10
Plate (2)	6584	9	560	10
Screen (1)	X	X	X	X
Screen (2)	5963	10	508	10
18 th February 2008				
Bulk	1020	13	92	14
Plate (1)	563	13	52	14
Plate (2)	106	13	13	14
Screen (1)	79	13	11	14
Screen (2)	285	13	28	14
13 th March 2008				
Bulk	413	13	39	14
Plate (1)	X	X	X	X
Plate (2)	X	X	X	X
Screen (1)	2613	11	225	12
Screen (2)	407	13	39	14

Table A4.04. Original measurement and corrected concentrations for iron

$y = 11.58x - 231.2$	original measured	error	corrected	error
	concentration	nM	nM	nM
8 th January 2008				
Bulk	2403	11	228	14
Plate (1)	10504	9	927	13
Plate (2)	1856	11	180	14
Screen (1)	X	X	X	X
Screen (2)	2939	10	274	14
18 th February 2008				
Bulk	6205	12	556	15
Plate (1)	704	12	81	15
Plate (2)	132	13	31	15
Screen (1)	787	12	88	15
Screen (2)	882	12	96	15
13 th March 2008				
Bulk	930	12	100	15
Plate (1)	1010	12	107	15
Plate (2)	X	X	X	X
Screen (1)	1602	11	158	14
Screen (2)	1555	11	154	14

A4.02 Concentrations of Trace Metals in the 2008 Broadwater Samples

Table A4.05 concentrations of trace metals, both calculated through the correction factor or as directly measured.

2008 Julian Day	8	49	73	87	130	143	171	199	227	
Al, nM	ULW	262 ± 42	281 ± 42	283 ± 42	309.5 ± 4.8	207 ± 13	261.3 ± 1.8	367 ± 12	452.5 ± 5.7	307.4 ± 9.6
plate 1		499 ± 37	352 ± 40	X	319.5 ± 4.0	274.7 ± 2.2	455.7 ± 7.3	625 ± 10	1681 ± 15	287.9 ± 2.5
plate 2		350 ± 40	439 ± 38	X	308.6 ± 4.5	269.3 ± 2.1	287.6 ± 2.0	456.3 ± 2.7	250.7 ± 4.8	260.1 ± 4.2
screen 1		X	263 ± 42	339 ± 40	495 ± 13	255.1 ± 5.1	3576 ± 42	657 ± 11	653.6 ± 3.7	581.2 ± 2.2
screen 2		312 ± 41	293 ± 41	305 ± 41	328.1 ± 1.6	215.3 ± 1.8	1127 ± 32	458.9 ± 7.9	459.1 ± 2.7	349 ± 12
Mn, nM	ULW	526 ± 10	92 ± 14	39 ± 14	20.7 ± 0.5	18.2 ± 0.7	17.5 ± 0.6	4.2 ± 0.1	4.8 ± 0.1	25.5 ± 1.4
plate 1		634 ± 10	52 ± 13	X	165.4 ± 7.8	54.6 ± 0.5	56.8 ± 3.0	8.7 ± 0.2	7.5 ± 0.1	32.9 ± 0.6
plate 2		560 ± 10	13 ± 14	X	286.1 ± 3.1	41.3 ± 0.6	47.0 ± 0.3	7.0 ± 0.2	2.4 ± 0.2	20.6 ± 0.2
screen 1		X	11 ± 14	225 ± 12	164 ± 14	33.0 ± 0.5	16.9 ± 0.4	7.9 ± 0.1	8.4 ± 0.1	24.0 ± 0.02
screen 2		508 ± 10	28 ± 14	39 ± 13	88.5 ± 4.3	24.6 ± 0.2	13.8 ± 0.1	9.9 ± 0.2	5.0 ± 0.1	12.7 ± 0.4
Fe, nM	ULW	228 ± 14	556 ± 15	100 ± 15	107.5 ± 2.2	119.1 ± 3.5	171.4 ± 2.5	97.5 ± 2.2	93.1 ± 2.1	350.5 ± 6.6
plate 1		927 ± 13	81 ± 15	107 ± 15	115.5 ± 2.4	66.0 ± 0.3	126 ± 12	108.6 ± 2.6	108.7 ± 0.4	157.5 ± 2.0
plate 2		180 ± 14	31 ± 15	X	115.6 ± 2.2	85.4 ± 0.7	125.6 ± 0.3	100.1 ± 1.4	43.3 ± 5.9	149.8 ± 2.7
screen 1		X	88 ± 15	158 ± 14	104.9 ± 3.4	69.5 ± 0.6	158.7 ± 2.4	145.6 ± 1.5	94.6 ± 0.7	284.4 ± 0.7
screen 2		274 ± 14	96 ± 15	154 ± 14	X	87.8 ± 1.2	160.8 ± 3.1	115.2 ± 0.1	80.8 ± 2.3	183.2 ± 1.3

Table A4.05 continued.

2008 Julian Day		8	49	73	87	130	143	171	199	227
Co, nM	ULW				1.6 ± 0.2	1.2 ± 0.2	1.0 ± 0.1	1.1 ± 0.1	1.2 ± 0.2	4.2 ± 0.3
	plate 1				1.8 ± 0.1	1.7 ± 0.1	1.7 ± 0.2	1.4 ± 0.1	1.3 ± 0.1	0.8 ± 0.1
	plate 2				1.8 ± 0.1	1.3 ± 0.1	1.40 ± 0.01	1.3 ± 0.1	1.2 ± 0.2	1.0 ± 0.1
	screen 1				1.4 ± 0.2	1.2 ± 0.1	1.2 ± 0.1	1.2 ± 0.1	1.00 ± 0.01	2.20 ± 0.01
	screen 2				X	1.4 ± 0.04	1.1 ± 0.1	1.2 ± 0.1	0.9 ± 0.1	1.4 ± 0.1
Cu, nM	ULW				24.1 ± 1.1	11.4 ± 0.6	11.3 ± 0.5	24.4 ± 0.7	17.0 ± 0.7	15.8 ± 0.8
	plate 1				19.9 ± 0.4	11.1 ± 0.3	18.3 ± 1.1	22.6 ± 0.5	17.0 ± 0.1	7.6 ± 0.2
	plate 2				37.7 ± 0.6	11.4 ± 0.5	15.6 ± 0.1	22.6 ± 0.3	3.1 ± 1.3	8.0 ± 0.2
	screen 1				16.0 ± 0.7	13.2 ± 0.3	13.1 ± 0.4	27.2 ± 0.3	14.7 ± 0.1	12.4 ± 0.1
	screen 2				X	11.5 ± 0.3	11.9 ± 0.4	24.8 ± 0.6	14.0 ± 0.3	11.2 ± 0.4
As, nM	ULW				10.9 ± 0.2	7.7 ± 0.4	8.7 ± 0.3	12.6 ± 0.5	13.4 ± 0.4	15.2 ± 0.2
	plate 1				9.8 ± 0.2	8.5 ± 0.1	9.2 ± 0.2	11.6 ± 0.3	13.8 ± 0.2	14.6 ± 0.3
	plate 2				9.4 ± 0.2	8.3 ± 0.3	9.7 ± 0.1	12.1 ± 0.3	13.3 ± 0.2	14.8 ± 0.3
	screen 1				9.4 ± 0.3	8.3 ± 0.2	9.0 ± 0.2	12.1 ± 0.2	12.2 ± 0.3	13.9 ± 0.01
	screen 2				X	8.0 ± 0.1	8.6 ± 0.2	11.6 ± 0.3	11.9 ± 0.2	13.5 ± 0.5

Within the table there are four categories of data, of which three are colour coded. An X indicates that the sample could not be resolved whether through the standard additions or calibration not being within the appropriate concentration range for that sample or that it was lost during sampling. Grey data (shown as Julian day 8, 49 and 73) are those which had their concentrations back calculated through an assessment of the correlation of specific samples based on the Fisher F test (see above). Data highlighted in red are outliers; outlier limits are $\pm 2.7\sigma$. Due to the nature of trace metal work and its potential for contamination they were not included in the further investigation.

A4.03 Student's t-test calculations and results

The following section introduces the calculation and results for a Student's t-test. There are two tests: i) H_0 the statistical probability that a mean sample EF is the same as a system value, in this case, unity with a value of 1.0 and ii) or H_0 the statistical probability that comparative data set samples have the same mean. For these calculations the arithmetic mean for plate and screen sampled microlayers for each element are first compared to unity and then against each other. The calculation of t statistics is as per Miller and Miller (1993).with the results compared to the statistical tables in Miller and Miller (1993). All tests were conducted as one tailed tests under the presumption that there is enrichment of an analyte in the SML and that this increases as the depth of the SML sampled decreases.

$$t = \frac{(\bar{x} - \mu_0) \cdot \sqrt{n}}{\sigma} \quad \text{Eqn. A4.01}$$

Where \bar{x} is the mean, μ_0 is the system value, in the case an EF equal to unity, 1.0, n is the sample size and σ is the standard deviation of the samples.

Calculation of the t statistic comparing between two sample arithmetic means is given by Equation A4.02.

$$t = \frac{(\bar{x}_{plate} - \bar{x}_{screen})}{\sqrt{\frac{\sigma_{plate}^2}{n_{plate}} + \frac{\sigma_{screen}^2}{n_{screen}}}}$$

The results for the first and second tests are provided in the Tables below, Table A4.06 and A4.07.

Table A4.06. Student's t-test comparing sample seasonal EF against unity, 1.0.

		mean	sigma	n	t	df = n-1	P	p
Al	plate	1.26	0.37	15	2.7	14	2.65	99 %
	screen	1.26	0.29	15	3.5	14	3.01	99.5 %
Mn	plate	1.57	0.96	14	2.2	13	2.18	97.5 %
	screen	1.14	0.66	13	0.7	12	0.69	75 %
Fe	plate	0.70	0.35	15	-3.3	14	3.01	99.5 %
	screen	0.91	0.41	16	-0.8	15	0.69	75 %
Co	plate	1.05	0.43	12	0.4	11	0.26	60 %
	screen	0.89	0.27	11	-1.4	10	1.38	90 %
Cu	plate	0.95	0.43	12	-0.4	11	0.26	60 %
	screen	0.94	0.18	11	-1.0	10	0.7	75 %
As	plate	0.99	0.08	12	-0.2	11		
	screen	0.95	0.07	11	-2.2	10	1.8	95 %

Table A4.06. Student's t-test comparing sample seasonal EF, plate versus screen.

		mean	sigma	n	t	df = (nP + nS) - 1	P	p
Al	plate	1.26	0.37	15	-0.03	29	0.26	60 %
	screen	1.26	0.29	15				
Mn	plate	1.57	0.96	14	1.39	26	1.31	90 %
	screen	1.14	0.66	13				
Fe	plate	0.70	0.35	15	-1.52	30	1.31	90 %
	screen	0.91	0.41	16				
Co	plate	1.05	0.43	12	1.09	22	0.69	75 %
	screen	0.89	0.27	11				
Cu	plate	0.95	0.43	12	0.04	22		NONE
	screen	0.94	0.18	11				
As	plate	0.99	0.08	12	1.32	22	0.69	75 %
	screen	0.95	0.07	11				

Chapter Six: Appendix

Tables of sum of squares error (SSE) concentration residuals for model fits to the observations

Table A6.01. Log(10) SSE, H_2O_2 residual fits for NMO repeat experiments

	initial	intermediate	constant	total
sw -(1)	4.0	5.2	5.5	5.7
sw -(2)	NC	NC	5.2	5.2
Fc 4.4% -(1)	NC	3.9	4.6	4.7
Fc 4.4% -(2)	NC	1.3	2.2	2.3
Fc 8.8% -(1)	NC	5.1	5.7	5.8
Fc 8.8% -(2)	NC	5.1	5.5	5.7
mixed 8.8 % -(1)	NC	3.9	5.3	5.3
mixed 8.8 % -(2)	NC	3.8	4.9	4.9

Table A6.02. Log(10) SSE, Fe(II) residual fits for NMO repeat experiments

	initial	intermediate	constant	total
sw -(1)	-11.48	-4.29	-4.44	-4.06
sw -(2)	NC	NC	-2.41	-2.41
Fc 4.4% -(1)	NC	-1.53	-0.66	-0.60
Fc 4.4% -(2)	NC	0.20	0.32	0.57
Fc 8.8% -(1)	NC	-1.26	0.37	0.38
Fc 8.8% -(2)	NC	-1.26	-1.79	-1.15
mixed 8.8 % -(1)	NC	-4.06	0.99	0.99
mixed 8.8 % -(2)	NC	-0.83	0.41	0.44

Table A6.03. Log(10) SSE, H_2O_2 residual fits for light comparison experiments

	initial	intermediate	constant	total
11 % 2.0 μm filtered NMO	UVB	3.4	4.5	4.4
	Full	3.2	4.5	5.0
	UVA+PAR	3.0	4.1	4.7
	UVA	3.3	3.8	4.5
	PAR	NC	2.1	3.0
0.5 mg L ⁻¹ humic acid	UVB	2.5	3.7	5.0
	Full	1.6	3.8	5.4
	UVA+PAR	2.1	4.9	5.4
	UVA	1.9	3.7	5.2
	PAR	NC	2.7	3.3
2.0 mg L ⁻¹ humic acid	UVB	5.0	5.8	6.1
	Full	4.8	5.5	5.7
	UVA +PAR	4.7	5.2	5.6
	UVA	4.5	5.0	5.7
	PAR	3.9	4.6	5.1

Table A6.04. Log(10) SSE, Fe(II) residual fits for light comparison experiments

		initial	intermediate	constant	total
11 % 2.0 μm filtered NMO	UVB	1.42	1.27	0.87	1.72
	Full	0.80	1.26	1.41	1.70
	UVA+PAR	0.14	0.70	1.00	1.21
	UVA	0.01	0.01	0.92	1.02
	PAR	NC	0.50	-1.30	0.50
0.5 mg L ⁻¹ humic acid	UVB	-1.09	-0.35	0.98	1.00
	Full	1.32	1.86	2.30	2.47
	UVA+PAR	0.03	1.16	0.23	1.23
	UVA	0.03	0.96	2.02	2.06
	PAR	NC	0.70	1.80	1.83
2.0 mg L ⁻¹ humic acid	UVB	-0.14	0.19	1.08	1.16
	Full	0.25	-0.36	0.92	1.02
	UVA +PAR	0.80	-0.75	0.16	0.90
	UVA	0.44	-0.95	1.69	1.71
	PAR	-0.06	-0.21	1.06	1.11

Bibliography

Agogue, H. et al., 2004. Comparison of samplers for the biological characterization of the sea surface microlayer. *Limnology and Oceanography-Methods*, 2: 213-225.

Alldredge, A.L., Passow, U. and Logan, B.E., 1993. The abundance and significance of a class of large, transparent organic particles in the ocean. *Deep-Sea Research Part I-Oceanographic Research Papers*, 40(6): 1131-1140.

Aller, J.Y., Kuznetsova, M.R., Jahns, C.J. and Kemp, P.F., 2005. The sea surface microlayer as a source of viral and bacterial enrichment in marine aerosols. *Journal of Aerosol Science*, 36(5-6): 801-812.

Andreae, M.O., 1978. Distribution and speciation of arsenic in natural waters and some marine algae. *Deep-Sea Research*, 25(4): 391-402.

Andreae, M.O., 1986. Chemical species in seawater and marine particulates. In: M. Bernhard, F.E. Brinckman and P.J. Sadler (Editors), *The Importance of Chemical "Speciation" in Environmental Processes*. Life Science Research Reports. Springer-Verlag, Berlin, pp. 301 - 336.

Andreae, M.O. and Froelich, P.N., 1984. Arsenic, antimony and germanium biogeochemistry in the baltic sea. *Tellus Series B-Chemical and Physical Meteorology*, 36(2): 101-117.

Andreae, M.O. and Klumpp, D., 1979. Biosynthesis and release of organiarsenic compounds by marine algae. *Environmental Science & Technology*, 13(6): 738-741.

Antonowicz, J. and Trojanowski, J., 2010. Surface microlayer in eutrophic lake: Variability in heavy metals contents. *Polish Journal of Ecology*, 58(4): 671-680.

Ashton, A. and Chan, R., 1987. Monitoring of microgram per liter concentrations of trace-metals in seawater - The choice of methodology for sampling and analysis. *Analyst*, 112(6): 841-844.

Averett, R.C., Leenheer, J.A., McKnight, D.M. and Thorn, K.A., 1989. Humic substances in the Suwannee River, Georgia; interactions, properties, and proposed structures. 87-557, US Geological Survey.

Baes, C.F. and Mesmer, R.E., 1976. *The Hydrolysis of Cations*, 489. John Wiley & Sons, New York.

Bagu, A.N., Johnson, A.G.R., Nazhat, N.B. and Saadalla-Nazhat, R.A., 1988. A simple spectrophotometric determination of hydrogen peroxide at low concentrations in aqueous solutions. *Analytica Chimica Acta*, 204: 349 - 353.

Balzano, S., Statham, P.J., Pancost, R.D. and Lloyd, J.R., 2009. Role of microbial populations in the release of reduced iron to the water column from marine aggregates. *Aquatic Microbial Ecology*, 54(3): 291-303.

Barb, W.G., Baxendale, J.H., George, P. and Hargrave, K.R., 1951. Reactions of ferrous and ferric ions with hydrogen peroxide. 1. The ferrous ion reaction. *Transactions of the Faraday Society*, 47(5): 462-500.

Barbeau, K., 2006. Photochemistry of organic iron(III) complexing ligands in oceanic systems. *Photochemistry and Photobiology*, 82: 1505 - 1516.

Barbeau, K., Rue, E.L., Bruland, K.W. and Butler, A., 2001. Photochemical cycling of iron in the surface ocean mediated by microbial iron(III)-binding ligands. *Nature*, 413(6854): 409-413.

Barbeau, K., Rue, E.L., Trick, C.G., Bruland, K.T. and Butler, A., 2003. Photochemical reactivity of siderophores produced by marine heterotrophic bacteria and cyanobacteria based on characteristic Fe(III) binding groups. *Limnology and Oceanography*, 48(3): 1069-1078.

Barker, D.R. and Zeitlin, H., 1972. Metal-ion concentrations in sea-surface microlayer and size-separated atmospheric aerosol samples in Hawaii. *Journal of Geophysical Research*, 77(27): 5076-5086.

Barringer, J.L. et al., 2011. Distribution and seasonal dynamics of arsenic in a shallow lake in northwestern New Jersey, USA. *Environmental Geochemistry and Health*, 33(1): 1-22.

Batley, G.E. and Gardner, D., 1977. Sampling and storage of natural-waters for trace-metal analysis. *Water Research*, 11(9): 745-756.

Behra, P. and Sigg, L., 1990. Evidence for redox cycling of iron in atmospheric water droplets. *Nature*, 344(6265): 419-421.

Belzile, N., Devitre, R.R. and Tessier, A., 1989. Insitu collection of diagenetic iron and manganese oxyhydroxides from natural sediments. *Nature*, 340(6232): 376-377.

Bergquist, B.A., Wu, J. and Boyle, E.A., 2007. Variability in oceanic dissolved iron is dominated by the colloidal fraction. *Geochimica et Cosmochimica Acta*, 71(12): 2960-2974.

Bertsch, P.M., Miller, W.P., Anderson, M.A. and Zelazny, L.W., 1989. Coprecipitation of iron and aluminium during titration of mixed Al-3+, Fe-3+, and Fe-2+ solutions. *Clays and Clay Minerals*, 37(1): 12-18.

Bichsel, Y. and von Gunten, U., 1999. Oxidation of iodide and hypiodous acid in the disinfection of natural waters. *Environmental Science & Technology*, 33(22): 4040-4045.

Bielski, B.H.J., 1978. Re-evaluation of spectral and kinetic properties of HO₂ and (O[·])₂ free-radicals. *Photochemistry and Photobiology*, 28(4-5): 645-649.

Bigg, E.K., Leck, C. and Tranvik, L., 2004. Particulates of the surface microlayer of open water in the central Arctic Ocean in summer. *Marine Chemistry*, 91(1-4): 131-141.

Blanchard, D.C. and Syzdek, L., 1970. Mechanism for water-to-air transfer and concentration of bacteria. *Science*(170): 626.

Blough, N.V. and Del Vecchio, R., 2002. Chromophoric DOM in the coastal environment. In: D. Hansell and C.A. Carlson (Editors), *Biogeochemistry of Marine Dissolved Organic Matter*. Academic Press, Amsterdam, pp. 509 - 546.

Bowen, H.J.M., 1966. *Trace Elements in Biochemistry*. Academic Press, London.

Bowie, A.R., Achterberg, E.P., Mantoura, R.F.C. and Worsfold, P.J., 1998. Determination of sub-nanomolar levels of iron in seawater using flow injection with chemiluminescence detection. *Analytica Chimica Acta*, 361(3): 189-200.

Bristow, L., 2009. Tracing nitrogen flow across the southern North Sea: A stable isotope approach, University of East Anglia, Norwich.

Broecker, W.S. and Peng, T.H., 1971. The vertical distribution of radon in the Bomex area. *Earth and Planetary Science Letters*, 11: 99 - 108.

Brugmann, L., Bernard, P.C. and Vangrieken, R., 1992. Geochemistry of suspended matter from the Baltic Sea. 2. Results of bulk trace-metal analysis by AAS. *Marine Chemistry*, 38(3-4): 303-323.

Bruland, K.W., 1983. Trace elements in sea water. In: J.P. Riley and R. Chester (Editors), Chemical Oceanography. Academic Press, London, pp. 157-220.

Bruland, K.W., Franks, R.P., Knauer, G.A. and Martin, J.H., 1979. Sampling and analytical methods for the determination of copper, cadmium, zinc, and nickel at the nanogram per liter level in sea-water. *Analytica Chimica Acta*, 105(1): 233-245.

Bruland, K.W. and Rue, E., 2002. Analytical methods for the determination of concentrations and speciation of iron. In: D.R. Turner and K.A. Hunter (Editors), The Biogeochemistry of Iron in Seawater. Wiley New York, pp. 255 - 289.

Buffe, M.O., Schumacher, J., Meylan, S., Jekel, M. and von Gunten, U., 2006. Ozonation and advanced oxidation of wastewater: Effect of O₃ dose, pH, DOM and HO center dot-scavengers on ozone decomposition and HO center dot generation. *Ozone-Science & Engineering*, 28(4): 247-259.

Bull, C., McClune, G.J. and Fee, J.A., 1983. The mechanism of iron EDTA catalyzed superoxide dismutation. *Journal of the American Chemical Society*, 105(16): 5290-5300.

Burnol, A. and Charlet, L., 2010. Fe(II) - Fe(III)-bearing phases as a mineralogical control on the heterogeneity of arsenic in southeast asian groundwater. *Environmental Science & Technology*: 7541-7547.

Buxton, G.V., Greenstock, C.L., Helman, W.P. and Ross, A.B., 1988. Critical-review of rate constants for reactions of hydrated electrons, hydrogen-atoms and hydroxyl radicals (·OH/·O⁻) in aqueous-solution. *Journal of Physical and Chemical Reference Data*, 17(2): 513-886.

Campos, M., Farrenkopf, A.M., Jickells, T.D. and Luther, G.W., 1996. A comparison of dissolved iodine cycling at the Bermuda Atlantic Time-Series station and Hawaii Ocean Time-Series Station. *Deep-Sea Research Part II-Topical Studies in Oceanography*, 43(2-3): 455-466.

Campos, M., Sanders, R. and Jickells, T., 1999. The dissolved iodate and iodide distribution in the South Atlantic from the Weddell Sea to Brazil. *Marine Chemistry*, 65(3-4): 167-175.

Carlson, D.J., 1982. A field-evaluation of plate and screen microlayer sampling techniques. *Marine Chemistry*, 11(3): 189-208.

Christensen, H., Sehested, K. and Corfitzen, H., 1982. Reactions of hydroxyl radicals with hydrogen peroxide at ambient and elevated temperatures. *Journal of Physical Chemistry*, 86(9): 1588-1590.

Clifford, D. and Donaldson, D.J., 2007. Direct experimental evidence for a heterogeneous reaction of ozone with bromide at the air-aqueous interface. *Journal of Physical Chemistry A*, 111(39): 9809-9814.

Coale, K.H., Johnson, K.S., Stout, P.M. and Sakamoto, C.M., 1992. Determination of copper in sea-water using a flow-injection method with chemiluminescence detection. *Analytica Chimica Acta*, 266(2): 345-351.

Compiano, A.M., Romano, J.C., Garabetian, F., Laborde, P. and Delagiraudiere, I., 1993. Monosaccharide composition of particulate hydrolyzable sugar fraction in surface microlayers from brackish and marine waters. *Marine Chemistry*, 42(3-4): 237-251.

Cooper, W.J., Zika, R.G., Petasne, R.G. and Plane, J.M.C., 1988. Photochemical formation of H₂O₂ in natural-waters exposed to sunlight. *Environmental Science & Technology*, 22(10): 1156-1160.

Covington, A.K., Whalley, P.D. and Davison, W., 1983. Procedures for the measurement of pH in low ionic-strength solutions including fresh-water. *Analyst*, 108(1293): 1528-1532.

Craig, P.S., Shaw, T.J., Miller, P.L., Pellechia, P.J. and Ferry, J.L., 2008. Use of multiparametric techniques to quantify the effects of naturally occurring ligands on the kinetics of Fe(II) oxidation. *Environmental Science & Technology*, 43(2): 337-342.

Croot, P.L. and Laan, P., 2002. Continuous shipboard determination of Fe(II) in polar waters using flow injection analysis with chemiluminescence detection. *Analytica Chimica Acta*, 466: 261 - 273.

Crosby, S.A. et al., 1983. Surface-areas and porosities of Fe(III)-derived and Fe(II)-derived oxyhydroxides. *Environmental Science & Technology*, 17(12): 709-713.

Cross, J.N. et al., 1987. Contaminant concentrations and toxicity of sea-surface microlayer near Los Angeles, California. *Marine Environmental Research*, 23(4): 307-323.

Crow, S.A., Ahearn, D.G., Cook, W.L. and Bourquin, A.W., 1975. Densities of bacteria and fungi in coastal surface films as determined by a membrane-adsorption procedure. *Limnology and Oceanography*, 20(4): 644 - 646.

Cunliffe, M. et al., 2009a. Comparison and validation of sampling strategies for the molecular microbial analysis of surface microlayers. *Aquatic Microbial Ecology*, 57(1): 69-77.

Cunliffe, M. et al., 2009b. Dissolved organic carbon and bacterial populations in the gelatinous surface microlayer of a Norwegian fjord mesocosm. *Fems Microbiology Letters*, 299(2): 248-254.

Cunliffe, M. et al., 2009c. Comparison of bacterioneuston and bacterioplankton dynamics during a phytoplankton bloom in a fjord mesocosm. *Applied and Environmental Microbiology*, 75(22): 7173-7181.

Cuong, D.T., Karuppiah, S. and Obbard, J.P., 2008. Distribution of heavy metals in the dissolved and suspended phase of the sea-surface microlayer, seawater column and in sediments of singapore's coastal environment. *Environmental Monitoring and Assessment*, 138(1-3): 255-272.

Davison, W., 1993. Iron and manganese in lakes. *Earth-Science Reviews*, 34(2): 119-163.

de Jong, J.T.M. et al., 1998. Dissolved iron at subnanomolar levels in the Southern Ocean as determined by ship-board analysis. *Analytica Chimica Acta*, 377(2-3): 113-124.

Del Vecchio, R. and Blough, N.V., 2002. Photobleaching of chromophoric dissolved organic matter in natural waters: kinetics and modeling. *Marine Chemistry*, 78(4): 231-253.

Dickson, A.G., 1984. pH scales and proton-transfer reactions in saline media such as sea-water. *Geochimica et Cosmochimica Acta*, 48(11): 2299-2308.

Dickson, A.G., 1993. The measurement of sea-water pH. *Marine Chemistry*, 44(2-4): 131-142.

Doi, T., Obata, H. and Maruo, M., 2004. Shipboard analysis of picomolar levels of manganese in seawater by chelating resin concentration and chemiluminescence detection. *Analytical and Bioanalytical Chemistry*, 378(5): 1288-1293.

Duce, R.A. et al., 1972. Enrichment of heavy metals and organic compounds in the surface microlayer of Narrangansett Bay, Rhode Island. *Science*, 176: 161 - 163.

Eiden, G.C., Barinaga, C.J. and Koppenaal, D.W., 1997. Beneficial ion/molecule reactions in elemental mass spectrometry. *Rapid Communications in Mass Spectrometry*, 11(1): 37-42.

Ellison, S.L.R. and Thompson, M., 2008. Standard additions: myth and reality. *Analyst*, 133(8): 992-997.

Emerson, S. et al., 1982. Environmental oxidation rate of manganese(II) - bacterial catalysis. *Geochimica et Cosmochimica Acta*, 46(6): 1073-1079.

Emmenegger, L., King, D.W., Sigg, L. and Sulzberger, B., 1998. Oxidation kinetics of Fe(II) in a eutrophic Swiss lake. *Environmental Science & Technology*, 32(19): 2990-2996.

Emmenegger, L., Schonenberger, R.R., Sigg, L. and Sulzberger, B., 2001. Light-induced redox cycling of iron in circumneutral lakes. *Limnology and Oceanography*, 46(1): 49-61.

Eriksen, T.E., Lind, J. and Merenyi, G., 1981. Chemiluminescence of 5-aminophthalazine-1,4-dione in the presence of hydrogen peroxide. *Journal of the Chemical Society, Faraday Transactions 1*, 77: 2137 - 2148.

Evans, E.H. and Giglio, J.J., 1993. Interferences in inductively coupled plasma mass-spectrometry - A review. *Journal of Analytical Atomic Spectrometry*, 8(1): 1-18.

Faust, B.C. and Hoigne, J., 1989. Photolysis of Fe(III)-hydroxy complexes as sources of OH radicals in clouds, fog and rain. *Atmospheric Environment*, 24A(1): 79 - 89.

Faust, B.C. and Zepp, R.G., 1993. Photochemistry of aqueous iron(III) polycarboxylate complexes - roles in the chemistry of atmospheric and surface waters. *Environmental Science & Technology*, 27(12): 2517-2522.

Feldmann, I., Tittes, W., Jakubowski, N., Stuewer, D. and Giessmann, U., 1994. Performance-characteristics of inductively-coupled plasma-mass spectrometry with high-mass resolution. *Journal of Analytical Atomic Spectrometry*, 9(9): 1007-1014.

Fischer, A.C., Kroon, J.J., Verburg, T.G., Teunissen, T. and Wolterbeek, H.T., 2007. On the relevance of iron adsorption to container materials in small-volume experiments on iron marine chemistry: Fe-55-aided assessment of capacity, affinity and kinetics. *Marine Chemistry*, 107(4): 533-546.

Fox, M.A. and Whitesell, J.K., 2004. *Organic Chemistry*. Jones and Bartlett, London.

Franklin, B., 1773. Oil on Water, pp. letter

Fujii, M., Rose, A.L., Waite, T.D. and Omura, T., 2006. Superoxide-mediated dissolution of amorphous ferric oxyhydroxide in seawater. *Environmental Science & Technology*, 40(3): 880-887.

Fujii, M., Rose, A.L., Waite, T.D. and Omura, T., 2010. Oxygen and superoxide-mediated redox kinetics of iron complexed by humic substances in coastal seawater. *Environmental Science & Technology*, 44(24): 9337-9342.

Furrer, G. and Stumm, W., 1986. The coordination chemistry of weathering. 1. Dissolution kinetics of delta-Al₂O₃ and BeO. *Geochimica et Cosmochimica Acta*, 50(9): 1847-1860.

Garabetian, F., Romano, J.C., Paul, R. and Sigoillot, J.C., 1993. Organic-matter composition and pollutant enrichment of sea-surface microlayer inside and outside slicks. *Marine Environmental Research*, 35(4): 323-339.

Garcia-Flor, N. et al., 2005. Comparison of sampling devices for the determination of polychlorinated biphenyls in the sea surface microlayer. *Marine Environmental Research*, 59(3): 255-275.

Garland, J.A. and Curtis, H., 1981. Emission of iodine from the sea-surface in the presence of ozone. *Journal of Geophysical Research-Oceans and Atmospheres*, 86(NC4): 3183-3186.

Garland, J.A., Elzerman, A.W. and Penkett, S.A., 1980. The mechanism for dry deposition of ozone to seawater surfaces. *Journal of Geophysical Research-Oceans and Atmospheres*, 85(NC12): 7488-7492.

Garrett, W.D., 1965. Collection of slick-forming materials from the sea surface. *Limnology and Oceanography*, 10: 602 - 605.

Garrett, W.D., 1967. The organic composition of the ocean surface. *Deep Sea Research*, 14: 221 - 227.

Garrett, W.D., 1974. Comments on "Laboratory comparisons of four surface microlayer samplers" (R. F. Hatcher and B. C. Parker) *Limnology and Oceanography*, 19(1): 166 - 167.

Gasparovic, B., Kozarac, Z., Saliot, A., Cosovic, B. and Mobius, D., 1998. Physicochemical characterization of natural and ex-situ reconstructed sea-surface microlayers. *Journal of Colloid and Interface Science*, 208(1): 191-202.

Gerringa, L.J.A., Rijkenberg, M.J.A., Timmermans, K.R. and Buma, A.G.J., 2004. The influence of solar ultraviolet radiation on the photochemical production of H₂O₂ in the equatorial atlantic ocean. *Journal of Sea Research*, 51(1): 3-10.

Giessmann, U. and Greb, U., 1994. High-resolution ICP-MS - A new concept for elemental mass-spectrometry. *Fresenius Journal of Analytical Chemistry*, 350(4-5): 186-193.

Glasby, G.P. and Schulz, H.D., 1999. E-H, pH diagrams for Mn, Fe, Co, Ni, Cu and As under seawater conditions: Application of two new types of E-H, pH diagrams to the study of specific problems in marine geochemistry. *Aquatic Geochemistry*, 5(3): 227-248.

Glaze, W.H. and Kang, J.W., 1989. Advanced oxidation processes - description of a kinetic-model for the oxidation of hazardous materials in aqueous media with ozone and hydrogen-peroxide in a semibatch reactor. *Industrial & Engineering Chemistry Research*, 28(11): 1573-1580.

Gledhill, M. and van den Berg, C.M.G., 1994. Determination of complexation of iron(III) with natural organic complexing ligands in seawater using cathodic stripping voltammetry. *Marine Chemistry*, 47(1): 41-54.

Goldstone, J.V., Pullin, M.J., Bertilsson, S. and Voelker, B.M., 2002. Reactions of hydroxyl radical with humic substances: Bleaching, mineralization, and production of bioavailable carbon substrates. *Environmental Science & Technology*, 36(3): 364-372.

Goldstone, J.V. and Voelker, B.M., 2000. Chemistry of superoxide radical in seawater: CDOM associated sink of superoxide in coastal waters. *Environmental Science & Technology*, 34(6): 1043-1048.

Gonzalez-Davila, M., Santana-Casiano, J.M. and Millero, F.J., 2006. Competition between O₂ and H₂O₂ in the oxidation of Fe(II) in natural waters. *Journal of Solution Chemistry*, 35(1): 95-111.

Grassian, V.H., 2005. *Environmental Catalysis*. CRC Press, Taylor & Francis Group, 700 pp.

Gray, R.D., 1969. Kinetics of oxidation of copper (I) by molecular oxygen in perchloric acid-acetonitrile solutions. *Journal of the American Chemical Society*, 91(1): 56-&.

Grebel, J.E., Pignatello, J.J. and Mitch, W.A., 2010. Effect of halide ions and carbonates on organic contaminant degradation by hydroxyl radical-based advanced oxidation processes in saline waters. *Environmental Science & Technology*, 44(17): 6822-6828.

Granic, G., Trefry, J.H. and Keaffaber, J.J., 1994. Ozonation products of bromine and chlorine in seawater aquaria. *Water Research*, 28(5): 1087-1094.

Grotti, M. et al., 2001. Temporal distribution of trace metals in Antarctic coastal waters. *Marine Chemistry*, 76(3): 189-209.

Guitart, C., Garcia-Flor, N., Miquel, J.C., Fowler, S.W. and Albaiges, J., 2010. Effect of the accumulation of polycyclic aromatic hydrocarbons in the sea surface microlayer on their coastal air-sea exchanges. *Journal of Marine Systems*, 79(1-2): 210-217.

Haag, W.R. and Hoigne, J., 1983a. Ozonation of bromide-containing waters - kinetics of formation of hypobromous acid and bromate. *Environmental Science & Technology*, 17(5): 261-267.

Haag, W.R. and Hoigne, J., 1983b. Ozonation of water containing chlorine or chloramines - reaction-products and kinetics. *Water Research*, 17(10): 1397-1402.

Haag, W.R., Hoigne, J. and Bader, H., 1982. Ozonation of bromide-containing drinking waters - formation kinetics of secondary bromine compounds. *Vom Wasser*, 59: 237-251.

Haber, F. and Weiss, J., 1932. Über die katalyse des hydroperoxydes. *Die Naturwissenschaften*, 20(51): 948 - 950.

Hama, T., Yanagi, K. and Hama, J., 2004. Decrease in molecular weight of photosynthetic products of marine phytoplankton during early diagenesis. *Limnology and Oceanography*, 49(2): 471-481.

Hamilton, E.I. and Clifton, R.J., 1979. Techniques for sampling the air-sea interface for estuarine and coastal waters. *Limnology and Oceanography*, 24(1): 188 - 193.

Hansard, S.P., Easter, H.D. and Voelker, B.M., 2011. Rapid reaction of nanomolar Mn(II) with superoxide radical in seawater and simulated freshwater. *Environmental Science & Technology*, 45(7): 2811-2817.

Hansard, S.P. and Landing, W.M., 2009. Determination of iron(II) in acidified seawater samples by luminol chemiluminescence. *Limnology and Oceanography-Methods*, 7: 222-234.

Hardy, J.T., 1982. The sea surface microlayer: Biology, chemistry and anthropogenic enrichment. *Progress in Oceanography*, 11: 307 - 328.

Hardy, J.T., 1997. Biological effects of chemicals in the sea-surface microlayer. In: P.S. Liss and R.A. Duce (Editors), *The Sea Surface and Global Change*. Cambridge University Press, Cambridge, pp. 339 - 370.

Hardy, J.T., Apts, C.W., Crecelius, E.A. and Fellingham, G.W., 1985. The sea-surface microlayer - Fate and residence times of atmospheric metals. *Limnology and Oceanography*, 30(1): 93-101.

Hardy, J.T. and Cleary, J., 1992. Surface microlayer contamination and toxicity in the German Bight. *Marine Ecology-Progress Series*, 91(1-3): 203-210.

Hardy, J.T. et al., 1987. The sea-surface microlayer of Puget Sound .2. Concentrations of contaminants and relation to toxicity. *Marine Environmental Research*, 23(4): 251-271.

Hardy, J.T. et al., 1990. Aquatic surface microlayer contamination in Chesapeake Bay. *Marine Chemistry*, 28(4): 333-351.

Harvey, G.R. and Springer-Young, M., 1988. Ozone in seawater and lake water - A reversible reservoir. *Geophysical Research Letters*, 15(11): 1199-1201.

Harvey, G.W., 1966. Microlayer collection from the sea surface: A new method and initial results. *Limnology and Oceanography*, 11: 608 - 613.

Harvey, G.W. and Burzell, L.A., 1972. A simple microlayer method for small samples. *Limnology and Oceanography*, 17: 156 - 157.

Hatcher, R.F. and Parker, B.C., 1974. Laboratory comparisons of four surface microlayer samplers. *Limnology and Oceanography*, 19: 162 - 165.

Havens, K.E. and Heath, R.T., 1990. Phytoplankton succession during acidification with and without increasing aluminum levels. *Environmental Pollution*, 68(1-2): 129-145.

Heikes, B.G., 1984. Aqueous H₂O₂ production from O₃ in glass impingers. *Atmospheric Environment*, 18(7): 1433-1445.

Heller, M.I. and Croot, P.L., 2010a. Kinetics of superoxide reactions with dissolved organic matter in tropical Atlantic surface waters near Cape Verde (TENATSO). *Journal of Geophysical Research-Oceans*, 115.

Heller, M.I. and Croot, P.L., 2010b. Superoxide decay kinetics in the Southern Ocean. *Environmental Science & Technology*, 44(1): 191-196.

Hem, J.D., 1977. Reactions of metal-ions at surfaces of hydrous iron-oxide. *Geochimica et Cosmochimica Acta*, 41(4): 527-538.

Hem, J.D., 1978. Redox processes at surfaces of manganese oxide and their effects on aqueous metal-ions. *Chemical Geology*, 21(3-4): 199-218.

Hoigne, J. and Bader, H., 1975. Ozonation of water - role of hydroxyl radicals as oxidizing intermediates. *Science*, 190(4216): 782-784.

Hoigne, J. and Bader, H., 1976. Role of hydroxyl radical reactions in ozonation processes in aqueous-solutions. *Water Research*, 10(5): 377-386.

Hoigne, J. and Bader, H., 1983a. Rate constants of reactions of ozone with organic and inorganic-compounds in water. 1. Non-dissociating organic-compounds. *Water Research*, 17(2): 173-183.

Hoigne, J. and Bader, H., 1983b. Rate constants of reactions of ozone with organic and inorganic-compounds in water. 2. Dissociating organic-compounds. *Water Research*, 17(2): 185-194.

Hoigne, J., Bader, H., Haag, W.R. and Staehelin, J., 1985. Rate constants of reactions of ozone with organic and inorganic-compounds in water .3. Inorganic-compounds and radicals. *Water Research*, 19(8): 993-1004.

Hopkinson, B.M. and Barbeau, K.A., 2007. Organic and redox speciation of iron in the eastern tropical North Pacific suboxic zone. *Marine Chemistry*, 106(1-2): 2-17.

Horst, D. and Zabel, M., 1996. *Marine Geochemistry*. Springer-Verlag, Berlin.

Hortnagl, P., Perez, M.T. and Sommaruga, R., 2010. Living at the border: A community and single-cell assessment of lake bacterioneuston activity. *Limnology and Oceanography*, 55(3): 1134-1144.

Houk, R.S. et al., 1980. Inductively coupled argon plasma as an ion-source for mass-spectrometric determination of trace-elements. *Analytical Chemistry*, 52(14): 2283-2289.

Hsu, Y.C., Chen, T.Y., Chen, J.H. and Lay, C.W., 2002. Ozone transfer into water in a gas-inducing reactor. *Industrial & Engineering Chemistry Research*, 41(1): 120-127.

Hunter, K.A., 1980a. Microelectrophoretic properties of natural surface-active organic-matter in coastal seawater. *Limnology and Oceanography*, 25(5): 807-822.

Hunter, K.A., 1980b. Processes affecting particulate trace-metals in the sea-surface microlayer. *Marine Chemistry*, 9(1): 49-70.

Hunter, K.A., 1997. Chemistry of the sea-surface microlayer. In: P.S. Liss and R.A. Duce (Editors), *The Sea Surface and Global Change*. Cambridge University Press, Cambridge, pp. 287 - 320.

Hunter, K.A. and Liss, P.S., 1981. Polarographic measurement of surface-active material in natural waters. *Water Research*, 15: 203 - 215.

Hutchins, D.A., Ditullio, G.R. and Bruland, K.W., 1993. Iron and regenerated production - evidence for biological iron recycling in 2 marine environments. *Limnology and Oceanography*, 38(6): 1242-1255.

Jarvis, K.E., Gray, A.L. and Houk, R.S., 1997. *Handbook of Inductively Coupled Plasma Mass Spectrometry*. Blackie Academic & Professional Bury St. Edmunds, 380 pp.

Jeandel, C., Caisso, M. and Minster, J.F., 1987. Vanadium behaviour in the global ocean and in the Mediterranean Sea. *Marine Chemistry*, 21(1): 51-74.

Ji, H., Sha, Y., Xin, H. and Qi, Y., 2009. Measurement of trace manganese (II) by catalytic kinetic spectrophotometric method. *Journal of Ocean University of China*, 8(2): 127-132.

Jickells, T.D. and Spokes, L.J., 2001. Atmospheric iron inputs to the ocean. In: D.R. Turner and K.H. Hunter (Editors), *The Biogeochemistry of Iron in Seawater*. IUPAC Series on Analytical and Physical Chemistry of Environmental Systems. John Wiley & Sons Ltd, Chichester, pp. 396.

Johnston, J.H. and Lewis, D.G., 1983. A detailed study of the transformation of ferrihydrite to hematite in an aqueous medium at 92°C. *Geochimica et Cosmochimica Acta*, 47(11): 1823-1831.

Joy, P., Gilbert, E. and Eberle, S.H., 1980. A quantitative investigation of the reaction of ozone with para-toluenesulfonic acid in aqueous-solution as a model-compound for anionic detergents. *Water Research*, 14(10): 1509-1516.

Kieber, R.J., Zhou, X.L. and Mopper, K., 1990. Formation of carbonyl-compounds from UV-induced photodegradation of humic substances in natural waters - fate of riverine carbon in the sea. *Limnology and Oceanography*, 35(7): 1503-1515.

King, D.W., 1998. Role of carbonate speciation on the oxidation rate of Fe(II) in aquatic systems. *Environmental Science & Technology*, 32(19): 2997-3003.

King, D.W., 2000. A chemiluminescence based FIA system for Fe(II) analysis, pp. 5.

King, D.W., Aldrich, R.A. and Charnecki, S.E., 1993. Photochemical redox cycling of iron in NaCl solution. *Marine Chemistry*, 44(2-4): 105-120.

King, D.W., Lounsbury, H.A. and Millero, F.J., 1995. Rates and mechanism of Fe(II) oxidation at nanomolar total iron concentrations. *Environmental Science & Technology*, 29(3): 818-824.

Kjelleberg, S., Stenstrom, T.A. and Odham, G., 1979. Comparative-study of different hydrophobic devices for sampling lipid surface-films and adherent microorganisms. *Marine Biology*, 53(1): 21-25.

Klopf, L.L. and Nieman, T.A., 1983. Effect of iron(II), cobalt(II), copper(II), and manganese(II) on the chemi-luminescence of luminol in the absence of hydrogen-peroxide. *Analytical Chemistry*, 55(7): 1080-1083.

Kohler, J.T., Altomare, R.E. and Kittrell, J.R., 1975. Catalytic decomposition of hydrogen peroxide by manganese-alumina. *Industrial & Engineering Chemistry Product Research and Development*, 14(1): 36-40.

Kopacek, J., Klementova, P. and Norton, S.A., 2005. Photochemical production of ionic and particulate aluminum and iron in lakes. *Environmental Science & Technology*, 39(10): 3656-3662.

Kosak-Channing, L.F. and Helz, G.R., 1983. Solubility of ozone in aqueous solutions of 0-0.6 M ionic strength at 5-30-degress-C. *Environmental Science & Technology*, 17(3): 145-149.

Kosaka, K., Yamada, H., Matsui, S., Echigo, S. and Shishida, K., 1998. Comparison among the methods for hydrogen peroxide measurements to evaluate advanced oxidation processes: Application of a spectrophotometric method using copper(II) ion and 2,9 dimethyl-1,10-phenanthroline. *Environmental Science & Technology*, 32(23): 3821-3824.

Kuma, K., Nakabayashi, S. and Matsunaga, K., 1995. Photoreduction of Fe(III) by hydroxycarboxylic acids in seawater. *Water Research*, 29(6): 1559-1569.

Kuma, K., Nakabayashi, S., Suzuki, Y., Kudo, I. and Matsunaga, K., 1992. Photoreduction of Fe(III) by dissolved organic substances and existence of Fe(II) in seawater during spring blooms. *Marine Chemistry*, 37(1-2): 15-27.

Kuznetsova, M., Lee, C. and Aller, J., 2005. Characterization of the proteinaceous matter in marine aerosols. *Marine Chemistry*, 96(3-4): 359-377.

Laglera, L.M. and van den Berg, C.M.G., 2007. Wavelength dependence of the photochemical reduction of iron in Arctic seawater. *Environmental Science & Technology*, 41(7): 2296-2302.

Larsson, K., Odham, G. and Sodergren, A., 1974. On Lipid surface films on the sea. I. A simple method for sampling and studies of composition. *Marine Chemistry*, 2(1): 49 - 57.

Lee, J.D. et al., 2009. Year-round measurements of nitrogen oxides and ozone in the tropical North Atlantic marine boundary layer. *Journal of Geophysical Research-Atmospheres*, 114.

Lelieveld, J. et al., 2004. Increasing ozone over the Atlantic Ocean. *Science*, 304(5676): 1483-1487.

Lion, L.W. and Leckie, J.O., 1981. The biogeochemistry of the air-sea interface. *Annual Review of the Earth and Planetary Science Letters*, 9: 449 - 486.

Liss, P.S., 1975. Chemistry of the sea surface microlayer. In: J.P. Riley and G. Skirrow (Editors), *Chemical Oceanography*. Academic Press, London, pp. 193 - 243.

Liss, P.S. and Duce, R.A. (Editors), 1997. *The Sea Surface and Global Change*. Cambridge University Press, Cambridge, 519 pp.

Liu, Q. et al., 2001. Kinetics and mechanisms of aqueous ozone reactions with bromide, sulfite, hydrogen sulfite, iodide, and nitrite ions. *Inorganic Chemistry*, 40(17): 4436-4442.

Logager, T., Holcman, J., Sehested, K. and Pedersen, T., 1992. Oxidation of ferrous ions by ozone in acidic solutions. *Inorganic Chemistry*, 31(17): 3523-3529.

Logan, B.E., Passow, U., Alldredge, A.L., Grossart, H.P. and Simon, M., 1995. Rapid formation and sedimentation of large aggregates is predictable from coagulation rates (half-lives)

of transparent exopolymer particles (Tep). Deep-Sea Research Part II-Topical Studies in Oceanography, 42(1): 203-214.

Lorenzen, C.J., 1967. Determination of chlorophyll and pheo-pigments - spectrophotometric equations. Limnology and Oceanography, 12(2): 343-&.

Louie, H., Wu, M., Di, P., Snitch, P. and Chapple, G., 2002. Direct determination of trace elements in sea-water using reaction cell inductively coupled plasma mass spectrometry. Journal of Analytical Atomic Spectrometry, 17: 587 - 591.

Lovato, M.E., Martin, C.A. and Cassano, A.E., 2009. A reaction kinetic model for ozone decomposition in aqueous media valid for neutral and acidic pH. Chemical Engineering Journal, 146(3): 486-497.

Luo, Y. et al., 2009. A new luminol derivative as a fluorescent probe for trace analysis of copper(II). Microchimica Acta, 164(3-4): 411-417.

Majestic, B.J., Anbar, A.D. and Herckes, P., 2009. Elemental and iron isotopic composition of aerosols collected in a parking structure. Science of the Total Environment, 407(18): 5104-5109.

Maldonado, M.T., Strzepek, R.F., Sander, S. and Boyd, P.W., 2005. Acquisition of iron bound to strong organic complexes, with different Fe binding groups and photochemical reactivities, by plankton communities in Fe-limited subantarctic waters. Global Biogeochemical Cycles, 19(4).

Martino, M., Mills, G.P., Woeltjen, J. and Liss, P.S., 2009. A new source of volatile organoiodine compounds in surface seawater. Geophysical Research Letters, 36.

McBain, J.W. and Humphreys, C.W., 1932. The microtome method of the determination of the absolute amount of adsorption. Journal of Physical Chemistry, 36(1): 300 - 311.

McKay, W.A., Stephens, B.A. and Dollard, G.J., 1992. Laboratory measurements of ozone deposition to sea-water and other saline solutions. Atmospheric Environment Part A-General Topics, 26(17): 3105-3110.

McLaren, J.W., Mykytiuk, A.P., Willie, S.N. and Berman, S.S., 1985. Determination of trace-metals in seawater by inductively coupled plasma mass-spectrometry with preconcentration on silica-immobilized 8-hydroxyquinoline. Analytical Chemistry, 57(14): 2907-2911.

Measures, C.I. and Vink, S., 2000. On the use of dissolved aluminum in surface waters to estimate dust deposition to the ocean. *Global Biogeochemical Cycles*, 14(1): 317-327.

Mehlorn, R.J., 1986. The interaction of inorganic species with biomembranes. In: M. Bernhard, F.E. Brinckman and P.J. Sadler (Editors), *The Importance of Chemical "Speciation" in Environmental Processes*. Life Science Research Reports. Springer-Verlag, Berlin, pp. 85 - 98.

Merenyi, G., Ling, J. and Eriksen, T.E., 1990. Luminol chemiluminescence: Chemistry, excitation, emitter *Journal of Bioluminescence and Chemiluminescence*, 5: 53 - 56.

Meunier, L., Laubscher, H., Hug, S.J. and Sulzberger, B., 2005. Effects of size and origin of natural dissolved organic matter compounds on the redox cycling of iron in sunlit surface waters. *Aquatic Sciences*, 67(3): 292-307.

Micinski, E., Ball, L.A. and Zafiriou, O.C., 1993. Photochemical oxygen activation - superoxide radical detection and production-rates in the eastern Caribbean. *Journal of Geophysical Research-Oceans*, 98(C2): 2299-2306.

Mignon, C. and Nicolas, E., 1998. The trace metal recycling component in the north-western Mediterranean. *Marine Pollution Bulletin*, 36(4): 273-277.

Miles, C.J. and Brezonik, P.L., 1981. Oxygen-consumption in humic-colored waters by a photochemical ferrous-ferric catalytic cycle. *Environmental Science & Technology*, 15(9): 1089-1095.

Miller, C.J., Rose, A.L. and Waite, T.D., 2009. Impact of natural organic matter on H₂O₂-mediated oxidation of Fe(II) in a simulated freshwater system. *Geochimica et Cosmochimica Acta*, 73(10): 2758-2768.

Miller, J.C. and Miller, J.N., 1993. *Statistics for Analytical Chemistry*. Ellwood series in analytical chemistry 3rd ed. Ellis Horwood PTR Prentice Hall, New York.

Miller, W.L., King, D.W., Lin, J. and Kester, D.R., 1995. Photochemical redox cycling of iron in coastal seawater. *Marine Chemistry*, 50(1-4): 63-77.

Millero, F.J., 1985. The effect of ionic interactions on the oxidation of metals in natural waters. *Geochimica et Cosmochimica Acta*, 49(2): 547-553.

Millero, F.J., 1987. Estimate of the life time of superoxide in seawater. *Geochimica et Cosmochimica Acta*, 51(2): 351-353.

Millero, F.J., 2006. Chemical Oceanography. CRC Press, Taylor & Francis Group.

Millero, F.J. and Sotolongo, S., 1989. The oxidation of Fe(II) with H₂O₂ in seawater. *Geochimica et Cosmochimica Acta*, 53(8): 1867-1873.

Millero, F.J., Sotolongo, S. and Izaguirre, M., 1987. The oxidation kinetics of Fe(II) in seawater. *Geochimica et Cosmochimica Acta*, 51(4): 793-801.

Millero, F.J., Woosley, R., Ditrolio, B. and Waters, J., 2009. Effect of ocean acidification on the speciation of metals in seawater. *Oceanography*, 22(4): 72-85.

Millero, F.J., Yao, W.S. and Aicher, J., 1995. The speciation of Fe(II) and Fe(III) in natural waters. *Marine Chemistry*, 50(1-4): 21-39.

Moffett, J.W. and Zafiriou, O.C., 1993. The photochemical decomposition of hydrogen-peroxide in surface waters of the eastern Caribbean and Orinoco river. *Journal of Geophysical Research-Oceans*, 98(C2): 2307-2313.

Moffett, J.W. and Zika, R.G., 1983. Oxidation-kinetics of Cu(I) in seawater - implications for its existence in the marine-environment. *Marine Chemistry*, 13(3): 239-251.

Moffett, J.W. and Zika, R.G., 1987. Reaction-kinetics of hydrogen-peroxide with copper and iron in seawater. *Environmental Science & Technology*, 21(8): 804-810.

Momzikoff, A. et al., 2004. Field study of the chemical characterization of the upper ocean surface using various samplers. *Limnology and Oceanography-Methods*, 2: 374-386.

Moore, C.A., Farmer, C.T. and Zika, R.G., 1993. Influence of the Orinoco river on hydrogen-peroxide distribution and production in the eastern Caribbean. *Journal of Geophysical Research-Oceans*, 98(C2): 2289-2298.

Mopper, K. et al., 1995. The role of surface-active carbohydrates in the flocculation of a diatom bloom in a mesocosm. *Deep-Sea Research Part II-Topical Studies in Oceanography*, 42(1): 47-73.

Mopper, K. et al., 1991. Photochemical degradation of dissolved organic-carbon and its impact on the oceanic carbon-cycle. *Nature*, 353(6339): 60-62.

Narvekar, P.V. and Singbal, S.Y.S., 1993. Dissolved aluminum in the surface microlayer of the eastern Arabian Sea. *Marine Chemistry*, 42(2): 85-94.

Nelder, J.A. and Mead, R., 1965. A simplex-method for function minimization. *Computer Journal*, 7(4): 308-313.

Nolan, C.V., Fowler, S.W. and Teyssie, J.L., 1992. Cobalt speciation and bioavailability in marine organisms. *Marine Ecology-Progress Series*, 88(2-3): 105-116.

Nolting, R.F., Gerringa, L.J.A., Swagerman, M.J.W., Timmermans, K.R. and de Baar, H.J.W., 1998. Fe (III) speciation in the high nutrient, low chlorophyll Pacific region of the Southern Ocean. *Marine Chemistry*, 62(3-4): 335-352.

O'Sullivan, D.W., Hanson, A.K. and Kester, D.R., 1995. Stopped-flow luminol chemiluminescence determination of Fe(II) and reducible iron in seawater at subnanomolar levels. *Marine Chemistry*, 49(1): 65-77.

O'Sullivan, D.W., Neale, P.J., Coffin, R.B., Boyd, T.J. and Osburn, S.L., 2005. Photochemical production of hydrogen peroxide and methylhydroperoxide in coastal waters. *Marine Chemistry*, 97(1-2): 14-33.

Ortega-Retuerta, E., Passow, U., Duarte, C.M. and Reche, I., 2009. Effects of ultraviolet B radiation on (not so) transparent exopolymer particles. *Biogeosciences*, 6(12): 3071-3080.

Pattenden, N.J., Cambray, R.S. and Playford, K., 1981. Trace and major elements in the sea-surface microlayer. *Geochimica et Cosmochimica*, 45: 93 - 100.

Peng, T.H., Broecker, W.S., Mathieu, G.G. and Li, Y.H., 1979. Radon evasion rates in the Atlantic and Pacific oceans as determined during the Geosecs program. *Journal of Geophysical Research-Oceans and Atmospheres*, 84(NC5): 2471-2486.

Peng, T.H., Takahashi, T. and Broecker, W.S., 1974. Surface radon measurements in the North Pacific Ocean station Papa. *Journal of Geophysical Research*, 79: 1772 - 1780.

Perfiliev, Y.D., Benko, E.M., Pankratov, D.A., Sharma, V.K. and Dedushenko, S.K., 2007. Formation of iron(VI) in ozonalysis of iron(III) in alkaline solution. *Inorganica Chimica Acta*, 360(8): 2789-2791.

Petasne, R.G. and Zika, R.G., 1987. Fate of superoxide in coastal sea-water. *Nature*, 325(6104): 516-518.

Peterson, M.L. and Carpenter, R., 1983. Biogeochemical processes affecting total arsenic and arsenic species distributions in an intermittently anoxic fjord. *Marine Chemistry*, 12(4): 295-321.

Plane, J.M.C. et al., 1997. Photochemistry in the sea-surface microlayer. In: P.S. Liss and R.A. Duce (Editors), *The Sea Surface and Global Change*. Cambridge University Press, Cambridge, pp. 71 - 92.

Planquette, H. et al., 2007. Dissolved iron in the vicinity of the Crozet Islands, Southern Ocean. *Deep-Sea Research Part II-Topical Studies in Oceanography*, 54(18-20): 1999-2019.

Plavsic, M., Gasparovic, B. and Cosovic, B., 2007. Copper complexation and surfactant activity of organic matter in coastal seawater and surface microlayer samples from north Norwegian fjords and NW Mediterranean Region. *Fresenius Environmental Bulletin*, 16(4): 372-378.

Quiroz-Vazquez, P., White, K.N. and Siguee, D.C., 2008. Aluminium, silicon and transition metal dynamics in a non-polluted lake: Aquatic concentrations and phytoplankton uptake. *Hydrobiologia*, 607: 131-142.

Reinthalter, T., Sintes, E. and Herndl, G.J., 2008. Dissolved organic matter and bacterial production and respiration in the sea-surface microlayer of the open Atlantic and the western Mediterranean Sea. *Limnology and Oceanography*, 53(1): 122-136.

Rich, H.W. and Morel, F.M.M., 1990. Availability of well-defined iron colloids to the marine diatom *Thalassiosira-weissflogii*. *Limnology and Oceanography*, 35(3): 652-662.

Rijkenberg, M.J.A. et al., 2005. The influence of UV irradiation on the photoreduction of iron in the Southern Ocean. *Marine Chemistry*, 93(2-4): 119-129.

Rijkenberg, M.J.A. et al., 2008. Enhancement of the reactive iron pool by marine diatoms. *Marine Chemistry*, 109(1-2): 29-44.

Rijkenberg, M.J.A. et al., 2006. Iron-binding ligands in Dutch estuaries are not affected by UV induced photochemical degradation. *Marine Chemistry*, 100(1-2): 11-23.

Rochelle-Newall, E.J. and Fisher, T.R., 2002. Production of chromophoric dissolved organic matter fluorescence in marine and estuarine environments: An investigation into the role of phytoplankton. *Marine Chemistry*, 77(1): 7-21.

Rose, A.L. and Waite, D., 2006. Role of superoxide in the photochemical reduction of iron in seawater. *Geochimica et Cosmochimica Acta*, 70(15): 3869-3882.

Rose, A.L. and Waite, T.D., 2002. Kinetic model for Fe(II) oxidation in seawater in the absence and presence of natural organic matter. *Environmental Science & Technology*, 36(3): 433-444.

Rose, A.L. and Waite, T.D., 2003a. Kinetics of iron complexation by dissolved natural organic matter in coastal waters. *Marine Chemistry*, 84(1-2): 85-103.

Rose, A.L. and Waite, T.D., 2003b. Predicting iron speciation in coastal waters from the kinetics of sunlight-mediated iron redox cycling. *Aquatic Sciences*, 65(4): 375-383.

Rose, A.L. and Waite, T.L., 2001. Chemiluminescence of luminol in the presence of iron(II) and oxygen: Oxidation mechanism and implications for its analytical use. *Analytical Chemistry*, 73(24): 5909 - 5920.

Roy, E.G., Wells, M.L. and King, D.W., 2008. Persistence of iron(II) in surface waters of the western subarctic Pacific. *Limnology and Oceanography*, 53(1): 89-98.

Rue, E.L. and Bruland, K.W., 1995. Complexation of iron(III) by natural organic-ligands in the central North Pacific as determined by a new competitive ligand equilibration adsorptive cathodic stripping voltammetric method. *Marine Chemistry*, 50(1-4): 117-138.

Rush, J.D. and Bielski, B.H.J., 1985. Pulse radiolytic studies of the reactions of HO₂/O₂⁻ with Fe(II)/Fe(III) ions - the reactivity of HO₂/O₂⁻ with ferric ions and its implication on the occurrence of the Haber-Weiss reaction. *Journal of Physical Chemistry*, 89(23): 5062-5066.

Rush, J.D., Maskos, Z. and Koppenol, W.H., 1990. Distinction between hydroxyl radical and ferryl species. *Methods in Enzymology*, 186: 148-156.

Sakamoto-Arnold, C.M. and Johnson, K.S., 1987. Determination of picomolar levels of cobalt in seawater by flow-injection analysis with chemiluminescence detection. *Analytical Chemistry*, 59(14): 1789-1794.

Salomons, W. and Baccini, P., 1986. Chemical species and metal transport in lakes. In: M. Bernhard, F.E. Brinckman and P.J. Sadler (Editors), *The Importance of Chemical "Speciation" in Environmental Processes*. Life Science Research Reports. Springer-Verlag, Berlin, pp. 193 - 216.

Sanders, J.G. and Windom, H.L., 1980. The uptake and reduction of arsenic species by marine-algae. *Estuarine and Coastal Marine Science*, 10(5): 555-567.

Santana-Casiano, J.M., Gonzalez-Davila, M. and Millero, F.J., 2006. The role of Fe(II) species on the oxidation of Fe(II) in natural waters in the presence of O₂ and H₂O₂. *Marine Chemistry*, 99(1-4): 70-82.

Santana-Casiano, J.M., Gonzalez-Davila, M., Rodriguez, M.J. and Millero, F.J., 2000. The effect of organic compounds in the oxidation kinetics of Fe(II). *Marine Chemistry*, 70(1-3): 211-222.

Santos, A.L. et al., 2009. Short-term variability of abundance, diversity and activity of estuarine bacterioneuston and bacterioplankton. *Journal of Plankton Research*, 31(12): 1545-1555.

Scott, M.J., 1991. Kinetics of adsorption and redox processes on iron and manganese oxides: Reactions of As(III) and Se(IV) at goethite and birnessite surfaces.

Sedlak, D.L. and Hoigne, J., 1993. The role of copper and oxalate in the redox cycling of iron in atmospheric waters. *Atmospheric Environment Part A-General Topics*, 27(14): 2173-2185.

Sehested, K., Holcman, J., Bjergbakke, E. and Hart, E.J., 1984. Formation of ozone in the reaction of OH with O₃(-) and the decay of the ozonide ion radical at pH 10-13. *Journal of Physical Chemistry*, 88(2): 269-273.

Seitz, W.R. and Hercules, D.M., 1972. Determination of trace amounts of iron(II) using chemiluminescence analysis. *Analytical Chemistry*, 44(13): 2143-&.

Shaked, Y., 2008. Iron redox dynamics in the surface waters of the Gulf of Aqaba, Red Sea. *Geochimica et Cosmochimica Acta*, 72(6): 1540-1554.

Shaked, Y., Erel, Y. and Sukenik, A., 2004. The biogeochemical cycle of iron and associated elements in Lake Kinneret. *Geochimica et Cosmochimica Acta*, 68(7): 1439-1451.

Shine, J.P. and Wallace, G.T., 1996. Flux of surface-active organic complexes of copper to the air-sea interface in coastal marine waters. *Journal of Geophysical Research-Oceans*, 101(C5): 12017-12026.

Sieburth, J.M.N. et al., 1976. Dissolved organic-matter and heterotrophic microneuston in surface microlayers of North-Atlantic. *Science*, 194(4272): 1415-1418.

Sima, J. and Makanova, J., 1997. Photochemistry of iron(III) complexes. *Coordination Chemistry Reviews*, 160: 161-189.

Skogerboe, R.K. and Wilson, S.A., 1981. Reduction of ionic species by fulvic-acid. *Analytical Chemistry*, 53(2): 228-232.

Sohrin, Y., Matsui, M., Kawashima, M., Hojo, M. and Hasegawa, H., 1997. Arsenic biogeochemistry affected by eutrophication in Lake Biwa, Japan. *Environmental Science & Technology*, 31(10): 2712-2720.

Song, W.J., Ma, W.H., Ma, J.H., Chen, C.C. and Zhao, J.C., 2005. Photochemical oscillation of Fe(II)/Fe(III) ratio induced by periodic flux of dissolved organic matter. *Environmental Science & Technology*, 39(9): 3121-3127.

Southworth, B.A. and Voelker, B.M., 2003. Hydroxyl radical production via the photo-fenton reaction in the presence of fulvic acid. *Environmental Science & Technology*, 37(6): 1130-1136.

Spokes, L.J. and Liss, P.S., 1995. Photochemically induced redox reactions in seawater, 1. Cations. *Marine Chemistry*, 49: 201 - 213.

Staehelin, J. and Hoigne, J., 1982. Decomposition of ozone in water - rate of initiation by hydroxide ions and hydrogen peroxide. *Environmental Science & Technology*, 16(10): 676-681.

Staehelin, J. and Hoigne, J., 1985. Decomposition of ozone in water in the presence of organic solutes acting as promoters and inhibitors of radical chain reactions. *Environmental Science & Technology*, 19(12): 1206-1213.

Steigenberger, S. and Croot, P.L., 2008. Identifying the processes controlling the distribution of H₂O₂ in surface waters along a meridional transect in the eastern Atlantic. *Geophysical Research Letters*, 35(3).

Steigenberger, S., Statham, P.J., Volker, C. and Passow, U., 2010. The role of polysaccharides and diatom exudates in the redox cycling of Fe and the photoproduction of hydrogen peroxide in coastal seawaters. *Biogeosciences*, 7(1): 109-119.

Stolle, C., Nagel, K., Labrenz, M. and Jurgens, K., 2009. Bacterial activity in the sea-surface microlayer: in situ investigations in the Baltic Sea and the influence of sampling devices. *Aquatic Microbial Ecology*, 58(1): 67-78.

Stolle, C., Nagel, K., Labrenz, M. and Jurgens, K., 2010. Succession of the sea-surface microlayer in the coastal Baltic Sea under natural and experimentally induced low-wind conditions. *Biogeosciences*, 7(9): 2975-2988.

Stone, A.T. and Morgan, J.J., 1984. Reduction and dissolution of manganese(III) and manganese(IV) oxides by organics .2. Survey of the reactivity of organics. *Environmental Science & Technology*, 18(8): 617-624.

Strmecki, S., Plavsic, M., Steigenberger, S. and Passow, U., 2010. Characterization of phytoplankton exudates and carbohydrates in relation to their complexation of copper, cadmium and iron. *Marine Ecology-Progress Series*, 408: 33-46.

Stumm, W. and Morgan, J.J., 1996. *Aquatic Chemistry - Chemical Equilibria and Rates in Natural Waters*. John Wiley and Son, New York, 1022 pp.

Sturgeon, R.E., Berman, S.S., Willie, S.N. and Desaulniers, J.A.H., 1981. Pre-concentration of trace-elements from sea-water with silica-immobilized 8-hydroxyquinoline. *Analytical Chemistry*, 53(14): 2337-2340.

Sugiyama, M., Hori, T., Kihara, S. and Matsui, M., 2005. Geochemical behavior of trace elements in Lake Biwa. *Limnology*, 6(2): 117-130.

Sulzberger, B. and Laubscher, H., 1995. Reactivity of various types of iron(III) (hydr)oxides towards light - induced dissolution. *Marine Chemistry*, 50(1-4): 103-115.

Sunda, W.G., 1984. Measurement of manganese, zinc and cadmium complexation in seawater using chelex ion exchange equilibria. *Marine Chemistry*, 14(4): 365-378.

Sunda, W.G. and Huntsman, S.A., 1988. Effect of sunlight on redox cycles of manganese in the southwestern Sargasso Sea. *Deep-Sea Research Part A-Oceanographic Research Papers*, 35(8): 1297-1317.

Sunda, W.G. and Huntsman, S.A., 1994. Photoreduction of manganese oxides in seawater. *Marine Chemistry*, 46(1-2): 133-152.

Sunda, W.G., Huntsman, S.A. and Harvey, G.R., 1983. Photo-reduction of manganese oxides in seawater and its geochemical and biological implications. *Nature*, 301(5897): 234-236.

Tedetti, M. and Sempere, R., 2006. Penetration of ultraviolet radiation in the marine environment. A review. *Photochemistry and Photobiology*, 82(2): 389-397.

Thompson, A.M. and Zafiriou, O.C., 1983. Air-sea fluxes of transient atmospheric species. *Journal of Geophysical Research-Oceans and Atmospheres*, 88(NC11): 6696-6708.

Tomiyasu, H., Fukutomi, H. and Gordon, G., 1985. Kinetics and mechanism of ozone decomposition in basic aqueous-solution. *Inorganic Chemistry*, 24(19): 2962-2966.

Trick, C.G. and Wilhelm, S.W., 1995. Physiological-changes in the coastal marine cyanobacterium *synechococcus* sp Pcc-7002 exposed to low ferric ion levels. *Marine Chemistry*, 50(1-4): 207-217.

Trojanowski, J. and Antonowicz, J., 2011. Heavy metals in surface microlayer in water of Lake Gardno. *Archives of Environmental Protection*, 37(1): 75-88.

Turner, S.M. and Liss, P.S., 1989. A cryogenic technique for sampling the sea surface microlayer for trace gases. In: J.P. Riley and R. Chester (Editors), *Chemical Oceanography: The Sea/Air Exchange Program*. Academic Pres.

Uchida, S., Satoh, Y., Yamashiro, N. and Satoh, T., 2004. Determination of hydrogen peroxide in water by chemiluminescence detection, (II): Theoretical analysis of luminol chemiluminescence processes. *Journal of Nuclear Science and Technology*, 41(9): 898-906.

Urban, N.R., Gorham, E., Underwood, J.K., Martin, F.B. and Ogden, J.G., 1990. Geochemical processes controlling concentrations of Al, Fe, and Mn in Nova-Scotia lakes. *Limnology and Oceanography*, 35(7): 1516-1534.

Ussher, S.J. et al., 2009. Investigation of iron(III) reduction and trace metal interferences in the determination of dissolved iron in seawater using flow injection with luminol chemiluminescence detection. *Analytica Chimica Acta*, 652(1-2): 259-265.

van den Berg, C.M.G. and Kramer, J.R., 1979. Determination of complexing capacities of ligands in natural-waters and conditional stability-constants of the copper-complexes by means of manganese-dioxide. *Analytica Chimica Acta*, 106(1): 113-120.

van Vleet, E.S. and Williams, P.M., 1980. Sampling sea-surface films - A laboratory evalutaion of techniques and collecting materials. *Limnology and Oceanography*, 25(4): 764-770.

Vermilyea, A.W., Hansard, S.P. and Voelker, B.M., 2010. Dark production of hydrogen peroxide in the Gulf of Alaska. *Limnology and Oceanography*, 55(2): 580-588.

Villinski, J.E., Saiers, J.E. and Conklin, M.H., 2003. The effects of reaction-product formation on the reductive dissolution of MnO₂ by Fe(II). *Environmental Science & Technology*, 37(24): 5589-5596.

Voelker, B.M., Morel, F.M.M. and Sulzberger, B., 1997. Iron redox cycling in surface waters: Effects of humic substances and light. *Environmental Science & Technology*, 31(4): 1004-1011.

Voelker, B.M. and Sedlak, D.L., 1995. Iron reduction by photoproduced superoxide in seawater. *Marine Chemistry*, 50(1-4): 93-102.

Voelker, B.M., Sedlak, D.L. and Zafiriou, O.C., 2000. Chemistry of superoxide radical in seawater: Reactions with organic Cu complexes. *Environmental Science & Technology*, 34(6): 1036-1042.

Voelker, B.M. and Sulzberger, B., 1996. Effects of fulvic acid on Fe(II) oxidation by hydrogen peroxide. *Environmental Science & Technology*, 30(4): 1106-1114.

Vogel, A.I., 1989. *Vogel's textbook of quantitative chemical analysis*. Harlow: Prentice Hall.

Volker, C. and Wolf-Gladrow, D.A., 1999. Physical limits on iron uptake mediated by siderophores or surface reductases. *Marine Chemistry*, 65(3-4): 227-244.

von Gunten, U., 2003. Ozonation of drinking water: Part 1. Oxidation kinetics and product formation. *Water Research*, 37(7): 1443-1467.

von Gunten, U. and Hoigne, J., 1994. Bromate formation during ozonation of bromide-containing waters - interactions of ozone and hydroxyl radical reactions. *Environmental Science & Technology*, 28(7): 1234-1242.

Waite, T.D. and Morel, F.M.M., 1984. Photoreductive dissolution of colloidal iron-oxides in natural-waters. *Environmental Science & Technology*, 18(11): 860-868.

Walling, C., 1975. Fentons reagent revisited. *Accounts of Chemical Research*, 8(4): 125-131.

Watanabe, K., Shimiya, M., Ogura, T., Shitanda, I. and Itagaki, M., 2008. Flow injection analysis of manganese(II) with umbelliferone as a novel chemiluminescent reagent. *Bunseki Kagaku*, 57(9): 741-746.

Weber, L., Volker, C., Schartau, M. and Wolf-Gladrow, D.A., 2005. Modeling the speciation and biogeochemistry of iron at the Bermuda Atlantic Time-series Study site. *Global Biogeochemical Cycles*, 19(1).

Wedepohl, K.H., 1995. The composition of the continental-crust. *Geochimica et Cosmochimica Acta*, 59(7): 1217-1232.

Weiss, J., 1935. Investigations on the radical HO₂ in solution. *Transactions of the Faraday Society*, 31: 668 - 681.

Weiss, R.F., 1970. Solubility of nitrogen, oxygen and argon in water and seawater. *Deep-Sea Research*, 17(4): 721-726.

Wells, M.L. and Mayer, L.M., 1991. The photoconversion of colloidal iron oxyhydroxides in seawater. *Deep Sea Research Part A. Oceanographic Research Papers*, 38(11): 1379-1395.

Westerhoff, P., Song, R., Amy, G. and Minear, R., 1997. Applications of ozone decomposition models. *Ozone-Science & Engineering*, 19(1): 55-73.

White, E.M., Vaughan, P.P. and Zepp, R.G., 2003. Role of the photo-Fenton reaction in the production of hydroxyl radicals and photobleaching of colored dissolved organic matter in a coastal river of the southeastern United States. *Aquatic Sciences*, 65(4): 402-414.

Wilcoxon, F., 1945. Individual comparisons by ranking method. *Biometrics Bulletin*, 1(6): 80 - 83.

Williams, J.G. and Gray, A.L., 1988. High dissolved solids and ICP-MS: Are they compatible? *Analytical Proceedings*, 25: 385 - 388.

Williams, P.M. et al., 1986. Chemical and microbiological studies of sea-surface films in the southern Gulf of California and off the west-coast of Baja-California. *Marine Chemistry*, 19(1): 17-98.

Williams, R.J.P., 2002. Recent aspects of aluminium chemistry and biology: A survey. *Coordination Chemistry Reviews*, 228(2): 93-96.

Williams, R.J.P. and Frausto da Silva, J.J.R., 1996. *The Natural Selection and Life's Chemistry*. Oxford University Press, Oxford, 646 pp.

Witt, M.L.I., Skrabal, S., Kieber, R. and Willey, J., 2007. Photochemistry of Cu complexed with chromophoric dissolved organic matter: implications for Cu speciation in rainwater. *Journal of Atmospheric Chemistry*, 58(2): 89-109.

Wright, J., 2002. Seawater: Its Composition, Properties And Behaviour. Open University - Oceanography. Butterworth-Heinemann, Oxford, 168 pp.

Wu, J.F. and Boyle, E.A., 1997. Low blank preconcentration technique for the determination of lead, copper, and cadmium in small-volume seawater samples by isotope dilution ICPMS. *Analytical Chemistry*, 69(13): 2464-2470.

Wu, J.F. and Luther, G.W., 1995. Complexation of Fe(III) by natural organic-ligands in the northwest Atlantic-Ocean by a competitive ligand equilibration method and a kinetic approach. *Marine Chemistry*, 50(1-4): 159-177.

Wurl, O. and Holmes, M., 2008. The gelatinous nature of the sea-surface microlayer. *Marine Chemistry*, 110(1-2): 89-97.

Wurl, O., Miller, L., Ruttgers, R. and Vagle, S., 2009. The distribution and fate of surface-active substances in the sea-surface microlayer and water column. *Marine Chemistry*, 115(1-2): 1-9.

Xiao, C.B., Palmer, D.A., Wesolowski, D.J., Lovitz, S.B. and King, D.W., 2002. Carbon dioxide effects on luminol and 1,10-phenanthroline chemiluminescence. *Analytical Chemistry*, 74(9): 2210-2216.

Yacobi, Y.Z., Kalikhman, I., Gophen, M. and Walline, P., 1993. The spatial-distribution of temperature, oxygen, plankton and fish determined simultaneously in Lake Kinneret, Israel. *Journal of Plankton Research*, 15(6): 589-601.

Yamada, N., Takahashi, J. and Sakata, K., 2002. The effects of cell-gas impurities and kinetic energy discrimination in an octopole collision cell ICP-MS under non-thermalized conditions. *Journal of Analytical Atomic Spectrometry*, 17(10): 1213-1222.

Yang, R.J. and van den Berg, C.M.G., 2009. Metal complexation by humic substances in seawater. *Environmental Science & Technology*, 43(19): 7192-7197.

Yocis, B.H., Kieber, D.J. and Mopper, K., 2000. Photochemical production of hydrogen peroxide in Antarctic waters. *Deep-Sea Research Part I-Oceanographic Research Papers*, 47(6): 1077-1099.

Yuan, J.C. and Shiller, A.M., 1999. Determination of subnanomolar levels of hydrogen peroxide in seawater by reagent-injection chemiluminescence detection. *Analytical Chemistry*, 71(10): 1975-1980.

Yuan, J.C. and Shiller, A.M., 2001. The distribution of hydrogen peroxide in the southern and central Atlantic Ocean. *Deep-Sea Research Part II-Topical Studies in Oceanography*, 48(13): 2947-2970.

Yuan, J.C. and Shiller, A.M., 2004. Hydrogen peroxide in deep waters of the North Pacific Ocean. *Geophysical Research Letters*, 31(1).

Zafiriou, O.C., 1990. Chemistry of superoxide ion-radical (O₂-) in seawater. 1. Pk-Star-Asw (H₂O₂) and uncatalyzed dismutation kinetics studied by pulse-radiolysis. *Marine Chemistry*, 30(1-3): 31-43.

Zafiriou, O.C., Voelker, B.M. and Sedlak, D.L., 1998. Chemistry of the superoxide radical (O₂-) in seawater: Reactions with inorganic copper complexes. *Journal of Physical Chemistry A*, 102(28): 5693-5700.

Zepp, R.G. and Cline, D.M., 1977. Rates of direct photolysis in aquatic environment. *Environmental Science & Technology*, 11(4): 359-366.

Zhang, Z.B., Cai, W.J., Liu, L.S., Liu, C.Y. and Chen, F.Z., 2003a. Direct determination of thickness of sea surface microlayer using a pH microelectrode at original location. *Science in China Series B-Chemistry*, 46(4): 339-351.

Zhang, Z.B., Liu, L.S., Liu, C.Y. and Cai, W.J., 2003b. Studies on the sea surface microlayer. II. The layer of sudden change of physical and chemical properties. *Journal of Colloid and Interface Science*(264): 148 - 159.

Zhou, J., Mopper, K. and Passow, U., 1998. The role of surface-active carbohydrates in the formation of transparent exopolymer particles by bubble adsorption of seawater. *Limnology and Oceanography*, 43(8): 1860-1871.